UNIVERSITÀ
DI PAVIA

PhD IN BIOMEDICAL SCIENCES

DEPARTMENT OF BRAIN AND BEHAVIORAL SCIENCES

"MOLECULAR MARKERS IN DIFFUSE GLIOMAS: DIAGNOSTIC AND THERAPEUTIC TARGETS"

PhD Tutor: Enrico Marchioni

PhD dissertation of

Giulia Berzero

a.a. 2019/2020

In loving memory of Professor Arrigo Moglia (1947-2020)

Index

List of widely accepted abbreviations not defined in the text:

cDNA=complementary DNA

CGH-array=Comparative Genomic Hybridization - array

CNS=Central Nervous System

CNV=copy number variation

CSF=cerebrospinal fluid

DNA=deoxyribonucleic acid

FFPE=formalin-fixed paraffin-embedded

G-CIMP=Glioma-CpG Island Methylator Phenotype

GBM=glioblastoma

HLA=human leukocyte antigen

KPS=Karnofsky Performance Status

LGG=lower grade gliomas

MRI=magnetic resonance imaging

mRNA=messenger RNA

NGS=next generation sequencing

OS=overall survival

PCR=polymerase chain reaction

PCV=procarbazine, CCNU, vincristine

PET=positron emission tomography

PFS=progression-free survival

RNA=ribonucleic acid

SNP=single nucleotide polymorphism

SNV=single nucleotide variant

WES=whole exome sequencing

WGS=whole genome sequencing

WHO=world health organization

Introduction: molecular markers in diffuse gliomas

Diagnosis and classification

Histology and its limitations. Gliomas form a heterogeneous group of tumors that have been traditionally classified based on histological class and grade. Histological class reflects the similarities between tumor cells and the putative cell of origin, and it is assessed based on morphologic features on hematoxylin-eosin sections and on the expression of lineage-associated proteins on immunohistochemistry. Grade is attributed based on mitotic activity, the presence of anaplasia, necrosis and endothelial proliferation, whicht reflect an increasing degree of malignancy (Figure 1) (Perry and Wesseling, 2016) (Gladson, Prayson and Liu, 2010).

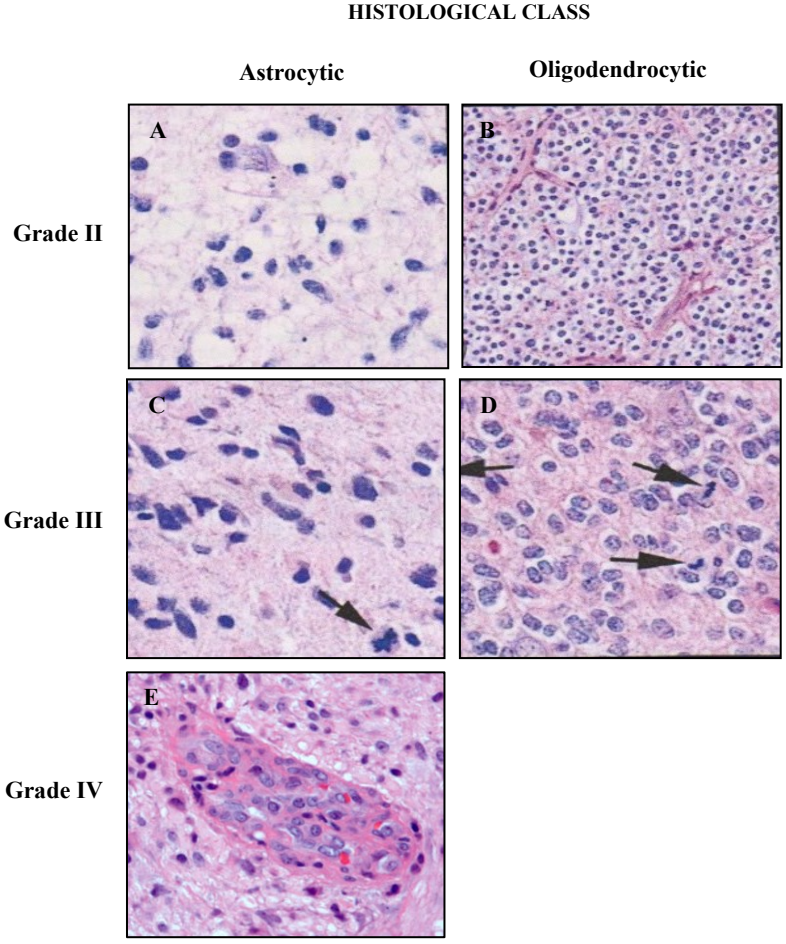

Figure 1. Histological features in diffuse gliomas. Panel A: diffuse astrocytoma with hypercromatic nuclei (WHO grade II). Panel B: oligodendroglioma with uniform rounded nuclei, branched capillaries and characteristic clear perinuclear haloes (WHO grade II). Panel C: anaplastic astrocytoma with mitotic activity (arrow) (WHO grade III). Panel D: anaplastic oligodendroglioma displaying increased mitotic activity (arrows) (WHO grade III). Panel E: glioblastoma showing endothelial cell proliferation (WHO grade IV). Panel A-D: modified from Perry and Wesseling, 2016. Panel E: from Gladson *et al.,* 2010.

The 2007 WHO classification of the Tumors of the Nervous System (Louis *et al.*, 2007) relied entirely on these cardinal principles, dividing gliomas based on presumptive cell lineage (astrocytic, oligoastrocytic or oligodendroglial) and grade (I-IV). Grade I was reserved to circumscribed astrocytomas with benign behavior (e.g., pilocytic astrocytoma), grade II was attributed to astrocytic or oligodendrocytic tumors with cytological atypia, grade III was assigned to those showing anaplasia and mitotic figures, and grade IV was assigned to those showing microvascular proliferation and/or necrosis (Table 1).

Table 1. Main glioma diagnostic entities in the 2007 WHO classification of Tumors of the Central Nervous System (Louis *et al.*, 2007).

Histological class	**Histological subtype**	**Grade**
Astrocytic tumors	Pilocytic astrocytoma	I
	Subependymal giant cell astrocytoma	I
	Diffuse astrocytoma	II
	Pleomorphic xanthoastrocytoma	II
	Anaplastic astrocytoma	III
	Glioblastoma	IV
Oligoastrocytic tumors	Oligoastrocytoma	II
	Anaplastic oligoastrocytoma	III
Oligodendroglial tumors	Oligodendroglioma	II
	Anaplastic oligodendroglioma	III

However, it progressively became evident that histology was affected by a high degree of inter-observer variability and that grade was not always sufficient to separate entities characterized by different malignant behavior, especially in the case of lower grade gliomas (Perry and Wesseling, 2016).

The road towards an "integrated" diagnosis. The discovery that lower grade gliomas, as well as glioblastomas arising from the former, frequently harbored hotspot mutations in the *IDH1* (codon 132) and *IDH2* (codon 172) genes (Parsons *et al.*, 2008) (Yan *et al.*, 2009) represented a real breakthrough in the understanding of gliomagenesis. *IDH1* and *IDH2* mutations, thereafter referred to as *IDH* mutations, were found to characterize astrocytomas and oligodendrogliomas with diffusely infiltrative behavior and to be absent in other cerebral and extracerebral tumors (Yan *et al.*, 2009). *IDH*-mutant gliomas displayed indeed different clinical and molecular features compared to *IDH*-wildtype tumors. Differently from *IDH*-wildtype gliomas, which associated with *EGFR* amplification and chromosome 10 loss, *IDH*-mutant gliomas associated with chromosome 1p/19q codeletion and *MGMT* promoter methylation (Yan *et al.*, 2009) (Sanson *et al.*, 2009). The chromosome 1p/19q codeletion is a genetic alteration consisting in the allelic loss of the entire short arm of chromosome 1 and the entire long arm of chromosome 19, with a centromeric breakpoint. This chromosomal alteration had been reported since the 1990s as a distinguishing feature of oligodendroglial tumors (Reifenberger *et al.*, 1994),

making intriguing its association with *IDH* mutations. This association was confirmed by a large genomic study that disclosed that all 1p/19q codeleted gliomas harbored *IDH1* or *IDH2* mutations, while instead not all *IDH*-mutant gliomas harbored the 1p/19q codeletion (Labussière *et al.*, 2010).

As confirmed by unsupervised clustering analyses, the *IDH* mutation and the chromosome 1p/19q codeletion allowed to identify three robust non-overlapping glioma groups characterized by different sets of genetic alterations (Figure 2) (Cancer Genome Atlas Research Network *et al.*, 2015) (Suzuki *et al.*, 2015):

1) *IDH*-mutant, 1p/19q codeleted gliomas, commonly appearing as oligodendrogliomas and showing *TERT* promoter (96-98%), *CIC* (58-62%), *NOTCH1* (31%), *FUBP1* (29-31%), and *PIK3CA* (20%) mutations;

2) *IDH*-mutant, 1p/19q non-codeleted gliomas, commonly appearing as astrocytomas and showing *TP53* mutations (94-99%) and *ATRX* alterations (77-86%);

3) *IDH*-wildtype gliomas, characterized by molecular alterations commonly found in primary glioblastomas, including *EGFR* amplifications (38%), *CDKN2A* deletions (63%), chromosome 7 gain (56%), chromosome 10 loss (63%), and *TERT* promoter mutations (64%).

The observation that the three molecular groups identified by unsupervised clustering analysis were more concordant with the *IDH* and the 1p/19q codeletion status than with histological class (Cancer Genome Atlas Research Network *et al.*, 2015) provided a strong rationale for using the *IDH* and the 1p/19q codeletion status for the classification of lower grade gliomas.

The 2016 WHO classification of Tumors of the Central Nervous System. Based on this evidence, in 2016, it was released an update to the WHO classification, incorporating the *IDH* mutation and the chromosome 1p/19q codeletion into the definition of different nosological entities (Louis *et al.*, 2016) (Table 2): oligodendrogliomas were defined by the presence of the *IDH* mutation and the chromosome 1p/19q codeletion, while astrocytomas were defined as either *IDH*-mutant or *IDH*-wildtype tumors lacking the 1p/19q codeletion. The diagnosis of "oligoastrocytoma" was highly discouraged, as genetic testing was supposed to allow assigning tumors with mixed histological features either to the group of *IDH*-mutant 1p/19q codeleted oligodendrogliomas (*TERT* promoter, *CIC* and/or *FUBP1*-mutant) or to the group of *IDH*-mutant astrocytomas (*TP53*-mutant and/or *ATRX*-inactivated). Integrating genetic features to histology represented a real paradigm shift in a classification scheme that had until then relied entirely on histology, adding a level of objectivity that had until then been missing.

Figure 2. Main genetic alterations in the three glioma subgroups identified by the *IDH* mutation and the chromosome 1p/19q codeletion status. Modified from Suzuki *et al.,* 2015.

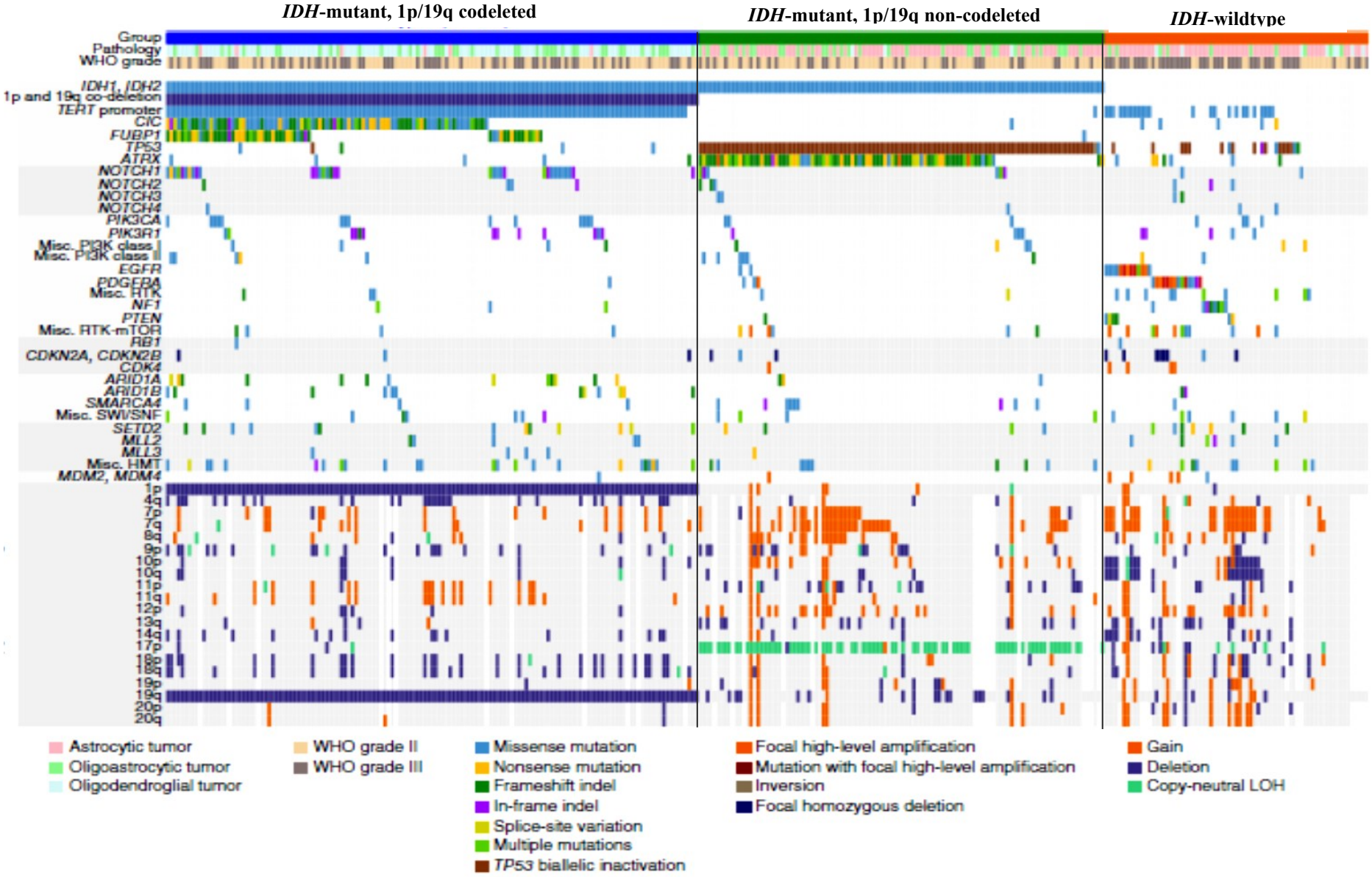

The observation that *IDH* mutations were found in oligodendrogliomas and astrocytomas with diffusely infiltrating appearance but not in gliomas with circumscribed growth (e.g., pilocytic astrocytomas, pleomorphic xanthoastrocytomas) ultimately led to separate circumscribed from diffuse gliomas, based on the observation that these two groups of tumors that do not share the same genetic drivers (Louis *et al.*, 2016). This represented a great conceptual advance considering that, until then, entities like pilocytic astrocytomas had been grouped together with diffuse astrocytomas based on their morphological features (Table 1 and Table 2).

Table 2. Main diagnostic entities for the group of diffuse gliomas according to the 2016 WHO classification (Louis *et al.,* 2016).

Molecular group	**Integrated diagnosis**	**Grade**
IDH-mutant, 1p/19q codeleted	Oligodendroglioma, *IDH*-mutant 1p/19q codeleted	II
	Anaplastic oligodendroglioma, *IDH*-mutant 1p/19q codeleted	III
IDH-mutant, 1p/19q non-codeleted	Diffuse astrocytoma, *IDH*-mutant	II
	Anaplastic astrocytoma, *IDH*-mutant	III
	Glioblastoma, *IDH*-mutant	IV
IDH-wildtype	Diffuse astrocytoma, *IDH*-wildtype	II
	Anaplastic astrocytoma, *IDH*-wildtype	III
	Glioblastoma, *IDH*-wildtype	IV
	Diffuse midline gliomas, *H3K27M*-mutant	IV

The 2016 WHO classification also introduced a novel tumor entity, named "diffuse midline glioma, H3 K27M-mutant". This entity designates gliomas with a diffuse pattern of growth, located along the midline (e.g., thalamus, brainstem, spinal cord) and harboring K27M mutations in the *H3F3A* gene (Louis *et al.*, 2016). Diffuse midline H3 K27M-mutant gliomas are invariably *IDH*-wildtype and, based on their reported outcome in the pediatric population, they are supposed to be associated with poor prognosis. For this reason, in the 2016 WHO classification, diffuse midline H3 K27M-mutant gliomas are invariably considered as grade IV malignancies regardless of the presence of anaplasia, necrosis, and/or endothelial proliferation (Louis *et al.*, 2016).

Prognosis and response to cytotoxic treatments

Predictors of overall survival. Besides their value for purposes of diagnostic classification, the *IDH* mutation and the chromosome 1p/19q codeletion represent important prognostic and predictive markers. Patients with *IDH*-mutant tumors have longer OS compared to patients with *IDH*-wildtype tumors. This observation is valid across tumor grades (Yan *et al.*, 2009) (Sanson *et al.*, 2009) and remains true after adjusting for age, grade, genetic profile and treatment, suggesting that the *IDH* mutation represents an independent predictor of OS (Sanson *et al.*, 2009).

The chromosome 1p/19q codeletion, which is invariably associated with *IDH1* or *IDH2* mutations, seems to confer an additional survival benefit (Cairncross *et al.*, 1998), *IDH*-mutant 1p/19q codeleted tumors having longer OS compared to *IDH*-mutant 1p/19q non-codeleted gliomas and, especially, *IDH*-wildtype gliomas (Labussière *et al.*, 2010). The prognostic stratification based on molecular subgroups ultimately provides more accurate prognostic estimates than histology (Figure 3) (Cancer Genome Atlas Research Network *et al.*, 2015) (Tabouret *et al.*, 2016), emphasizing the robustness of the classification scheme relying on molecular markers.

As shown in Figure 3, *IDH*-wildtype gliomas are associated with the poorest prognosis (Labussière *et al.*, 2010) (Cancer Genome Atlas Research Network *et al.*, 2015) (Tabouret *et al.*, 2016). The main prognostic indicators in this group, epidemiologically enriched with grade IV malignancies, are *TERT* promoter mutation and *EGFR* amplification, which allow an accurate prognostic separation of glioblastomas (Labussière *et al.*, 2014a). Evidence suggests that these two molecular alterations might have a prognostic role also in *IDH*-wildtype grade II and III gliomas, so that, together with whole chromosome 7 gain and whole chromosome 10 loss, they have been proposed by the cIMPACT consortium as biomarkers of aggressive clinical behavior in *IDH*-wildtype lower grade gliomas (Brat *et al.*, 2018) (Tesileanu *et al.*, 2020).

Predictors of response to alkylating agents. Besides having an inherent prognostic value, some molecular markers are also predictive of the response to cytotoxic treatments, so that they are currently used for treatment decisions. *IDH* mutations have been consistently associated with improved responses to alkylating agents including temozolomide and PCV (Houillier *et al.*, 2010). As demonstrated by clinical trials conducted in this population, patients with *IDH*-mutant grade II (Buckner *et al.*, 2016) and grade III (Cairncross et al. 2014) gliomas show longer PFS and OS if treated with radiation plus PCV compared to radiation alone. Gliomas that, besides the *IDH* mutation, also harbor the chromosome 1p/19q codeletion, show even better responses to alkylating agents (Houillier *et al.*, 2010), in line with the sharp chemosensitivity reported for 1p/19q codeleted oligodendrogliomas in early studies (Cairncross *et al.*, 1998) (van den Bent *et al.*, 2003). Clinical trials conducted in patients with *IDH*-mutant 1p/19q codeleted gliomas confirmed that they experience a substantial benefit in terms of both PFS and OS with the addition of PCV to radiation (Cairncross *et al.*, 2013) (van den Bent *et al.*, 2013).

Figure 3. Prognostic stratification of grade II and III diffuse gliomas based on molecular subgroup (panel A,C) or histology (panel B,D). Panel A: prognostic stratification of WHO grade II gliomas based on molecular subgroups; blue line = *IDH*-mutant, 1p/19q codeleted, green line = *IDH*-mutant, 1p/19q non-codeleted; red line = *IDH*-wildtype (median OS: 176 vs. 99 vs. 57 months, p < 0.0001). Panel B: prognostic stratification of WHO grade II gliomas based on histological class; orange line = oligodendrogliomas; purple line = oligoastrocytomas; grey line = astrocytomas (median OS: 123 vs. 118 vs. 101 months, p=0.45). Panel C: prognostic stratification of WHO grade III gliomas based on molecular subgroups; blue line = *IDH*-mutant, 1p/19q codeleted, green line = *IDH*-mutant, 1p/19q non-codeleted; red line = *IDH*-wildtype (median OS: 120 vs. 47 vs. 20 months, p <0.0001). Panel D: prognostic stratification of WHO grade III gliomas based on histological class; orange line = oligodendrogliomas; purple line = oligoastrocytomas; grey line = astrocytomas (median OS: 62 vs. 38 vs. 29 months, p=0.0012). Unpublished data from the OncoNeuroTek database, Hopitaux Universitaires Pitié-Salpetrière- Charles Foix, Paris, France.

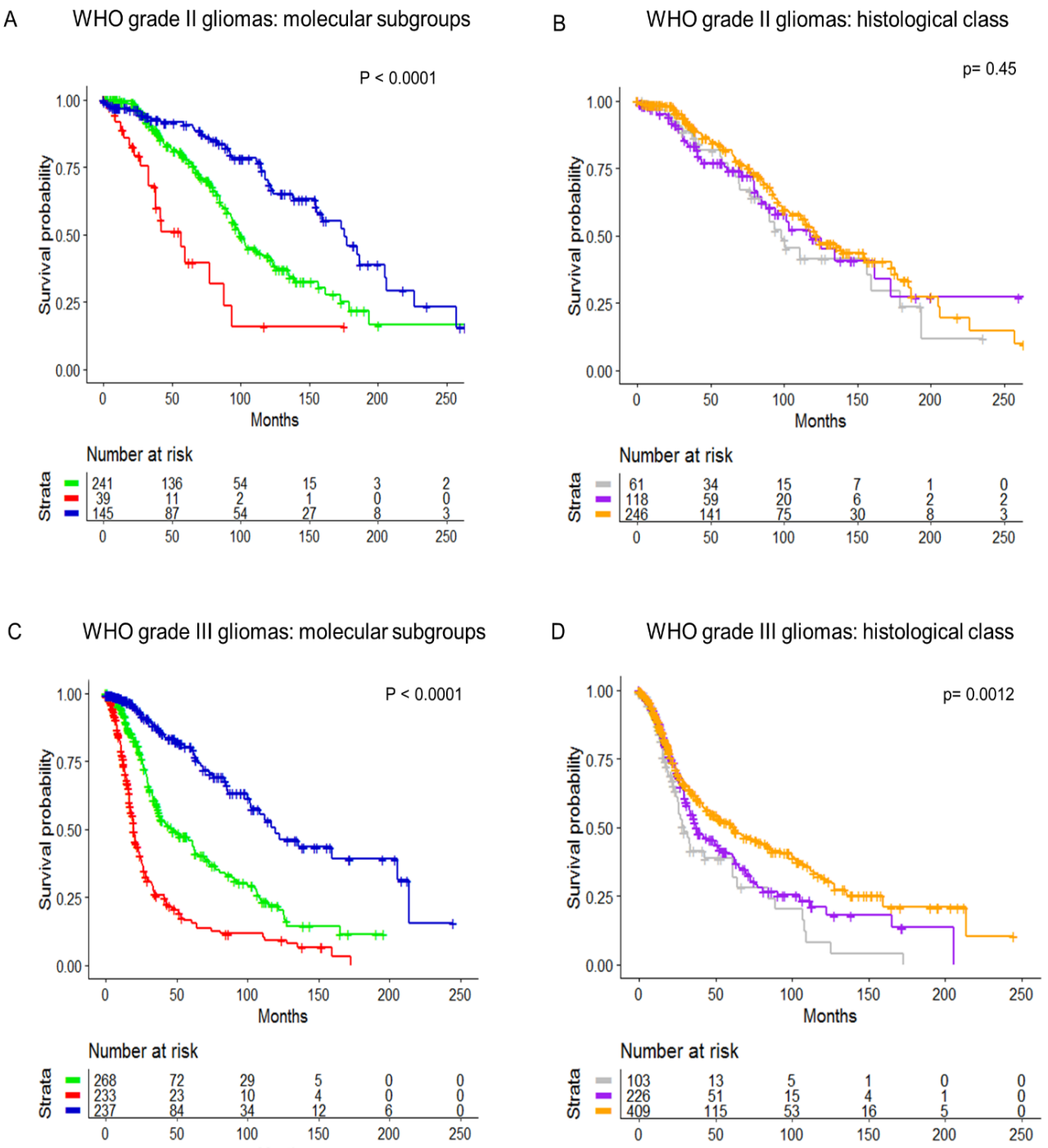

The biological mechanisms underlying the increased chemosensitivity associated with the *IDH* mutation and the chromosome 1p/19q codeletion have not been completely unraveled. *IDH*-mutant tumors are associated with a status of DNA hypermethylation that has been referred to as "glioma-CpG island methylator phenotype (G-CIMP)" (Noushmehr *et al.*, 2010) (Turcan *et al.*, 2012). This status of DNA hypermethylation is related to the intracellular accumulation of 2-hydroxyglurate (2HG), an oncometabolite that results from the neomorphic activity of IDH-mutant enzymes. The intracellular accumulation of 2HG inhibits a number of α-ketoglutarate-dependent dioxygenases, including histone and DNA demethylases, causing a state of DNA hypermethylation (Turcan *et al.*, 2012) (Xu *et al.*, 2011) (Chowdhury *et al.*, 2011). Among the genetic loci hypermethylated in G-CIMP gliomas, there is the promoter of the gene *MGMT*, encoding for a DNA-repair protein whose physiologic function is to reverse the cross-linking between the double strands of DNA, such as the one caused by alkylating agents. *MGMT* promoter methylation results in the silencing of this gene and thus in an increased sensitivity to alkylating agents, as their activity is no longer counteracted by physiological DNA repair. *MGMT* promoter methylated gliomas are associated with better responses to alkylating agents (Esteller *et al.*, 2000) (Hegi *et al.*, 2005), whether *IDH*-mutant or not (Wick *et al.*, 2016) (Wick *et al.*, 2012).

The evidence that some molecular markers provide solid prognostic and predictive information has led the scientific community to revise treatment recommendations accordingly. The latest guidelines of the European Association of Neuro-Oncology (EANO) for astrocytic and oligodendrocytic tumors integrated molecular markers with known prognostic significance (*IDH* mutation, 1p/19q codeletion, *MGMT* promoter methylation status) to classical prognostic factors (age, performance status, extent of resection, grade) to provide updated recommendations for patient management (Weller *et al.*, 2017):

- *IDH*-mutant 1p/19q codeleted oligodendrogliomas (grade II) can be managed by observation after complete resection or if the patient is younger than 40 years-old and has no neurological deficits;
- *IDH*-mutant 1p/19q codeleted anaplastic oligodendrogliomas (grade III) should be treated with radiotherapy followed by PCV;
- *IDH*-mutant astrocytomas (grade II) can be managed by observation after gross total resection or if the patient is younger than 40 years-old and has no neurological deficits;
- *IDH*-mutant anaplastic astrocytomas (grade III) should be treated with concomitant or sequential radiochemotherapy with PCV or temozolomide;
- *IDH*-wildtype astrocytomas (grade II) have not yet been attributed a standard of treatment and several options ranging from radiotherapy alone to concomitant radiochemotherapy are considered acceptable based on age, performance status, and *MGMT* promoter methylation status;
- *IDH*-wildtype anaplastic astrocytomas (grade III) should receive concomitant radiochemotherapy with temozolomide followed by adjuvant temozolomide, similarly to glioblastomas (Stupp *et al.*, 2005);
- *IDH*-wildtype glioblastomas (grade IV) should receive concomitant radiochemotherapy with temozolomide followed by adjuvant temozolomide (Stupp *et al.*, 2005) if ≤ 70 years-old and with good performance status.

Targeted therapies

As emphasized in previous chapters, molecular markers have capital importance for the classification, prognostic stratification, and management of patients with diffuse gliomas. Besides these important functions, some molecular alterations can also represent therapeutic targets, being available specific inhibitors. Though the use of targeted therapies for diffuse gliomas is still in its infancy, there is great hope they will ultimately enter clinical practice, providing novel options especially for disseminated and recurrent tumors. Hereafter, we will briefly describe some of the targeted therapies that are being experimented in gliomas in the context of clinical trials or as part of expanded access programs.

IDH inhibitors

Besides diffuse gliomas, *IDH* mutations are detected in acute myeloid leukemias, cholangiocarcinomas, enchondromas, chondrosarcomas, and other uncommon malignancies (Dang, Yen and Attar, 2016). *IDH1* and *IDH2* encode for homonymous intracellular enzymes that normally convert isocitrate to α-ketoglutarate (αKG) via oxidative decarboxylation. Altering key residues within the active site of the enzyme, hotspot mutations in *IDH1* (codon 132) and *IDH2* (codon 172) confer a neomorphic enzymatic activity that results in the conversion of αKG to 2-hydroxyglutarate (2HG), which accumulates intracellularly (Dang *et al.*, 2009) (Figure 4).

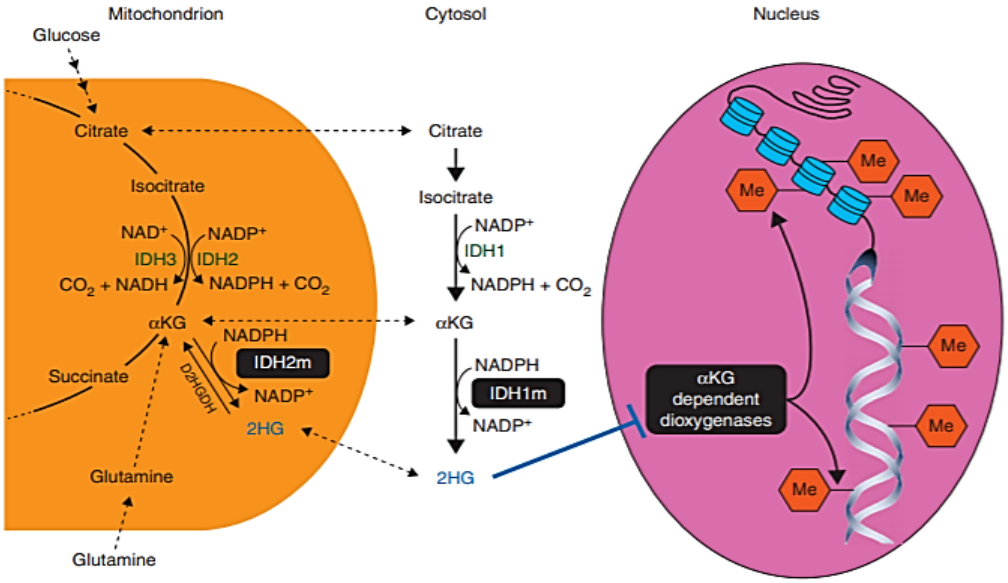

Figure 4. IDH1 and IDH2 normal function, and neomorphic enzymatic activity of mutant IDH1 (IDH1m) and mutant IDH2 (IDH2m). Modified from Dang et al. 2016.

The mutant isoforms of the enzymes IDH1 and IDH2 can be effectively targeted by IDH inhibitors, small molecules that bind to the catalytic site of the mutant enzyme, blocking the conformational change required for the enzyme to convert αKG to 2HG (Kaminska *et al.*, 2019). By preventing the conversion of αKG to 2HG,

IDH inhibitors prevent the intracellular accumulation of 2HG and, thus, its oncogenic effects. Several molecules, inhibiting either the mutant isoform of IDH1 (AG-120, IDH305), the mutant form of IDH2 (AG-221), or both (AG-881) are currently being experimented in the context of basket trials for *IDH*-mutant malignancies (Table 3) (Kaminska *et al.*, 2019). While these agents have already demonstrated a good safety profile and promising results in patients with hematological malignancies (Kaminska *et al.*, 2019), their efficacy in patients with diffuse gliomas is still pending the results of early trials.

Table 3. IDH inhibitors that are currently being experimented in patients with diffuse gliomas. Modified from Dang et al. 2016.

Molecule	**Target**	**Phase of ongoing trials**	**Clinical trial identifier (clinicaltrials.gov)**
AG-120	IDH1 R132H	I	NCT02073994
IDH305	IDH1 R132H	II	NCT02977689; NCT02987010
AG-221	IDH2	I/II	NCT02273739
AG-881	pan-IDH1/2	I	NCT02481154

EGFR inhibitors

EGFR amplifications are detected in about 60% of *IDH*-wildtype glioblastomas, resulting in an increased oncogenic signal by the tyrosine kinase receptor EGFR (An *et al.*, 2018). First-generation EGFR inhibitors (gefinitib, erlotinib, lapatinib) act by orthosterically blocking the binding pocket of its tyrosine kinase domain. While these agents showed substantial activity in patients with *EGFR*-mutant non-small cell lung cancer, they were associated with deceiving results in GBM patients (Lee *et al.*, 2020). Second-generation EGFR inhibitors (afatinib, dacomitinib), designed to irreversibly bind to the tyrosine kinase domain of EGFR, have recently been experimented in the context of phase II clinical trials (Reardon *et al.*, 2015) (Sepúlveda-Sánchez *et al.*, 2017), with limited clinical efficacy. These disappointing results have prompted to design a third generation of EGFR inhibitors (rociletinib, AZD9291) that have shown encouraging efficacy in preclinical models. Anti-EGFR monoclonal antibodies (cetuximab, panitumumab, nimotuzumab) have shown little promise for the treatment of GBM because of limited blood-brain barrier penetration (An *et al.*, 2018), while the antibody-drug conjugate ABT-414 (depatuxizumab mafodotin) showed some activity in recurrent glioblastoma (van den Bent *et al.*, 2017) (Van Den Bent *et al.*, 2020) warranting further exploration despite frequent corneal toxicity.

Besides *EGFR* amplification, glioblastomas might present intragenic deletions resulting in the rearrangement of the EGFR. The most common rearrangement detected in patients with GBM is referred to as EGFRvIII. Being constitutively active, EGFRvIII promotes several tumorigenic functions including cell proliferation, invasion, and angiogenesis (An *et al.*, 2018). As most EGFR inhibitors display little or no inhibitory effect over EGFRvIII, specific strategies are being experimented to counteract its detrimental effects, including vaccination (rindopepimut). However, despite initial hopes, vaccination with EGFRvIII ultimately failed to demonstrate its

efficacy in a randomized trial conducted in a large cohort of glioblastoma patients (Weller, Butowski, *et al.*, 2017).

RAF and MEK inhibitors

BRAF V600E is an activating mutation that leads to the constitutive activation of BRAF, a serine/threonine protein kinase of the RAF family that promotes cell proliferation and survival (Figure 5, panel A and B). Though more common in melanoma, non-small cell lung cancer, and colorectal cancers, *BRAF* V600E mutations are detected in a proportion of diffuse and circumscribed gliomas, including pleomorphic xanthoastrocytomas (60-80%), gangliogliomas (20-70%), pilocytic astrocytomas (10%), *IDH*-wildtype glioblastomas and anaplastic astrocytomas (3%) (Schreck, Grossman and Pratilas, 2019). The constitutive activation of BRAF that is associated with V600E mutations can be effectively inhibited by RAF inhibitors, small molecules that selectively inhibit the kinases of the RAF family (Figure 5, panel C) (Schreck, Grossman and Pratilas, 2019) (Hagen and Trinh, 2014). RAF inhibitors (vemurafenib, dabrafenib, encorafenib) are commonly used in association with MEK inhibitors (cobimetinib, trametinib, binimetinib) (Figure 5, panel C), small molecules that prevent the activation of ERK, a downstream signaling molecule that is often responsible for the acquired resistance to RAF inhibitors (Schreck, Grossman and Pratilas, 2019).

Figure 5. Functional consequences of BRAF V600E mutations and mechanism of action of RAF and MEK inhibitors. Panel A: Physiological condition in which, following the binding of extracellular growth factors to the corresponding tyrosine kinase membrane receptor, MAPK signaling pathway is activated to promote cell proliferation and survival. Panel B: In presence of *BRAF* V600E mutations, BRAF is constitutively activated, regardless of the binding of growth factors, resulting in a sustained promotion of cell proliferation and survival. Panel C: The administration of RAF (vemurafenib, dabrafenib, encorafenib) and MEK (cobimetinib, trametinib, binimetinib) inhibitors can stop the constitutive stimulation associated with *BRAF* V600 mutations. Modified from Hagen and Trinh, 2014.

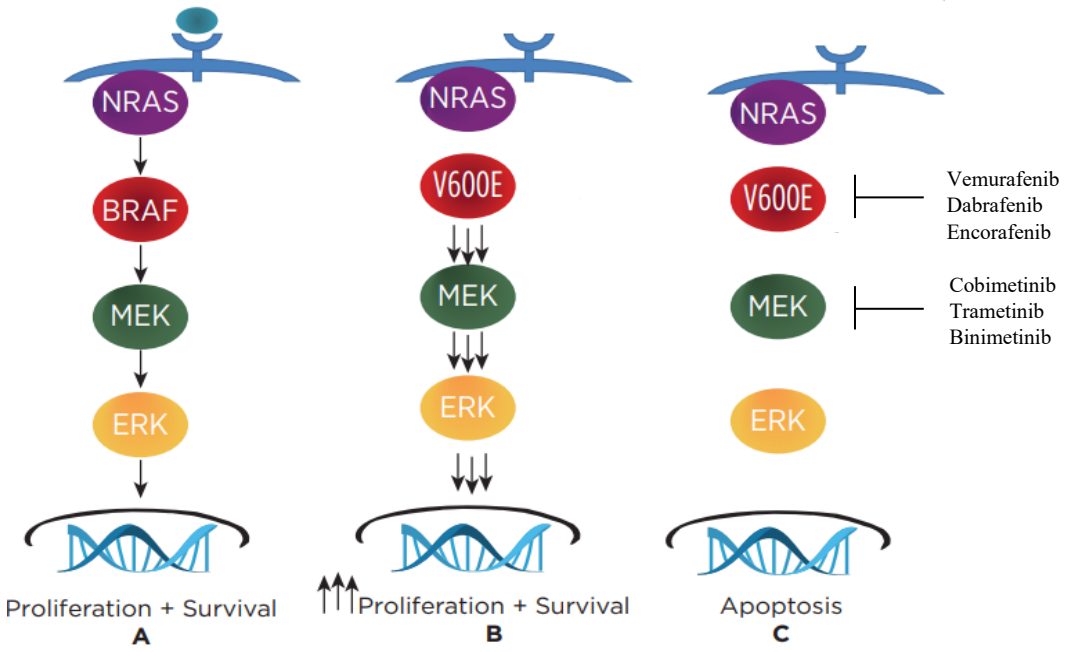

RAF and MEK inhibitors have to date been approved by the European Medicine Agency only for the treatment of *BRAF* V600-mutant melanoma. As a result, data on the efficacy of these agents in adult and pediatric patients with diffuse and circumscribed gliomas is limited to isolated cases or small cohorts of patients treated within basket trials (Kaley *et al.*, 2018) (Wen, Alexander, *et al.*, 2018) (Wen, De Greve, *et al.*, 2018). With these limitations, preliminary results suggest that RAF and MEK inhibitors are associated with favorable and prolonged responses in a substantial proportion of patients, encouraging further studies.

FGFR inhibitors

Hotspot *FGFR1* mutations (N546 and K656) have been detected in a number of human cancers, including diffuse and circumscribed gliomas, dysembryoplastic neuroepithelial tumors, and glioneuronal tumors (Picca *et al.*, 2018) (Dyson *et al.*, 2016) (Rivera *et al.*, 2016) (Ryall *et al.*, 2016) (Gessi *et al.*, 2014) (Schwartzentruber *et al.*, 2012). *FGFR1* N546 and K656 mutations result in the constitutive activation of the FGFR1 (Bennett *et al.*, 2016), promoting cell proliferation, differentiation, and survival. Though overall uncommon in gliomas, activating *FGFR1* mutations can be effectively targeted by FGFR tyrosine kinase inhibitors including JNJ-42756493, BGJ398, TAS-120 and AZD4547, small molecules that inhibit FGFR-mediated signaling by occupying the ATP binding pockets of their tyrosine kinase domains (Table 4) (Facchinetti *et al.*, 2020) (Touat *et al.*, 2015).

Table 4. FGFR inhibitors in clinical development for gliomas and other solid tumors. Modified from Facchinetti *et al.*, 2020.

Molecule	**Targets**	**Inhibition type**	**Phase of ongoing trials**	**Clinical trial identifier (clinicaltrials.gov)**
Erdafitinib (JNJ-42756493)	FGFR1-4	reversible	II/III	NCT02465060
Infigratinib (BGJ398)	FGFR1-3	reversible	II/III	NCT01975701
Pemigatinib (INCB054828)	FGFR1-3	reversible	II/III	NCT03822117
Rogaratinib (BAY1163877)	FGFR1-3	reversible	II/III	NCT04125693
Derazatinib (ARQ087)	FGFR1-4	reversible	II	NCT01752920
TAS-120	FGFR1-4	covalent	II	NCT02052778
AZD4547	FGFR1-3	reversible	II	NCT04439240
Debio 1347 (CH5183284)	FGFR1-3	reversible	II	NCT03834220
LY2874455	FGFR1-4	reversible	I	NCT01212107

Besides *FGFR1*-mutant tumors, FGFR inhibitors can be used to treat gliomas harboring *FGFR3-TACC3* fusions. *FGFR3-TACC3* are oncogenic gene fusions, detected in about 3% of *IDH*-wildtype glioblastomas and lower grade gliomas, that commonly result from the in-frame fusion of the exon 17 of *FGFR3* and of the exon 11 of *TACC3* (Figure 6) (Di Stefano *et al.*, 2015) (Lasorella, Sanson and Iavarone, 2017).

Figure 6. *FGFR3-TACC3* rearrangements in *IDH*-wildtype glioblastomas and lower grade gliomas. Genomic localization of the *FGFR3* and *TACC3* loci (upper row). In the *FGFR3-TACC3* variant reported in gliomas, the genomic rearrangement causes the juxtaposition of exon 17 (and a small portion of intron 17) of the *FGFR3* gene with intron 10 of the *TACC3* gene, leading to in-frame fusion of exon 17 of *FGFR3* and exon 11 of *TACC3* (intermediate row). This fusion structure is one of the most frequent variants identified in gliomas. The structure of the FGFR3-TACC3 fusion protein is shown in the bottom row and invariably includes the tyrosine kinase (TK) domain of FGFR3 and the coiled-coil domain of TACC3. Modified from Lasorella *et al*., 2017.

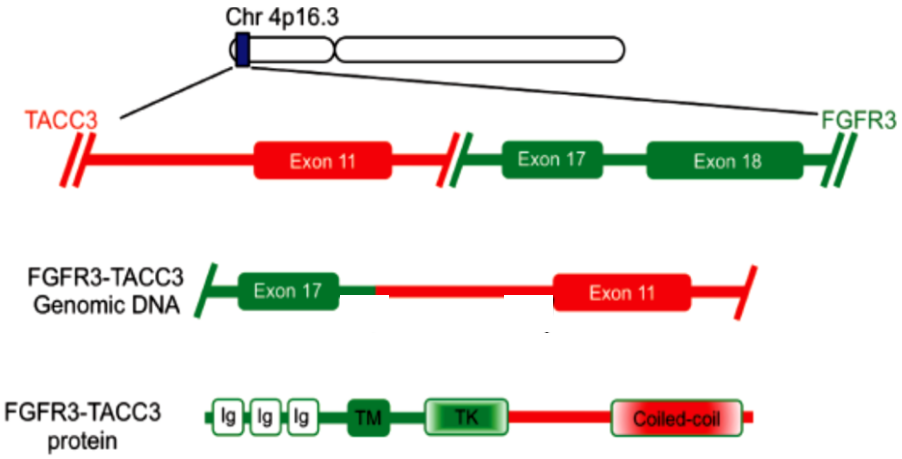

Though the signaling events operating downstream of FGFR-TACC and executing its oncogenic functions are not completely understood, evidence suggests that *FGFR3-TACC3* fusions might be tumor-initiating events, conferring to the tumor a distinctive metabolic profile (Frattini *et al.*, 2018). Resulting in the constitutive activation of FGFR3, *FGFR3-TACC3* fusions confer a strong sensitivity to FGFR inhibitors, observation that is consistent with data from preclinical models and early clinical trials (Lasorella, Sanson and Iavarone, 2017) (Di Stefano *et al.*, 2015). The strong and protracted responses observed following targeted therapy in patients with gliomas with *FGFR3-TACC3* fusions highlight the importance of screening for this rare but actionable genetic alteration that is typical of *IDH*-wildtype gliomas.

Multikinase inhibitors

Some kinase inhibitors do not specifically target a single receptor (or family of receptors) but show a broad effect on multiple kinases. This is the case of regorafenib, an oral inhibitor that targets multiple kinases involved in angiogenesis (VEGFR1-3, TIE2), cell proliferation (KIT, RET, RAF1, BRAF), microenvironment regulation (PDGFR, FGFR), and tumor immunity (CSF1R). Regorafenib has been recently experimented in patients with recurrent GBM in a multicenter, randomized, controlled phase II clinical trial, showing a significant improvement of overall survival compared to standard treatment (Lombardi *et al.*, 2019). Based on these encouraging results, regorafenib is currently being experimented in newly diagnosed glioblastoma (NCT03970447) and in recurrent glioblastoma after failure of antiangiogenics (NCT04051606).

Single nucleotide polymorphisms associated with glioma risk: correlations with tumor genotype

Background

Diffuse gliomas are the most common malignant primary brain tumors in adults. Despite being devastating tumors, little is known about their etiology and, aside from the exposure to ionizing radiation, which accounts for very few cases, no environmental or lifestyle factors have been unambiguously linked to glioma risk (Bondy *et al.*, 2008). Recent genome-wide association studies (GWAS) have, however, enlightened our understanding of gliomagenesis by identifying SNPs at multiple independent loci influencing glioma risk (Shete *et al.*, 2009) (Wrensch *et al.*, 2009) (Sanson *et al.*, 2011) (Stacey *et al.*, 2011) (Jenkins *et al.*, 2012) (Kinnersley *et al.*, 2015) (Melin *et al.*, 2017). While understanding the functional bases of these risk loci offers the prospect of gaining insights into glioma development, few have been deciphered. Notable exceptions are the 17p13.1 locus, where the risk SNP rs78378222 disrupts *TP53* polyadenylation (Stacey *et al.*, 2011) and the 5p15.33 locus, where the risk SNP rs10069690 creates a splice-donor site leading to an alternate splicing isoform of *TERT* lacking telomerase activity (Killedar *et al.*, 2015). Since the etiological basis of glioma subtypes is likely to reflect different developmental pathways it is not surprising that subtype-specific associations have been shown for GBM (5p15.33, 7p11.2, 9p21.3, 11q14.1, 16p13.33, 16q12.1, 20q13.33 and 22q13.1) and non-GBM (1q44, 2q33.3, 3p14.1, 8q24.21, 10q25.2, 11q21, 11q23.2, 11q23.3, 12q21.2, 14q12 and 15q24.2) (Melin *et al.*, 2017). Recent large-scale sequencing projects have identified the *IDH* mutation, *TERT* promoter mutation, and the chromosome 1p/19q codeletion as cancer drivers in glioma. These findings have improved the subtyping of diffuse gliomas (Cancer Genome Atlas Research Network *et al.*, 2015) (Eckel-Passow *et al.*, 2015) so that this information has been incorporated into the 2016 WHO classification of glial tumors (Louis *et al.*, 2016). Since these genetic alterations are early events in glioma development, any relationship between the SNPs associated with glioma risk and molecular profile should provide insights into gliomagenesis. Evidence for the existence of such subtype specificity is already provided by the association of the 8q24.21 (rs55705857) risk variant with *IDH*-mutant 1p/19q codeleted gliomas (Enciso-Mora *et al.*, 2013). Additionally, it has been proposed that associations may exist between the SNPs at 5p15.33, at 9p21.3, and at 20q13.33 and *IDH*-wildtype gliomas (Di Stefano *et al.*, 2013), as well as between the SNP at 17p13.1 and gliomas harboring the *IDH* and the *TERT* promoter mutation but without 1p/19q codeletion (Eckel-Passow *et al.*, 2015).

To gain a more comprehensive understanding of the relationship existing between the 25 glioma risk loci recently reported to have a strong association with glioma risk (Melin *et al.*, 2017) and tumor subtype, we analyzed three patient series, totaling 2648 cases. Since, generally, the functional bases of GWAS cancer risk

loci appear to be through regulatory effects (Sud, Kinnersley and Houlston, 2017), we analyzed Hi-C and gene expression data to gain insight into the likely target gene(s) of glioma risk SNPs.

Patients and methods

Data sources. We analyzed data from three non-overlapping datasets: 1) the TCGA dataset, 2) the French GWAS dataset, and 3) the French sequencing dataset, described thereafter.

1) TCGA dataset: Raw genotyping files (.CEL) for the Affymetrix Genomewide version 6 array were downloaded for germline (i.e., whole blood) DNA of glioma patients from The Cancer Genome Atlas (TCGA, dbGaP study accession: phs000178.v1.p1). Controls were collected among publicly accessible genotype data generated by the Wellcome Trust Case–Control Consortium 2 analysis of 2699 individuals from the 1958 British birth cohort (1958-BC) (Power and Elliott, 2006). Genotypes were generated using the Affymetrix Power Tools Release 1.20.5 using the Birdseed (v2) calling algorithm and PennCNV (Wang *et al.*, 2007). After quality control, there were 521 TCGA glioma cases and 2648 controls. Tumor molecular data (*IDH* mutation, 1p/19q codeletion, *TERT* promoter mutation) were obtained from Ceccarelli et al. (Ceccarelli *et al.*, 2016). Further data (*EGFR* amplifications and/or activating mutations, *CDKN2A* deletions) were obtained from the cBioportal for cancer genomics (Gao *et al.*, 2013).

2) French GWAS dataset: The French GWAS dataset (Sanson *et al.*, 2011) (Kinnersley *et al.*, 2015) comprised 1423 patients with newly diagnosed grade II–IV diffuse glioma attending the Service de Neurologie Mazarin, Groupe Hospitalier Pitié-Salpêtrière, Paris, France. Controls (n = 1190) were ascertained from the SU.VI.MAX (SUpplementation en VItamines et Mineraux AntioXydants) study of 12,735 healthy subjects (women aged 35–60 years; men aged 45–60 years) (Hercberg *et al.*, 2004). Tumors from patients were snap-frozen in liquid nitrogen and DNA was extracted using the QIAmp DNA minikit, according to the manufacturer's instructions (Qiagen, Venlo, LN, USA). DNA was analyzed for large-scale CNVs by CGH-array. For tumors not analyzed by CGH-array, the 1p/19q codeletion status was assessed using PCR microsatellites, while *EGFR*-amplification and *CDKN2A-p16-INK4a* homozygous deletion were assessed by quantitative PCR. The *IDH1*, *IDH2* and *TERT* promoter mutation status was assigned by Sanger sequencing.

3) French sequencing dataset: Eight hundred and fifteen patients newly diagnosed grade II–IV diffuse glioma were ascertained through the Service de Neurologie Mazarin, Groupe Hospitalier Pitié-Salpêtrière, Paris, France. Genotypes for the 25 risk SNPs were obtained by universal-tailed amplicon sequencing in conjunction with Miseq technology (Illumina Inc.). Genotypes were called using the GATK (Genome Analysis ToolKit, version 3.6-0-g89b7209) software. Duplicated samples and individuals with low call rate (< 90%) were excluded from subsequent analyses (n = 111). Molecular profiling of tumor samples was carried out as per the French GWAS cohort. Unrelated French controls were obtained from the 3C Study Group (3C Study Group, 2003), a population-based prospective study of the relationship between vascular factors and dementia carried out in

Bordeaux, Montpellier, and Dijon (France). Genotyping of controls was performed using Illumina Human 610-Quad BeadChips. To recover untyped genotypes, imputation using the IMPUTE2 software was performed using 1000 genomes multi-ethnic data (1000 G phase 1 integrated variant set release v3) as reference. SNPs genotypes were retained if call rates were > 98%, the Hardy–Weinberg equilibrium *P* value was > 1×10^{-6}, and minor allele frequency was > 1%. After quality control, 704 cases and 5527 controls were available for analysis.

Statistical analysis. Test of association between SNP and glioma molecular subgroup was performed using SNPTESTv2.5 under an additive frequentist model. Where appropriate, principal components, generated using common SNPs, were included in the analysis to limit the effects of cryptic population stratification that otherwise might cause inflation of test statistics. Eigenvectors for the TCGA study were inferred using smartpca (part of EIGENSOFTv2.4) by merging cases and controls with phase II HapMap samples. To ensure reliability when restricting cases to per-group low sample counts, imputed genotypes were thresholded at a probability > 0.9 (e.g. –method threshold in SNPtest) for the TCGA and French-GWAS studies. For the French sequencing study, we used –method expected, as we were comparing genotypes from directly sequenced cases against imputed controls. We compared control frequencies to those from European 1000 genomes project to ensure the validity of this approach. Meta-analyses were performed using the fixed-effects inverse-variance method based on the β estimates and the standard errors from each study using META v1.6. Cochran's *Q* statistic was used to test for heterogeneity.

Risk allele number and age at diagnosis. For imputed SNPs, a genotype probability threshold > 0.9 was used. The age and survival distribution of cases carrying additive combinations of risk alleles were assessed for the 25 SNPs across the molecular subgroups. Trend lines were estimated using linear regression in *R* and plotted using the *ggplot2* package. Association between risk allele number and age was assessed using the Pearson correlation test.

Survival analysis. Survival plots were generated using the *survfit* package in *R* which computes an estimate of a survival curve for censored data using the Kaplan–Meier method. Log-rank tests were used to compare curves between groups. Overall survival was estimated using sample size formulae for comparative binomial trials. The Cox proportional-hazards regression model was used to investigate the association between survival and age, grade, molecular group, and number of risk alleles. Individuals were excluded if they died within a month from surgery. The date of surgery was used as a proxy for the date of diagnosis.

Expression quantitative trait locus analysis. We searched for expression quantitative trait loci in 10 brain regions using the V6p GTEx portal (https://gtexp ortal .org/home/) and in whole blood using the blood eQTL browser (https ://molge nis58 .targe t.rug.nl/blood eqtlb rowse r/).

Hi‑C analysis. We examined for significant contacts between glioma risk SNPs and nearby genes using the HUGIn browser, which is based on the analysis by Schmitt et al. (Schmitt *et al.*, 2016). We restricted the analysis

to Hi-C data generated on H1 Embryonic Stem Cell and Neuronal Progenitor cell lines, as originally described by Dixon et al. (Dixon *et al.*, 2015). Plotted topologically associating domain boundaries were obtained from the insulating score method (Crane *et al.*, 2015) at 40-kb bin resolution. We searched for significant interactions between bins overlapping the glioma risk SNP and all other bins within 1 Mb at each locus (i.e., "virtual 4C").

Gene set enrichment analysis. Gene set enrichment analysis was carried out using gene sets from the Molecular Signatures Database v6.0 restricted to the C2 canonical pathways sets (*n*=1329). Analysis was carried out using default settings except for removing restrictions on gene set size. RSEM normalised mRNASeq expression data for 20,501 genes in the 676 glioma cases from TCGA were downloaded from the Broad Institute TCGA GDAC (http://gdac.broadinstitute.org/). These were assigned molecular group using sample information from Ceccarelli et al. (Ceccarelli *et al.*, 2016).

Results

Descriptive characteristics of the three datasets. We studied three non-overlapping patient cohorts of Northern European ancestry, totaling 2648 cases and 9365 controls. For 1689 out of the 2648 cases, information on somatic *IDH* mutation, *TERT* promoter, and chromosome 1p/19q codeletion status was available. These data allowed to define five molecular subgroups of glioma (Figure 7):

a) **triple-positive**: *IDH*-mutant, *TERT* promoter mutant, 1p/19q codeleted (n=349)
b) ***TERT-IDH***: *IDH*-mutant, *TERT* promoter mutant, 1p/19q non-codeleted (n=78)
c) ***IDH*-only**: *IDH*-mutant, *TERT* promoter wildtype, 1p/19q non-codeleted (n=450)
d) ***TERT*-only**: *IDH*-wildtype, *TERT* promoter mutant, 1p/19q non-codeleted (n=540)
e) **triple-negative**: *IDH*-wildtype, *TERT* promoter wildtype, 1p/19q non-codeleted (n=243).

As only 29 cases were classified as *IDH* mutant, *TERT* promoter wildtype, and 1p/19q codeleted, we restricted subsequent analyses to the five groups described above. Table 5 recapitulates sample distribution in each of the three dataset based on molecular subgroup (triple-positive, *TERT-IDH*, *IDH*-only, *TERT*-only, triple negative) and integrated diagnosis according to the 2016 WHO classification (i.e., *IDH*-mutant astrocytoma, *IDH*-wildtype astrocytoma, *IDH*-mutant 1p/19q codeleted oligodendroglioma, *IDH*-mutant glioblastoma, and *IDH*-wildtype glioblastoma).

Figure 7. Scheme recapitulating the molecular classification of tumor samples performed in the present study, based on the *IDH*, *TERT* promoter, and chromosome 1p/19q codeletion status.

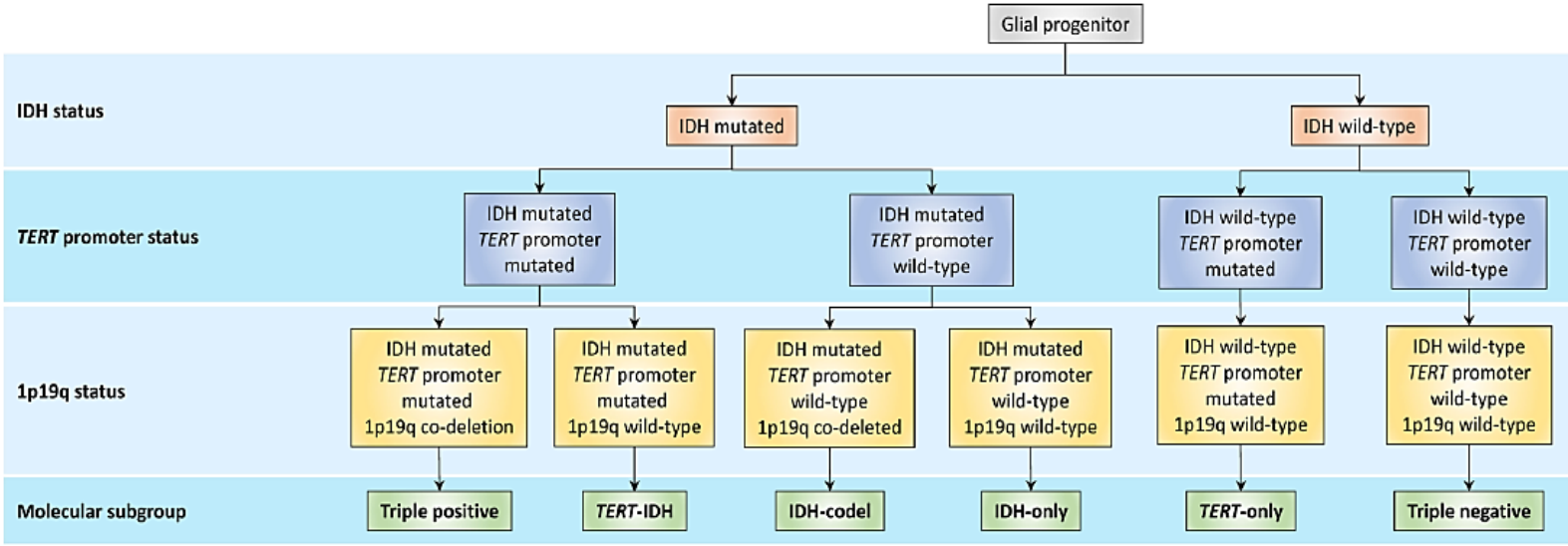

Table 5. Overview of the distribution of tumors in the TCGA, French GWAS, and French sequencing datasets, based on molecular group and integrate diagnosis.

Dataset	Controls	Cases (GBM/non-GBM)	Case groupings																	
			IDH status		*EGFR*		*CDKN2A*		Molecular subgroup						WHO 2016 classification					
			mut	wt	amp	wt	del	wt	IDH-only	*TERT*-IDH	*TERT*-only	Triple −ve	Triple +ve	Total	AstroIDH-mut	Astro IDH-wt	Oligo 1p19q	GBM IDH-mut	GBM IDH-wt	Total
TCGA	2648	521 (183/338)	293	228	246	270	254	262	100	4	45	10	65	224	166	51	116	10	171	514
French GWAS	1190	1423 (430/993)	366	498	118	628	173	573	169	46	309	141	85	750	188	214	95	27	233	757
French seq	5527	704 (181/523)	427	277	101	592	144	549	181	28	185	92	199	685	178	114	218	31	148	689
Total	9365	2648 (795/1854)	1086	1003	465	1490	571	1384	450	78	539	243	349	1659	532	379	429	68	552	1960

SNP selection. The 25 SNPs analyzed in the present study are reported in Table 6 (Melin *et al.*, 2017). All of them exhibited a consistent direction of effect with that previously reported, albeit some weakly (Figure 8).

Table 6. Overview of the 25 glioma risk SNPs analyzed in the study.

Locus	SNP identifier	Alleles	Glioma association
1p31.3	rs12752552	**T**/C	GBM
1q32.1	rs4252707	G/**A**	Non-GBM
1q44	rs12076373	**G**/C	Non-GBM
2q33.3	rs7572263	**A**/G	Non-GBM
3p14.1	rs11706832	A/**C**	Non-GBM
5p15.33	rs10069690	C/**T**	GBM
7p11.2	rs75061358	T/**G**	GBM
7p11.2	rs11979158	**A**/G	GBM
8q24.21	rs55705857	A/**G**	Non-GBM
9p21.3	rs634537	T/**G**	GBM
10q24.33	rs11598018	**C**/A	Non-GBM
10q25.2	rs11196067	A/**T**	Non-GBM
11q14.1	rs11233250	**C**/T	GBM
11q21	rs7107785	**T**/C	Non-GBM
11q23.2	rs648044	**A**/G	Non-GBM
11q23.3	rs12803321	**G**/C	Non-GBM
12q21.2	rs1275600	**T**/A	Non-GBM
14q12	rs10131032	**G**/A	Non-GBM
15q24.2	rs77633900	G/**C**	Non-GBM
16p13.3	rs2562152	A/**T**	GBM
16p13.3	rs3751667	C/**T**	Non-GBM
16q12.1	rs10852606	T/**C**	GBM
17p13.1	rs78378222	T/**G**	All
20q13.33	rs2297440	T/**C**	GBM
22q13.1	rs2235573	**G**/A	GBM

Relationship between risk SNP and molecular subgroup. In the first instance, we examined whether the associations at the 25 risk loci were broadly defined by *IDH* status. We observed significant association for *IDH*-mutant gliomas with 1q44 (rs12076373), 2q33.3 (rs7572263), 3p14.1 (rs11706832), 8q24.21 (rs55705857), 11q21 (rs7107785), 11q23.3 (rs12803321), 14q12 (rs10131032), 15q24.2 (rs77633900) and 17p13.1 (rs78378222) risk SNPs. In addition, we found a strong association between the risk SNPs at 5p15.33 (rs10069690), 7p11.2 (rs75061358), 9p21.3 (rs634537), and 20q13.33 (rs2297440) and *IDH*-wildtype gliomas.

Of particular note was the finding that many of the risk loci recently discovered which were reported to be associated with non-GBM (1q44, 2q33.3, 3p14.1, 11q21, 14q12, 15q24.2) (Melin *et al.*, 2017) showed a strong association with *IDH*-mutant gliomas.

Figure 8. Association between the 25 loci and the GBM (pink)/ non-GBM (purple) subgroup. Horizontal red lines correspond to an odds ratio of 1.0.

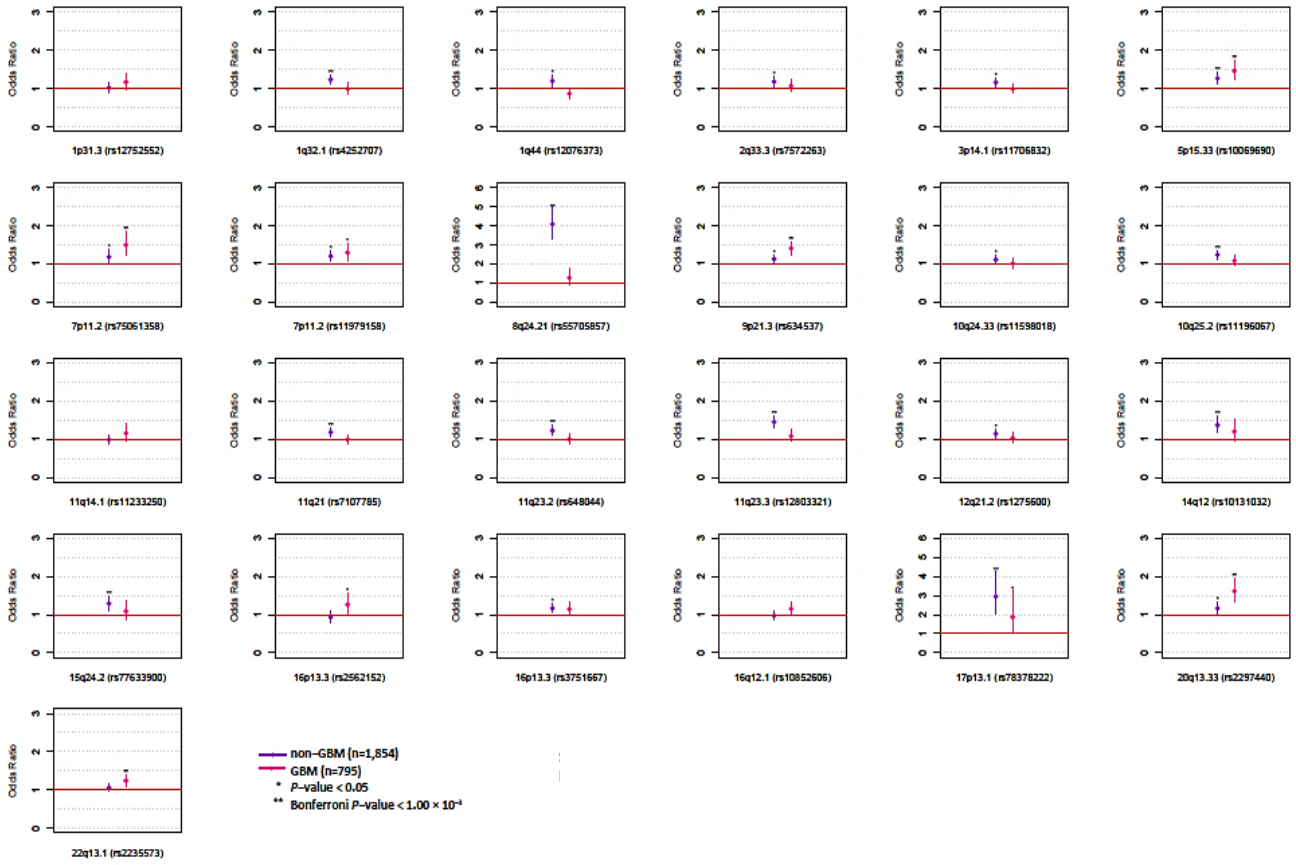

Following on from this, we performed a more detailed analysis stratifying gliomas based on molecular subgroups (Figure 9). We found a strong association with *IDH*-mutant tumors at 8q24.21 (rs55705857) that was especially string for triple-positive gliomas [$P = 1.27 \times 10^{-37}$, OR = 9.30 (6.61–13.08)], which correspond to oligodendrogliomas according to the 2016 WHO classification. Furthermore, we confirmed the previously reported associations at 5p15.33 (rs10069690), 9p21.3 (rs634537), 17p13.1 (rs78378222) and 20q13.33 (rs2297440) with *TERT*-only glioma (Eckel-Passow *et al.*, 2015). Finally, we found suggestive evidence for an association between 22q13.1 (rs2235573) and *TERT*-only gliomas, as well as between 11q21 (rs7107785), 11q23.2 (rs648044), and 12q21.2 (rs1275600) and triple-positive gliomas.

In addition to the data on the *IDH*, *TERT* promoter, and 1p/19q codeletion status, for 1955 tumors we had information on *EGFR* amplification and *CDKN2A* deletion (Table 5). Using these data, we searched for associations between the 25 risk SNPs and *EGFR* amplification and *CDKN2A* deletion. In particular, we focused on the 7p11.2 (rs75061358 and rs11979158) and the 9p21.3 (rs634537) risk loci, since they respectively map

in (or near) *EGFR* and *CDKN2A*. Indeed, at 7p11.2, the intergenic variant rs75061358, which is located in the genomic vicinity of *EGFR,* was associated with *EGFR*-amplified tumors. The association with *EGFR* amplification was instead less strong for the SNP rs11979158, which is intronic within *EGFR* itself. At 9p21.3, the SNP rs634537, which is intronic within *CDKN2B-AS1* and in the vicinity of *CDKN2A* and *CDKN2B*, was not associated with *CDKN2A* deletion. Since low grade gliomas are more commonly *EGFR*-wildtype and *p16*-wildtype, many non-GBM risk SNPs were strongly associated with these tumors and, notably, 2q33.3 (rs7572263), 3p14.1 (rs11706832), 8q24.21 (rs55705857), 10q25.2 (rs11196067), and 11q23.3 (rs12803321).

Figure 9. Association between the 25 risk loci and glioma subgroup (orange=*TERT*-only group; yellow=*IDH*-only group; green=*TERT-IDH* group; dark red=triple-positive group; blue=triple-negative group). Faint horizontal red lines correspond to an odds ratio of 1.0.

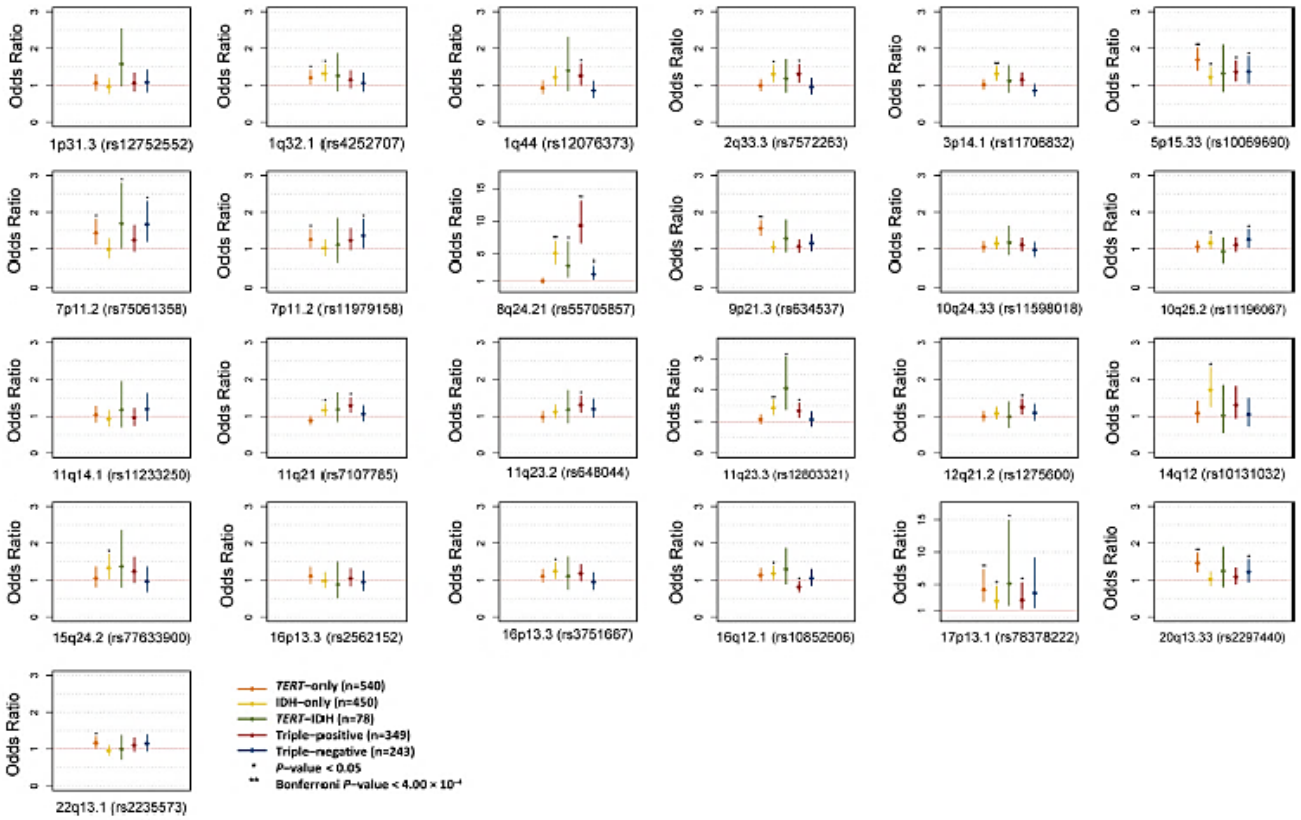

Polygenic contribution to age at diagnosis and patient survival. Consistently with previous reports (Cancer Genome Atlas Research Network *et al.*, 2015) (Eckel-Passow *et al.*, 2015), patient survival depended on molecular subgroup, patients with triple-positive tumors having the best prognosis and patients with *TERT*-only tumors having the worst outcome. We investigated whether a higher burden of glioma risk alleles was associated with earlier age at diagnosis (which would suggest an influence on glioma initiation) or with OS (which would suggest an influence on glioma progression). We found no significant association between age and risk allele number, nor in the whole cohort or in the individual molecular groups. Examining each SNP individually, only rs55705857 at 8q24.21 was nominally associated with age. Then, we used the Cox Proportional-Hazards

Regression to investigate whether the number of risk alleles was associated with OS. Intriguingly, we found that a higher number of glioma risk alleles was associated with increased survival ($P < 10^{-4}$). This observation remained true in the triple-positive, triple-negative, and *TERT*-only but not in the *IDH*-only and the *TERT-IDH* subgroup. The risk loci at 1q32.1 (rs4252707) (P = 0.012), 11q21 (rs7107785) (P = 0.017), and 11q23.3 (rs12803321) (P = 0.016) and were nominally associated with OS, independently of age and molecular subgroup. Age, grade, and molecular group impacted OS, as expected ($P < 10^{-15}$).

Biological inference of risk loci. Since spatial proximity and chromatin looping interactions are fundamental factors for the regulation of gene expression (Rao *et al.*, 2014), we interrogated physical interactions at risk loci using Hi-C data. We also performed expression quantitative trait locus (eQTL) analysis using mRNA expression data for ten brain regions using the GTEx portal. We identified significant Hi-C contacts from the genomic regions that encompass 14 out of the 25 risk loci, implicating a number of presumptive candidate genes. For two of those, candidacy was supported by eQTL data (Table 7). Notably, there was a significant looping interaction between the risk SNP at 2q33.3 and *IDH1*/*IDH1-AS1*, as well as between with the risk SNP at 7p11.2 and *EGFR/EGFR-AS1*, the risk SNP at 9p21.3 and *CDKN2A/CDKN2B*, the risk SNP at 1q32.1 and *NFASC*, and the risk SNP at 3p14.1 and *LRIG1*. At the 8q24.21 locus, Hi-C data revealed a significant interaction between the risk SNP rs55705857 and *MYC*. Additionally, the risk SNP rs12803321 at 11q23.3 was significantly associated with *PHLDB1* expression.

Pathway analysis. To potentially gain further insight into the biological basis of subtype associations, we performed gene set enrichment analysis analyzing gene expression data from TCGA. While we did not identify any significantly altered gene sets (at FDR q value < 0.1), we identified an upregulation of the PI3K signaling pathway in the group of triple positive gliomas.

Discussion

Our findings provide further support for subtype-specific associations for glioma risk loci. Specifically, we confirmed the strong relationship between the variant at 8q24.21 (rs55705857) and triple-positive glioma, and we substantiated the proposed associations between the variant at 5p15.33 (rs10069690) and the variant at 20q13.33 (rs2297440) and *TERT*-mutant glioma, between the variant at 9p21.3 (rs634537) and *TERT*-only glioma, and between the variant at 17p13.1 (rs78378222) and *TERT-IDH* glioma. Although preliminary, and in part speculative, our analysis delineates potential disease mechanisms across the 25 glioma risk loci by identifying associations with genes involved in telomere maintenance, in the EGFR-AKT, the NAD, and the p53 pathway, and genes involved in neural development (Table 7) (Figure 10).

Table 7. Biological interference of risk loci with candidate genes. *TN*=triple negative; *TP*=triple positive; *$P < 0.05$, **significant after adjustment for multiple comparisons.

Locus	SNP	Molecular group	IDH, *EGFR*, *CDKN2A* status	eQTL (tissue)/Hi-C	Commentary
1p31.3	rs12752552	–	–	*JAK1* (brain)/*RAVER2*, *JAK1*, *UBE2U*, *CACHD1*	JAK1 is involved in actomyosin contractility in tumour cells and stroma to aid metastasis [46]
1q32.1	rs4252707	*TERT*-only*, IDH-only*	IDHmut*, *EGFR*wt*, *CDKN2A*wt*	*NFASC*	NFASC is a cell adhesion molecule involved in axon subcellular targeting and synapse formation during neural development [1]
1q44	rs12076373	TP*	IDHmut**	*AKT3*, *ZBTB18*, *SDCCAG8*	AKT3 is highly expressed in brain, regulates cell signalling in response to insulin and growth factors [4], involved in regulation of normal brain size [28]
2q33.3	rs7572263	IDH-only*, TP*	IDHmut**, *EGFR*wt*, *CDKN2A*wt*	*IDH1*, *IDH1-AS1*	IDH mutant protein overexpression increases glioma cell radiation sensitivity [29]
3p14.1	rs11706832	IDH-only**	IDHmut**, EGFRwt*, *CDKN2A*wt*	*LRIG1* (blood), *SLC25A26* (blood)/*LRIG1*	–
5p15.33	rs10069690	*TERT*-only**, IDH-only*, TP*, TN*	IDHmut*, IDHwt**, *EGFR*amp**, *EGFR*wt*, *CDKN2A*del*, *CDKN2A*wt**	–	rs10069690 affects *TERT* splicing [24]
7p11.2	rs75061358	*TERT*-only*, *TERT*-IDH*, TN*	IDHwt**, *EGFR*amp**, *CDKN2A*wt*	–	–
7p11.2	rs11979158	*TERT*-only*, TN*	IDHwt*, *EGFR*amp*, *EGFR*wt*, *CDKN2A*del*, *CDKN2A*wt*	*EGFR*, *EGFR-AS1*	–
8q24.21	rs55705857	IDH-only**, *TERT*-IDH*, TP**, TN*	IDHmut**, *EGFR*wt*, *CDKN2A*wt**, *CDKN2A*del**	*PCAT1*, *PCAT2*, *CASC8*, *CASC11*, *MYC*, *PVT1*	–
9p21.3	rs634537	*TERT*-only**	IDHwt**, *EGFR*amp*, *EGFR*wt*, *CDKN2A*del*, *CDKN2A*wt**	*CDKN2A*, *CDKN2B-AS1*	–
10q24.33	rs11598018	–	IDHmut*, *EGFR*wt*	*GSTO1*, *GSTO2* *SH3PXD2A*	Correlated SNP to rs11598018 associated with telomere length likely through *OBFC1* [7]
10q25.2	rs11196067	IDH-only*, TN*	IDHmut*, IDHwt*, *EGFR*wt*, *CDKN2A*wt*	*TCF7L2*, *VTI1A*, *HABP2*	TCF7L2 modifies beta-catenin signalling and controls oligodendrocyte differentiation [69]
11q14.1	rs11233250	–	–	–	–
11q21	rs7107785	IDH-only*, TP*	IDHmut**, *EGFR*wt*, *CDKN2A*del*	*RP11-712B9.2* (brain)	–
11q23.2	rs648044	TP*	IDHmut*, *EGFR*wt**, *CDKN2A*wt**	*NNMT*, *ZBTB16*	NNMT is upregulated in GBM, NAD metabolism important in glioma [23]
11q23.3	rs12803321	IDH-only**, *TERT*-IDH*, TP*	IDHmut**, *EGFR*wt**, *CDKN2A*wt**, *CDKN2A*del*	*PHLDB1* (brain)	PHLDB1 is an insulin-responsive protein that enhances Akt activation [70]
12q21.2	rs1275600	TP*	IDHmut*, *EGFR*wt**, *CDKN2A*wt**, *CDKN2A*del*	*KRR1*, *GLIPR1*	GLIPR1 is targeted by TP53 [43]
14q12	rs10131032	IDH-only*	IDHmut**, *EGFR*wt*, *CDKN2A*del*, *CDKN2A*wt*	*NPAS3*	NPAS3 is a tumour suppressor for astrocytoma [37]
15q24.2	rs77633900	IDH-only*	IDHmut**, *EGFR*wt*, *CDKN2A*wt*	*SCAPER*	–
16p13.3	rs2562152	–	–	–	–
16p13.3	rs3751667	IDH-only*	IDHmut*, *EGFR*amp*, *EGFR*wt*, *CDKN2A*wt*	*RP11-161M6.2* (brain), *SOX8* (blood)	SOX8 is strongly expressed in brain and may be involved in neural development [47]
16q12.1	rs10852606	IDH-only*, TP* (−ve)	–	*HEATR3* (brain)	HEATR3 may be involved in NOD2-mediated NF-kappa B signalling [67]
17p13.1	rs78378222	*TERT*-only**, IDH-only*, *TERT*-IDH*, TP*	IDHmut**, IDHwt*, *EGFR*amp*, *EGFR*wt*, *CKDN2A*wt**, *CDKN2A*del*	–	rs78378222 affects *TP53* 3'UTR polyadenylation processing [51]
20q13.33	rs2297440	*TERT*-only**, TN*	IDHwt**, *EGFR*amp**, *EGFR*wt*, *CDKN2A*del*, *CDKN2A*wt*	*STMN3* (brain), *LIME1* (blood), *ZGPAT* (blood), *EEF1A2* (blood)	Overexpression of STMN3 promotes growth in GBM cells [68]
22q13.1	rs2235573	*TERT*-only*	IDHwt*	*CTA-228M9.3* (brain)	–

Telomere maintenance is central to cell immortalization (Walsh, Wiencke, *et al.*, 2015) and is generally considered to require mutually exclusive mutations in either the *TERT* promoter or the *ATRX* gene. The risk alleles at 5p15.33 (*TERT*) and 10q24.33 (*OBFC1*) are associated with increased leukocyte telomere length, thereby supporting a relationship between SNP genotype and biology (Walsh, Codd, *et al.*, 2015) (Walsh, Wiencke, *et al.*, 2015) (C. Zhang *et al.*, 2015). While dysregulation of the telomere gene *RTEL1* has traditionally been assumed to represent the functional basis of the 20q13.33 locus, the glioma risk SNP does not map to the

locus associated with telomere length (Codd *et al.*, 2013) (Melin *et al.*, 2017). Intriguingly, our analysis instead implicates *STMN3*, at 20q13.33, whose over-expression promotes growth in GBM cells (Y. Zhang *et al.*, 2015), suggesting an alternative mechanism by which this SNP could influence glioma development. With respect to the 5p15.33 (*TERT*) and the 10q24.33 (*OBFC1*) loci, it is unclear whether the effect on glioma risk is solely related to telomere length or is pleiotropic and involves multiple factors. For example, the rs10069690 at 5p15.33 is strongly associated with *TERT*-only glioma, yet the *TERT* promoter mutation increases telomerase activity without necessarily affecting telomere length (Ceccarelli *et al.*, 2016). An intriguing hypothesis to test would be to examine the impact of allele-specific effects of rs10069690 on telomere length in the context of gliomas carrying the *TERT* promoter mutation.

The *EGFR-AKT* pathway involves *EGFR* at 7p11.2, *LRIG1* at 3p14.1, *PHLDB1* at 11q23.3, and *AKT3* at 1q44. We showed a significant interaction between the risk SNP rs11979158 at 7p11.2 and *EGFR*, consistent with a cis-regulatory effect on gene expression. Although the mechanistic bases of the 7p11.2 locus have long been suspected to involve *EGFR* and is strongly associated with classical GBM, emerging evidence suggests that additional components of the *EGFR-AKT* signaling pathway are implicated by non-GBM SNPs. At the *IDH*-only associated locus 3p14.1, *LRIG1* is highly expressed in the brain and negatively regulates the epidermal growth factor receptor (EGFR) signaling pathway (Gur *et al.*, 2004). Reduced *LRIG1* expression is linked to tumor aggressiveness, temozolomide resistance, and radioresistance (Wei *et al.*, 2015) (Yang *et al.*, 2015). Downstream components of *EGFR-AKT* signaling are implicated at 11q23.3 via *PHLDB1*, as well as at 1p31.3 via *JAK1* and at 1q44 via *AKT3*. The risk allele rs12803321 is associated with increased expression of *PHLDB1*, an insulin-responsive protein that enhances Akt activation (Zhou *et al.*, 2010). *AKT3* at 1q44 is highly expressed in the brain and appears to respond to EGF in a PI3K-dependent manner (Okano *et al.*, 2000), GBM cells containing amplified AKT3 having enhanced abilities of DNA repair that result in an increased resistance to radiation and alkylating agents (Turner *et al.*, 2015). The risk allele rs12752552 at 1p31.3 is associated with increased *JAK1* expression in the brain tissue. Since *JAK1* can be activated by EGF phosphorylation, it might be involved in astrocyte formation (Shuai *et al.*, 1993). The 3p14.1 and 11q23.3 loci are strongly associated with *EGFR* amplification negative gliomas, with a consistent albeit non-significant trend at 1p31.3 and at 1q44, consistent with elevated upstream *EGFR* activation masking their functional effects.

The *NAD* pathway involves *IDH1* at 2q33.3 and *NNMT* at 11q23.2. At 2q33.3, we detected a significant Hi-C interaction between the glioma risk SNP rs7572263 and *IDH1*/*IDH1-AS1*. Overexpression of *IDH1*-mutant proteins has been reported to sensitize glioma cells to radiation (Li *et al.*, 2013), providing an interesting mechanism to test the allele-specific effects of this SNP. The *IDH* mutation causes a deregulation of NAD signaling (Yan *et al.*, 2009). Therefore, at 11q23.2, which is strongly associated with *IDH*-mutant gliomas, the most convincing molecular mechanism is via *NNMT*, which encodes the nicotinamide *N*-methyltransferase and is highly expressed in GBM relative to normal brain, causing methionine depletion-mediated DNA hypomethylation and accelerated tumor growth (Jung *et al.*, 2017).

The p53 pathway is involved at 17p13.1, where the risk SNP rs78378222 affects *TP53* 3'-UTR poly-adenylation processing. In addition, the p53 target GLIPR1 (Ren *et al.*, 2006) is implicated at 12q21.2. Moreover, 12q21.2 is most strongly associated with triple-positive glioma, which does not feature *TP53* mutation, consistent with wild-type p53 protein being required for the SNP to exert a functional effect.

Lastly, evidence suggests that genes with established roles in neural development may also be involved. While the risk SNP rs4252707 at 1q32.1 is within the intron of *MDM4*, the strongest evidence for a mechanistic effect was observed with *NFASC*. Neurofascin is involved in synapse formation during neural development (Ango *et al.*, 2004) and, therefore, represents an attractive functional candidate for the association with glioma. Additionally, at 16p13.3 and 20q13.33, implicated genes *SOX8* and *STMN3* are strongly expressed in the brain and thought to play a role in neural development (Schepers *et al.*, 2000) (Y. Zhang *et al.*, 2015). At 10q25.2, implicated gene *TCF7L2* modifies beta-catenin signaling and controls oligodendrocyte differentiation (Zhao *et al.*, 2016). Intriguingly, 10q25.2 has previously been reported to be a risk locus for colorectal cancer (Wang *et al.*, 2014), a tumor driven by WNT signaling. However, the risk SNP is not correlated with rs11196067, raising the possibility of tissue-specific regulation across a wider region.

Figure 10. Illustrative scheme of the relationship between glioma risk loci, corresponding molecular alterations, and associated biological pathways.

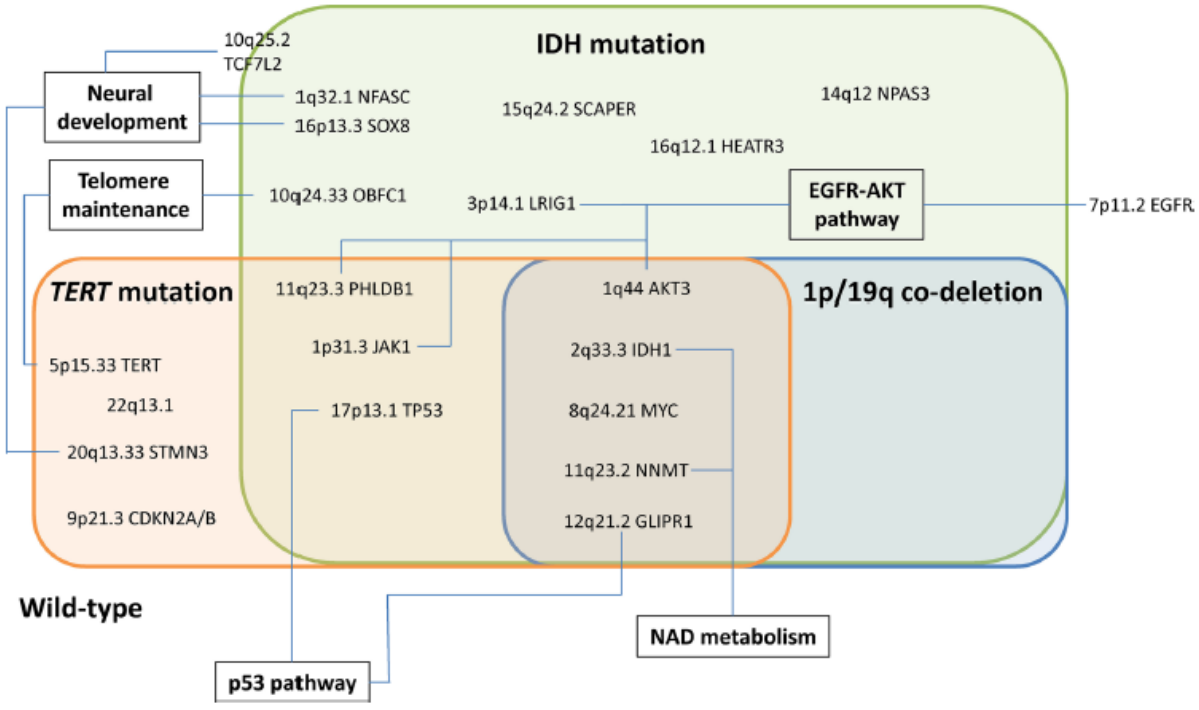

As with many cancers, the exact point at which each risk SNPs exerts its functional impact on glioma oncogenesis remains to be elucidated, and we did not demonstrate a relationship between higher risk allele number and younger age at diagnosis. Surprisingly, we found a significant association between a higher number

of risk alleles and improved outcome. This result was consistent across the prognostic molecular groups, suggesting that our observations not due to an over-representation of the more favorable prognostic groups among patients with a higher burden of risk alleles. In addition, the distribution of risk allele numbers did not differ across the four groups (P = 0.3, ANOVA test). Collectively our findings suggest that, independent of other prognostic factors, the greater the number of risk alleles carried, the better the outcome.

In conclusion, we performed the most comprehensive association study between molecular subgroup and the 25 recently identified glioma risk loci to date. While confirming previous observations, we showed that most risk loci are associated with the *IDH* mutation. Through the integration of Hi-C and eQTL data, we have additionally sought to define candidate target genes underlying the associations. Our observations highlight pathways critical to glioma susceptibility, notably neural development and NAD metabolism, as well as EGFR-AKT signaling. Intriguingly, we showed here that the number of risk alleles is consistently associated with better outcome. Functional investigation in tumor and neural progenitor-based systems will be required to fully elucidate these molecular mechanisms. In addition, as *IDH*-mutant tumors have been shown to reshape their tridimensional chromatin organization, future analyses might reveal new regulatory interactions (Flavahan *et al.*, 2016). Indeed, our current analysis is based on defining glioma subgroups using only three molecular markers. Given the extent of the missing heritability for glioma, further expansion of GWAS by international consortia is likely to result in the identification of additional risk variants. A more precise molecular subgrouping using data from ongoing large-scale tumor sequencing projects is likely to provide further insights into glial oncogenesis and suggest targets for novel therapeutic strategies.

Published in Acta Neuropathol. 2018 May;135(5):743-755.

Noninvasive techniques for the detection of *IDH* mutations

Liquid biopsies: detecting *IDH1* mutations from extracellular vesicles circulating in plasma

Background

Gliomas have been traditionally classified based on histological class and grade (Louis *et al.*, 2007). However, recent discoveries have highlighted that some molecular markers provide powerful diagnostic and prognostic information (Cancer Genome Atlas Research Network *et al.*, 2015). On these bases, the 2016 WHO classification of Tumors of the Central Nervous System has integrated molecular features to histology to allow a proper classification and prognostic stratification of diffuse gliomas (Louis *et al.*, 2016).

Histological analysis and molecular profiling are routinely performed on tumor specimens from surgical resection or biopsy. It follows that patients who cannot undergo surgery because of tumor location or severe comorbidities cannot receive a formal diagnosis of glioma and access adequate treatment. During the last few years, the efforts of the scientific community have thus been directed at developing techniques to acquire the molecular profile of a tumor from the analysis of tumor-derived material circulating in easily accessible bodily fluids such as plasma, a procedure commonly referred to as "liquid biopsy" (Best *et al.*, 2015). The routine use of liquid biopsies would have tremendous clinical implications for glioma patients, allowing to establish a molecular diagnosis of glioma and identify actionable molecular alterations in patients not amenable to surgery, but also to noninvasively monitor the molecular profile of the tumor during follow-up.

Liquid biopsies rely on the study of circulating tumor cells, on the amplification and sequencing of cell-free tumor DNA, or on the reverse transcription and sequencing of tumor-derived messenger RNA (mRNA) transported within extracellular vesicles (EV). EV are small particles surrounded by a lipid bilayer containing nucleic acids, proteins, and lipids, that are physiologically secreted in extracellular fluids, where they exert functions of intercellular communication. Based on their diameter and site of origin, two types of EV can be distinguished: microvesicles (MV), having a diameter up to 1300 nm and shedding from the plasma membrane, and exosomes (EXO), having a diameter of 30-150 nm and shedding from the endosomal reticulum. Being released in great amounts by neoplastic cells (Xu *et al.*, 2018), EV are emerging as an interesting substrate for liquid biopsies, as their cargo of nucleic acids is protected by the lipidic membrane from the degradation that normally occurs in plasma by circulating DNases.

While liquid biopsies were fruitful in patients with systemic tumors, especially when metastatic, transferring this approach to patients with brain tumors has proven challenging due to the limited amount of tumor material present in the systemic circulation, reason that led some groups to prefer the use of CSF over plasma (Bettegowda *et al.*, 2014) (Pentsova *et al.*, 2016) (De Mattos-Arruda *et al.*, 2015). Despite the intrinsic challenges related to the infiltrative nature of diffuse gliomas and the presence of the blood-brain barrier, some

research groups have succeeded in the detection of genetic alterations, including *EGFR* amplifications and rearrangements (Skog *et al.*, 2008) (Salkeni *et al.*, 2013) (Manda *et al.*, 2018) (Figueroa *et al.*, 2017), *IDH1* mutations (Boisselier *et al.*, 2012) (Chen *et al.*, 2013) (García-Romero *et al.*, 2017) and H3K27M mutations (Huang *et al.*, 2017) from the analysis of plasma or CSF. Nonetheless, the sensitivity and specificity of these approaches remain far from allowing their use in daily practice.

The aim of this study was to develop a technique to acquire the mutational status of *IDH1* from the analysis of tumor-derived EV circulating in plasma. The *IDH1* mutation was chosen due to its capital implications for the diagnosis and management of diffuse gliomas (Louis *et al.*, 2016) (Sanson *et al.*, 2009) (Weller *et al.*, 2017) (Dang, Yen and Attar, 2016).

Patients and methods

Patient enrolment. Patients were enrolled at the Neurosurgery Units of the Parma and Cremona hospitals between January 2018 and December 2018. Inclusion criteria were: 1) age ≥ 18 years-old; 2) radiological evidence of a brain lesion compatible with diffuse glioma, detected following the onset of neurological symptoms; 3) reasonable exclusion of alternative etiologies (vascular, inflammatory, infectious, traumatic, etc..) by noninvasive means; 4) clinical indication to perform surgical resection or biopsy. Demographic and clinical data from the patients included in the study were collected and stored in a dedicated database in anonymized form. The study was approved by the Ethics Committee of the IRCCS Mondino Foundation. All patients signed written informed consent for study participation.

Tumor volume assessment. Whenever available, preoperative MRI scans were collected and analyzed with the OleaSphere 3.0.16 software. Total tumor volume and contrast-enhancing tumor volume were obtained by semi-automatic segmentation of FLAIR and T1-weighted sequences after gadolinium injection, respectively. An illustrative example of tumor segmentation is reported in Figure 11.

Figure 11. Example of semi-automatic tumor segmentation using the OleaSphere 3.0.16 software in a patient with a left parieto-callosal glioblastoma. Panel A and B: axial FLAIR sequences. Panel C and D: axial T1-weigthed images after gadolinium injection.

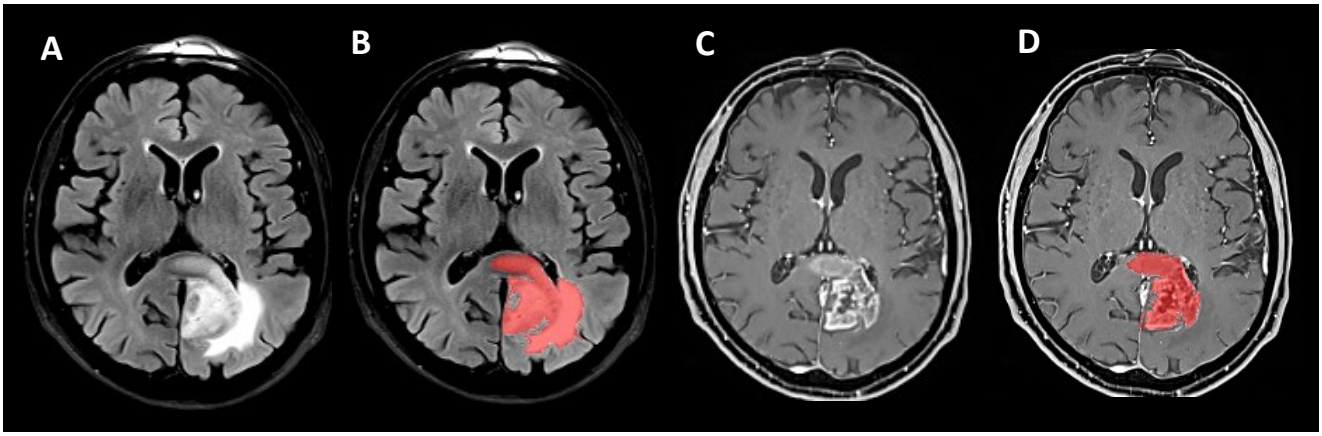

Biological sample collection. For each patient, we collected a sample of venous blood during the 48 hours preceding surgery (two sodium citrate tubes) and a fragment of tumor tissue during surgery. This approach was chosen to compare the mutational status of *IDH1* obtained by the analysis of EV with the mutational status obtained by the analysis of tumor tissue, and thus infer the sensitivity and specificity of the technique. Whole blood was centrifuged at 1,000 g for 15 minutes within one hour from collection to separate plasma, and then additionally centrifuged at 1,600 g for 20 minutes to remove platelets. Platelet-free plasma (2 to 3 ml) was then transferred to a new Eppendorf tube and stored at -80° C. The sample of tumor tissue collected during surgery was snap frozen at -80°C. Frozen plasma and tumor samples were then transferred to the Genomic and post-Genomic Center of the IRCCS Mondino Foundation for analysis. The histological analysis of surgical specimens was carried out in the Parma and Cremona hospitals as per common clinical practice, according to the dictates of the 2016 WHO classification (Louis *et al.*, 2016).

Tumor DNA extraction and *IDH1* sequencing. Tumor DNA was extracted from frozen tissue by automated extraction (Maxwell, Promega) using a LEV Blood DNA Kit as per manufacturer's instructions. Briefly, tumor samples were thawed on ice and then processed at room temperature. Each sample was added 300 µl of lysis buffer and 30 µl of proteinase K. Samples were vortexed and incubated at 56°C for at least 1 hour with mild agitation. Lysed tumor samples were then transferred into the cartridges. After adding 50 µl of elution buffer into the elution tubes and having positioned the plungers, automated DNA extraction was started. The concentration of tumor DNA obtained following extraction was assessed using a Nanodrop instrument. The *IDH1* status was obtained by standard PCR amplification followed by Sanger sequencing, using the following primers: F-GCGTCAAATGTGCCACTATC, R-cacatacaagttggaaatttctgg. Primers were centered on codon 132 that is where hotspot *IDH1* mutations recur in diffuse gliomas. Figure 12 reports, as an example, the electropherogram of an *IDH1*-wildtype and an *IDH1*-mutant sample. The *IDH1* mutation there illustrated is the R132H mutation, a missense mutation (G>A) that results in the substitution of an arginine with an histidine, which is far the most common *IDH1* mutation in diffuse gliomas (Yan *et al.*, 2009) (Sanson *et al.*, 2009).

Figure 12. Electropherogram of an *IDH1*-wildtype (left) and of an *IDH1* R2132H-mutant (right) sample obtained by standard PCR amplification and Sanger sequencing.

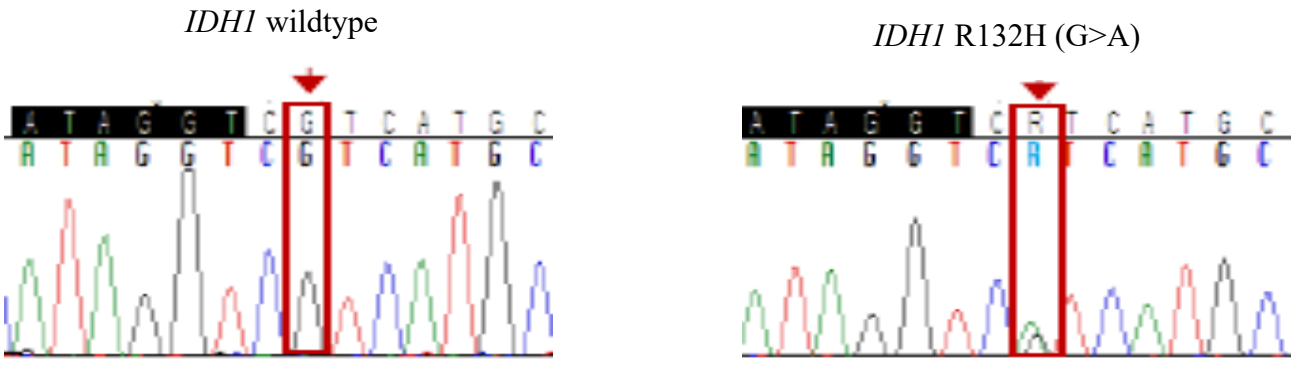

RNA extraction from tumor tissue and reverse transcription to cDNA. Tumor samples were thawed on ice, added 500 µl of Trizol, and incubated for 5 minutes at room temperature. Each sample was added 100 µl of chloroform and incubated 5 minutes at room temperature. Samples were vortexed and centrifuged at 12,000 g for 10 minutes at 4°C. Centrifugation allowed to separate three distinct phases, the upper of which was transferred into a novel tube. Samples were then added 500 µl of isopropyl acid and incubated 10 minutes at room temperature. After vigorous agitation, samples were centrifuged at 12,000 g for 10 minutes at 4°C. The supernatant was discarded and 1 ml of ethanol 75% was added to the pellet. Samples were then centrifuged at 7,600 g for 5 minutes at 4°C. The supernatant was discarded, and the RNA pellet was left to dry a few minutes at room temperature. The RNA pellet was then suspended in 11 µl of H2O-diethilproprionate. RNA concentration was measured using a Nanodrop instrument. Tumor-extracted RNA was then reverse transcribed to cDNA using an iScript cDNA Synthesis Kit (BioRad) according to manufacturer's instructions.

EV isolation. MV and EXO were isolated from plasma using a technique of differential centrifugation followed by ultracentrifugation (Sproviero *et al.*, 2018). Briefly, platelet-free plasma was thawed on ice and centrifuged at 20,000 g for 1 hour using a Centrifuge 5427-R (Eppendorf). The pellet was washed with filtered PBS and centrifuged for 1 hour at 20,000 g. The pellet was processed for MV analysis, while the supernatant was filtered through a 0.2 µm filter, transferred into a novel tube, and spun in an Optima MAX-TL Ultracentrifuge (Beckman Coulter) at 100,000 g for 1 hour at 4°C. After ultracentrifugation, the supernatant was discarded, and the EXO pellet was washed with 1 mL of filtered PBS at 100,000 g for 1 h at 4°C. The EXO pellet was then processed for EXO analysis.

The size and the concentration of MV and EXO was evaluated by Nanoparticle Tracking Analysis (NTA) using a NS300 instrument (NanoSight). To allow a more accurate analysis, MV and EXO samples were diluted with PBS to achieve an optimal concentration of 10^7–10^9 particles/mL. One mL of diluted sample was loaded into the machine and read at a rate of 30 frames per second. Three videos, lasting 60 seconds each, were recorded. Nanoparticle size and concentration were the extrapolated form the three videos using the NTA software version 2.2 (NanoSight). For subsequent analyses, the mean values of the three recordings were considered. Figure 13 reports, as an example, the diagrams depicting particle concentration in function of their size obtained using the NTA software.

Extraction, reverse transcription, and *IDH1* sequencing of cargo RNAs. Cargo RNAs were separately extracted from MV and EXO pellets using a miRNAeasy Mini Kit (Qiagen), according to the manufacturer's instructions. The quality and the concentration of the total RNA extracted from MV and EXO pellets were measured with a Bioanalyzer 2100 (Agilent) using an RNA 6000 Pico Kit.

Total RNA was reverse transcribed into cDNA using an iScript cDNA Synthesis Kit (BioRad) according to manufacturer's instructions. cDNA was then amplified and analyzed for *IDH1* R132H mutations by digital droplet PCR (ddPCR) using a SNP genotyping assay custom designed for the detection of this mutation (rs121913500) (Thermo Fisher). The probe for the detection of the *IDH1*-wildtype sequence was marked with VIC and the probe for the detection of the *IDH1* R132H-mutant sequence was marked with FAM. The PCR

mix was composed as follows: 10 µl of ddPCR Supermix for Probes 1x, 0.5 µl of mix SNP genotyping assay custom that included both probes (VIC/FAM) and primers, and 1 to 7.5 µl of DNase free water. The PCR mix was added 2 to 8.5 µl of cDNA, for a total volume of 20 µl. The cycling protocol was as follows: 95°C for 10 minutes followed by 94°C for 30 seconds, followed by 60°C for 1 minute, for a total of 40 cycles, after which there was an incubation at 98°C for 10 minutes, followed by indefinite conservation at 4°C.

Figure 13. Example of the diagrams reporting MV (left) and EXO (right) concentration (y-axis, particles/ml) depending on their size (x-axis, nm) obtained by Nanoparticle Tracking Analysis (NTA) using a NS300 instrument, NTA software version 2.2 (NanoSight).

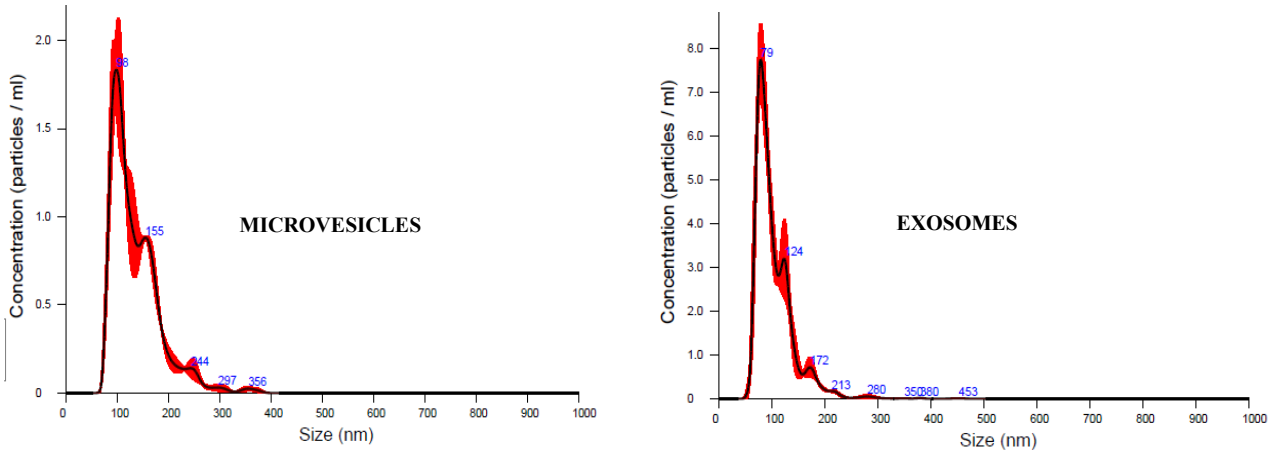

Statistical analyses. All statistical analyses were performed using "R" software packages. Descriptive statistics were used to summarize data. Quantitative variables were compared using the Mann-Whitney (Wilcoxon) test. The Spearman correlation test was used to assess correlations between variables. The threshold for statistical significance was p = 0.05.

Results

Patient characteristics. Out of the 24 patients enrolled, four were excluded from subsequent analyses as they received a histological diagnosis different from diffuse glioma (meningioma (1), glioneuronal tumor (1), brain metastasis (2)). Fourteen out of the 20 patients were male (14/20, 70%). Median age at the time of tumor diagnosis was 65.4 years-old (range: 31.3 – 80.5).

***IDH1* status from tumor DNA and integrated diagnosis**. *IDH1* mutations were detected by Sanger sequencing in 4 out of the 20 tumor samples (4/20, 20%). All four *IDH1* mutations were R132H. Final diagnosis according to the 2016 WHO classification was of *IDH*-mutant 1p/19q codeleted oligodendroglioma (grade II) in three cases (3/20, 15%), *IDH*-mutant anaplastic astrocytoma (grade III) in one case (1/20, 5%), *IDH*-wildtype anaplastic astrocytoma (grade III) in one case (1/20, 5%), and *IDH*-wildtype glioblastoma (grade IV) in 15 cases (15/20, 75%).

EV diameter and concentration. MV tended to have larger diameter (median: 103.5 vs. 93.9 nm, p=0.04) but lower concentrations (median: 1.4 vs. 2.2 x 10^{11} particles/ml, p=0.13) compared to EXO. The concentrations of MV and EXO were compared with a cohort of healthy controls previously analyzed at our laboratory using the same methods (Sproviero *et al.*, 2018). We found that glioma patients had significantly higher concentrations of both MV and EXO (mean MV concentration: 2.1 vs 0.4 x 10^{11} particles/ml, p=0.001; mean EXO concentration: 3.4 vs 0.3 x 10^{11} particles/ml, p=0.002) in plasma compared to healthy subjects.

Clinical-biological correlations. We then assessed whether total tumor volume or enhancing tumor volume could influence the concentration of EV detected in plasma, as suggested by other reports (Boisselier *et al.*, 2012). We did not find any significant correlation between total or enhancing tumor volume and MV or EXO concentration. We found instead a correlation between MV and EXO concentration and histological grade: patients with grade IV gliomas tended to have higher MV and EXO concentrations compared to patients with grade II and III gliomas (median MV concentration: 1.55 vs. 1.11 x 10^{11} particles/ml, p=0.066; median EXO concentration: 2.34 vs. 1.32 x 10^{11} particles/ml, p=0.081).

Concentration and integrity of cargo RNAs extracted from EV. The median concentration of total RNAs extracted from MV was 419 pg/µl (range: 209 – 958) and the median concentration of total RNAs extracted from EXO was 371 pg/µl (range: 74 – 1901) (p=0.52). As evident in Figure 14, the RNA fragments extracted from MV and EXO were mostly < 300 nucleotides in length. RNA Integrity Numbers ranged from 2 to 6.8, reflecting a mild to moderate RNA degradation.

Figure 14. Example of the RNA profiles from a sample of MV (left panel) and a sample of EXO (right panel) obtained using a Bioanalyzer 2100 (Agilent) with the RNA 6000 Pico Kit. The y-axis indicates fluorescence intensity (fluorescence units, FU) and the x-axis indicates nucleotide length (nt).

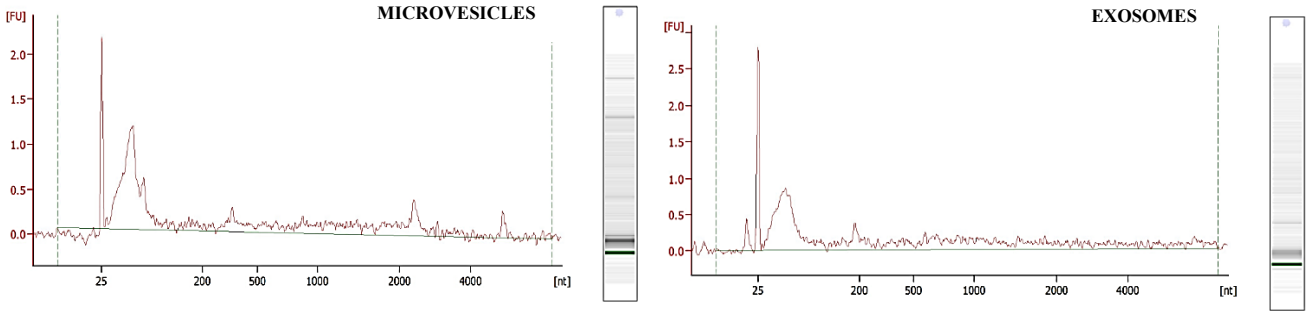

***IDH1* status from EV.** The cDNA reverse transcribed from cargo RNAs was analyzed for *IDH1* mutations by ddPCR. Because of the low quality and concentration of the RNA extracted from MV and EXO, we first tested our PCR conditions using samples of cDNAs reverse transcribed from RNA obtained from tumor tissue. To this purpose, we reverse transcribed the cDNA from an *IDH1*-wildtype tumor and one *IDH1* R132H-mutant tumor in order to verify the signal from both probes. Figure 15 reports the result of the analysis in ddPCR for the *IDH1*-mutant sample, showing, as expected, an *IDH1*-mutant curve, as well as an *IDH1*-wildtype curve that

corresponds to non-tumoral cells included in the sample. This test confirmed that established PCR conditions allowed an adequate cDNA amplification and an accurate detection of both the *IDH1*-mutant and the *IDH1*-wildtype signal. The *IDH*-wildtype sample showed instead, as expected, only the signal for the *IDH*-wildtype probe (not shown).

Figure 15. Results of the experiment of ddPCR using a sample of cDNA from an *IDH1* R132H-mutant tumor tissue.

CHANNEL 1: *IDH1R132H*-mutant probe (FAM)

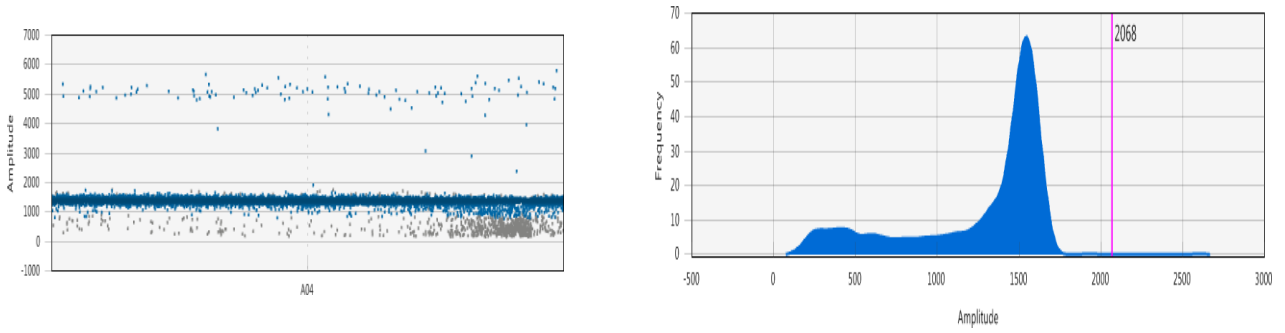

CHANNEL 2: *IDH1*-wildtype probe (VIC)

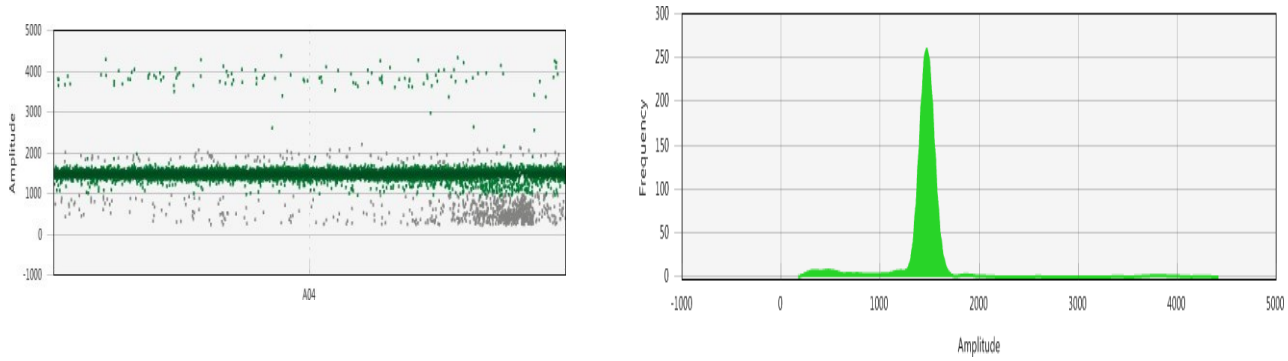

Verified that our PCR conditions were suitable, we repeated the same experiment using samples of cDNA reverse transcribed from the cargo RNAs extracted from MV and EXO. Regrettably, even using different samples and increasing cDNA volumes, we could not obtain a sufficient number of droplets for analysis (around 4,000 vs. over 10,000 using cDNA from tumor tissue) neither with MV or EXO pellets. Therefore, the present assay, which provided accurate results on cDNA from tumor tissue, did not allow an accurate detection of the *IDH1* mutation using cDNA from EV. This observation suggests that the quantity and quality of cargo RNAs represents a limiting factor for the detection of *IDH1* mutations using this approach.

Discussion

In the present study, we collected plasma samples from 20 patients with diffuse gliomas, we isolated EV, extracted cargo RNAs, and analyzed the cDNAs obtained from their reverse transcription for the presence of

IDH1 mutations. In parallel, we tested for *IDH1* mutations tumor samples from the same patients to evaluate whether the mutational status obtained from plasmatic EV corresponded to the mutational status obtained from tumor tissue.

Our isolation method allowed to separate two different populations of EV, corresponding to MV and EXO, each with a plasmatic concentration in the order of magnitude of 10^{11} particles per ml. The median concentrations of EV reported in literature for glioma patients widely range across studies from 4 x 10^{10} (Osti *et al.*, 2019) to 4 x 10^{12} (Chen *et al.*, 2013) particles/ml, highlighting how isolation methods, initial plasma volume, and measurement conditions strongly affect this measure. Nonetheless, when the same conditions of isolation and measurement were used, glioma patients consistently had plasmatic concentrations of MV and EXO 5 to 10 times higher than healthy subjects (Osti *et al.*, 2019) (Noerholm *et al.*, 2012). As only a minor proportion of the EV detected in plasma is expected to be of tumor origin (Fraser *et al.*, 2019), the substantial difference between glioma patients and healthy subjects is probably attributable not only to the presence of tumor-derived EV but also to a reactive secretion of EV from normal cells.

The concentration of EV in plasma did not correlate with total tumor volume nor with enhancing tumor volume, though volumetric analysis could be performed only in a subset of patients. EV concentration correlated instead with histological grade: patients with glioblastomas (grade IV) had higher median EV concentrations compared to patients with lower grade (grade II-III) tumors. This difference cannot be merely explained by blood brain barrier damage (as no correlation between enhancing tumor volume and EV concentration was found), additional biological features (e.g., increased cell turnover, angiogenesis, tumor microenvironment) probably contributing to the increased EV concentration observed in patients with high-grade tumors.

The concentration of cargo RNAs extracted from plasmatic EV was similar for MV and EXO. BioAnalyzer profiles highlighted that most of the cargo of MV and EXO was represented by small RNAs of less than 300 nucleotides in length. As highlighted by other reports, these fragments probably include small non-coding RNAs (e.g., miRNAs and repetitive elements) (Noerholm *et al.*, 2012), as well as degraded RNAs of longer size, such as mRNAs and tRNAs (Gonda *et al.*, 2013). This observation suggest that one of the reasons for the failure of our experiment was that the length of the mRNA fragments we are able to retrieve from EV was insufficient to allow an effective reverse transcription and amplification of the region of interest. We are currently planning to repeat the experiments using a more sensitive method for RNA extraction in the attempt to overcome this issue.

Other research groups have previously used EV as a substrate for the noninvasive detection of *IDH1* mutations (Chen *et al.*, 2013) (García-Romero *et al.*, 2017). One group used a combination of BEAMing and ddPCR for the analysis of cDNAs reverse transcribed from mRNAs extracted from EV circulating in plasma or CSF (Chen *et al.*, 2013). While the analysis of the EV isolated from CSF correctly identified 5 out of 8 *IDH1*-mutant patients, the analysis of the EV isolated from plasma failed to correctly identify *IDH1* mutations, probably due to the limited volume of plasma used in the experiments (1 ml per sample). As tumor-derived EV represent only a minority of the EV detected in the systemic circulation, larger volumes of plasma are probably needed to dispose of sufficient amounts of tumor material.

As, besides RNA, the cargo of EV also includes DNA fragments, another group has tried to obtain the mutational status of *IDH1* through the analysis of DNA extracted from plasmatic EV using a technique of DNA pre-amplification followed by Fast Cold PCR (García-Romero *et al.*, 2017). While, indeed, all four *IDH1*-mutant patients were correctly identified by the analysis of plasmatic EV, 6 out of 17 *IDH*-wildtype patients were falsely labelled as *IDH*-mutant, highlighting the very low specificity of the assay. As evidenced by our and previous observations, further research is needed to improve the sensitivity and specificity of these approaches and obtain a reliable technique of liquid biopsy to use in daily practice.

Unpublished data

Magnetic resonance spectroscopy for 2-hydroxyglutarate detection and monitoring

Background

IDH1 and *IDH2* mutations have important diagnostic, prognostic, and therapeutic implications for the management of patients with diffuse gliomas (Louis *et al.*, 2016) (Sanson *et al.*, 2009) (Weller *et al.*, 2017). These two genes encode for intracellular enzymes that normally convert isocitrate to α-ketoglutarate via oxidative decarboxylation. By altering key residues within the active site of the enzyme, hotspot mutations in *IDH1* (codon 132) and *IDH2* (codon 172) (Yan *et al.*, 2009) result in a neomorphic enzymatic activity, with the conversion of α-ketoglutarate to 2-hydroxyglutarate (2HG) that accumulates intracellularly (Dang *et al.*, 2009). This metabolite can be detected *in vivo* by magnetic resonance spectroscopy (MRS) (Andronesi *et al.*, 2012) (Kalinina *et al.*, 2012), thus providing information on *IDH* mutational status.

Novel methods for imaging acquisition and processing have progressively allowed to resolve the spectral overlap between 2HG and other metabolites (Andronesi *et al.*, 2012) (Choi *et al.*, 2013) (Kalinina *et al.*, 2012), improving the sensitivity and specificity of MRS for 2HG detection. Among those, we recently reported on the high accuracy of Mescher–Garwood point-resolved spectroscopy (MEGA-PRESS) in preoperative patients (Branzoli *et al.*, 2018). While the preoperative prediction of the *IDH* status remains indeed an important application of MRS, the encouraging results achieved in recent years have prompted to explore other potential uses, including treatment planning (Jafari-Khouzani *et al.*, 2016) and response assessment following cytotoxic or targeted therapies (Andronesi *et al.*, 2016) (Andronesi *et al.*, 2018). However, the sensitivity and specificity of this technique in patients who have undergone surgery and chemoradiation have not yet been evaluated in large cohorts of patients in a "real-world" setting.

In the present study, we investigated the clinical, radiological, and molecular factors influencing 2HG detection by MEGA-PRESS in untreated and pretreated glioma patients and assessed the ability of MRS to capture tumor response and progression in a subgroup of patients with *IDH*-mutant gliomas followed longitudinally by MRS while receiving cytotoxic or targeted therapies.

Patients and methods

Patient enrollment. Patients were prospectively enrolled at the Pitié-Salpêtrière Hospital (Paris, France) between October 2014 and July 2018. Inclusion criteria comprised: (1) age ≥ 18 years-old, (2) suspected or histologically-confirmed diffuse glioma with tumor volume > 6 ml on T2/FLAIR images, (3) KPS > 60, and (4)

ability to provide written informed consent. Enrolled patients were divided into two cohorts based on whether they had (or not) previously received surgery and antitumoral treatments:

- **cohort 1**: treatment-naïve patients with suspected diffuse glioma on imaging, candidate to receive surgery (biopsy or resection) (Branzoli *et al.*, 2018)

- **cohort 2:** patients with histologically confirmed *IDH*-mutant diffuse glioma diagnosed upon biopsy or resection. Patients in this group had also possibly received (or were actively receiving at the time of MRS) cytotoxic treatments, including radiotherapy and/or chemotherapy. A subgroup of patients who had a measurable peak of 2HG on MRS and were about to start a novel line of treatment (either cytotoxic or targeted) underwent longitudinal MRS assessments to assess whether 2HG variations on MRS paralleled tumor response.

All patients enrolled in the study underwent the collection of plasma and urine samples at the time of their baseline MRS. Plasma and urines were collected in the hour preceding MRS and were stored at -80°C until the analysis. For patients in cohort 1, we also collected a sample of tumor during surgery, which was snap-frozen at -80°C.

The study was approved by the local Ethics Committee (CPP-Paris VI). All biological samples and clinico-pathological data were collected upon written informed consent in accordance with the tenets of the Declaration of Helsinki. All subjects provided written informed consent for study participation.

MRI/MRS acquisition protocol. MRI/MRS scans were acquired using a 3T whole-body system (MAGNETOM Verio, Siemens, Erlangen, Germany) equipped with a 32-channel receive-only head coil. The protocol included T2-weighted FLAIR and basal T1-weighted sequences for voxel placement and tissue segmentation. MRS was acquired using a single-voxel MEGA-PRESS sequence as previously described (TR=2s, TE=68ms, 128 averages, scan time = 9 min), with editing pulses applied at 1.9 and 7.5 ppm (Branzoli *et al.*, 2018). Water suppression was performed using VAPOR and outer volume suppression techniques (Tkác *et al.*, 1999). A non-water suppressed scan was acquired for the quantification of absolute metabolite concentrations. The established size of the spectroscopic volume of interest (VOI) was 8 cm^3, though, in case of need, it was decreased down to 6 cm^3 to minimize partial volume effects.

MRS post-processing. Frequency and phase corrections were performed on single spectra based on the total choline signal at 3.2 ppm, using in-house written Matlab routines. The final edited spectra were obtained by subtracting the spectra acquired at the edit-on and edit-off conditions, allowing for the detection of the 2HG signal at 4.05 ppm (Figure 16). Spectral quantification was performed using the LCModel method (Provencher, 2001) based on the water reference scan, assuming a bulk water concentration in tumors of 55.5 mM and correcting for water transverse T2 relaxation time (150 ms) (Madan *et al.*, 2015). The basic set of metabolites included 2HG, γ-aminobutyric acid (GABA), glutamate (Glu), glutamine (Gln), glutathione, *N*-acetylaspartate

(NAA), *N*-acetylaspartylglutamate (NAAG), and experimentally measured macromolecular spectrum. Additional metabolites, including creatine + phosphocreatine (tCr), choline (tCho), Glu+Gln (Glx), lactate (Lac), myo-inositol (Ins), and NAA + NAAG (tNAA) were quantified from edit-off data. Based our previous findings (Branzoli *et al.*, 2018), the Cramer Rao lower bounds (CRLB) threshold for 2HG detection was set to 50%.

Figure 16. Example of the volumes of interest (FLAIR images, panel A-C) and resulting spectra (panel D-F) in one *IDH1*-mutant glioma (panel A,D), one *IDH1/2*-wildtype glioma (panel B,E), and one healthy tissue (panel C,F). In the spectra from the *IDH1*-mutant glioma (panel D), a peak of 2HG can be observed at 4.02 ppm. The 2HG peak is instead absent in the spectra from the *IDH*-wildtype glioma (panel E) and from the healthy tissue (panel F). In vivo MEGA-PRESS (black line), LCModel fits (red line), 2HG contribution (green line), and residuals (blue line). GABA+ = GABA + macromolecules, Glx = glutamate + glutamine, NAA = *N*-acetylaspartate. Modified from Branzoli *et al.*, 2018.

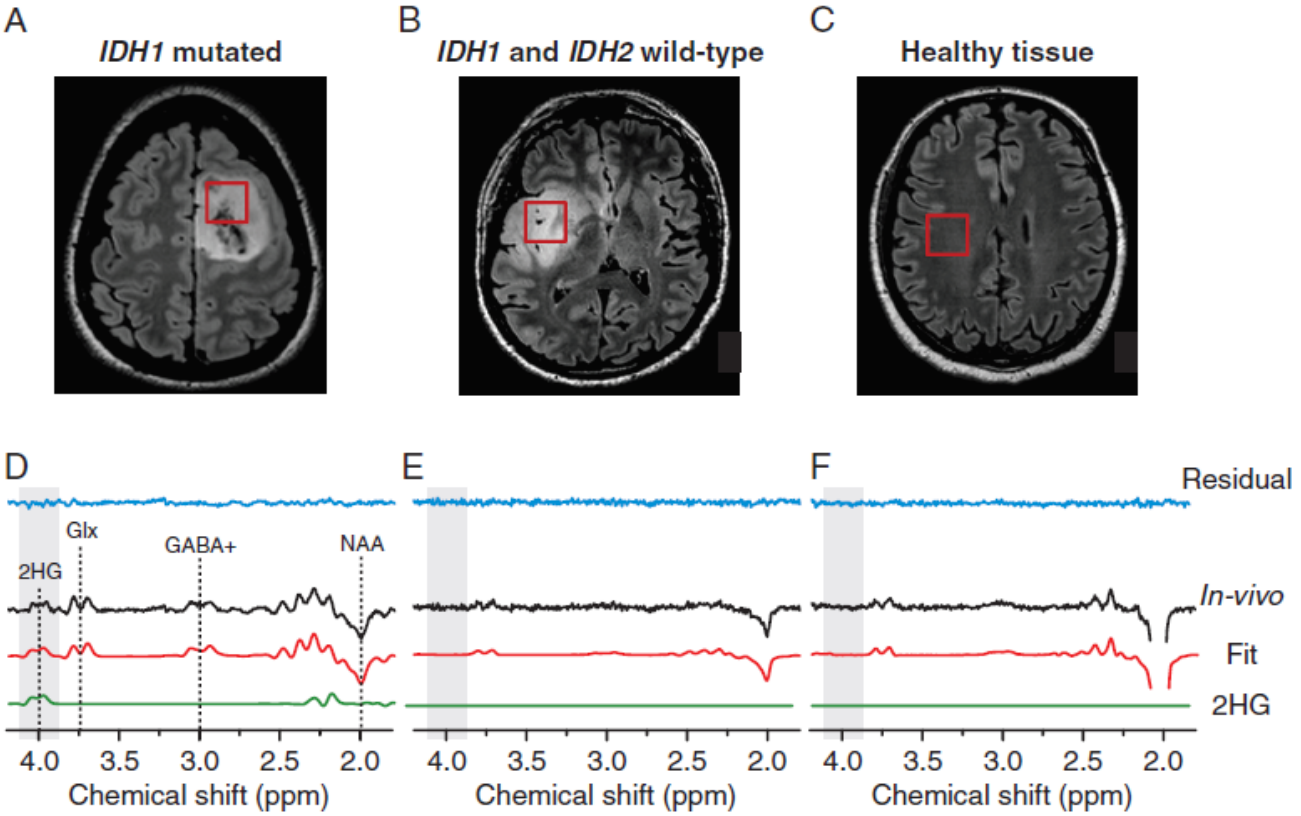

Morphological imaging features. Total tumor volume and the volume of intratumoral cystic/necrotic areas were estimated from the segmentation of FLAIR images using the ITK-SNAP software (www.itksnap.org). The fraction of the VOI filled with tumor tissue was estimated by overlaying tumor masks obtained from ITK-SNAP with the corresponding VOI. Neuroradiological presentation was defined as either "expansive" [if the size of T1 abnormality was almost equal to the size of FLAIR abnormality] or "infiltrative" [if the size of T1 abnormality was much smaller than the size of FLAIR abnormality], according to the VASARI feature set v1.1. For all patients who had an available contrast MRI acquired for clinical purposes during the four weeks preceding or following MRS, we examined T1-weigthed sequences after gadolinium injection to determine whether any areas of contrast-enhancement were included in the VOI.

Control MRIs performed for clinical purposes by patients in cohort 2 who underwent longitudinal MRS assessments were systematically reviewed by a neuroradiologist who assessed tumor response using the Response Assessment in Neuro-Oncology (RANO) criteria for high- and low-grade gliomas (van den Bent *et al.*, 2011) (Wen *et al.*, 2010).

Immunohistochemical and molecular studies on tumor specimens. Integrated diagnoses were established by board-certified neuropathologists according to the 2016 WHO classification of Tumors of the CNS (Louis *et al.*, 2016). Immunohistochemistry was performed on 4-µm-thick FFPE sections using an automated system (Benchmark XT, Ventana Medical System Inc, Tucson AZ, USA) for the assessment of IDH1 R132H (Dianova, H09), p53 (DAKO, DO.7) and ATRX (SIGMA, polyclonal) expression. All tumors negative for IDH1 R132H on immunohistochemistry were evaluated for *IDH1* and *IDH2* mutations by DNA sequencing. Briefly, tumor DNA was extracted from snap-frozen tissue (QIAamp DNA Mini Kit, Qiagen) or FFPE sections (GeneJET FFPE DNA purification kit, Thermo Scientific) as per manufacturers' instructions. The mutational status of *IDH1* and *IDH2* was determined by NGS or by the Sanger method after standard PCR amplification, using previously reported primers (Labussière *et al.*, 2010). CNVs were assessed by CGH-array (Labussière *et al.*, 2016) or inferred from NGS data. For patients in cohort 1, we estimated the proportion of *IDH*-mutant cells in the tumor sample either from NGS data (i.e., number of mutant reads over total number of reads) or from the visual assessment of the chromatograms obtained from Sanger sequencing.

2HG concentrations in tumor tissue, plasma, and urine. Snap-frozen tumor samples from patients in cohort 1 and from an independent group of glioma patients identified in the OncoNeuroTek database (Pitié-Salpêtrière, Paris) were analyzed by gas chromatography-mass spectrometry (GC-MS/MS) to assess 2HG concentrations, as previously described (Branzoli *et al.*, 2018). Plasma and urine samples from all patients included in the study were analyzed for 2HG concentrations using the same method.

Statistical analyses. Differences in the distribution of categorical variables between groups were assessed using Fisher's exact test. P-values were adjusted for multiple testing according to the Benjamini and Hochberg false discovery rate. A q-value of 0.05 (2-sided) was considered as statistically significant. Differences between mean values of quantitative variables were tested with a two-sided Student's t test. Multidimensional association tables were used to explore associations between variables. Statistically significant correlations between variables were assessed using the Spearman correlation test. OS was defined as the time between diagnosis and death (or last follow-up in censored patients). Survival curves were calculated using the Kaplan-Meier method. Statistically significant differences between survival curves were assessed using the Log-Rank test. A Log-Rank test p-value <0.05 (two-sided) was considered as statistically significant. The Cox model was used to evaluate the effect of quantitative variables on survival and for multivariate survival analyses. Statistical analyses were performed using SPSS and R software packages.

Results

Cohort description. We prospectively enrolled and studied 70 consecutive patients, including 24 patients with suspected diffuse glioma enrolled before surgery and naive of any anti-cancer therapy (cohort 1) (Branzoli *et al.*, 2018) and 46 patients with histologically confirmed *IDH*-mutant glioma (cohort 2). Among the latter, 22 patients were studied at first tumor progression after surgery and had not yet received any cytotoxic or targeted treatment, while 24 patients were analyzed after having received (or while actively receiving) antitumoral treatments. Eighteen patients who had a detectable peak of 2HG on MRS and were about to start a line of cytotoxic (n=12) or targeted (n=6) therapy underwent longitudinal MRS assessments for 2HG monitoring.

Clinical, radiological, and molecular factors affecting 2HG detection by MRS. MEGA-PRESS correctly identified a peak of 2HG at 4.05 ppm in 52 out of 67 patients with *IDH*-mutant tumors and in none of the patients with *IDH*-wildtype tumors, corresponding to a sensitivity of 79% and a specificity of 100%.

2HG detection is affected by previous surgical resection and antitumoral treatments. 2HG detection was affected by a history of surgery (consisting of either biopsy or resection) (p=0.03) and cytotoxic treatments (radiotherapy and/or chemotherapy) (p=0.01). Consistently, MRS sensitivity decreased from 95% in untreated patients (Branzoli *et al.*, 2018) to 83% in patients who had only received surgery to 62% in patients who had received both surgery and cytotoxic treatments. 2HG levels estimated by MRS were lower in patients who had undergone surgery compared to patients who had not (median: 1.5 vs. 2.7 mM, p=0.011) (Figure 17, panel A), and were lower in patients who had received cytotoxic treatments compared to patients who had not (median: 0.8 vs. 2.3 mM, p=0.0079) (Figure 17, panel B). Patients who were actively receiving chemotherapy at the time of MRS had lower 2HG levels compared to patients who were not actively receiving treatment (median: 0.2 vs. 2.25 mM, p=0.0011) (Figure 17, panel C).

Figure 17. Dot plots comparing 2HG levels estimated by MRS (y axis, mM) in different patient groups (x-axis).

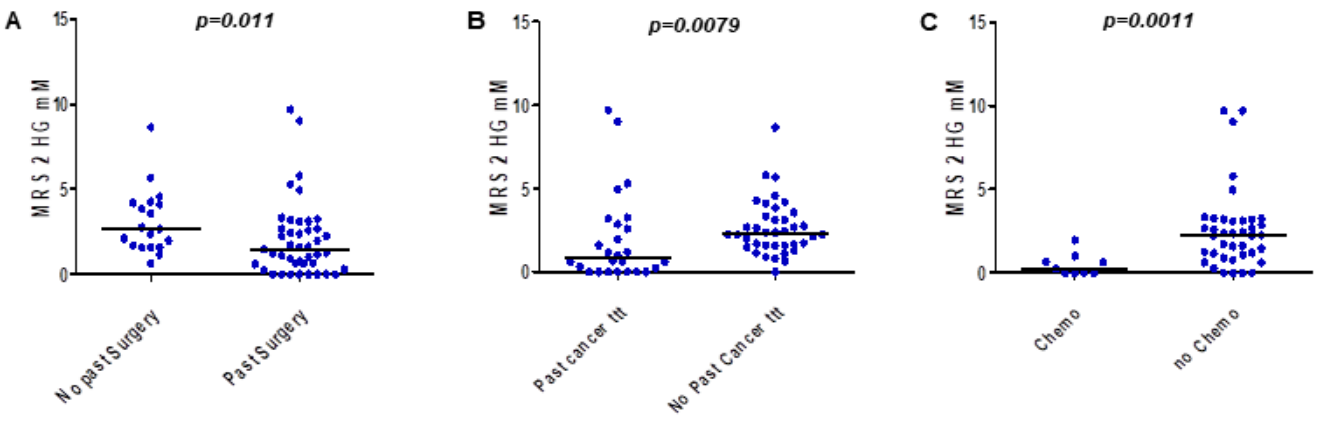

2HG detection is affected by tumor volume and cellular density. We tried to assess whether the decreased ability to detect the peak of 2HG in patients who had received surgery and antitumoral treatments could be

attributed to the reduction of viable tumor cells that is associated with these interventions. We found that 2HG detection was facilitated by higher tumor volumes (p=0.02), better voxel coverage (p=0.04), and "expansive" presentation (p=0.06), while it was hampered by the presence of intratumoral cysts/necrosis (p=0.04). Nor the presence or the extent of contrast enhancement within the voxel (p=1) impacted 2HG detection. Consistently, MRS sensitivity was substantially affected by tumor volume (83% for tumor volumes ≥ 27 cm^3 and 94% for tumor volumes ≥ 54 cm^3) and voxel coverage (84% for voxel coverage ≥ 72% and 94% for voxel coverage ≥ 90%). 2HG levels estimated by MRS directly correlated with tCho levels (p<0.0001) (Figure 18, panel A), reflecting cell turnover, and inversely correlated with Ins levels (p=0.0025) (Figure 18, panel B), reflecting gliosis. These findings consistently point to the density of tumor cells within the voxel as a determining factor for 2HG detection.

Figure 18. Scatter plots illustrating the correlation between 2HG levels estimated by MRS (y-axis, mM) and tCho levels (panel A), Ins levels (panel B), and the percentage of *IDH*-mutant reads (panel C).

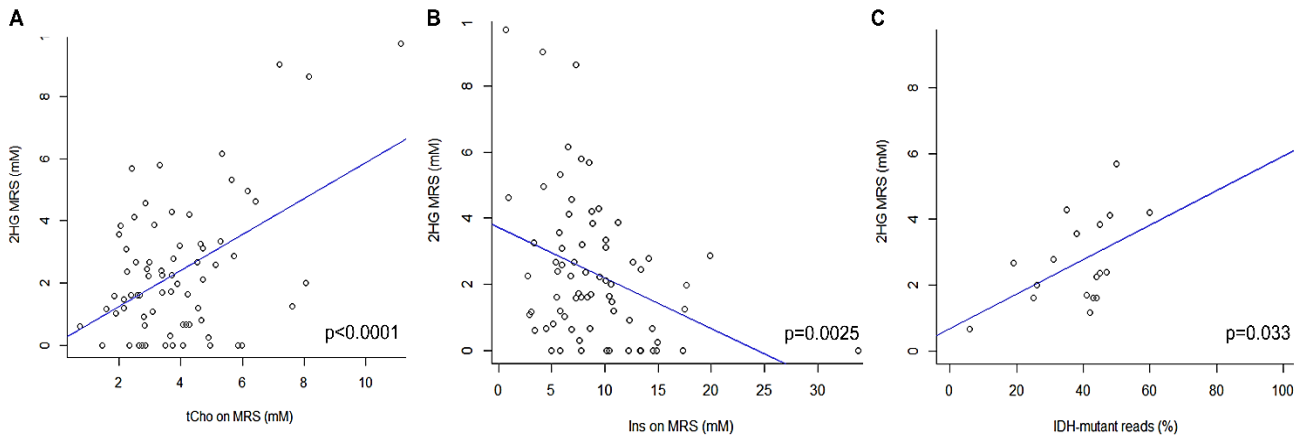

2HG levels on MRS correlate with the proportion of *IDH*-mutant reads. As our findings suggested that the proportion of tumor cells in the voxel might affect 2HG detection, for patients in cohort 1, we assessed whether 2HG levels measured by MRS correlated with the proportion of *IDH*-mutant reads in the surgical sample. We found that the proportion of *IDH*-mutant reads in the surgical sample correlated with 2HG levels estimated by MRS (p=0.033) (Figure 18, panel C).

2HG levels depend on the type of *IDH* mutation. We then assessed whether, besides the number of *IDH*-mutant reads, the type of *IDH* mutation and the presence of the chromosome 1p/19q codeletion could affect 2HG levels estimated by MRS. Patients with *IDH2* mutations had higher 2HG levels than patients with *IDH1* mutations (median: 5.68 vs. 1.97 mM, p=0.014). Patients with minoritarian *IDH1* mutations had lower 2HG levels than patients with *IDH1* R132H mutations and patients with *IDH2* R172K mutations (median: 1.12 vs. 2.06 vs. 5.68 mM, p=0.0025). The chromosome 1p/19q codeletion did not seem to impact 2HG levels, nor in *IDH1*-mutant (p=0.97) or in *IDH2*-mutant (p=1) patients.

2HG concentrations measured by GC-MS/MS in tumor tissue showed similar trends, with higher 2HG levels in *IDH2*-mutant compared to *IDH1*-mutant and *IDH*-wildtype tumors (median: 129.93 vs. 70.86 vs. 0.96 nmol/mg, p<0.001), lower 2HG levels in patents with minoritarian *IDH1* mutations compared to *IDH1* R132H mutations (50.19 vs. 115.00 nmol/mg, p=0.18) and no statistically significant effect of the chromosome 1p/19q codeletion.

2HG levels at progression and their prognostic value. As, among patients with *IDH*-mutant gliomas, pretreated subjects more frequently showed low or undetectable 2HG compared to untreated individuals, we sought to determine whether this observation merely reflected a more advanced stage of disease. We found that patients studied at progression did not always show elevated 2HG levels and, especially, 1p/19q non-codeleted patients who, more commonly than 1p/19q codeleted patients, displayed low or undetectable 2HG levels at progression (Figure 19, panel A and B). Median 2HG levels estimated by MRS at progression were lower in patients with 1p/19q non-codeleted gliomas compared to patients with 1p/19q codeleted gliomas studied in the same setting (median: 0.6. vs. 3.7 mM, p=0.015), consistently with the observation that, differently from 1p/19q codeleted gliomas, 1p/19q non-codeleted tumors display lower and lower 2HG levels the more time elapses from surgery (Figure 19, panel C and D).

Figure 19. Dot plots illustrating 2HG levels estimated by MRS (y axis, mM) in patients with *IDH*-mutant, 1p/19q codeleted gliomas (panel A,C) and in patients with *IDH*-mutant, 1p/19q non-codeleted gliomas (panel B,D) depending on the timing of MRS (x-axis) (panel A,B) and on the time elapsed from surgery (x-axis, days) (panel C,D). After Su before TTT=after surgery but before the administration of antitumoral treatments, TTini or FU=after initial treatment, P1=first progression, P2=second progression, P3 P4= third or fourth progression.

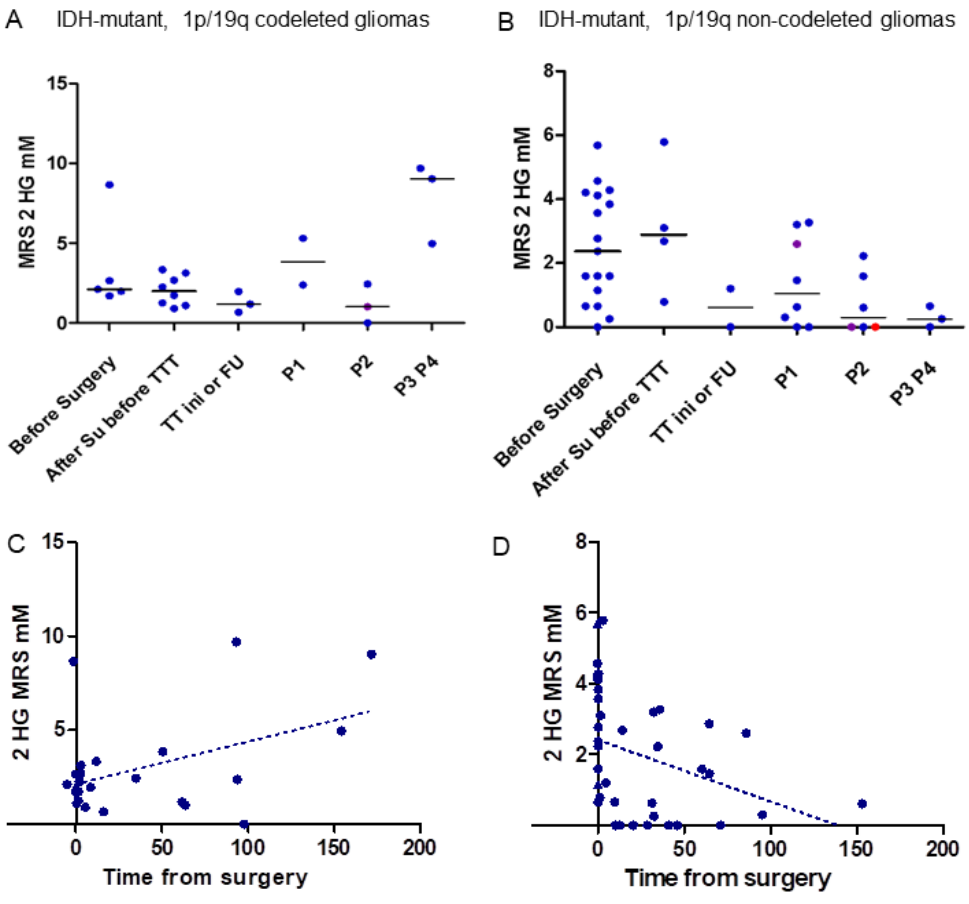

As not all patients displayed detectable 2HG at progression, we sought to determine whether this could have some prognostic significance. While, indeed, 2HG detection (p=0.006) was associated with prolonged OS on univariate analyses, together with disease stage (p=0.001), histological grade (p=0.033) and 1p/19q codeletion (p=0.049), only disease stage remained a significant predictor of OS on multivariate analyses (p=0.003, HR 3.61, 95% CI: 1.53-8.50). This observation suggests that the lack of detectable 2HG at progression simply reflects disease evolution and is not an independent predictor of OS.

2HG rapidly decreases following treatment with IDH inhibitors. Six patients underwent longitudinal MRS assessments during treatment with IDH inhibitors [AG-120 (n=4), AG-221 (n=2)]. In all patients, MRS showed a rapid and dramatic decrease of 2HG levels within days of starting treatment (Figure 20). However, this decrease was not always accompanied by a parallel reduction in tumor volume, suggesting that it more likely reflected a pharmacodynamic effect rather than an actual tumor response. Four patients eventually experienced tumor progression during follow-up, which was accompanied by a parallel increase of 2HG levels in three. Interestingly, in one 1p/19q non-codeleted patient, tumor progression occurred in absence of a detectable peak of 2HG on MRS (patient n°4 in Figure 20).

Figure 20. Diagrams illustrating the changes in 2HG levels (upper row) and tumor volume (bottom row) following treatment with *IDH* inhibitors in five out of the six patients who underwent longitudinal monitoring by MRS. The blue background corresponds to treatment period.

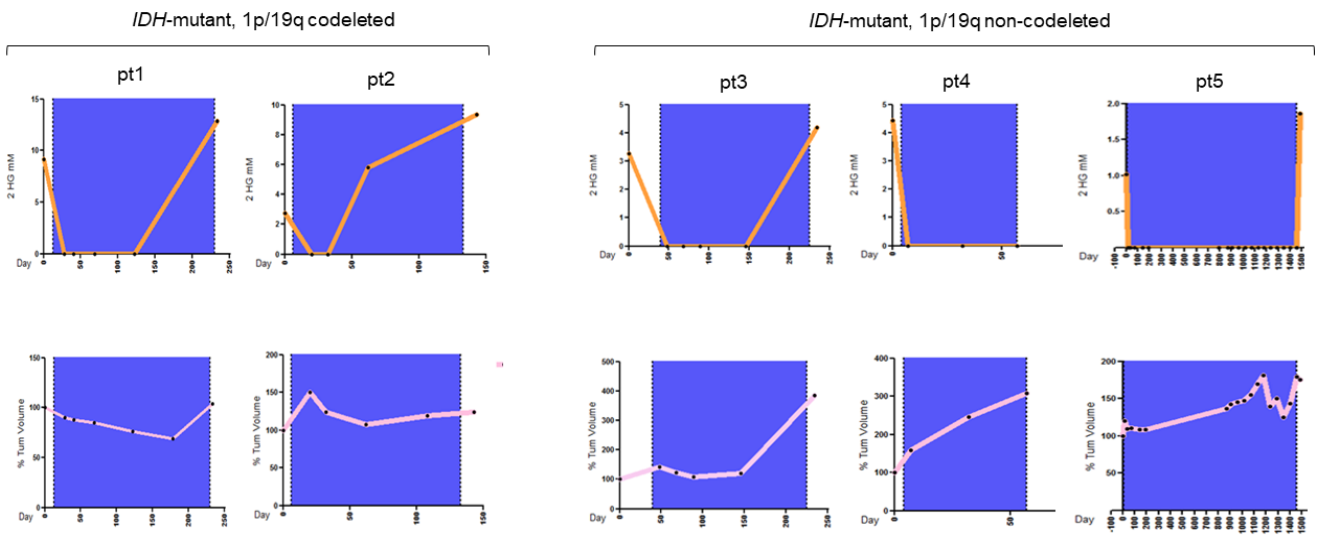

MRS for 2HG monitoring captures tumor response after cytotoxic treatments. Twelve patients in cohort 2 underwent longitudinal assessments by MRS while receiving cytotoxic treatments (temozolomide (n=2), PCV (n=2), PCV-radiotherapy (n=3), radiotherapy-PCV (n=5)). In all cases, MRS showed a decrease in 2HG levels during treatment (Figure 21, panel A), which was consensual with clinical and radiological evolution.

Figure 21. Diagrams illustrating the variations in mean 2HG levels estimated by MRS (y axis, mM) during follow-up in patients receiving cytotoxic treatments. Panel A: whole cohort; panel B: 1p/19q codeleted gliomas; panel C: 1p/19q non-codeleted gliomas. In both 1p/19q codeleted and 1p/19q non-codeleted patients, a substantial decrease of 2HG levels is evident since first follow-up MRS. F1=first follow-up MRS, F2=second follow-up MRS, F3=third follow-up MRS.

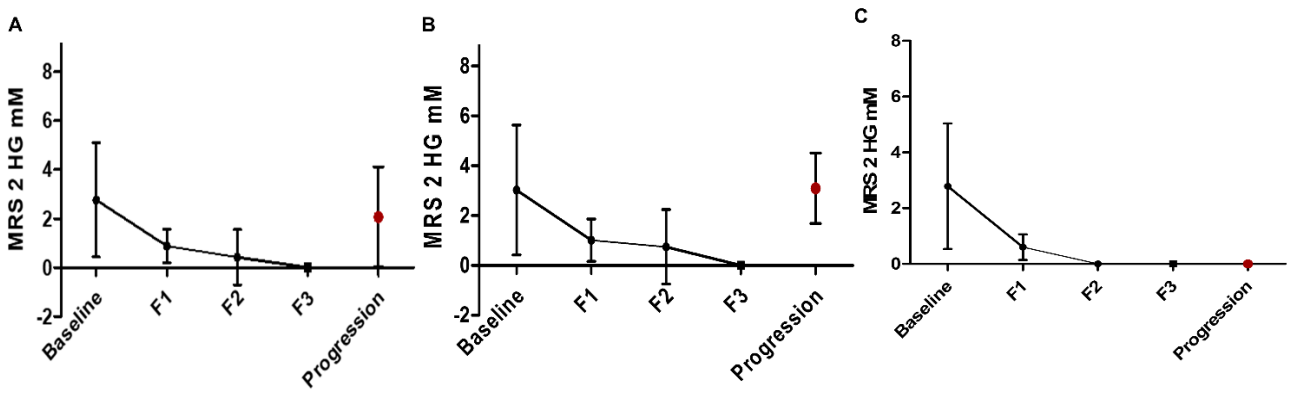

2HG decrease occurred and continued over weeks following the start of cytotoxic treatment, a substantial reduction being evident since first follow-up MRI. 2HG decrease on MRS often preceded tumor response on conventional imaging, suggesting that it could be used as an early marker of treatment response in *IDH*-mutant patients receiving cytotoxic treatments. 2HG decrease was similar in 1p/19q codeleted (Figure 21, panel B) and in 1p/19q non-codeleted patients (Figure 21, panel C) and seemed more rapid following the sequence radiotherapy-PCV than following the sequence PCV-radiotherapy (not shown). Three patients eventually experienced tumor progression during follow-up, but only a single patient, with a 1p/19q codeleted glioma, had a detectable peak of 2HG at progression.

2HG levels estimated by MRS correlate with 2HG concentration in tumor tissue and plasma. Finally, we evaluated whether, besides with MRS, 2HG levels could be reliably monitored by measuring 2HG concentrations in easily accessible bodily fluids, such as plasma or urine. 2HG concentrations in plasma seemed to correlate both with 2HG levels estimated by MRS (p=0.028) and with 2HG concentrations in tumor tissue by GC-MS/MS (p=0.13). 2HG concentrations in urine instead did not correlate neither with 2HG levels estimated by MRS (p=0.63) nor with 2HG concentrations in tumor tissue (p=0.72), suggesting that they do not accurately reflect 2HG accumulation in tumor tissue.

Discussion

Using MEGAPRESS, we had developed a highly sensitive and specific method for the preoperative prediction of the *IDH* status in patients with diffuse gliomas (Branzoli *et al.*, 2018). While showing a sensitivity of 95% in untreated patients, the sensitivity of our technique was 62% in pretreated patients. As suggested by our analysis, this drop in sensitivity is probably attributable to the reduction of tumor volume and viable tumor cells that follows surgical resection and cytotoxic treatments, which affect the ability of MRS to detect the 2HG peak.

Interestingly, we observed that 2HG levels estimated by MRS correlated with the type of *IDH* mutation, being the highest in patients with *IDH2* mutations and the lowest in patients with minoritarian *IDH1* mutations. This observation was consistent with previous reports showing that 2HG levels are higher in *IDH2*- compared to *IDH1*-mutant gliomas (Emir *et al.*, 2016) (Ward *et al.*, 2013). Notably, the different *IDH* mutations are associated with different glioma types, *IDH2* mutations being more frequent in 1p/19q codeleted oligodendrogliomas, and minoritarian *IDH1* mutations being commonly associated with astrocytomas and in brainstem gliomas (Picca *et al.*, 2018), suggesting a possible influence of additional factors, such as tumor microenvironment, on 2HG levels.

Subgroup analysis allowed to disclose a significant difference in 2HG levels at progression between 1p/19q codeleted and 1p/19q non-codeleted gliomas. While 1p/19q codeleted gliomas maintained high levels of 2HG during tumor evolution, non-codeleted gliomas more commonly showed low or undetectable 2HG levels, suggesting that, for 1p/19q non-codeleted gliomas, 2HG might no longer be required for tumor progression. Indeed, *IDH* mutations are frequently lost at recurrence as additional "tertiary" oncogenic alterations appear, while the epigenetic changes induced by 2HG do not regress after the loss of the *IDH* mutation or 2HG removal (Turcan *et al.*, 2012). The loss of DNA methylation in recurrent *IDH*-mutant gliomas has been associated with a more aggressive phenotype (de Souza *et al.*, 2018), the majority of these G-CIMP-low tumors having alterations affecting the RB pathway (e.g., *CDKN2A/B* homozygous deletion and/or *CDK4* amplification).

Longitudinal MRS monitoring allowed to capture 2HG decrease in patients receiving IDH inhibitors, reduction that occurred within days of starting treatment but that reflected a pharmacodynamic effect and not a corresponding tumor response. Patients receiving cytotoxic treatments showed instead a slower reduction in 2HG levels, occurring over weeks, that, however, was always consensual with tumor volume variations. The decrease in 2HG levels seemed more rapid in patients receiving the combination radiotherapy-PCV compared to patients receiving radiotherapy-PCV, observation that is consistent with the clinical and radiological responses observed in daily practice. At progression, not all patients showed a consensual rise of 2HG levels, suggesting that MRS might not be an accurate tool for the early detection of tumor progression.

The attempt to use 2HG concentrations in urine as a surrogate biomarker were disappointing because of the lack of correlation with 2HG concentrations in tumor tissue. 2HG concentrations in plasma correlated instead with both 2HG levels on MRS and with 2HG concentrations in tumor tissue, encouraging further explorations on plasmatic 2HG concentrations as biomarker for the longitudinal assessment of tumor response and progression.

Manuscript in preparation

Clinical-molecular characterization of rare subgroups of *IDH*-wildtype gliomas

Gliomas in patients with neurofibromatosis type 1

Background

Neurofibromatosis type 1 (NF1) is an autosomal dominant disorder resulting in a tumor predisposition syndrome affecting about 100,000 people in the United States (1 in 3,000 individuals) (Uusitalo *et al.*, 2015). Individuals with NF1 suffer from a wide range of clinical manifestations related to an increased risk of malignant and non-malignant conditions (Gutmann *et al.*, 2017). NF1 is caused by germline mutations in the *NF1* tumor suppressor gene, which encodes for a GTPase-activating protein called neurofibromin that functions as a negative regulator of the RAS oncoprotein. Neurofibromin regulates cell growth and survival by accelerating the conversion of active GTP-bound RAS to its inactive GDP-bound form. Thus, loss of neurofibromin expression, as seen in tumors associated with NF1, is predicted to lead to increased cell growth and survival through hyperactivation of RAS (Brems *et al.*, 2009).

Recent genome-wide studies have revealed that sporadic malignancies including gliomas (both lower grade gliomas and glioblastomas) have haploinsufficient or nullizygous loss of *NF1*, indicating that *NF1* functions as a somatic tumor suppressor gene in the general population (Philpott *et al.*, 2017). NF1 patients are predisposed to develop brain tumors, with gliomas occurring in 15–20% of individuals with NF1 (Uusitalo *et al.*, 2016) (Seminog and Goldacre, 2013). Besides low-grade gliomas of the optic pathway (Blanchard *et al.*, 2016) that occur in about 15% of affected children, NF1 patients are also prone to develop non-optic gliomas, more frequently later in life, which manifest with a spectrum of histological subtypes including high-grade gliomas (Sellmer *et al.*, 2017). Although the predisposition to develop CNS tumors in patients with NF1 is well recognized, the molecular features of gliomas occurring in patients with NF1 have remained obscure, preventing the development and the application of novel therapeutic approaches. It is also unclear whether the molecular profiles of NF1-gliomas recapitulate the subtypes recently identified in sporadic gliomas (Ceccarelli *et al.*, 2016). Here we report a comprehensive analysis of NF1-gliomas. We defined distinct features in low- and high-grade tumors, and comparatively evaluated the genomic features of syndromic NF1 and sporadic gliomas.

Patients and Methods

Sample cohort. Glioma frozen samples and matched peripheral blood samples were available from NF1 patients who underwent surgical treatment. Samples were obtained from the Onconeurotek Tumorbank of the Pitié-Salpêtriere Hospital (Paris, France), the Istituto Neurologico Besta (Milano, Italy), the MD Anderson Cancer Center (Houston, Texas, USA), and from collaborators in the United States, France, Spain, South Korea, Germany, and United Kingdom. All samples were obtained after informed consent and approval of the

institutional review boards of the hospitals where patients were treated. All samples belonged to patients diagnosed with NF1 syndrome according to the National Institutes of Health Consensus Development Conference (1988). Samples were collected from 56 NF1 patients. From 1 patient 4 spatially distinct samples were obtained, for a total of 59 samples. Blood DNA was available for 43 out of the 56 patients and was used for WES and *NF1* germline mutation calling to confirm the clinical diagnosis and to identify SNVs from matched tumor-normal pairs. The cohort included 35 low-grade gliomas (23 pilocytic astrocytomas, 5 gangliogliomas, 3 xanthoastrocytomas, 2 optic pathway gliomas, 1 diffuse glioma, and 1 low-grade calcifying astrocytoma) and 24 high-grade gliomas (13 GBM, 6 anaplastic astrocytomas, 1 anaplastic diffuse glioma, 1 anaplastic ganglioglioma, 1 anaplastic xanthoastrocytoma, 1 gliosarcoma, and 1 anaplastic astrocytoma). The median age of patients at time of surgery was 20 years, with 22 pediatric (< 16 years) and 33 adult (> 16 years) patients (for one patient age was unknown).

WES. Sequencing libraries were generated from 1 μg of genomic DNA using Agilent SureSelect Human All Exon kit (Agilent Technologies, California, USA) following the manufacturer's recommendations. Libraries were sequenced using the Illumina HiSeq platform (150-bp paired end). We performed quality control according to the following procedure, discarding: (1) a read pair if either 1 read contained adapter contamination, (2) a read pair if more than 10% of bases were uncertain in either 1 read, and (3) a read pair if the proportion of low-quality bases was over 50% in either 1 read. Cleaned sequencing reads had an average error rate <1% and a Phred quality score of Q30. Burrows–Wheeler Aligner was used to map the paired-end clean reads to the human reference genome (GRCh37/hg19). After sorting with SAMtools and marking duplicates with Broad Picard, we computed coverage and depth based on BAM files. Sequencing depth had a mean of 103× and a median of 91×, with a mean of 99.78% coverage in the target region. Aligned reads were further processed using GATK to remove low mapping quality reads (mapping quality score ≥ 20) and re-aligned in the genomic regions around potential indels. The quality scores were then recalculated for the cleaned BAM files. To eliminate additional potential mapping artifacts, we excluded variants within 50-bp intervals, whose sequences aligned more than 3 times in the whole genome. To confirm that tumor and blood samples from the same patient were properly paired, we performed a 'fingerprint' analysis using NGS CheckMate, a model-based method evaluating the correlation between variant allele fractions, defined as the ratio of the number of reads supporting a non-reference allele to the total number of reads, estimated from two samples at known SNP sites.

Mutation calling and pathogenicity prediction. Somatic SNVs and indels were identified in tumors with matched normal samples by integrating the results from five algorithms for variant calling: VarScan2, Freebayes, Strelka, MuTect, and VarDict. In tumor samples for which blood DNA was unavailable, nucleotide variants were identified using GATK HaplotypeCaller followed by the correction with a virtual normal as a substitute for the missing matched normal to filter out germline variants. The virtual normal was built from a set of 433 public samples from healthy, unrelated individuals sequenced to high depth in the context of the 1000 Genomes Project. To reduce false positive events, all somatic variants detected by matched normal and virtual

normal methods were further filtered according to the following criteria: (i) variant-supporting read count ≥ 2; (ii) variant allele frequency ≥ 0.05; (iii) average variant position in variant-supporting reads (relative to read length) ≥ 0.1 and ≤ 0.9; (iv) average distance to effective 3′ end of variant position in variant-supporting reads (relative to read length) ≥ 0.2; (v) fraction of variant-supporting reads from each strand ≥ 0.01; (vi) average mismatch quality difference (variant - reference) ≤ 50; (vii) average mapping quality difference (reference - variant) ≤ 50.

Somatic variants were annotated using the AnnoVar algorithm, which aggregates information from genomic and protein resources (GENECODE, UniProt, dbNSFP) with cancer (COSMIC, ClinVar) and non-cancer (dbSNP, 1000 Genomes, Kaviar, Haplotype Reference Consortium, Exome Aggregation Consortium, NHLBI Exome Variant Server) variant databases. Among the annotated variants, we selected only those producing a direct effect on the protein sequence (missense, truncating, stoploss, splicing variants, frameshift, and in-frame indels). Variants reported in the non-cancer databases with a minor allele frequency ≥ 0.05 were classified as germline polymorphisms and excluded. Additionally, variants occurring in very large genes and in highly paralogous genes were filtered out as common sequencing artifacts.

GATK HaplotypeCaller was used to call germline variants occurring in *NF1* and in genes previously implicated in NF1-like syndromes. Identified variants were processed to remove false positives as described above. The functional effect of missense SNVs and in-frame indels was determined using multiple prediction algorithms. MutationTaster2, Polyphen2, Provean, and SIFT were applied to predict the pathogenicity of missense SNVs. The pathogenic effect of in-frame indels was determined using FATHMM-Indel, Provean, SIFT-Indel, and VEST-Indel. Variants predicted as damaging by two or more algorithms were classified as pathogenic mutations. To distinguish between germline and somatic events of the *NF1* gene detected in tumor without a matching normal, we used the algorithm implemented by Chapuy et al. (Chapuy *et al.*, 2018).

DNA copy number analysis. Somatic copy number was estimated from WES reads using the GATK copy number protocol. The coverage depth of aligned reads was analyzed to detect CNVs using a hidden Markov model for change-point detection. A normal DNA reference was created by integrating copy number from NF1 patient blood samples and used for the comparison with CNVs detected in tumor samples to encapsulate sequencing noise and identify somatic events. GISTIC2 was used to integrate results from individual patients and identify genomic regions recurrently amplified or deleted in NF1-gliomas. Chromosomes X and Y copy numbers in normal and tumor samples were estimated from WES data using CNVkit to confirm patient gender and to compute chromosome X tumor ploidy.

mRNA sequencing and unsupervised cluster analysis. mRNA was purified from total RNA using poly-T oligo-attached magnetic beads. The mRNA was first fragmented randomly by the addition of a fragmentation buffer. First-strand cDNA was synthesized using random hexamer primers and M-MuLV reverse transcriptase (RNase H-). Second-strand cDNA synthesis was subsequently performed using DNA polymerase I and RNase H. Double-stranded cDNA was purified using AMPure XP beads. Remaining overhangs of the purified double-

stranded cDNA were converted into blunt ends via exonuclease/polymerase activities. After adenylation of the 3′ ends of DNA fragments, a NEBNext Adaptor with hairpin loop structure was ligated to prepare for hybridization (NEB Next Ultra RNA Library Prep Kit). Libraries were sequenced on an Illumina HiSeq platform (150-bp paired end). Sequencing quality was assessed through error rate and base quality distributions of reads for each sample. We filtered the raw data, removing reads containing adaptors and reads containing more than 10% of bases that could not be determined, and reads including over 50% bases with a Phred quality score ≤ 5. Cleaned reads had error rate mean ≤ 2% and Q30 ≥ 90% for all samples.

The reads were aligned to the human reference genome (GRCh37/hg19) using STAR and the expression was quantitated at gene level using featureCounts, a count-based estimation algorithm. Downstream analysis of gene expression was performed in the R statistical environment. We applied GC-correction for the within normalization step and upper-quantile for the between phase, according to a described pipeline (Risso *et al.*, 2011). Most variable genes (1,330) among 29 NF1-glioma samples were used for consensus clustering on the Euclidean distance matrix (10,000 random samplings using 70% of the 29 samples). Best sample clustering (Calinski and Harabasz criterion) was obtained with $k = 2$ groups. Differential expression analysis was then performed between the two groups of samples, and the list of the 100 most differentially expressed genes (two-sided Mann–Whitney–Wilcoxon (MWW) test) was used to construct a heat map comprising the whole data set. Samples were clustered using the hierarchical clustering algorithm based on the Ward linkage method and the Euclidean distance as implemented in R.

Gene ontology networks. Gene ontology enrichment was computed using either: (1) MWW-Gene Set Test (GST), when a full ranked list of genes was available; or (2) Fisher's exact test, when only a list of significant genes was available. The significant gene ontology terms from MWW-GST ($q < 0.001$, absolute NES > 0.6) or Fisher's exact test ($q < 0.01$) analysis were further analyzed using the Enrichment Map application of Cytoscape. In the network, nodes represent the terms and edges represent known term interactions and are defined by the number of shared genes between the pair of terms. The size of the nodes is proportional to the number of genes in the category. A cut-off was set to the overlapping coefficient (> 0.5) to select overlapping gene sets.

Assembly of the transcriptional interactomes and master regulator analysis. To identify master regulators of the gene expression signature activated in the high-grade LGm6 *IDH* wildtype pan-glioma *ATRX* mutant (8 samples) versus *ATRX* wild-type (40 samples) subgroup, we used the transcriptional network assembled from gene expression profiles of the *IDH*-wildtype pan-glioma dataset using the RGBM algorithm from our previous works (Mall *et al.*, 2018) (Frattini *et al.*, 2018). The transcriptional interactome comprised 300,969 interactions between a predefined set of 2,137 transcriptional regulators and 12,656 target genes. We used the same workflow for master regulator analysis and activity described in the same papers. As a result, we obtained 89 master regulators, 41 of which were enriched in *ATRX* mutant samples (two-sided MWW-GST adjusted $P < 0.01$, absolute NES> 0.6, and two-sided MWW test for differential activity adjusted $P < 0.01$).

DNA methylation analysis and integrative analysis with the TCGA *IDH*-wildtype cohort. Methylation analysis of NF1-glioma genomic DNA was performed using the Illumina Human 850K EPIC Infinium Methylation BeadChip. Array data were imported in the R statistical framework using the Minfi package and normalized using functional normalization. NF1-glioma DNA methylation profiles were classified in one of the pan-glioma methylation clusters by a nearest neighbor classifier using the 1,233 cancer-specific DNA methylation probes obtained by intersecting the 1,300 probes used by Ceccarelli et al. (Ceccarelli *et al.*, 2016) and those available on the 850K EPIC Infinium Methylation platform. For the joint unsupervised analysis of the TCGA cohort and the NF1 tumors, we first dichotomized the data using a β value > 0.25 as a threshold for positive DNA methylation. This binarization tends to mitigate the effects of variable tumor purity between the TCGA cohort and the NF1 cohort. Unsupervised hierarchical clustering on the 1,233 CpG sites was then applied using a binary distance metric for clustering and Ward's method for linkage. The dendrogram has two main branches, one corresponding to *IDH*-mutant tumors and one corresponding to *IDH*-wildtype tumors. The Calinski and Harabasz curve had two local maxima at $k = 2$ and $k = 5$. Cutting the tree with 5 groups resulted in cluster 3 containing 100% of the NF1 tumors (31 of 31 samples with DNA methylation assay) and 95% (62 of 65) sporadic LGm6 tumors.

Integrative expression and DNA methylation analysis. We analyzed differences in DNA methylation level between the subgroups of low-grade NF1-gliomas characterized by differential activation of immune cells. After removing probes targeting X and Y chromosomes and probes not associated with promoters, the final methylation data matrix comprised 11 low-grade gliomas (5 low-immune and 6 high-immune) and 105,956 probes. Differential methylation analysis was then performed between low- and high-immune samples of the low-grade cohort using a two-sided MWW test ($P < 0.01$ and absolute methylation fold-change > 0.3), and the list of the 259 most differentially methylated probes (229 hyper- and 30 hypo-methylated) was used to construct a heatmap comprising the whole dataset. Samples were clustered using the hierarchical clustering algorithm based on the Ward linkage method and the Euclidean distance, as implemented in R. Furthermore, differential expression analysis was also performed on the two groups of samples (9 low-immune and 10 high-immune) using the two-sided MWW test ($P < 0.01$ and absolute expression fold-change > 1; 15 up- and 109 down-regulated) for integrative analysis. The primary probe for each gene was chosen as the one located closest to the –100-bp position in the promoter relative to the transcription start site; this location should be in a key region of the promoter to correlate with expression changes. Integration of the normalized gene expression and DNA methylation gene lists identified a total of 115 of 11,979 unique genes with both significant DNA methylation and RNAseq gene expression changes between low- and high-immune lower-grade samples. In particular, 68 of the 115 genes were significantly hyper-methylated and down-regulated in low-grade/low-immune compared to low-grade/high-immune samples. Finally, a starburst plot for comparison of DNA methylation and RNAseq gene expression data was constructed using log10 (*P* value) for DNA methylation (*x* axis) and gene expression (*y* axis) for each gene.

Pairwise mutual exclusivity and co-occurrence of somatic alterations. Pairwise mutually exclusive somatic alterations were identified using CoMEt with the 'exhaustive' option. Pairwise co-occurrence was tested by Fisher's exact test. Statistically significant exclusion and co-occurrence patterns were visualized using Cytoscape with edge thickness representing –log10 (*P* value).

Mutational signatures. The R package DeConstructSigs was used to determine the proportion of COSMIC signatures as defined by Alexandrov et al. (Alexandrov *et al.*, 2013).

Dirichlet-multinomial regression for mutational spectra. The correlation between mutational spectrum as a response variable (C>T, C>A, C>G, T>C, T>A, and T>G) and age, grade, and *ATRX* mutational status as predictor variables was determined by a Dirichlet-multinomial model.

Clonality estimation. Allele mutations and copy number calls for each sample were loaded into maftools to obtain mutational clones using the inferHeterogeneity function.

Neoantigen prediction. For all samples analyzed with both Exome-seq and RNAseq available, the four-digit HLA type was predicted using Polysolver, Optitype, Phlat, and Seq2hla, respectively. HLA type was determined if predictions were consistent in any one of the following conditions: (1) Polysolver and Optitype, (2) Polysolver and Phlat, (3) Polysolver and Seq2hla, (4) Optitype and Phlat, or (5) Optitype and Seq2hla. Missense mutations were then used to generate a list of all possible 9-mers. The binding affinity of the mutant and the wildtype peptide to patient's germline HLA alleles was predicted using netMHCpan-4.0. High-affinity binders were defined as those with a half-maximum inhibitory concentration (IC_{50}) equal to or below 500 nM. Low-affinity wildtype allele binders were defined as having an IC_{50} greater than 500 nM. Accordingly, a mutant-specific binder was referred to as a neoantigen when the mutant IC_{50} was below 500 nM and the wildtype IC_{50} was above 500 nM.

In vitro peptide-HLA I binding assay. Peptide-HLA class I in vitro binding affinities were determined as described previously (Harndahl *et al.*, 2009). Purified recombinant HLA class I heavy chains were diluted into a refolding buffer (tris-maleate buffer, pH 6.6) containing β 2-microglobulin and serial 10-fold dilutions (0.01 nM to 200 μM) of the test peptide, and incubated for 48 hours at 18°C to allow for equilibrium to be reached in PBS. The HLA concentration was 1.25 nM, and β2-microglobulin concentration was 10 nM. Complex formation was detected using a proximity based luminescent oxygen channeling immunoassay. Donor beads were obtained preconjugated with streptavidin from Perkin Elmer; acceptor beads were conjugated in house with W6/32, a pan-specific anti-HLA class I mouse monoclonal antibody (Sigma-Aldrich, MABN1783, 1 mg ml-1) using standard procedures as described by the manufacturer. Binding affinity (*K*d) was determined as previously described (Harndahl *et al.*, 2009) using the GraphPad Prism software 6.0.

C-circle assay. The C-circle assay was done as previously described (Henson *et al.*, 2009). Data are presented as the average of three technical replicates for each DNA sample.

RT–qPCR. Total RNA was prepared using the AllPrep DNA/RNA/Protein Mini Kit (Qiagen) according to the manufacturer's instructions, and cDNA was synthesized using SuperScript II Reverse Transcriptase (Invitrogen). Reverse transcription quantitative PCR (RT–qPCR) was performed with a 7500 Real Time PCR thermal cycler system (Applied Biosystems), using SYBR Green PCR Master Mix (Applied Biosystems). Data are presented as -Δ C_T (C_T18S - C_T selected gene) of triplicate samples (C_T, threshold cycle). Experiments were repeated three times with similar results.

Genomic qPCR. Genomic DNA from blood and tumor samples was assayed by quantitative PCR (qPCR) using SYBR Green PCR Master Mix (Applied Biosystems). Dimethyl sulfoxide was added at a final concentration of 5% for amplification of the *INK4A* gene. Fluorescence intensities were detected using 7500 Real Time PCR thermal cycler (Applied Biosystems), and C_T values were calculated using High-Resolution Melt Software v2.0 (Applied Biosystems). Standard curves for test and reference primers were generated using dilution series of genomic DNA. Each dilution was tested in triplicate. The C_T values (the cycle at which the change in fluorescence for the SYBR dye passes a significance threshold) were used for data normalization. ΔC_T values (C_T18S - C_T selected gene) of triplicate samples were used to calculate copy number changes relative to control DNA. Experiments were repeated three times with similar results.

Bi-allelic mutation analysis of *NF1*. To determine whether the two different mutations detected in an individual tumor were on the same or on separate alleles, the genomic DNA or cDNA (obtained from reverse transcription using Superscript II reverse transcriptase, Invitrogen) fragments that included the two mutations were amplified using AccuPrime taq DNA polymerase high fidelity. PCR products of the corrected size were purified using QIAquick PCR Purification Kit (Qiagen), subcloned into plasmid pCR Blunt II TOPO, and used to transform *Escherichia coli*. DNA was isolated from individual colonies resistant to kanamycin and subjected to Sanger sequencing reaction using sense or anti-sense primers to detect one of the two mutations in the sense or the anti-sense sequence, respectively. Results were analyzed using Sequencer 5.4.6 (Gene Codes Corporation). The sequence of each identified mutation was confirmed in at least two independent plasmid clones.

Immunohistochemistry. Immunostaining was performed as previously described (Frattini *et al.*, 2018). For ATRX immunohistochemistry, deparaffinization and immunolabeling of sections were performed by a fully automatic immunohistochemistry system, Ventana BenchMark XT (Roche), using a streptavidin–peroxidase complex with diaminobenzidine as chromogen and hematoxylin counterstaining of nuclei. Primary ATRX antibody was from Sigma-Aldrich (HPA001906) and was used at 1:200 dilution. Images were acquired under 20× magnification using an Olympus IX70 microscope equipped with a digital camera. For immune cell marker analysis, tumor sections were deparaffinized in xylene and rehydrated in a graded series of ethyl alcohol. Antigen retrieval was performed in citrate solution pH 6.0 (CD20 and CD68) or Tris-EDTA solution pH 9.0 using a decloaking chamber (7 min for CD3 and CD8 and 15 min for GZMB). After peroxidase blocking in 3% H2O2 for 15 min, slides were blocked for 1 hour in 10% horse or goat serum, 0.25% Triton X-100, and 1× PBS.

Primary antibodies were incubated at 4°C overnight: CD3 (Dako, A0452, 1:200), CD8 (Leica NCLL-CD8-4B11, 1:200), GZMB (Leica, PA0291, ready to use), CD20 (Leica, NCLL-CD20-L26, 1:200), and CD68 (Sigma, HPA048982, 1:2,000). Sections were incubated in horseradish peroxidase-conjugated secondary antibody (Dako Envision+ System HRP Labelled Polymer ready to use anti-mouse and anti-rabbit, K4000 and K4003, respectively) for 30 minutes and 3,3-di-amino-benzidine (Vector) was used as substrate. Nuclei were counterstained with hematoxylin (Sigma). Slides were dehydrated and mounted. Five to 11 images for each section were acquired under 20× magnification using an Olympus IX70 microscope equipped with a digital camera. Positive cells were counted in an area of 0.15 mm^2. Results are shown as average number of positive cells per 0.15 mm^2. Comparisons between two groups were analyzed by *t*-test with Welch correction (two-sided, unequal variance).

Statistical analysis. Comparisons between groups were analyzed by *t*-test with Welch correction (two-sided, unequal variance) and/or the MWW non-parametric test. Results in bar graphs are expressed as mean ± standard deviation for the indicated number of observations. Box plots and scatter plots show the median value and the first to the third quartile, and whiskers indicate the smallest and largest values. All statistical analyses were performed using the GraphPad Prism software 6.0 or the R software.

Results

Cohort characteristics. The tumor cohort analyzed in this study was composed of 59 glioma samples from 56 patients (33 females and 23 males) meeting the clinical criteria for NF1. Tumor samples were from 22 children (age range: 2–15 years) and 33 adults (age range: 18–63 years) (one patient lacked age information), and were classified as low grade (grades I and II, n=35) and high grade (grades III and IV, n=24) gliomas. Children developed mostly low-grade tumors (77% of pediatric gliomas were low grade), while high grade gliomas occurred primarily in adults (78% of high-grade tumors were observed in adults) (Figure 22, panel a). Age and grade distribution in our cohort is consistent with the notion that NF1-gliomas are primarily benign during childhood, whereas malignant gliomagenesis occurs later in life (Gutmann *et al.*, 2002) (Helfferich *et al.*, 2016). WES was performed in the 59 NF1-glioma samples and in matched blood DNA (available for 43 patients) and was used to call germline and somatic SNVs, small insertions and deletions (indels), and CNVs. We validated each class of germline and somatic DNA sequence alterations discovered by WES through secondary assays. Germline and somatic SNVs were confirmed by Sanger sequencing of matched blood and tumor DNA. Across variant types, we validated 93% of SNVs, which were therefore referred to as verified variants. We determined the functional effects of each missense mutation and in-frame indel by applying a pathogenicity prediction platform including eight independent algorithms. Recurrent WES-detected somatic CNVs were estimated by GISTIC2.0 and confirmed by qPCR of genomic DNA (CNV validation rate: 96%). We also carried out mRNA expression analysis from RNA sequencing of 29 tumors and DNA methylation of 31 tumors.

The landscape of germline NF1 gene mutations in glioma patients. To determine the pattern and frequency of predisposing *NF1* gene mutations in patients who developed glioma, we analyzed blood DNA by WES. We also inferred the germline status of NF1 mutations from the analysis of tumor-only samples using a recently described computational approach (Chapuy *et al.*, 2018). We found germline mutations inactivating the *NF1* gene (typically truncating and frameshift) in 51 of the 56 (91%) patients analyzed. The 91% *NF1* germline mutation rate is within the highest frequencies previously reported in NF1 patients. Among the identified *NF1* germline mutations, 32 variants had previously been reported in NF1 patients (http://www.hgmd.cf.ac.uk), whereas 19 were new pathogenic variants. We did not find pathogenic germline variants in genes previously implicated in NF1-like syndromes (*SPRED1, BRAF, CBL, GNAS, HRAS, KRAS, MAP2K1, MAP2K2, MLH1, MSH2, MSH6, NF2, NRAS, PMS2, PTPN11, RAF1, RASA2, RIT1, SHOC2, SOS1, SOS2*) (Messiaen *et al.*, 2009). The comparative analysis of blood and tumor DNA revealed that variant allele frequency of constitutive *NF1* mutations increased, resulting in loss of heterozygosity in the majority of tumors. The spectrum of *NF1* mutations in patients who developed gliomas did not cluster into specific domains of the NF1 protein, and the distribution of mutations was not related to patient age or tumor grade (Figure 22, panel b). These findings are in agreement with the broad distribution of germline mutations of the *NF1* gene previously reported in unselected NF1 patients (Gutmann *et al.*, 2017). They also indicate that the probability of developing a brain tumor is not dependent on particular patterns of *NF1* gene mutations in the patient's germline. We found that, in addition to the pathogenic *NF1* germline variant, seven tumors harbored a second *NF1* somatic mutation. This finding is consistent with previous studies that reported frequent somatic *NF1* mutations in neurofibromas from NF1 patients (Laycock-van Spyk *et al.*, 2011). We used four of seven tumor samples for which DNA or RNA was available to amplify a single fragment that included both germline and somatic mutations, cloned the amplified genomic or complementary DNA, and sequenced individual clones. As expected, we found that multiple clones for each tumor contained only the germline or somatic mutation, indicating that the two mutations reside on different alleles.

The landscape of somatic genomic alterations cooperating with *NF1* for glioma development. The application of a stringent somatic mutation-calling algorithm to the cohort of NF1-gliomas resulted in 1,007 high-confidence somatic mutations across 59 tumors, including 838 SNVs and 169 indels, 767 of which were predicted to carry pathogenic effects. Mutation burden increased with grade and age, adult high-grade gliomas having a six-fold higher mutation load than low-grade tumors in children (Figure 22, panel c–e). Statistically significant CNVs comprised gains at 5q31.3 (*FGF1*), 5p15.33 (*TERT*), 4q31.21 (*IL15*), and 17p13.2 (*KIF1C*), and losses at 9p21.3 (*CDKN2A/CDKN2B*). The *IDH1* gene, which is frequently mutated in sporadic low-grade gliomas and in the G-CIMP group of glioblastomas (Yan *et al.*, 2009), was wildtype in all 59 NF1-gliomas, regardless of grade and age. Similarly, mutations of *H3.3* histone genes, genetic lesions frequently found in sporadic pediatric gliomas (Schwartzentruber *et al.*, 2012), were absent in pediatric or adult NF1-gliomas.

Figure 22. Analysis of germline and somatic mutations in NF1-glioma patients. Panel a: The relative frequency distribution of age at diagnosis is represented by density plot: the overall distribution of NF1-glioma patients (dashed black line, $n = 55$) by age identifies two peaks, 13.5 and 38.8 years. Low-grade gliomas (blue line, $n = 32$) occur more frequently in children, while high-grade gliomas (red line, $n = 23$) are diagnosed more frequently in adults. Panel b; Germline mutations in the *NF1* gene identified in NF1-glioma patients by WES. The spectrum of *NF1* germline variants (SNVs and indels) is represented with each mutation shown only once per patient. We identified *NF1* germline pathogenic mutation in 51 of 56 (91%) patients. Patients no. 47 and no. 52 had one additional pathogenic germline mutation. Panel c: Scatter plot showing the number of somatic mutations (SNVs and indels) occurring in low-grade and high-grade NF1-glioma ($P = 7.4 \times 10^{-5}$). Panel d: Scatter plot showing the number of somatic mutations occurring in pediatric and adult patients ($P = 9.8 \times 10^{-4}$). Panel e: Scatter plot showing the number of mutations according to grade and age ($P = 3.8 \times 10^{-3}$, high-grade versus low-grade adult gliomas; $P = 0.025$, adult versus pediatric low-grade gliomas; $P = 0.06$, low-grade versus high-grade pediatric gliomas; $P = 0.07$, pediatric versus adult high-grade gliomas. Scatter plots show median and interquartile range. Median and range of mutations are reported below each plot.

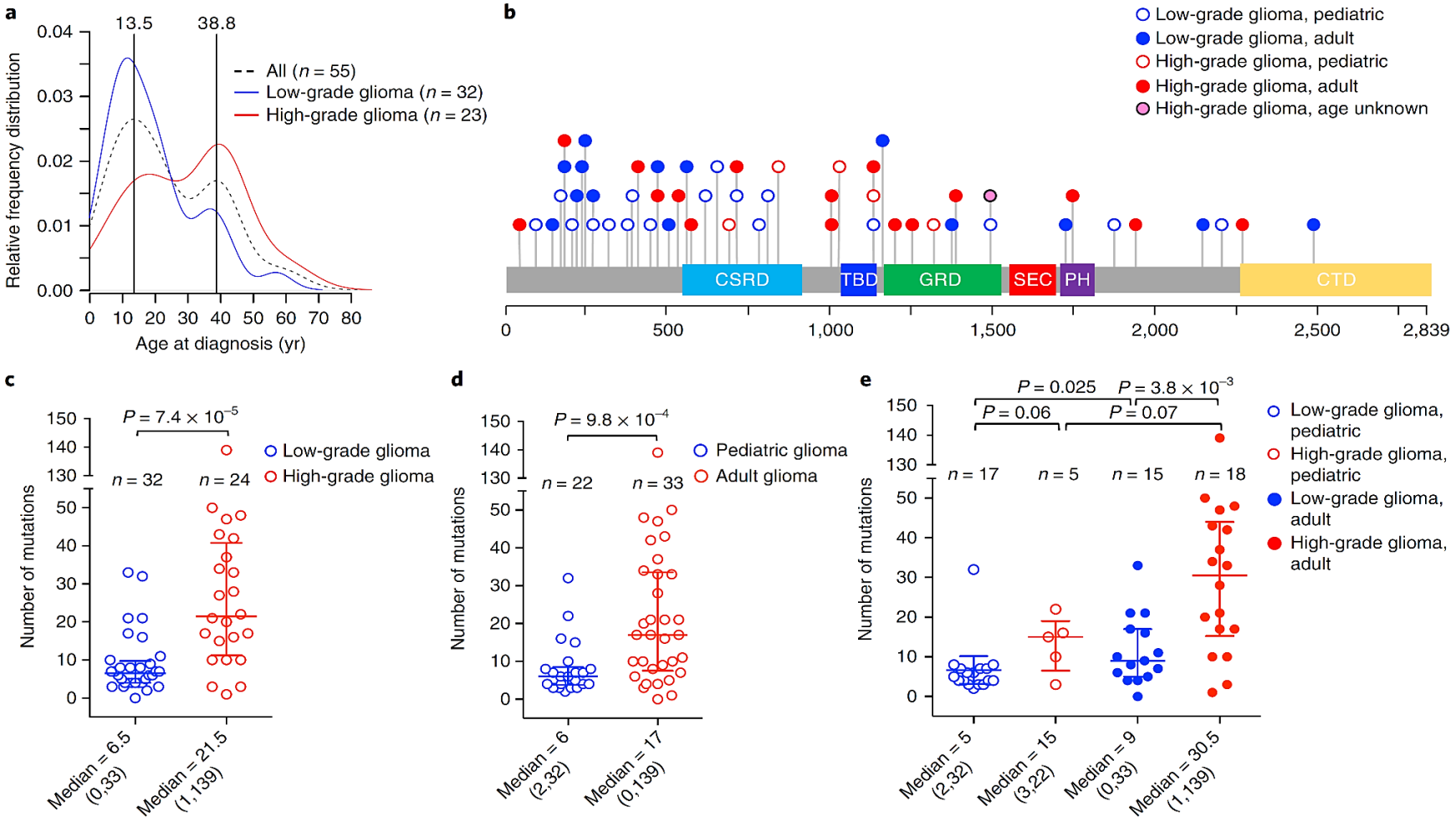

Additionally, the landscape of SNVs in low-grade NF1-gliomas was markedly different from that of high-grade tumors. Sporadic gliomas frequently harbor genetic alterations that cause telomere elongation. This process is typically carried out through mutations in the *TERT* gene promoter in *IDH*-wildtype tumors (Ceccarelli *et al.*, 2016). Conversely, in sporadic lower grade gliomas of the adult harboring co-occurring mutations of *IDH1* and *TP53*, the telomerase-independent alternative lengthening of telomeres (ALT) is sustained by inactivating mutations of *ATRX*, a gene encoding a chromatin remodeler and epigenetic modifier protein (Ceccarelli *et al.*, 2016). In NF1-glioma, we failed to detect mutations in the *TERT* promoter by targeted sequencing but we found copy number gain of the *TERT* gene more frequently in low-grade than in high-grade tumors (47% vs. 12%, P = 9×10^{-3}) (Figure 23). Despite the absence of *IDH1* mutations, high-grade NF1-glioma frequently harbored inactivating mutations of *ATRX* (9/24, 38%), while this alteration was very rare in low-grade tumors (1/32, 3%) (Figure 23).

Figure 23. Landscape of somatic genomic alterations in NF1-glioma. Integrated matrix of 59 glioma samples from 56 patients and gene variants (SNVs, indels, and CNVs) observed in NF1-glioma (left panel, high-grade glioma; right panels, low-grade glioma). Rows and columns represent genes and tumor samples, respectively. Genomic alterations, age, histology, and *NF1* germline mutations are indicated. NF1-glioma samples are sorted by their mutation profiles, except for patient no. 5, hypermutated high-grade glioma, and patient no. 39, including four spatially distinct glioma samples, which are shown at the last columns of left and right panel, respectively. Recurrently mutated genes are selected for their previously established association with glioma (*ATRX*, *CDKN2A*, *TP53*, *PIK3CA/B*, *PTEN*, *BRAF*, *FGFR1* and *FGF1*, *PRKCA*, *TERT*), cancer biology (*DOCK2/3/6*, *FDZ3/8*, *BCL9/9L*, *TOP2/3B*), and immune functions (*IL15*, *DGKQ*). Genes are sorted according to higher frequency (percentage of patients) in high-grade (top, red) or low-grade gliomas (bottom, blue), respectively. Validations by Sanger sequencing (SNVs) and quantitative-genomic PCR (gains and losses) are indicated by yellow and green triangles, respectively. LOH, loss of heterozygosity.

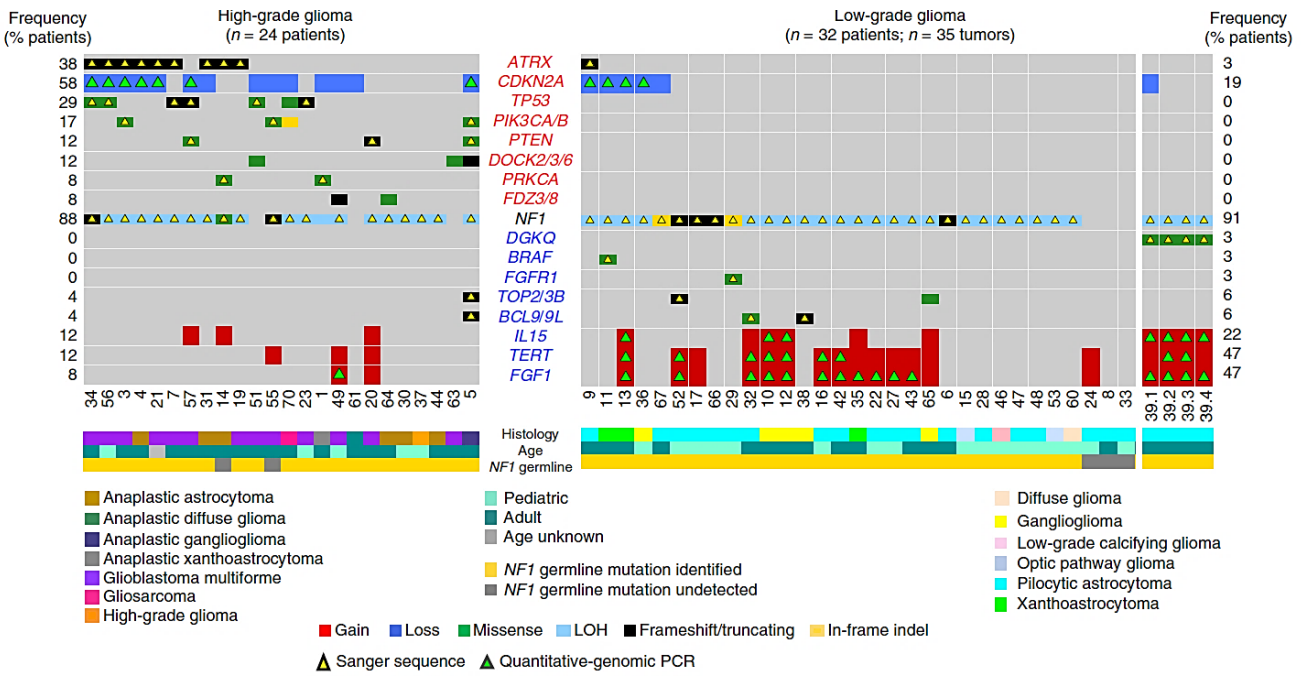

ATRX mutations were mutually exclusive with *TERT* gene copy number gain and co-occurred with copy number loss of *CDKN2A/CDKN2B*, which was also more frequent in high-grade (58%) in comparison to low-grade tumors (19%), and with *TP53* mutations, which were absent in low-grade NF1-glioma (Figure 23). The *ATRX*

mutation emerged from a multinomial regression model including age and grade as the only independent predictor of somatic mutational spectrum in protein-coding regions ($P = 1.1 \times 10^{-3}$). In conclusion, together with *TP53* mutations and *CDKN2A* copy number losses, *ATRX* mutations characterize high- but not low-grade gliomas from NF1 patients.

Gene pathway analysis performed on CNVs and SNVs that had been selected for pathogenic features indicated that five biological pathways were commonly targeted, often in a mutually exclusive manner. In total, 22 of 24 (92%) high-grade and 24 of 32 (75%) low-grade NF1-gliomas harbored genetic alterations in one or more of five key biological processes. These included the PI3-kinase pathway, which was more frequently targeted in high-grade (50%) compared with low-grade (3%) NF1-gliomas ($P = 4.7 \times 10^{-5}$), the transcription / chromatin regulation pathway, which was disrupted in high-grade at higher frequency than low-grade NF1-gliomas (83% and 38%, respectively, $P = 9.1 \times 10^{-4}$), and RNA splicing, affecting 42% of high grade and 12% of low grade ($P = 0.03$). Conversely, the MAP kinase pathway was more frequently targeted in low-grade than high-grade tumors (59% and 29%, respectively, $P = 0.03$). Genetic alterations of cilium/centrosome occurred in a significant fraction of NF1-gliomas but were similarly distributed in high- and low-grade NF1-gliomas.

Validation and functional characterization of ATRX inactivation in high-grade NF1-gliomas. Functional annotation revealed that *ATRX* mutations were damaging events, predicted to generate truncated or inactive ATRX proteins (Figure 24, panel a). In accordance with the increased frequency of high-grade tumors in older patients, we also found that *ATRX* mutations in NF1-gliomas primarily occurred in adults. Conversely, *ATRX* mutations were rare in children as only 1 of the 22 pediatric NF1-gliomas harbored an *ATRX* mutation (Figure 24, panel b). As *ATRX* mutations occurring in NF1-gliomas are predicted to severely impact ATRX protein expression, we sought to validate our sequencing findings in an independent dataset of 23 NF1-gliomas (16 high-grade and 7 low-grade) using FFPE samples and ATRX immunohistochemistry. Whereas ATRX protein expression was detected in 7 of 7 (100%) low-grade tumors, it was undetectable in 8 of 16 (50%) high-grade NF1-glioma samples ($P = 0.05$) (Figure 24, panel c and d). Thus, immunohistochemistry data converged with sequencing results and confirmed that approximately half of high-grade gliomas from NF1 patients lose ATRX expression, which is instead retained in low-grade tumors. Next, we asked whether the loss of ATRX is associated with the ALT phenotype in the context of NF1-gliomas. In primary tumors, ALT can be determined by measuring a specific type of circular and mostly single-stranded C-rich extrachromosomal telomeric repeat (C-circles) (Henson *et al.*, 2009). The C-circle assay of 21 NF1-gliomas from which genomic DNA was available showed that 10 of 10 gliomas harboring ATRX mutations scored positive for the presence of ALT-specific C-circles but only 1 of 11 (9%) tumors that retained a wild-type *ATRX* was positive for C-circles ($P = 2.3 \times 10^{-5}$) (Figure 24, panel e).

Figure 24. Analysis of *ATRX* somatic mutations in NF1-glioma patients. Panel a: *ATRX* mutations were identified by WES. The spectrum of *ATRX* somatic variants (SNVs and indels) is represented with each mutation shown only once per patient. We identified and validated by Sanger sequencing *ATRX* pathogenic mutations in 10 patients (1 low-grade glioma and 9 high-grade gliomas). Panel b: The relative frequency of age distribution is represented for all patients (dashed black line, $n = 55$), *ATRX* wild-type (green line, $n = 46$), and *ATRX* mutant gliomas (red line, $n = 9$). Panel c: Microphotographs of ATRX immunohistochemistry in gliomas from NF1 patients. Representative images are from a low-grade glioma (left) and a high-grade glioma (right). High-grade glioma samples were negative for ATRX expression whereas low-grade gliomas retained ATRX protein expression. Panel d: Contingency table shows loss of ATRX protein expression in 8 of 16 high-grade and in none of 7 low-grade NF1-gliomas ($P = 0.05$). Panel e: C-circle (CC) assay was performed to measure ALT activity in NF1-glioma samples. The scatter plot reports the normalized CC content for each glioma according to *ATRX* mutational status: *ATRX* wild-type (blue) and *ATRX* mutant gliomas (red). For each group the median with interquartile range is indicated. All *ATRX* mutant gliomas but only one *ATRX* wild-type glioma showed increased ALT activity (i.e., normalized CC content greater than 1; $P = 2.3 \times 10^{-5}$).

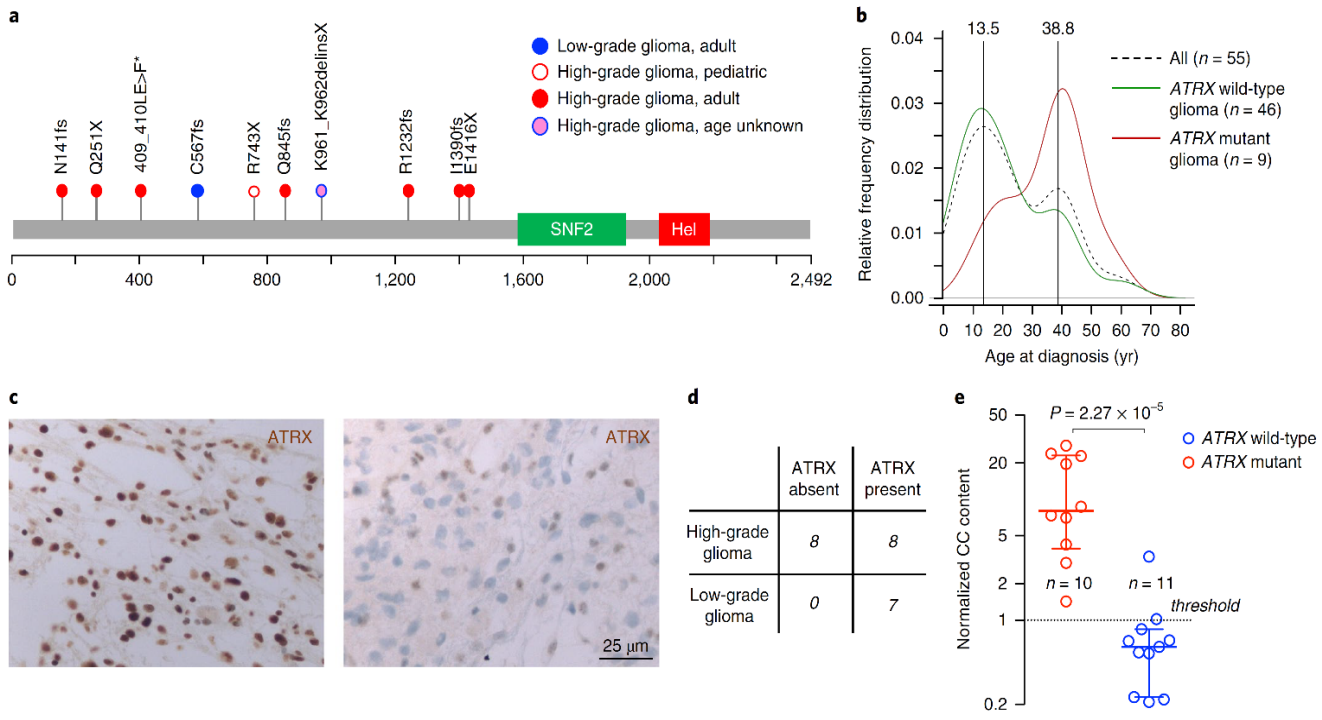

A subgroup of low-grade NF1-gliomas exhibits an enriched immune transcriptome and contains abundant cytolytic T lymphocyte infiltrates and tumor neoantigens. To segregate the RNA expression subtypes across the NF1-glioma dataset, we analyzed 29 RNA-sequencing (RNAseq) profiles from 10 high-grade and 19 low-grade NF1-gliomas through unsupervised consensus clustering based on the 1,330 most variable genes, which resulted in 2 main clusters. Cluster 1 (red) was specific for high-grade and cluster 2 (blue) for low-grade NF1-gliomas (Figure 25, panel a), indicating that tumor grading was the primary driver of transcriptome clustering. Next, we sought to identify the functional categories that characterize each cluster. A hierarchical clustering based on the 100 most differentially expressed genes between the 2 groups was constructed, from which we extracted the top and bottom 50 genes of the test statistics (Figure 25, panel b). We performed a functional analysis of gene expression categories differentially enriched in high-grade versus low-grade NF1-glioma samples using a recently described robust, two-sided, single-sample MWW-GST to inform the construction of a gene ontology enrichment map network (q<0.001, absolute normalized enrichment score > 0.6) (Frattini *et al.*, 2018). The network revealed that the genes enriched in high-grade NF1-gliomas belonged to categories involved in cell cycle and mitosis, chromosome organization, RNA metabolism, and neurogenesis,

whereas the biological functions activated in low-grade NF1-gliomas composed an interconnected network of immune response categories notably enriched for T lymphocyte effector functions (Figure 25, panel c and d).

Figure 25. Transcriptomic analysis of NF1-gliomas. Panel a: Consensus clustering on the Euclidean distance matrix based on the most variable genes among 29 NF1-glioma samples. The 10 high-grade samples fall in 1 cluster (red) and all low-grade samples ($n = 19$) fall in a different cluster (blue). Panel b: Hierarchical clustering of 29 NF1-gliomas by Euclidean distance with the Ward linkage method based on the 100 most differentially expressed genes. Panel c and d: Enrichment map network of statistically significant gene ontology categories in (c) ten high-grade and (d) 19 low-grade NF1-gliomas. Nodes represent gene ontology terms and lines their connectivity. Node size is proportional to number of genes in thegene ontology category and line thickness indicates the fraction of genes shared between groups. Gene network categories in NF1 high-grade gliomas are linked to mitotic progression, chromosome organization, and RNA biogenesis/regulation. Gene network categories in NF1 low-grade gliomas converge on proinflammatory immune response enriched for T lymphocyte effector functions. Panel e: Unsupervised clustering of single-sample enrichments of the categories in d. Low-grade NF1-gliomas are divided into two clusters (red and green), characterized by high- and low-immune gene set enrichments, respectively. Panel f: Tumor purity scores of low-grade/high-immune, low-grade/low-immune, and high-grade tumors computed by ESTIMATE. The low-grade/high-immune group has significantly lower tumor purity when compared with either the low-grade/low-immune or the high-grade glioma groups. Panel g: Immune scores of low-grade/high-immune, low-grade/low-immune, and high-grade tumors computed by ESTIMATE. Panel h–l: Enrichments of CD8+ T cell functions in low-grade/highimmune compared with low-grade/low-immune and high-grade gliomas. Boxplots report the z-scores and *P* values for published CD8+ T cell signatures. Scatter plots show median, interquartile, and minimum to maximum range.

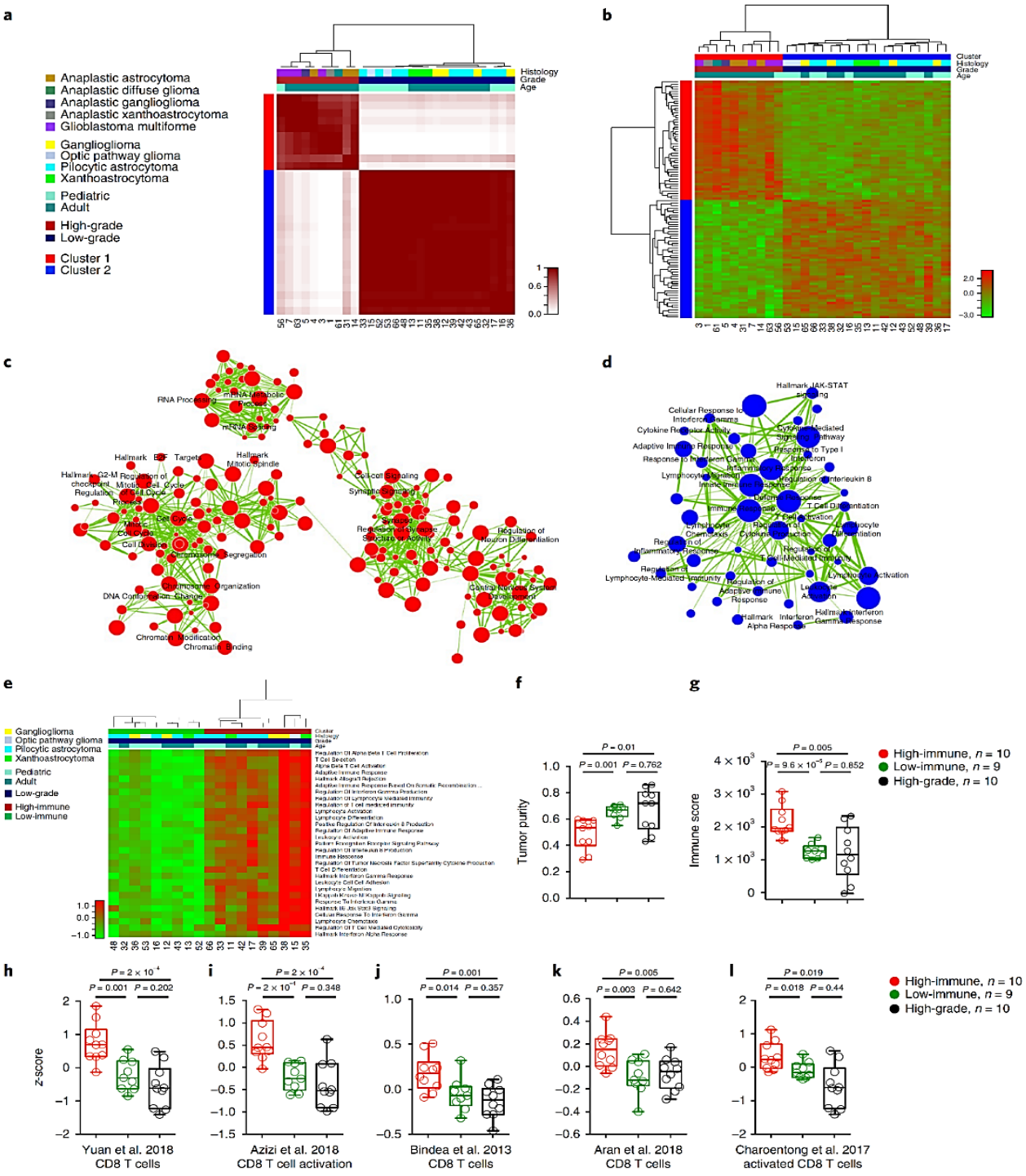

To recognize the individual low-grade tumors that exhibit immune cell activation, we applied single-sample MWW-GST using the enriched immune gene sets. The analysis showed that low-grade NF1-gliomas divided into two clusters, characterized by high- and low-immune gene expression, respectively (Figure 25, panel e). The application of ESTIMATE (Yoshihara *et al.*, 2013), a validated computational approach for the inference of the fraction of stromal/immune cells and consequently the tumor cell purity within tumor samples, showed that the low-grade/high-immune group had significantly lower tumor purity and higher immune score when compared with either the low-grade/low-immune or the high-grade groups (Figure 25, panel f and g). A transcriptomic-based analysis with five different CD8+ T cell specific gene expression signatures showed that low-grade/high-immune NF1-gliomas contain higher numbers of effector CD8+ T cells (Figure 25, panel h–l). This finding was confirmed by quantitative immunostaining for the T lymphocyte markers CD3 and CD8. Interestingly, the T cell infiltrates in high-immune NF1-gliomas included cells positive for granzyme B, the key cytolytic effector that is upregulated on CD8+ T cell activation, and productive responses to immunotherapies. Conversely, immunostaining for specific markers of B lymphocytes (CD20) and macrophages (CD68) indicated that these cell types are very rare in both high- and low-immune groups.

Recent data showed that aberrant DNA methylation of genes expressed by immune cells regulates the extent of immune infiltration in solid tumors (Jeschke *et al.*, 2017). Therefore, we asked whether the activation of an immune signature in NF1-gliomas might be driven by differential DNA methylation. Towards this aim, we profiled 11 of the low-grade NF1-gliomas previously analyzed by RNAseq with the 850K Epic Methylation platform. Clustering based on the probes differentially methylated between high- and low-immune tumors revealed that the low-immune group exhibited a larger number of hyper-methylated probes than the high-immune cluster (229 versus 30, $P < 0.01$). Functional gene ontology analysis of the genes corresponding to the hypermethylated probes in the low-immune group of NF1-gliomas identified enriched immune system categories. We further confirmed this finding by an integrated analysis of gene expression and DNA methylation, from which a total of 68 genes enriched for immune categories emerged as significantly hyper-methylated and down-regulated in low- versus high-immune NF1-gliomas. At least eight of these genes are involved in important T lymphocyte functions.

The execution of an effective anti-tumor immune response by effector T cells is typically driven by neoantigens generated by somatic mutations of cancer cells (Schumacher and Schreiber, 2015). To assess whether high- and low-immune NF1-glioma subtypes contain a different number of tumor-specific neoantigens, we evaluated NF1-gliomas profiled with matched germline/tumor WES and tumor RNAseq for HLA typing and tumor neoantigen identification. The analysis revealed that the high- but not the low-immune group of NF1-gliomas expressed neoantigens ($P = 0.0337$). To characterize the neoantigens identified in high-immune NF1-gliomas, we performed a homogenous, proximity-based assay that measures the affinity kinetics of mutant neoantigens and corresponding wild-type peptides for binding to their restricted HLA class I allele (Harndahl *et al.*, 2009). The mutant peptides bound with markedly higher affinity to HLA than their wildtype peptide counterpart, consistent with the mutations conferring enhanced HLA binding.

NF1-gliomas resemble the LGm6 subgroup of sporadic gliomas. Having identified the landscape of genetic and epigenetic features of NF1-gliomas, we sought to relate them to those of the different subgroups of sporadic gliomas that we have recently reported in a pan-glioma cohort from The Cancer Genome Atlas (TCGA) project (Ceccarelli *et al.*, 2016). We first compared the epigenetic features through an integrative analysis of DNA methylation profiles of NF1-gliomas and the TCGA pan-glioma dataset. We integrated NF1-gliomas with the TCGA pan-glioma cohort (n = 819) on 1,233 glioma specific methylation probes and performed a supervised classification of NF1-gliomas using a nearest neighbor classifier trained on sporadic gliomas. We also performed an unsupervised clustering merging sporadic TCGA gliomas and NF1-gliomas. Both supervised and unsupervised analyses showed that all of the NF1-glioma samples belonged to the LGm6 group of gliomas, which is characterized by the divergent survival between grade II and III tumors (pilocytic astrocytoma-like) and grade IV tumors (LGm6-GBM) (Figure 26, panel a).

Next, we used mathematical methods based on a multiple linear regression model to deconvolute mutation signatures that in other cancer types have been associated with distinct underlying mutational processes (Alexandrov *et al.*, 2013). The clustering of the TCGA pan-glioma cohort of *IDH*-wildtype tumors based on mutational signatures revealed that the large majority (86%) of sporadic gliomas belonged to a group (cluster 2) that displays a single mutational signature (signature 1). Conversely, a smaller group of tumors (cluster 1) was richer in mutational signatures, including signature 3, which has been associated with failure of DNA double-strand break-repair by homologous recombination (Alexandrov *et al.*, 2013). Although cluster 1 contained only 14% of *IDH*-wildtype gliomas, it included 20 of 48 (42%) LGm6 tumors, therefore manifesting a marked enrichment for this methylation group ($P = 8.1 \times 10^{-8}$). Interestingly, 100% of NF1-gliomas fell within cluster 1. The subset of sporadic LGm6 gliomas in cluster 1 exhibited significant enrichment for low-grade histology ($P = 0.02$) and, albeit not reaching statistical significance, there was a trend for increased frequency of NF1 mutations in this group.

Next, we explored in more detail the pattern of driver mutations and CNVs of the LGm6 group of sporadic gliomas to ask whether it was related to the landscape of somatic alterations of NF1-gliomas. We found that somatic mutations of the *NF1* gene are frequent in LGm6 tumors (25%). We also found that the key alterations identified in high-grade NF1-gliomas (*ATRX* and *TP53* mutations and *CDKN2A* deletions) were also highly recurrent in LGm6 grade III and IV tumors in the LGm6 subgroup (Figure 26, panel b).

Re-evaluation of the ATRX status revealed that the mutation of this gene is more frequent in this group than the other subtypes of sporadic *IDH*-wildtype gliomas (Figure 26, panel c). This was in contrast with grade II tumors that lacked *ATRX* mutations and displayed a greatly reduced frequency of mutations (Figure 26 panel b and c). Furthermore, we found that, whereas the clinical outcome of LGm6-GBM was poor regardless of the ATRX status, *ATRX* mutations conferred a significantly worse prognosis to the grade III LGm6 patients ($P = 0.03$), with a survival that was comparable to that of LGm6-GBM. In contrast, survival of patients with *ATRX* wild-type grade III LGm6 glioma was similar to patients with grade II LGm6 glioma (Figure 26, panel d).

Figure 26. NF1-gliomas resemble LGm6 subgroup of sporadic gliomas. Panel a: Heat map of DNA methylation data for the TCGA pan-glioma cohort and 31 NF1-gliomas according to the methylation clusters of sporadic gliomas (Ceccarelli *et al.*, 2016). Thirty-one of 31 NF1-glioma samples were assigned to the LGm6 methylation cluster, one of the methylation clusters that includes both low-grade and high-grade gliomas. Panel b: Oncoprint of selected somatic genomic alterations in the LGm6 group of gliomas from the TCGA dataset. Rows and columns represent genes and samples, respectively. Glioma grade was significantly associated with alterations of *ATRX*, *TP53*, *CDKN2A*, *PTEN*. $P = 0.01$, $P = 0.02$, $P = 0.04$, $P = 0.002$, respectively. Panel c: Barplot of *ATRX* non-synonymous somatic mutations occurring in phenotypic subtypes of *IDH*-wildtype gliomas (classic-like, mesenchymal-like, and LGm6) and LGm6 gliomas grouped by tumor grade. *ATRX* mutations were significantly enriched in grade III LGm6 ($P = 0.01$). Panel d: Kaplan–Meier survival analysis of LGm6 gliomas stratified according to histological grade and *ATRX* status for grade III gliomas: grade II (green curve), grade III *ATRX* mutant (blue curve), grade III *ATRX* wild-type (cyan curve), grade IV (red curve). The *ATRX* mutant grade III subgroup showed a significantly worse survival when compared with *ATRX* wild-type grade III patients ($P = 0.03$). Panel e: Master regulators (MR) in *ATRX*-mutant glioma. Gray curves represent the activity of each of the 10 MR with the highest (red) or lowest (blue) activity. Red or blue lines indicate individual *ATRX*-mutant samples displaying high or low activity, respectively, of the MR in *ATRX*-mutant compared with *ATRX*-wildtype (*P* value (left) and mean (right)). Panel f: Hierarchical clustering of MR activity in 48 high-grade LGm6 *IDH*-wildtype gliomas. Data were obtained using the Euclidean distance and Ward linkage method built on differential activity of MRs in *ATRX* mutant (red) versus *ATRX*-wildtype (black) tumors ($P < 0.01$). The activity of 41 of 89 MRs was increased in *ATRX* mutant samples. Panel g: Enrichment map network of statistically significant gene ontology categories for genes included in the regulons of the 10 MRs with the highest activity in *ATRX* mutant gliomas. Nodes represent gene ontology terms and lines their connectivity. Node size is proportional to number of genes in the gene ontology category and line thickness indicates the fraction of genes shared between groups.

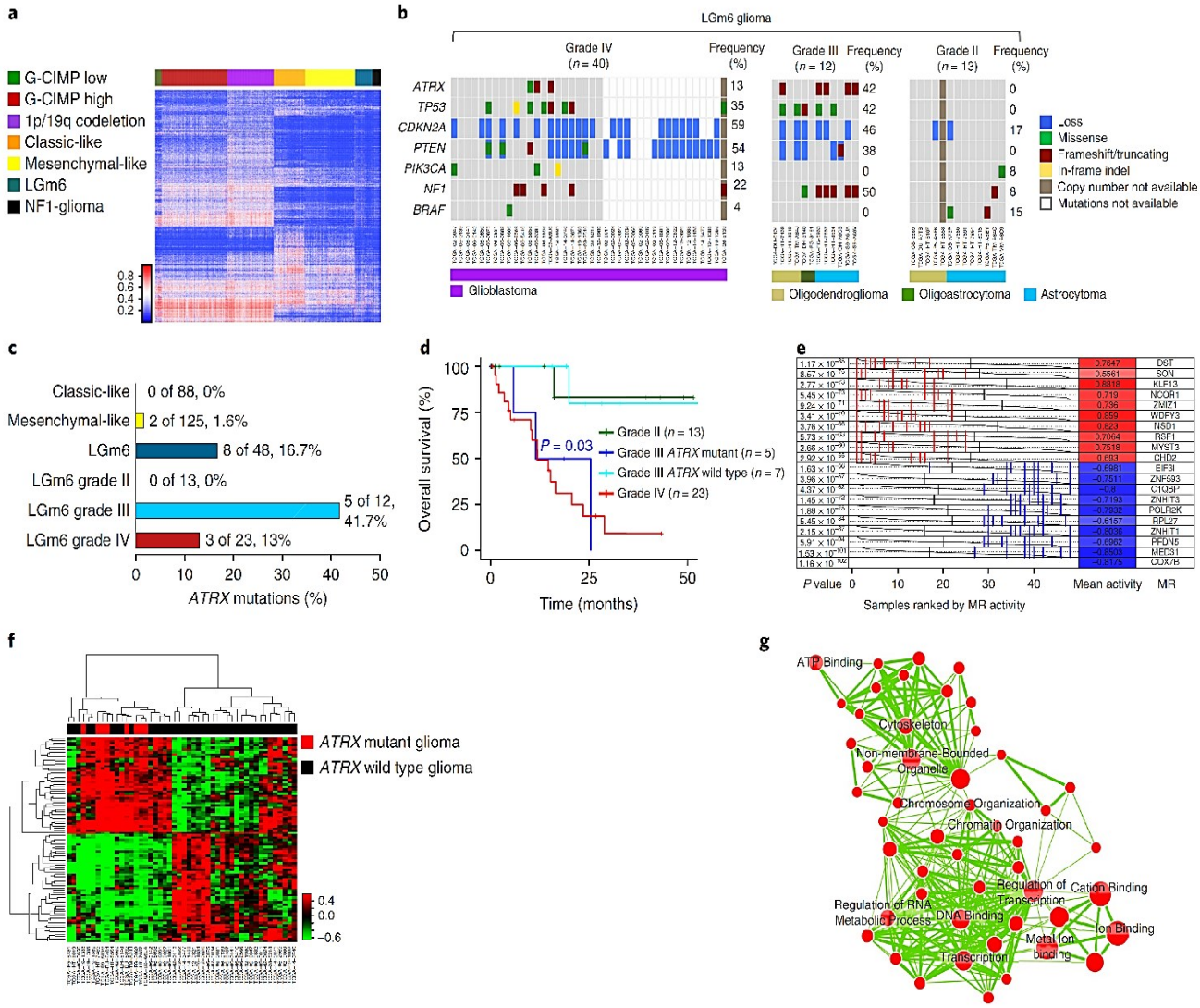

Finally, to identify the transcription factors that are causally involved as master regulators of the transcriptomic changes associated with loss of ATRX in the LGm6 group of *IDH*-wildtype gliomas, we used the transcriptional network assembled from a TCGA-derived pan-glioma cohort and applied the RGBM approach, a recently developed algorithm that involves gradient-boosting machines for the inference of gene regulatory networks.

We inferred the activity of master regulators enriched in *ATRX* mutant samples within the LGm6 cluster of *IDH*-wildtype gliomas by computing a score that integrates the ability of transcription factors to activate their targets in each individual tumor sample. The analysis resulted in 41 activated master regulators and 48 inhibited master regulators in the 8 *ATRX* mutant high-grade LGm6 samples compared with 40 *ATRX*-wildtype gliomas (Figure 26, panel e). Unsupervised consensus clustering based on the activity of master regulators resulted in two main clusters defined by the divergent activity of the two groups of master regulators. The first cluster included all *ATRX* mutant samples, whereas the second cluster was exclusively composed of *ATRX* wildtype samples (Figure 15, panel f). This finding independently validates the 41 activated master regulators as key drivers of the hallmark features of *ATRX*-mutant gliomas within the LGm6 group. The enrichment map network built from gene ontology categories and informed by the inferred targets of the 10 most active master regulators in *ATRX* mutant tumors indicated that chromatin and transcription regulation are among the most enriched functions (Figure 26, panel g). This is consistent with the role of the most active master regulators in *ATRX*-mutant gliomas (MYST3, CHD2, ZMIZ1, NCOR1, NSD1) as chromatin and epigenetic modifiers. The activation of a unique set of master regulators with important functions in chromatin remodeling and transcriptional coregulation as drivers of the *ATRX*-mutant transcriptome within the *IDH*-wildtype LGm6 cluster provides a clue to the molecular events that become deregulated and trigger global epigenomic remodeling and transcriptional changes following loss of ATRX function in brain tumors.

Discussion

Here we reported the landscape of genetic and epigenetic alterations of gliomas occurring in NF1 patients. It is important to consider that the inaccessible brain tumor location, the relatively benign behavior of brain lesions, the comorbidities, and the neurological deterioration associated with surgical intervention most frequently argue against surgery as choice of treatment for glioma patients with NF1 (Helfferich *et al.*, 2016). Therefore, the collection of glioma samples analyzed in this study represents the selected subset of tumor lesions that undergo surgical resection. Nonetheless, a comprehensive analysis of the complete spectrum of glioma grades throughout the lifespan of NF1 patients has allowed us to follow NF1 gliomagenesis and identify the genetic modules and the expression signatures that distinguish low- from high-grade tumors. We found that abundant infiltrates of activated T lymphocytes and mutation-derived neoantigens characterize a subset of low-grade gliomas, whereas high-grade tumors exhibit frequent mutations of *ATRX* typically co-occurring with alterations of *TP53* and *CDKN2A*. We also classified gliomas occurring in the context of the NF1 syndrome within a particular methylation subgroup of sporadic gliomas, the LGm6, that recapitulates mutational and epigenetic profiles of NF1-glioma. The discovery that *ATRX* mutations drive aggressiveness in NF1-glioma prompted re-evaluation of the mutational and clinical features of the sporadic glioma counterpart (LGm6), leading to a more accurate classification of the sporadic tumors that cluster into this group.

NF1 is associated with a heterogeneous glioma pattern in children and adults (Rodriguez *et al.*, 2008). Therefore, the dissection of the molecular landscape of glioma in NF1 patients required a comprehensive molecular study

of brain tumors that could not be limited to a particular age and/or glioma grade. We observed several features that differentiate low-grade gliomas — which are relatively more common in children — from the high-grade tumors that instead predominate in adults with NF1. Pediatric low-grade NF1-gliomas exhibit a very low mutation rate compared to high-grade tumors, with few recurrent somatic mutations. The only set of recurrently mutated genes in low-grade NF1-glioma are genes involved in the MAPK pathway, thus recapitulating the genetic features of sporadic pilocytic astrocytoma. Conversely, the mutation burden of high-grade glioma in NF1 patients was higher and was characterized by recurrent alterations composing a genetic module that includes loss-of-function events targeting *ATRX*, *TP53*, and *CDKN2A*. Loss of ATRX in high-grade NF1-glioma is unique when considered within the genetic contexts associated with *ATRX* mutations in sporadic gliomas, in which they are typically associated with mutations of *H3.3* in children or *IDH1* in adults. The inactivating mutations of the *ATRX* gene result in loss of a functional ATRX protein with at least two important mechanistic consequences: the development of the ALT phenotype and the activation of a transcriptional/chromatin remodeling gene expression signature in *ATRX*-mutant NF1-glioma.

Previous work reported that mouse models of low-grade glioma sustained by loss of NF1 manifest specific alterations of the immune microenvironment (Solga *et al.*, 2015). The analysis of human NF1-glioma confirms and extends this notion. We found that, compared to high-grade tumors, the gene expression signature more strongly enriched in low-grade NF1-gliomas is an immune signature including several effector lymphocyte categories. This has been confirmed by the finding that the high-immune group of low-grade NF1-glioma contains both rich infiltrates of T lymphocytes, some of which are endowed with cytolytic activity, and mutation-derived neoantigens that exhibited enhanced HLA binding. The reduced DNA methylation of immune genes expressed in low-grade/high-immune NF1-glioma is consistent with previous studies in which reduced methylation and increased expression of immune genes in human tumors was linked to tumor infiltration by lymphocytes characterized by demethylated and transcriptionally active genes involved in T lymphocyte functions that, on the contrary, were highly methylated and transcriptionally repressed in cancer cells (Jeschke *et al.*, 2017). Taken together, our findings suggest that the long indolent course of low grade NF1-gliomas that rarely progress to high-grade disease (Sellmer *et al.*, 2017) (Helfferich *et al.*, 2016) (Rodriguez *et al.*, 2008) may be preserved by the checks imposed by adaptive immunity. Further studies are ongoing to better define the characteristics of tumor infiltrating lymphocytes, as well as PDL-1 expression on tumor cells, in order to assess whether it exists a subgroup of patients that might benefit from treatment with immune checkpoint inhibitors. While data on NF1-gliomas are lacking, the dermal and plexiform neurofibromas of NF1 patients show increased PDL-1 expression (Wang *et al.*, 2018), supporting further investigations.

DNA methylation profiling classified NF1-gliomas within the LGm6 *IDH*-wildtype cluster of sporadic gliomas from our recent pan-glioma TCGA study (Ceccarelli *et al.*, 2016). Prompted by the discovery that high-grade *IDH*-wildtype gliomas in NF1 patients harbor frequent mutations of *ATRX*, we re-analyzed the LGm6 subgroup of sporadic tumors. We found that the original definition of pilocytic astrocytoma-like, which combined histological grade II and grade III tumors in the LGm6 cluster, is not an accurate representation of the biology of these tumors. Indeed, mutation pattern and clinical outcome of grade II-LGm6 gliomas diverge markedly

from those of grade III-LGm6 tumors harboring *ATRX* mutations, which are more similar to LGm6-GBM. This finding calls for a re-evaluation of the guidelines for the classification of *IDH*-wildtype gliomas, given that the LGm6 group exhibits a larger heterogeneity than previously described and requires analysis of the ATRX status for an accurate qualification. As previous studies have shown that ATRX loss increases sensitivity to DNA-damaging agents (Koschmann *et al.*, 2016), *ATRX* mutations may represent a point of therapeutic intervention for high-grade NF1-gliomas and LGm6 sporadic gliomas. Our study also suggests that, similarly to NF1-glioma, the comparative genomic analysis of other NF1-associated neoplasms with their sporadic counterpart may reveal distinct pathogenic mechanisms that could have therapeutic implications.

Published in Nat Med. 2019 Jan;25(1):176-187.

Diffuse midline gliomas

Background

Diffuse midline gliomas (MLG) are rare tumors occurring predominantly in children and young adults (Ostrom *et al.*, 2015). Genomic studies in pediatric MLG showed that these tumors frequently harbor K27M missense mutations in the *H3F3A* and the *HIST1H3B* genes, which encode variants of the histone H3 protein (Schwartzentruber *et al.*, 2012) (Wu *et al.*, 2012) (Buczkowicz *et al.*, 2014). While *HIST1H3B* mutations are anatomically restricted to the brainstem (Wu *et al.*, 2012) (Castel *et al.*, 2015), *H3F3A* mutations have been reported in MLG of various locations (Khuong-Quang *et al.*, 2012) (Buczkowicz *et al.*, 2014) (Castel *et al.*, 2015) (Solomon *et al.*, 2016). In pediatric MLG, these mutations associate with a more aggressive clinical phenotype and with poorer prognosis (Khuong-Quang *et al.*, 2012) (Sturm *et al.*, 2012). Based on these observations, the 2016 WHO classification introduced the category of "diffuse midline glioma, H3K27M-mutant" as a novel entity, which is invariably assigned grade IV even in absence of signs of anaplasia (Louis *et al.*, 2016).

In adults, less than 10% of diffuse gliomas arise from midline structures (Larjavaara *et al.*, 2007) (Ostrom *et al.*, 2015). Recent studies suggested that adult MLG may differ from both pediatric MLG and from adult supratentorial gliomas. *H3F3A* mutations have been reported in adult MLG but their prognostic significance in adults remains unclear (Aihara *et al.*, 2014) (Feng *et al.*, 2015). Actionable *IDH1* and *FGFR1* hotspot mutations have also been described in this population (Ryall *et al.*, 2016) (Zhang *et al.*, 2014), though their frequency and genotype associations remain unclear. Overall, the genomic landscape of adult MLG is poorly understood. Indeed, the availability of surgical specimens is limited in this population, as the surgical risks related to anatomical location, and the assumption of a limited survival benefit, often argue against surgery (Reyes-Botero *et al.*, 2012).

We assumed that unravelling the genomic landscape of these tumors will enable to better define the prognostic value of molecular biomarkers in this disease and to identify new therapeutic targets. In this study, we report the clinical, histological, and molecular characteristics of 116 adult patients with MLG and assess the prevalence and the prognostic significance of the major driver molecular alterations in this population.

Patients and methods

Patients and tumor samples. Patients (≥ 15 years-old) with a histological diagnosis of MLG were retrospectively identified in our database (OncoNeuroTek, Pitié-Salpêtrière Hospital, Paris; 1996–2017) according to the following criteria: 1) tumor arising from a midline location (i.e., thalamus, hypothalamus,

pineal region, brainstem, cerebellum or spinal cord) verified on neuroimaging at diagnosis; 2) histological diagnosis of diffuse glioma according to the 2016 WHO classification (Louis *et al.*, 2016); and 3) available follow-up data. All tumor samples underwent histological review and, if required, additional immunohistochemical studies to ensure an accurate diagnostic classification. Radiological analysis was performed by two investigators, who independently scored contrast enhancement (absent, mild/moderate, marked/avid) and necrosis (none, <5%, 6%–33%, 34%–67%, >67%) according to the Visually Accessible Rembrandt Images (VASARI) criteria. As controls, we used a set of supratentorial hemispheric diffuse gliomas with available tumor DNA from the OncoNeuroTek database. All tumor samples and clinical data were collected after acquiring written informed consent in accordance with the tenets of the Declaration of Helsinki.

DNA extraction and genotyping. DNA was extracted from FFPE or snap-frozen samples, as previously reported (Reyes-Botero *et al.*, 2014). Hotspot mutations in the *IDH1* (codon 132), *IDH2* (codon 172), *H3F3A* (codon 27 and 34), *HIST1H3B* (codon 27), *FGFR1* (codon 546 and 656), *BRAF* (codon 600), and *TERT* promoter (at −250 and −228) genes were assessed using the Sanger method after standard PCR amplification, as previously described (Reyes-Botero *et al.*, 2014) (Labussière *et al.*, 2014a). Whenever enough material was available, CGH-array was performed to determine *EGFR* amplification, *p16/CDKN2A* deletion, and chromosome 1p, 19q, 9p, 10p, and 10q losses, as previously described (Labussière *et al.*, 2016). *MGMT* promoter methylation status was determined by bisulfite conversion and subsequent nested methylation-specific PCR.

Immunohistochemical analyses. Immunohistochemistry for Ki67, IDH1 R132H and ATRX expression were performed as previously described (Reuss *et al.*, 2015). In particular, the loss of nuclear ATRX expression was considered specific when tumor cell nuclei were unstained while the nuclei of non-neoplastic cells were ATRX-positive. The anti-histone H3K27M-mutant antibody (ABE419; Millipore, Burlington, MA) was used at dilution 1/1000. Samples were considered H3K27M- or IDH1 R132H-mutant when immunohistochemistry was positive for the presence of the altered protein.

Statistical analysis. OS was defined as the time between tumor diagnosis and death. Patients who were still alive at last follow-up were censored. Survival curves were calculated using the Kaplan-Meier method. Statistically significant differences between survival curves were assessed using the log-rank test. A log-rank test p-value ≤ 0.05 (2-sided) was considered statistically significant. The Cox model was used to evaluate the effect of quantitative variables on survival and for multivariate survival analysis. The χ^2 and the Fisher's exact test were used to compare categorical variables, considering as significant p-values < 0.05. Hierarchical clustering and multidimensional representations were used to explore associations between variables. The Spearman correlation test was used to assess statistically significant associations. All statistical analyses were performed using R software packages.

Results

Clinical and histologic features of adult MLG. Out of 2649 patients with diffuse glioma of any location present in our database, we identified 116 patients (4.4%) fulfilling inclusion criteria (M/F 71/45; median age 46.5 years, range: 15–75) because of cerebellar (17), spinal (8), brainstem (30), thalamic (57) and diencephalic nonthalamic (4) gliomas (Figure 27). All the cases were reviewed by a neuropathologist and assigned an integrated diagnosis according to the 2016 WHO classification. The predominant histological aspect was of diffuse astrocytic gliomas, but other patterns were also observed, including the oligodendroglial, piloid, pseudo-ependymal, pleomorphic xanthoastrocytoma-like, and the embryonal tumor-like pattern. Eighty-four patients (84/109, 77%) underwent biopsy and 25 (25/109, 23%) a partial or subtotal resection. Sixty-eight patients (68/101, 67%) received combined chemoradiation with temozolomide as first-line therapy, 16 (16/101, 17%) received chemotherapy, and twelve (12/101, 12%) received radiation therapy alone. Four patients (4/101, 4%) did not receive any adjuvant treatment after initial diagnosis.

Figure 27. Illustrative examples of the location of tumors included in the study, and number of cases for each location.

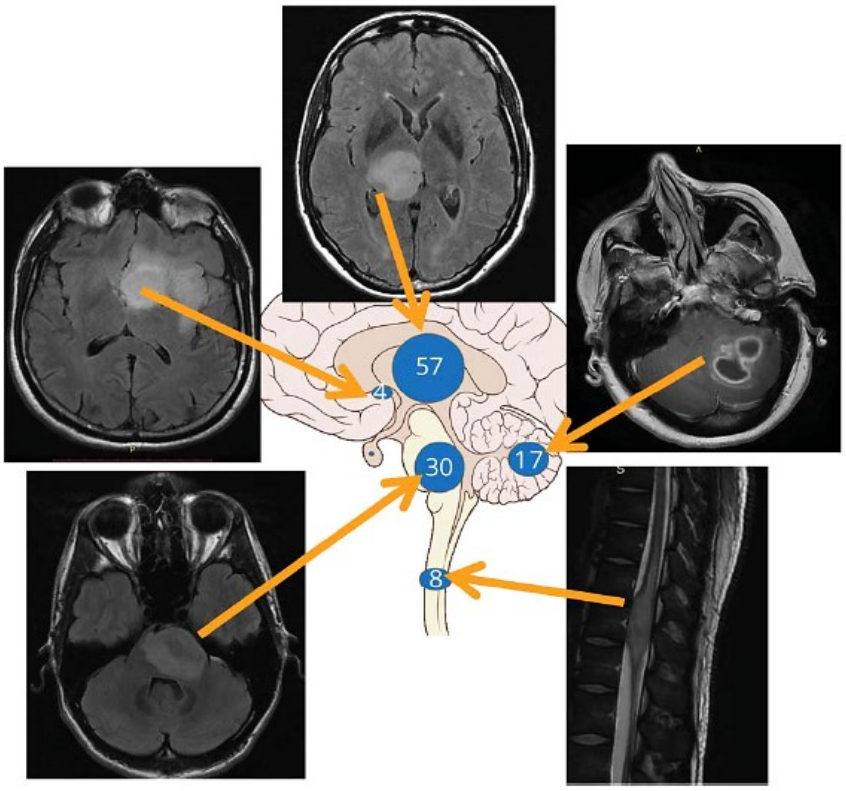

Molecular characterization of adult MLG revealed the presence of recurrent hotspot mutations in *FGFR1*. As diagnosis was based on tumor biopsy in most patients and tissue availability was limited, molecular analyses were focused on the alterations hypothesized to be the most relevant to the disease. Histone H3K27M

mutations were found in 38/110 patients (34%) and were associated with younger age at diagnosis (median: 33 vs. 53 years-old, $p = 6 \times 10^{-5}$). Histone H3 mutations were mutually exclusive with *IDH1* and inversely associated with *TERT* promoter mutation, *p16/CDKN2A* loss, and *EGFR* amplification (Table 8). Though found in all the locations, the H3K27M mutation was associated with the thalamic and spinal location (Figure 28) (Table 8). *IDH1* mutations were found in 6 patients (1 grade II, 4 grade III, 1 grade IV) out of 102 (6/102, 6%) and, strikingly, all 6 *IDH1*-mutant tumors were located in the brainstem (Figure 28) (6/24 vs. 0/78 for MLG not involving the brainstem, $p = 7.5.10^{-5}$). Only 1 out of the 5 *IDH1* mutations identified by sequencing was *IDH1* R132H, the remaining being p.Arg132Gly (R132G) (2 patients), p.Arg132Cys (R132C) (1 patient), and p.Arg132Leu (R132L) (1 patient). This observation contrasted with what observed in an independent group of non-midline *IDH1*-mutant gliomas drawn from our database (OncoNeuroTek): out of 2234 *IDH1*-mutant supratentorial gliomas, 2083 (93.2%) were R132H, 55 (2.5%) were R132G, 54 (2.4%) were R132C, 27 (1.2%) were R132S, and 15 (0.7%) were R132L (p=0.0001). These data indicate that *IDH*-mutant brainstem gliomas differ from supratentorial *IDH*-mutant gliomas with regard to the pattern of recurrent *IDH1* mutations and suggest that immunohistochemistry using the anti-IDH1 R132H antibody might not be a valid method for *IDH* screening in MLG.

Figure 28. Age, tumor location, tumor grade, and molecular alterations in our 116 patients with diffuse midline gliomas.

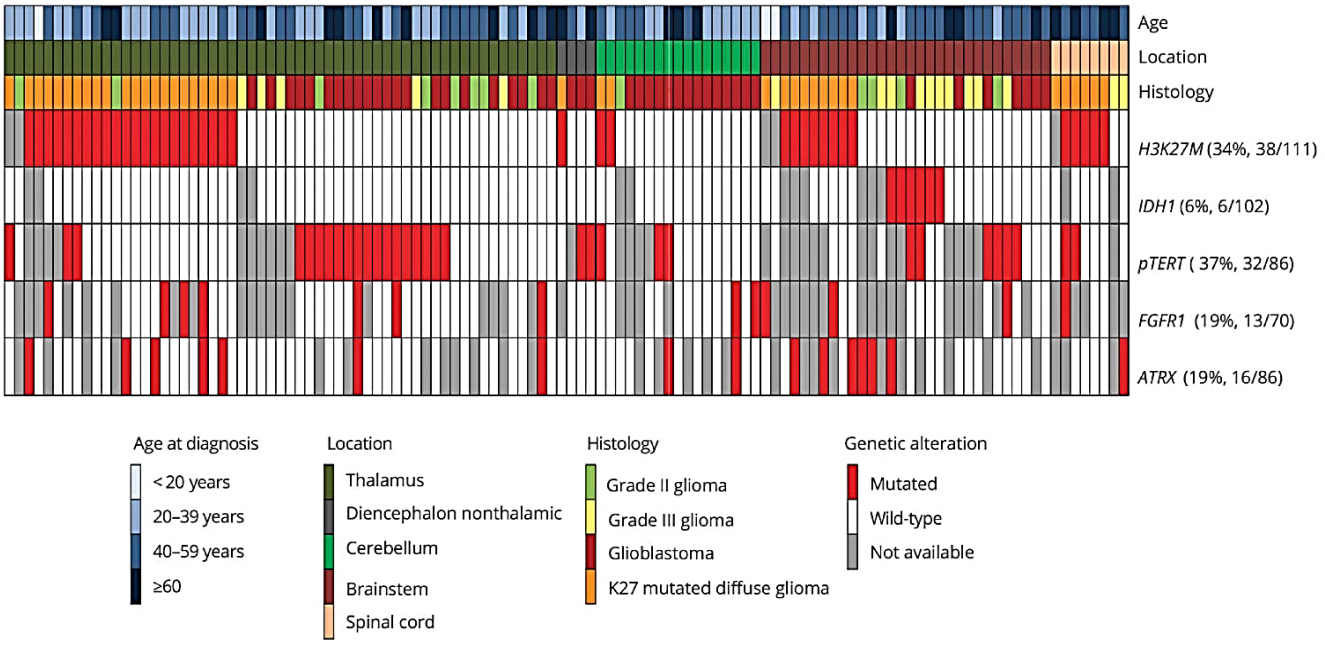

Fifty-nine patients were found to be *IDH*-wildtype and K27M-wildtype: this group of MLG — IDHwt-K27wt — had more frequent *TERT* promoter mutations (24/48, $p < 1 \times 10^{-5}$), *CDKN2A* deletions (7/24, p = 0.028), and *EGFR* amplifications (5/24, p = 0.016). No patient had *BRAF* V600 mutations (0/69).

Table 8. Clinical, histological, and molecular features in patients with H3 K27M-mutant (n=38) vs. H3 K27M-wildtype (n=73) MLG.

	K27M wild-type	K27M mutated	*p* Value
N	73	38	NA
Sex ratio (M/F)	1.52 (44/29)	1.53 (23/15)	0.98
Age at surgery, y, median (range)	53 (23–75)	33 (15–65)	<0.0001
Location, % (n)			0.04
Nonthalamic diencephalic	4 (3/73)	3 (1/38)	
Thalamic	45 (33/73)	58 (22/38)	
Brainstem	27 (20/73)	21 (8/38)	
Cerebellar	21 (15/73)	5 (2/38)	
Spinal cord	3 (2/73)	13 (5/38)	
Median OS, mo (95% CI)	15.0 months (10.4–19.7 months)	18.6 months (14.7–33.6 months)	0.65
IDH mutation, % (n)	17 (5/30)	0 (0/14)	0.16
ATRX loss, % (n)	15 (8/54)	26 (8/31)	0.25
pTERT mutation, % (n)	52 (27/52)	19 (5/27)	0.007
C228T	20	4	
C250T	7	1	
MGMT methylation, % (n)	38 (3/8)	0 (0/5)	0.23
FGFR1 mutation, % (n)	13 (6/46)	26 (6/23)	0.19
EGFR amplification, % (n)	23 (7/31)	0 (0/22)	0.03
P16 loss, % (n)	32 (10/31)	5 (1/22)	0.02

Recurrent *FGFR1* mutations affecting 2 hotspots were identified in 18% of patients (13/73): p.Asn546Lys (9 patients), p.Asn546Asp (2 patients), and p.Lys656Glu (2 patients). *FGFR1*-mutant tumors had various locations (Figure 28), including thalamus (7/37, 19%), brainstem (2/12, 17%), cerebellum (2/13, 15%), and spinal cord (1/3, 33%) (p = 0.9), and were found both in the K27M-mutant and in the K27M-wildtype group (Table 8). In order to investigate whether *FGFR1* mutations were specific to diffuse gliomas located along the midline, we sequenced 479 DNA samples from hemispheric gliomas drawn from our tumor bank (170 GBM, 151 grade III, and 157 grade II, of which 197 were *IDH*-mutant, 212 *IDH*-wildtype, and 70 undetermined) searching for *FGFR1* mutations. We found only one mutation in a patient with an *IDH*-wildtype GBM involving the corpus callosum, suggesting that *FGFR1* mutations are restricted to midline diffuse gliomas (13/73 vs. 1/479; p = $1.2.10^{-10}$). Our data were further confirmed by public data (cbioportal.org): out of 1722 patients with diffuse

gliomas, only 2 patients had activating *FGFR1* mutations (13/73 vs 2/1722; $p = 10^{-16}$): one GBM with a K656E mutation but no clinical information on location and one 1p/19q-codeleted *IDH1*-mutant frontal oligodendroglioma with a N546K mutation.

Then, we used hierarchical clustering to explore the associations between variables. This analysis showed that *IDH1* mutation clustered with brainstem location, *FGFR1* mutation clustered with loss of ATRX expression (p = 0.02), and *CDKN2A* deletion clustered with *EGFR* amplification (p = 0.0004) and with *TERT* promoter mutation (p = 0.01). Tumor grade, necrosis and contrast enhancement on imaging grouped together in a cluster. *FGFR1* mutations (p = 0.06) and ATRX loss (p = 0.05) tended to associate with younger age, while *TERT* promoter mutations (p = 0.1) and *EGFR* amplification (p = 0.05) tended to associate with older age at diagnosis.

Survival analyses. Median OS for the whole cohort was 17.3 months, with 17.3 months for thalamic, 16.3 months for brainstem, 19.7 months for cerebellar, and 23.0 months for spinal gliomas. Among the classical prognostic factors validated in diffuse gliomas, only poor KPS (p = 0.0007), high grade (p = 0.01), elevated proliferation index (expressed as Ki67%) (p = 0.003), and contrast enhancement (p = 0.007) were associated with poorer OS.

Although, according to the 2016 WHO classification, all K27M-mutant diffuse MLG are considered as grade IV tumors (Louis *et al.*, 2016), the presence of H3K27M mutations did not correlate with poorer prognosis in our series (median OS: 23 vs. 15 months, p = 0.7) (Table 9) (Figure 29, panel A).

Table 9. Median OS based on the presence vs. absence of definite genetic alterations.

Genetic alteration	Median OS (95% CI), mo, alteration present	Median OS (95% CI), mo, alteration absent	*p* Value
H3K27M mutation	23 (16.4–45.0)	15 (11.3–21.3)	0.7
FGFR1 mutation	45 (14.5–NA)	13.8 (8.3–18.6)	0.01
TERTp mutation	9.1 (5.7–14.8)	24.2 (18.6–45.0)	<0.0001
p16/CDKN2A deletion	9.9 (4.3–NA)	23.8 (16.9–46.1)	0.0001
EGFR amplification	4.3 (1.3–NA)	23.8 (16.2–40.4)	<0.0001
IDH1 mutation	54.1 (51.3–NA)	15.9 (12.2–19.3)	0.05
ATRX loss	19.7 (14.5–NA)	15.0 (11.6–18.5)	0.05
Loss of chromosome 10p	9.15 (2.0–NA)	32.0 (18.6–54.1)	0.016
Loss of chromosome 10q	9.8 (3.8–NA)	29.2 (18.0–52.2)	<0.0001
Loss of chromosome 9p	14.8 (9.1–NA)	32.0 (18.5–53.5)	0.03

We therefore investigated whether grading according to the WHO 2007 classification had a prognostic relevance in H3K27M-mutant gliomas and we found no difference in OS between WHO 2007 grade II to IV tumors, suggesting that H3K27M-mutant MLG represent a separated entity in adult patients. We hypothesized that prognostic effect of histone H3K27M could have been masked by the association with younger age, which is a favorable prognostic factor. We entered the two variables in a Cox model: however, neither K27M (p = 0.2) nor age (p = 0.07) were associated with poorer survival. Finally, by stratifying for single locations, we found that H3K27M mutations were associated with longer OS in thalamic MLG compared to wildtype tumors (29.2 vs 14.4 months, p = 0.04). In brainstem tumors, after excluding *IDH1*-mutant cases, we observed a similar trend (16.4 vs. 9.1 months, p = 0.24). Altogether, these data suggest that, in adults, the H3K27M mutation is not associated with poorer outcome, showing a different effect on survival compared to the pediatric population. *IDH1* mutation, ATRX loss, and *FGFR1* mutations were associated with longer survival (Table 9) (Figure 29, panel B and D).

Figure 29. Kaplan-Meier survival curves based on molecular profile. Panel A: survival curves for H3K27M-wildtype (pink line) vs. H3K27M-mutant (blue line) MLG (median OS: 15 vs. 23 months, p = 0.7). Panel B: survival curves for *IDH*-wildtype (pink line) vs. *IDH*-mutant (blue line) MLG (median OS: 15.9 vs. 54.1 months, p = 0.05). Panel C: survival curves based on H3K27M and *IDH* status (blue line = *IDH*-wildtype and H3K27M-wildtype, green line = H3K27M-mutant, pink line = *IDH*-mutant; median OS: 11.6 vs. 23.0 vs 54.1 months, p = 0.05). Panel D: survival curves for *FGFR1*-wildtype (pink line) vs. *FGFR1*-mutant (blue line) MLG (median OS: 13.8 vs. 45 months, p = 0.01).

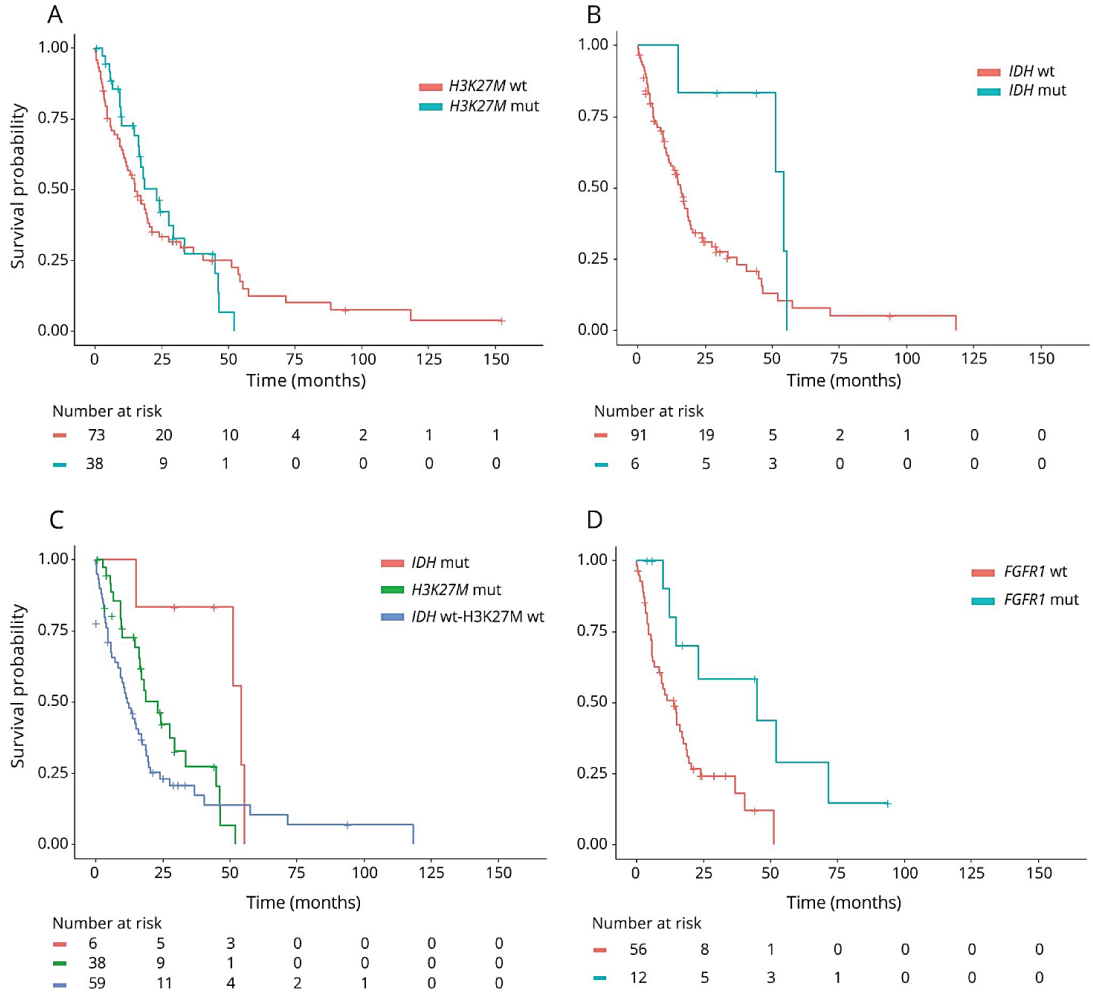

As *IDH1* mutations were present only in brainstem gliomas, we performed a subgroup analysis on this subset and found that it was associated with longer OS (54.1 vs. 11.9 months, p = 0.03). None of the *IDH1*-mutant brainstem MLG showed contrast enhancement (0/5 vs 6/10 in *IDH1*-wildtype brainstem gliomas, p < 0.05).
IDH wild-type–K27 wild-type patients showed the worst outcome (Figure 29, panel C). This group had frequent *TERT* promoter mutations, *CDKN2A* deletions, and *EGFR* amplifications, genetic alterations that are all associated with poorer OS. Loss of chromosomes 10q and 9p were also associated with poorer outcome (Table 9).
Finally, to identify independent prognostic factors, we performed multivariate survival analysis. Due to missing data, we limited the Cox model analysis to the most relevant (based on our data and current knowledge) and most documented variables: age, grade, H3K27M, *TERT* promoter, *IDH* and *FGFR1* status. On multivariate analysis, only *TERT* promoter (p<0.0001), *IDH* (p=0.007), and *FGFR1* (p=0.008) status were independent predictors of overall survival.

Discussion

This retrospective study shows that adult MLG constitute a heterogeneous group with mostly high-grade neoplasms and different clinical and histo-molecular characteristics compared to pediatric MLG and adult supratentorial high-grade gliomas. We identified two main subgroups based on the presence of H3K27M or *IDH1* mutations and found hotspot *FGFR1* mutations as a potential therapeutic target in this population.
The most prominent molecular subgroup consisted of H3K27M-mutant MLG, in line with previous studies showing a strong association between histone H3 mutations and the gliomagenesis of midline tumors (Buczkowicz *et al.*, 2014) (Schwartzentruber *et al.*, 2012) (Wu *et al.*, 2012) (Castel *et al.*, 2015) (Khuong-Quang *et al.*, 2012) (Sturm *et al.*, 2012) (Aihara *et al.*, 2014) (Feng *et al.*, 2015) (Reyes-Botero *et al.*, 2014) (Ryall *et al.*, 2016) (Meyronet *et al.*, 2017). However, we observed a lower prevalence of histone H3 mutations compared to pediatric high-grade thalamic and brainstem gliomas (70%–80%) (Buczkowicz *et al.*, 2014) (Wu *et al.*, 2012) (Castel *et al.*, 2015) (Khuong-Quang *et al.*, 2012). In addition, clinical and molecular features of patients from patients with histone H3 mutant MLG in our cohort differed from pediatric patients harboring the same molecular alteration (Buczkowicz *et al.*, 2014) (Wu *et al.*, 2012) (Khuong-Quang *et al.*, 2012). First, although histone H3 mutations were associated with younger age at diagnosis (median 33 vs. 53 years, $p = 6 \times 10^{-5}$), we found H3K27M mutations in patients over 60 years, indicating that screening for histone H3K27M mutations should always be performed, regardless of age, in adult patients with MLG. Moreover, in contrast to pediatric gliomas, we found that histone H3 mutations were not associated with a worse prognosis compared to other *IDH*-wildtype gliomas (Aihara *et al.*, 2014) (Meyronet *et al.*, 2017): in the largest group, i.e., thalamic MLG, H3 mutations were even associated with better outcome. While H3G34 and, to a lesser extent, H3K27 mutations have been associated with alternative telomere lengthening pathways in pediatric tumors, as reflected by frequent ATRX inactivation (Schwartzentruber *et al.*, 2012) (Khuong-Quang *et al.*, 2012) (Sturm *et al.*, 2012)

(Aihara *et al.*, 2014), we also found H3 mutations in association with *TERT* promoter mutations in 5 patients. Interestingly, in the subset of H3K27M-mutant gliomas, both ATRX loss and *TERT* promoter mutation tended to be associated with poorer outcome (median OS: 9.8 vs 24.2 months; p = 0.08; data not shown).

Another important driver in MLG was represented by *IDH* mutations, which specifically recurred in brainstem gliomas (6/24 vs 0/78 in other midline locations). The majority of *IDH1* mutations in this cohort were non-R132H, indicating that the widely used anti-R132H immunohistochemistry is not appropriate in brainstem gliomas and has probably led to underestimate the proportion of *IDH1*-mutant brainstem tumors (Theeler *et al.*, 2015). Systematic *IDH1* sequencing should be performed whenever feasible in brainstem gliomas. Indeed, as observed in hemispheric gliomas, the *IDH1* mutation is associated with improved outcome and may in part explain why adults with brainstem gliomas have better survival than children (Zhang *et al.*, 2014) (Theeler *et al.*, 2015). Besides their intrinsic prognostic implications, *IDH1* mutations may now be targeted by specific inhibitors (Dang, Yen and Attar, 2016), emphasizing how their identification by sequencing could open novel therapeutic options for patients affected by these tumors.

Besides the *IDH1* mutation, we identified other targetable hotspot mutations affecting the N546 and K656 residues of *FGFR1* in 18% of our patients. Differently from *IDH1*, *FGFR1* mutations were not associated with any specific location or any molecular subgroup. Somatic *FGFR1* N546 and K656 mutations were previously reported in several other cancer types, including a wide range of CNS tumors: rosette-forming glioneuronal tumors (Gessi *et al.*, 2014), dysembryoplastic neuroepithelial tumors (Rivera *et al.*, 2016), pilocytic astrocytomas (Jones *et al.*, 2013), diffuse leptomeningeal tumors with glial and neuronal markers (Dyson *et al.*, 2016), and pediatric thalamic gliomas (Schwartzentruber *et al.*, 2012) (Ryall *et al.*, 2016). Previous studies analyzed isolated cases or small cohorts, which make difficult the assessment of the incidence of *FGFR1* mutations in this population. *FGFR1* N546 and K656 mutants lead to the constitutive activation of FGFR1 and its downstream signaling and can be targeted by a number of oral FGFR inhibitors, currently under clinical evaluation in the context of clinical trials (Touat *et al.*, 2015), opening new therapeutic opportunities in this population.

Our study was limited by the scarcity of available tumor material, which led to narrow histological and molecular analyses. Therefore, genetic analyses were, whenever possible, restricted to a panel of selected molecular alterations, while several other samples were exhausted at the time of the analysis. However, the majority of the patients could be assessed for *TERT* promoter status, which was not covered by previous WES studies or was technically limited in WGS studies by the very low coverage of the *TERT* promoter region because of its high GC content (Wu *et al.*, 2012) (Zhang *et al.*, 2014). As observed in adult supratentorial GBM, *TERT* promoter mutation, which was detected in 37% of our patients, was associated with older age, grade IV, *EGFR* amplifications, loss of chromosome 10, *CDKN2A* deletion, and poor OS. The overall survival of these patients was particularly poor (9.1 vs. 24.2 months for patients without *TERT* promoter mutations), even compared to adult patients with hemispheric GBM followed at our institution (i.e., 13.5 months) (Nencha *et al.*, 2016), observation that might be related to the inability to resect these tumors.

Given the significant heterogeneity evidenced among adult MLG and the recurrence of potentially targetable molecular alterations, our findings reinforce the need for histologic confirmation and molecular analysis in adult patients with MLG. While *IDH1* and *TERT* promoter mutations might be of help for purposes of therapeutic stratification, we show here that histone H3 mutations do not confer worse prognosis in adult patients with MLG. The finding that MLG frequently harbor actionable *FGFR1* mutations has important clinical implications considering ongoing anti-FGFR clinical trials and reinforces the need for molecular analyses in this population. In these patients where surgery is high-risk, the development of liquid biopsies allowing the noninvasive assessment of these few hotspot mutations would be particularly relevant.

Published in Neurology. 2018 Jun 5;90(23):e2086-e2094.

IDH-wildtype low-grade gliomas

Background

Lower grade (i.e., WHO grade II and III) diffuse gliomas form a heterogeneous group of tumors including entities characterized by different malignant behavior. The *IDH* mutation and the chromosome 1p/19q codeletion represent the main diagnostic and prognostic markers in this group (Louis *et al.*, 2016) (Sanson *et al.*, 2009). The *IDH* mutation is an independent predictor of prolonged survival and its prevalence is inversely correlated with tumor grade (Sanson *et al.*, 2009).

IDH wildtype (*IDH*wt) grade II diffuse gliomas correspond to a rare subgroup of low-grade tumors associated with dismal prognosis and poor response to treatments (Metellus *et al.*, 2010). The relative rarity of *IDH*wt grade II diffuse gliomas hampers to perform large prospective studies in this tumor set. As a result, there is still conflicting evidence regarding the clinical and molecular profile associated with these tumors, and survival estimates widely range from 4.7 to 8.4 years across studies (Metellus *et al.*, 2010) (Suzuki *et al.*, 2015) (Chan *et al.*, 2015) (Aibaidula *et al.*, 2017), hampering to establish a standard of treatment.

Given the rarity of *IDH*wt grade II diffuse gliomas, most of the studies analyzed grade II and III gliomas altogether (Cancer Genome Atlas Research Network *et al.*, 2015) (Wijnenga *et al.*, 2017) to generate more solid data. However, evidence suggests that *IDH*wt grade II and grade III tumors significantly differ in terms of prognosis and biological behavior. While *IDH*wt grade III gliomas strikingly resemble primary glioblastomas (Cancer Genome Atlas Research Network *et al.*, 2015) (Tabouret *et al.*, 2016), *IDH*wt grade II neoplasms display less malignant features (Suzuki *et al.*, 2015) (Aibaidula *et al.*, 2017).

A recent consensus from the cIMPACT-NOW consortium has proposed that grade II and III *IDH*wt astrocytomas harboring *EGFR* amplification, and/or combined whole chromosome 7 gain and whole chromosome 10 loss (+7/-10), and/or *TERT* promoter mutation should be considered as *bona fide* glioblastomas, given their poor outcome (Brat *et al.*, 2018) (Tesileanu *et al.*, 2020), though these recommendations are not yet part of the WHO classification.

The aim of this study was to better define the outcome of *IDH*wt grade II diffuse gliomas compared to *IDH*-mutant (*IDH*mut) grade II and to *IDH*wt grade III diffuse gliomas, highlighting the main prognostic factors in this cohort.

Patients and methods

We performed a retrospective research in the OncoNeuroTek database (AP-HP, Groupe Hospitalier Pitié-Salpêtrière, Paris, France) for all patients diagnosed with WHO grade II and III diffuse gliomas between January

1989 and February 2020. After dividing WHO grade II and III gliomas in molecular subgroups based on their *IDH* and chromosome 1p/19q codeletion status (Labussière *et al.*, 2010) (Cancer Genome Atlas Research Network *et al.*, 2015), we focused on the subgroup of patients with *IDH*wt grade II gliomas. The clinical, radiological, histological, and molecular features of the patients in this subgroup were thoroughly reviewed to ensure an accurate patient selection. All available histological specimens were independently reviewed by two expert neuropathologists who assigned an integrated diagnosis according to the 2016 WHO classification (Louis *et al.*, 2016). Discordant assessments were resolved after collective discussion and additional immunohistochemical and molecular studies. Immunohistochemical staining for *IDH1* R132H, which was systematically performed in all cases, allowed to identify and exclude *IDH1*-mutant patients who were falsely negative on Sanger sequencing because of massive contamination of the tumor specimen with normal tissue. Immunostainings for ATRX, p53, H3K27M, FGFR3, EGFR, CD34, and neurofilaments allowed to better characterize and classify the tumor and to exclude circumscribed gliomas. Grading was assigned using widely accepted criteria that have recently been embraced by the cIMPACT consortium for lower grade *IDH*mut diffuse astrocytomas (Brat *et al.*, 2020): tumors with high cellularity, marked nuclear atypia and ≥ 2 mitoses (per 10 high power fields for biopsy specimens and per 30 high power fields Ki67 hotspots for resection specimens) were attributed grade III-IV histology (Louis *et al.*, 2016) (Brat *et al.*, 2020). Patients with midline tumors were excluded from the study if positive for the H3K27M mutation on immmunohistochemistry and/or DNA sequencing, as they are assigned grade IV according to the 2016 WHO classification. MRI scans acquired at diagnosis were systematically reviewed to verify that imaging features were compatible with diffuse glioma and to exclude the presence of gross nodules of contrast enhancement that would suggest that it was sampled the periphery of a higher grade neoplasm. Patients who, upon the revision of histological, molecular and MRI features, had a confirmed diagnosis of "diffuse astrocytoma, *IDH*-wildtype (grade II)" were included in subsequent analyses.

The clinical and paraclinical characteristics in patients with *IDH*wt grade II gliomas were analyzed and compared to patients with *IDH*wt grade III gliomas. We separately assessed how many patients in the group of *IDH*wt grade II and *IDH*wt III gliomas met the definition of "diffuse astrocytic glioma, IDH-wildtype, with molecular features of glioblastoma, grade IV" according to cIMPACT-NOW update 3 (Brat *et al.*, 2018) and compared their clinico-molecular features to patients with *IDH*wt tumors of the same grade not meeting this definition.

All tumor samples and clinical data were collected upon written informed consent in accordance with the tenets of the Declaration of Helsinki. The study was approved by the ethical committee CPP "Ile-de-France VI".

Molecular analyses. Tumor DNA was extracted from FFPE sections and/or from snap frozen tumor samples. DNA was extracted using commercial kits (GeneJET FFPE DNA purification kit, Thermo Scientific for FFPE sections; QIAamp DNA mini kit, Qiagen, for frozen tissue) or by automated DNA extraction (Maxwell®, Promega). The mutational status of *IDH1* (codon 132), *IDH2* (codon 172), *H3F3A* (codon 27 and 34), *FGFR1* (codons 546 and 656), *BRAF* (codon 600) and *TERT* promoter (-250 and -228) was obtained by Sanger

sequencing following standard PCR amplification, using previously reported primers (Labussière *et al.*, 2014a) (Reyes-Botero *et al.*, 2014) (Picca *et al.*, 2018) or by NGS. Information on copy number was acquired by CGH-array (Labussière *et al.*, 2016) or inferred from NGS data. *FGFR3-TACC3* fusions were assessed by RT-PCR amplification from RNA extracted from snap-frozen tumor tissue followed by Sanger sequencing (Di Stefano *et al.*, 2015). A subset of patients who tested negative for *FGFR3-TACC3* fusions on RT-PCR but had suggestive tumor cell morphology underwent a wider research for fusion genes using Illumina NGS panels: the Archer Comprehensive Thyroid Lung Fusion Plex (MiniSeq), which identifies rearrangements in *ALK, AKT1, BRAF, CALCA, CCND1, CTNNB1, DDR2, EGFR, ERBB2, FGFR1, FGFR2, FGFR3, FOXL4, GNAS, HRAS, IDH1, IDH2, KRAS, KRT20, KRT7, MAP2K1, MET, NRAS, NRG1, NTRK1, NTKR2, NTRK2, PIK3CA, PPARG, PTH, RAF1, RET, ROS1, SLC5A5, THADA, TTF*, or the AmpliSeq FOCUS (Miseq), which identifies rearrangements in *ABL1*, *ALK*, *AKT3*, *AXL, BRAF EGFR*, *ERBB2, ERG*, *ETV1*, *ETV4*, *ETV5*, *FGFR1*, *FGFR2*, *FGFR3*, *MET*, *NTRK1*, *NTRK2*, *NTRK3*, *PDGFRA*, *PPARG*, *RAF1*, *RET* and *ROS1*.

Statistical analyses. Categorical variables were compared using the Chi-square or the Fisher's exact test. Quantitative variables were compared using the Student t test or the Mann-Whitney test. OS was estimated by the Kaplan-Meier method and survival curves were compared using the log-rank test. The Cox model was used for continuous variables survival analyses. Hierarchical clustering and multidimensional association tables were used to explore associations between variables. The Pearson or the Spearman correlation test were used to assess statistically significant correlations between variables. For all analyses, the established threshold for statistical significance was $p = 0.05$. All statistical analyses were performed using "R" software packages.

Results

***IDH*wt grade II gliomas.** The clinical and molecular characteristics of the 47 patients who were assigned a diagnosis of "diffuse astrocytoma, *IDH*-wildtype (grade II)" upon centralized histological review are summarized in Table 10. The median age at diagnosis was 55.0 years-old (range: 19.6-82.1). Thirty-six patients were male (36/47, 77%). Median preoperative KPS was 90 (range: 70-100). Tumors commonly had their epicenter in the temporal lobe, extending to the fronto-basal lobe and the insula (28/47, 60%). Infiltration was commonly extensive, involving the ipsilateral deep grey matter (10/32, 57%), the cortex of adjacent lobes (5/32, 16%), the brainstem (3/32, 9%), and the contralateral hemisphere (5/32, 16%). As a consequence of tumor location, size, and highly infiltrative behavior, surgery commonly consisted of biopsy (27/44, 61%).

Strikingly, in this population of *IDH*wt, H3 K27- and G34-wildtype gliomas, immunohistochemical studies showed loss of ATRX nuclear expression in six cases (6/38, 16%). Seventeen patients were studied by NGS and 30 by Sanger sequencing plus CGH-array. The most common molecular alterations included *TERT* promoter mutations (23/45, 51%), whole chromosome 7 gain (10/37, 27%), and whole chromosome 10 loss

(10/41, 24%). *CDKN2A* deletions (5/43, 12%), *EGFR* amplifications (4/43, 9%), and chromosome 9p loss (3/42, 7%) were less common.

Table 10. Clinical and molecular features in the whole cohort of *IDH*wt grade II gliomas (n=47), in the subgroup of patients meeting the definition of "diffuse astrocytic glioma, *IDH*-wildtype, with molecular features of glioblastoma (grade IV)" (molecular GBM) (n=29) and in the subgroup of patients not meeting this definition (n=14). +7 = whole chromosome 7 gain; -10 = whole chromosome 10 loss.

	***IDH*wt grade II gliomas, whole cohort (n=47)**	***IDH*wt grade II gliomas meeting the definition of molecular GBM (n=29)**	***IDH*wt grade II gliomas NOT meeting the definition of molecular GBM (n=14)**	**p-value***
Age, median (range)	55.0 (19.6-82.1)	58.6 (20.8-82.1)	34.5 (19.6-65.4)	**0.00057**
Male gender	36/47 (77%)	24/29 (83%)	10/14 (71%)	0.44
Preoperative KPS, median (range)	90 (70-100)	90 (70-100)	90 (70-100)	0.83
Tumor location:				
Fronto-temporo-insular	28/47 (60%)	19/29 (66%)	5/14 (36%)	
Fronto- callosal or parieto-callosal	4/47 (9%)	4/29 (14%)	0/14 (0%)	**0.0055**
Other	11/47 (23%)	6/29 (21%)	5/14 (36%)	
Thalamo-mesencephalic	4/47 (9%)	0/29 (0%)	4/14 (29%)	
Extent of resection:				
Biopsy	27/44 (61%)	19/28 (68%)	7/12 (58%)	0.88
Partial resection	9/44 (20%)	5/28 (18%)	2/12 (17%)	
Gross total resection	8/44 (18%)	4/28 (14%)	3/12 (25%)	
Initial treatment:				
Chemotherapy alone	13/38 (34%)	10/25 (40%)	3/9 (33%)	
Sequential radiochemotherapy	7/38 (18%)	5/25 (20%)	1/9 (11%)	0.74
Stupp protocol	12/38 (32%)	7/25 (28%)	3/9 (33%)	
Radiotherapy alone	1/38 (3%)	0/25 (0%)	0/9 (0%)	
Surveillance	5/38 (13%)	3/25 (12%)	2/9 (22%)	
Radiological progression:				
Infiltrative	13/18 (72%)	11/15 (73%)	2/3 (67%)	0.45
Nodular enhancing	5/18 (28%)	4/15 (27%)	1/3 (33%)	
Molecular profile:				
TERT promoter mutation	23/45 (51%)	23/28 (82%)	0/14 (0%)	**<0.0001**
EGFR amplification	4/43 (9%)	4/26 (15%)	0/14 (0%)	0.28
+7	10/37 (27%)	10/26 (38%)	0/10 (0%)	**0.016**
-10	10/41 (24%)	10/26 (38%)	0/14 (0%)	**0.011**
combined +7/-10	7/41 (17%)	7/26 (27%)	0/14 (0%)	0.075
9p loss	3/42 (7%)	3/26 (12%)	0/14 (0%)	0.54
CDKN2A deletion	5/43 (12%)	3/26 (12%)	1/14 (7%)	1
Median OS, months	59.1	42.2	56.7	0.2

One patient with a temporal tumor harbored an activating *FGFR*1 mutation (1/26, 4%), and one patient with a bithalamic tumor harbored a *BRAF* V600G mutation (1/35, 3%). None of the tumors harbored *TP53* mutations (0/22), *PTEN* deletions (0/18), *PDGFRα* amplifications (0/17), or the chromosome 1p/19q codeletion (0/42). Twenty-nine patients underwent the research for fusion genes, with the detection of gene fusions in five (5/29, 17%), including four fusions *FGFR3* (exon 17 or 18) - *TACC3* (exon 5, 8, 11 or 23) and one fusion *FGFR3* (exon17) - *MYH14* (exon 23).

Initial treatment included concomitant radiochemotherapy with temozolomide followed by adjuvant temozolomide according to the Stupp protocol (12/38, 32%), sequential radio-chemotherapy with temozolomide or PCV (7/38, 18%), chemotherapy alone (13/38, 34%), or radiotherapy alone (1/38, 3%).

Tumor progression occurred either through an infiltrative pattern (Figure 30, panel A-D) or through the appearance of gross nodules of contrast enhancement (Figure 30, panel E-H). Patients with nodular progression showed poorer outcomes compared to patients evolving through an infiltrative pattern (median OS: 22 vs. 88 months, p=0.03).

Figure 30. Radiological patterns of progression. Panel A-D: example of an infiltrative pattern; MRI at progression (panel C,D) showed a marked extension of tumor infiltration along the right temporal lobe, the insula and the ipsilateral thalamus compared to baseline (panel A,B) without the appearance of enhancing abnormalities. Panel E-H: example of a nodular pattern; MRI at progression (panel G, H) showed the appearance of a gross nodule of contrast enhancement in the right insula surrounded by extensive perilesional edema that was not present at baseline (panel E,F).

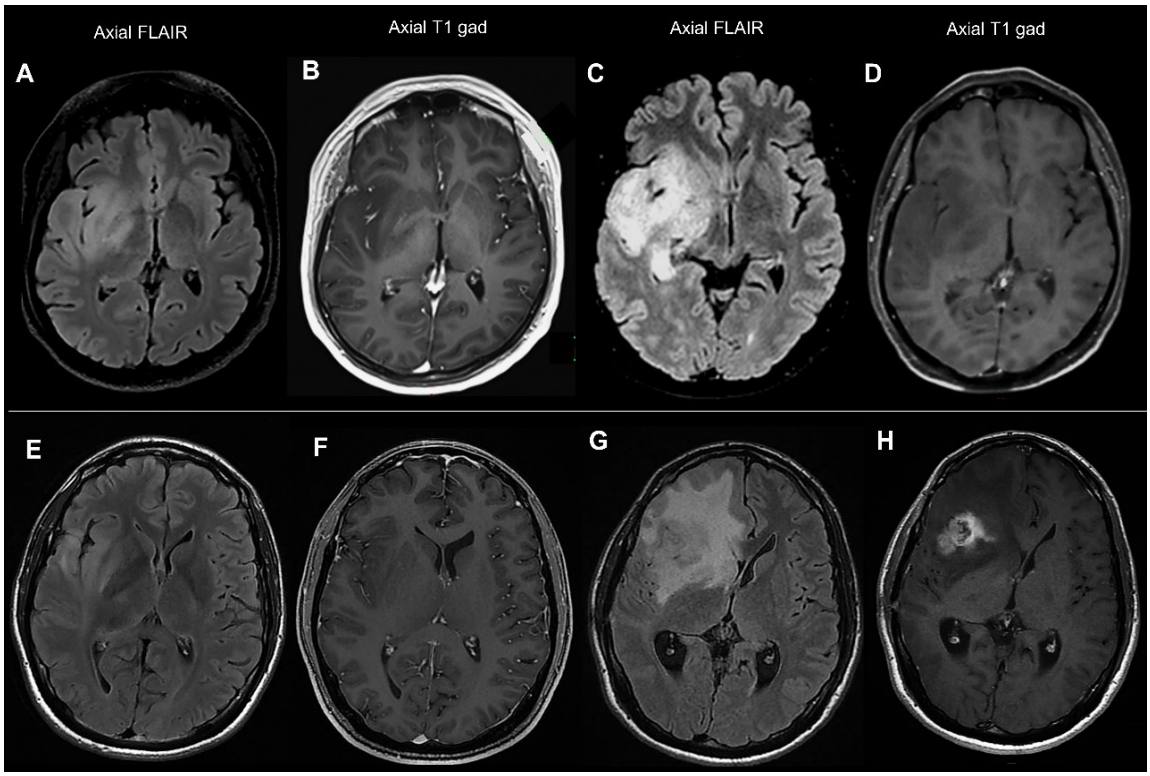

The median OS for *IDH*wt grade II gliomas was 59 months (vs. 101 months for *IDH*mut 1p/19q non-codeleted and 176 months for *IDH*mut 1p/19q codeleted gliomas, p<0.0001) (Figure 31, panel A). Higher preoperative KPS (p=0.04) was associated with improved OS. Whole chromosome 10 loss (median OS: 88 vs 33 months,

p=0.03), the +7/-10 signature (median OS: 88 vs 33 months, p=0.02), and chromosome 9p loss (median OS: 88 vs 19 months, p<0.0001) were associated with poorer OS. A similar trend was observed for whole chromosome 7 gain (median OS: 88 vs 41 months, p=0.2), *TERT* promoter mutations (median OS: 88 vs 41 months, p=0.2), and *CDKN2A* deletions (median OS: 59 vs. 42 months, p=0.3). Association matrix showed that whole chromosome 10 loss associated with whole chromosome 7 gain (p<0.001), *EGFR* amplifications (p<0.01), chromosome 9p loss (p<0.01), and *CDKN2A* deletions (p<0.01).

***IDH*wt grade III gliomas**. Table 11 compares the clinical and molecular features of *IDH*wt grade II (n=47) and grade III (n=255) gliomas. The median age at diagnosis for *IDH*wt grade III gliomas was 56.1 years-old (vs. 55.0 years-old, p=0.26). One-hundred-fifty-four patients (154/255, 60%) were male (vs. 36/47 (77%), p=0.048).

Table 11. Clinical and molecular features in *IDH*wt grade II (n=47) and *IDH*wt grade III (n=255) gliomas. +7 = whole chromosome 7 gain; -10 = whole chromosome 10 loss; RT-CHT = radiochemotherapy.

	***IDH*wt grade II and III gliomas, whole cohort (n=302)**	***IDH*wt grade II gliomas (n=47)**	***IDH*wt grade III gliomas (n=255)**	**p-value***
Age, median (range)	56.1 (8.5-84.1)	55.0 (19.6-82.1)	56.1 (8.5-84.1)	0.26
Male gender	190/302 (63%)	36/47 (77%)	154/255 (60%)	**0.048**
Preoperative KPS, median (range)	90 (20-100)	90 (70-100)	80 (20-100)	**0.0025**
Extent of resection				
Biopsy	142/270 (53%)	27/44 (61%)	115/237 (49%)	0.31
Partial resection	60/270 (22%)	9/44 (20%)	51/237 (22%)	
Gross total resection	68/270 (25%)	8/44 (18%)	60/237 (25%)	
Initial treatment:				
Chemotherapy alone	67/258 (26%)	14/38 (37%)	53/220 (24%)	
Concomitant or sequential RT-CHT	147/258 (57%)	18/38 (47%)	129/220 (59%)	**<0.001**
Radiotherapy alone	39/258 (15%)	1/38 (3%)	38/220 (17%)	
Surveillance	5/258 (2%)	5/38 (13%)	0/220 (0%)	
Molecular profile				
TERT promoter mutation	176/274 (64%)	23/45 (51%)	151/230 (66%)	**0.0092**
EGFR amplification	77/275 (28%)	4/43 (9%)	73/235 (31%)	**0.00088**
+7	102/206 (50%)	10/37 (27%)	91/173 (53%)	**0.0062**
-10	119/259 (46%)	10/41 (24%)	111/222 (50%)	**0.0010**
combined +7/-10	85/236 (36%)	7/41 (17%)	77/199 (39%)	**0.018**
9p loss	59/260 (23%)	3/42 (7%)	57/222 (26%)	**0.0082**
CDKN2A deletion	76/274 (27%)	5/43 (12%)	72/235 (31%)	**0.0033**
TP53 mutation	22/123 (18%)	0/22 (0%)	22/104 (21%)	**<0.0001**
Median OS, months	21.9	59.1	19.1	**< 0.0001**

Median preoperative KPS was 80 (vs. 90, p=0.0025). Surgery commonly consisted of biopsy (115/237, 49%) (p=0.31). Initial treatment was represented by concomitant or sequential radio-chemotherapy (129/220, 59%) or, less frequently, by chemotherapy (53/220, 24%) or radiotherapy (38/220, 17%) alone (p<0.001). Compared to *IDH*wt grade II, *IDH*wt grade III gliomas had a higher prevalence of *TERT* promoter mutations (151/230 (66%) vs. 23/45 (51%), p=0.0092), *EGFR* amplifications (73/235 (31%) vs. 4/43 (9%), p=0.00088), whole chromosome 7 gain (91/173 (53%) vs. 10/37 (27%), p=0.0062), whole chromosome 10 loss (111/222 (50%) vs. 10/41 (24%), p=0.0010), chromosome 9p loss (57/222 (26%) vs. 3/42 (7%), p=0.0082), *CDKN2A* deletions (72/235 (31%) vs. 5/43 (12%), p=0.0033), and *TP53* mutations (22/104 (21%) vs. 0/22 (0%), p<0.0001).
The median OS for *IDH*wt grade III gliomas was 19 months (vs. 59 months for *IDH*wt grade II gliomas, p<0.0001) (Figure 31, panel B). Younger age at diagnosis (p=0.0019) and higher preoperative KPS (p=0.0030) were associated with prolonged OS. *EGFR* amplification (median OS: 22 vs. 16 months, p=0.04) and whole chromosome 10 loss (median OS: 23 vs. 18 months, p=0.03) were associated with poorer OS, and a similar trend was observed for *TERT* promoter mutation (median OS: 22 vs. 17 months, p=0.05) and *CDKN2A* deletion (median OS: 20 vs. 16 months, p=0.05). Association matrix showed that whole chromosome 10 loss associated with whole chromosome 7 gain (p<0.001), *EGFR* amplifications (p<0.01), chromosome 9p loss (p<0.001) and *CDKN2A* deletions (p<0.01). *TERT* promoter mutations associated with whole chromosome 7 gain (p<0.001), *EGFR* amplifications (p=0.04), and older age at diagnosis (p=0.02).

***IDH*wt grade II and III gliomas meeting cIMPACT-NOW criteria for "Diffuse astrocytic glioma, *IDH*-wildtype, with molecular features of glioblastoma (grade IV)".** Twenty-nine patients in the group of *IDH*wt grade II gliomas (29/43, 67%) and 166 patients in the group of *IDH*wt grade III gliomas (166/224, 74%) met cIMPACT-NOW criteria for the definition of "diffuse astrocytic glioma, *IDH*-wildtype, with molecular features of glioblastoma (WHO grade IV)" (Brat *et al.*, 2018).
Patients with *IDH*wt grade II gliomas and molecular features of GBM were older (median age at diagnosis: 58.6 vs. 34.5, p=0.00057) and more frequently had fronto-temporo-insular tumors (19/29 (66%) vs. 5/14 (36%), p=0.0055) compared to patients with *IDH*wt grade II gliomas lacking defining molecular alterations (Table 10). Extent of resection (p=0.88) and treatment schemes (p=0.74) did not substantially differ between the two groups, as most patients had been treated before the publication of cIMPACT criteria. The median OS in patients with *IDH*wt grade II gliomas and molecular features of glioblastoma was 42 months (vs. 57 months in patients with *IDH*wt grade II gliomas lacking defining features, p=0.2). Neither age (p=0.31) nor molecular features of GBM (p=0.17) were associated with survival on Cox model.
Patients with *IDH*wt grade III gliomas and molecular features of GBM were older (median age at diagnosis: 58.8 vs. 43.9 years-old, p<0.0001) and more frequently received biopsy (80/149 (54%) vs. 19/47 (40%), p=0.063) compared to patients with *IDH*wt grade III gliomas lacking defining molecular alterations. The median OS patients with *IDH*wt grade III gliomas and molecular features of glioblastoma was 17 months (vs. 23 months for *IDH*wt grade III gliomas lacking defining features, p=0.07) (Figure 31, panel C). Age (p=0.0019), but not molecular features of GBM (p=0.058), was associated with survival on Cox model.

Figure 31. Survival curves. Panel A: survival curves for *IDH*mut 1p/19q codeleted (black line) vs. *IDH*mut 1p/19q non-codeleted (dark grey line) vs. *IDH*wt (light grey line) grade II gliomas (median OS: 176 vs. 101 vs. 59 months, p<0.0001). Panel B: survival curves for *IDH*wt grade II (grey line) vs. *IDH*wt grade III (black line) gliomas (median OS: 59 vs. 19 months, p<0.0001). Panel C: survival curves for patients with *IDH*wt grade III gliomas meeting (black line) and not meeting (grey line) the cIMPACT definition for molecular glioblastoma (median OS: 17 vs. 23 months, p=0.07). Panel D: survival curves for patients with *IDH*wt grade II (grey line) and *IDH*wt grade III (black line) gliomas meeting the cIMPACT definition of molecular glioblastoma (median OS: 42 vs. 17 months, p<0.0001). Panel E: survival curves for patients with *IDH*wt grade II (grey line) and grade III (black line) gliomas meeting the cIMPACT definition for molecular glioblastoma because of isolated *TERT* promoter mutations (median OS: 88 vs. 22 months, p=0.002). Panel F: survival curves for patients with *IDH*wt grade II (grey line) and grade III (black line) meeting the cIMPACT definition for molecular glioblastoma because of *EGFR* amplifications and/or the +7/-10 signature (median OS: 37 vs. 18 months, p=0.02).

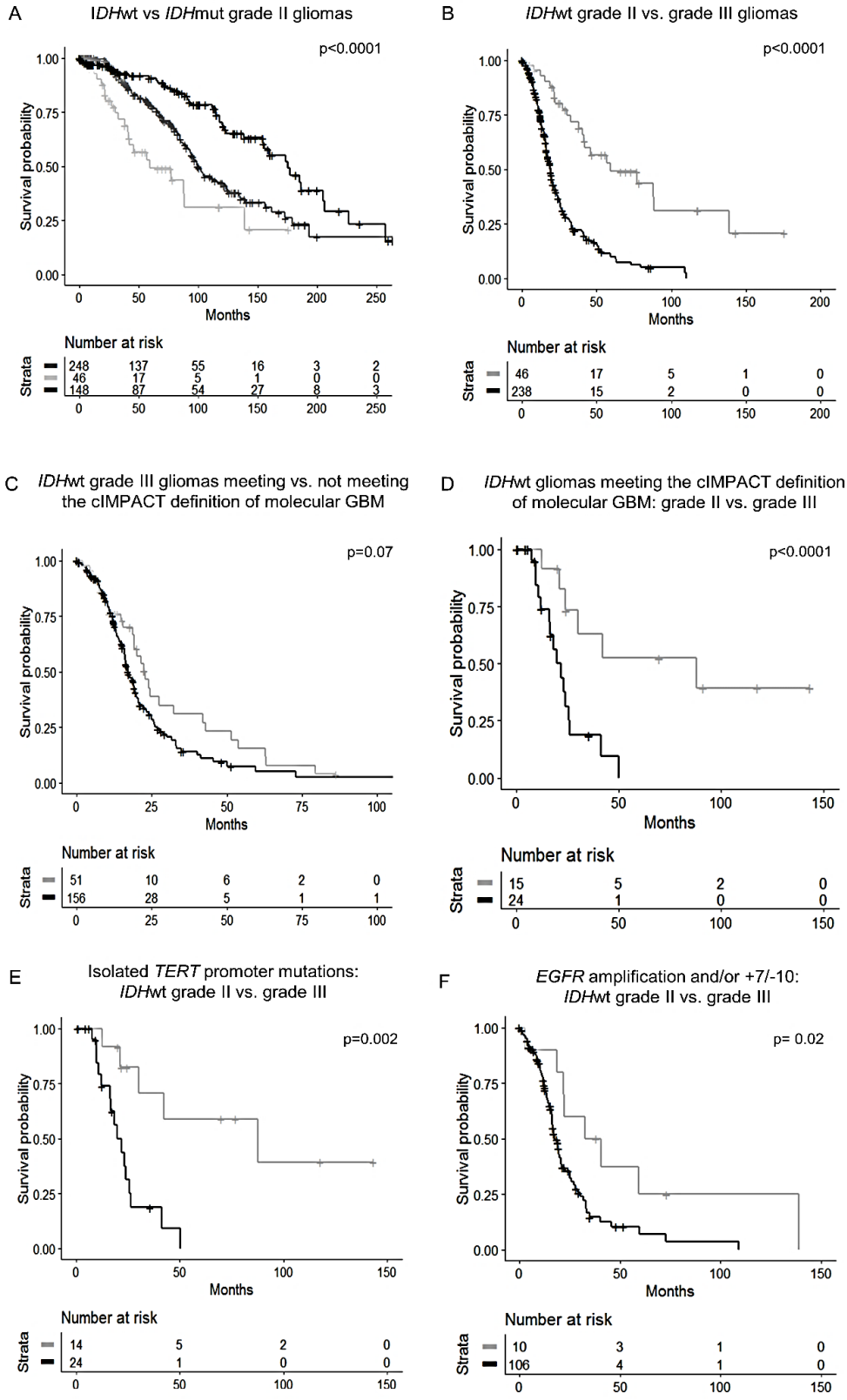

Therefore, despite meeting the same definition, *IDH*wt grade II and *IDH*wt grade III gliomas meeting the criteria for molecular GBM clearly had different OS (42 vs. 17 months, p<0.0001) (Figure 31, panel D). Table 12 compares clinical and molecular features in the two groups.

Table 12. Comparison between *IDH*wt grade II (n=29) and *IDH*wt grade III (n=166) gliomas meeting the cIMPACT-NOW criteria for molecular GBM. +7 = whole chromosome 7 gain; -10 = whole chromosome 10 loss; RT-CHT = radiochemotherapy.

	***IDH*wt grade II and III gliomas meeting the definition of molecular GBM (n=195)**	***IDH*wt grade II gliomas meeting the definition of molecular GBM (n=29)**	***IDH*wt grade III gliomas meeting the definition of molecular GBM (n=166)**	**p-value***
Age, median (range)	58.7 (20.8-83.0)	58.6 (20.8-82.1)	58.8 (22.2-83.0)	0.86
Male gender	124/195 (64%)	24/29 (83%)	100/166 (60%)	**0.022**
Preoperative KPS, median (range)	90 (60-100)	90 (70-100)	80 (60-100)	**0.026**
Extent of resection:				
Biopsy	99/177 (56%)	19/28 (68%)	80/149 (54%)	0.33
Partial resection	31/177 (18%)	5/28 (18%)	26/149 (17%)	
Gross total resection	47/177 (27%)	4/28 (14%)	43/149 (29%)	
Treatment:				
Chemotherapy alone	41/169 (24%)	10/25 (40%)	30/144 (21%)	
Concomitant or sequential RT-CHT	98/169 (58%)	12/25 (48%)	87/144 (60%)	**<0.0001**
Radiotherapy alone	27/169 (16%)	0/25 (0%)	27/144 (19%)	
Surveillance	3/169 (2%)	3/25 (12%)	0/144 (0%)	
Molecular profile:				
TERT promoter mutation	171/187 (91%)	23/28 (82%)	148/159 (93%)	0.12
EGFR amplification	77/180 (43%)	4/26 (15%)	73/155 (47%)	**0.0037**
+7	96/141 (68%)	10/26 (38%)	86/116 (74%)	**0.00089**
-10	114/170 (67%)	10/26 (36%)	105/145 (72%)	**0.00045**
combined +7/-10	83/151 (55%)	7/26 (27%)	76/126 (60%)	**0.00194**
9p loss	47/170 (28%)	3/26 (12%)	44/145 (30%)	0.057
Number of c-IMPACT criteria met:				
one	52/154 (34%)	20/26 (77%)	33/129 (26%)	**<0.0001**
two or three	102/154 (66%)	6/26 (23%)	96/129 (74%)	
Reason for meeting c-IMPACT criteria:				
TERT promoter mutation without *EGFR* amplification or +7/-10	43/156 (28%)	16/26 (62%)	28/131 (21%)	**<0.0001**
EGFR amplification and/or +7/-10 without *TERT* promoter mutation	15/156 (10%)	5/26 (19%)	10/131 (8%)	
TERT promoter mutation plus *EGFR* amplification and/or +7/-10	98/156 (63%)	5/26 (19%)	93/131 (71%)	
Median OS, months	19.2	42.2	17.2	**<0.0001**

Most patients in the group of *IDH*wt grade II gliomas met the definition of molecular GBM because of a single criterion, which was often represented by isolated *TERT* promoter mutations (16/26, 62%). Conversely, patients with *IDH*wt grade III gliomas generally met the definition of molecular GBM because of multiple criteria as, besides *TERT* promoter mutations, most of them had additional defining alterations such as *EGFR* amplifications or the +7/-10 signature (93/131, 71%).

We then evaluated the ability of the different cIMPACT criteria to capture tumor malignant behavior. Isolated *TERT* promoter mutations, without *EGFR* amplifications or the +7/-10 signature, were associated with a median OS of 88 months in *IDH*wt grade II and 22 months in *IDH*wt grade III gliomas (p=0.002) (Figure 31, panel E). Conversely, the presence of *EGFR* amplifications and/or of the +7/-10 signature, regardless of the presence of *TERT* promoter mutations, was associated with a median OS of 37 months in *IDH*wt grade II and of 18 months in *IDH*wt grade III gliomas (p=0.02) (Figure 31, panel F).

Discussion

From a large cohort of 1360 "lower grade" (i.e., grade II and III) gliomas, we extracted 101 *IDH*wt grade II gliomas, whose radiological, molecular, and histological features we thoroughly revised to guarantee a rigorous patient selection. We ensured to exclude *IDH1*-mutant gliomas falsely negative on Sanger sequencing because of contamination with normal tissue, peripheral samples of high grade *IDH*wt gliomas, and H3K27M-mutant midline gliomas. The analyses were then restricted to 47 patients who had a confirmed diagnosis of "diffuse astrocytoma, *IDH*-wildtype (grade II)" following centralized histological review, which was independently conducted by two expert neuropathologists through comprehensive morphological and immunohistochemical studies.

Representing less than 15% of low grade diffuse gliomas (Suzuki *et al.*, 2015) (Wijnenga *et al.*, 2017) (Hasselblatt *et al.*, 2018), *IDH*wt grade II gliomas are uncommon, especially in women, and are associated with older age at diagnosis, fronto-temporo-insular location and a highly invasive behavior (Metellus *et al.*, 2010), with frequent infiltration of adjacent cortex and deep grey matter (Izquierdo *et al.*, 2019). This highly infiltrative pattern accounts for the prevalence of biopsy over resection and the scarce tissue availability for translational studies. With no *TP53* mutations, and, as expected (Labussière *et al.*, 2010), no 1p19q codeletions, our *IDH*wt grade II gliomas correspond to the previously defined "triple negative" grade II gliomas (Metellus *et al.*, 2010): usually large and highly infiltrative fronto-temporal-insular tumors, which could be merely defined as *IDH*wt grade II diffuse gliomas.

Compared to *IDH*wt grade III gliomas, *IDH*wt grade II gliomas had a lower burden of molecular alterations, including *TERT* promoter mutations (51% vs 66%), *EGFR* amplifications (9% vs 31%), whole chromosome 7 gain (27% vs 53%), whole chromosome 10 loss (24% vs. 50%), chromosome 9p loss (7% vs 26%), and *CDKN2A* deletions (12% vs 31%). Their median OS was 59 months that, while much shorter than *IDH*mut grade II gliomas, was three times the median OS of *IDH*wt grade III tumors (19 months, p<0.0001). These

findings are in line with previous reports showing that, in lower grade gliomas, mitotic index has a heavier prognostic impact in *IDH*wt than in *IDH*mut gliomas (Suzuki *et al.*, 2015) (Olar *et al.*, 2015). Proliferative activity represents the main criterion to distinguish grade II and III gliomas, albeit the 2016 WHO classification does not provide clear thresholds for the evaluation of mitotic count. The use of different thresholds for grading assessment margin could explain the inconsistent results obtained in different studies on prognosis and molecular profile of *IDH*wt grade II and III gliomas and, in our view, represents an urgent issue to address in the forthcoming WHO classification. The grading criteria used here have been widely used in the past and have been adopted by the cIMPACT to separate grade II and III *IDH*mut diffuse astrocytomas (Brat *et al.*, 2020): in the same way, they allow here a prognostic stratification of *IDH*wt gliomas, suggesting that the same mitotic threshold is associated with different outcome in both *IDH*mut and *IDH*wt gliomas.

Out of the tumors meeting the cIMPACT-NOW definition of "Diffuse astrocytic glioma, *IDH*-wildtype, with molecular features of glioblastoma, WHO grade IV" (Brat *et al.*, 2018), only grade III had a survival similar to *IDH*wt glioblastomas, while grade II had a survival almost three times longer. In fact, more than half of the patients with *IDH*wt grade II gliomas in our series met cIMPACT-NOW criteria because of isolated *TERT* promoter mutations and this was not predictive of poor outcome. Indeed, *TERT* promoter mutations are detected in *IDH*mut 1p/19q codeleted diffuse gliomas a well as in several other primary brain tumors and are associated with different prognostic significance depending on the *IDH* status and tumor histology (Labussière *et al.*, 2014b) (Stichel *et al.*, 2018). These considerations suggest some caution when assimilating *IDH*wt grade II gliomas to molecular glioblastomas, especially if the sole criterion met is that of an isolated *TERT* promoter mutation.

The uncertainties on the malignant behavior of *IDH*wt grade II gliomas and their rarity have hampered to establish a standard of treatment for these tumors. As clinical trials conducted in low grade gliomas failed to indicate a clear treatment strategy for this population (Buckner *et al.*, 2016) (Baumert *et al.*, 2016) (Bell *et al.*, 2020), the guidelines of the European Association of Neuro-Oncology leave an ample margin of discretion on the choice of individual treatment schemes, suggesting that it should rely on age, KPS, and *MGMT* promoter methylation status (Weller *et al.*, 2017) that are recognized prognostic indicators in *IDH*wt diffuse gliomas. The absence of clinical standard advocates a careful multidisciplinary approach based on close clinical surveillance and case-by-case decisions.

Importantly, we found an actionable target in seven patients (24%), including one *BRAF* V600 mutation, one activating *FGFR1* mutation, and five *FGFR*3 fusions. *FGFR3-TACC3* fusions have been reported in only 3% of *IDH*wt grade II-IV gliomas but they are of high interest for clinicians as they can be targeted by specific inhibitors (Di Stefano *et al.*, 2015). Moreover, *FGFR3-TACC3* fusions characterize a subgroup of *IDH*wt gliomas with a specific molecular and metabolic profile (Di Stefano *et al.*, 2020) (Frattini *et al.*, 2018). While grade II *IDH*wt represent less than 10% of *IDH*wt gliomas, we found here an over-representation of *FGFR3* fusions compared to what is expected for the whole population of *IDH*wt gliomas, with four *FGFR3-TACC* fusions and one *FGFR3-MYH14* fusion out of 29 patients tested (17%; $p<0.01$). The systematic screening for fusion genes is therefore of special interest to better classify this population and provide therapeutic targets.

In conclusion, our results highlight the importance of grading for the whole group of *IDH*wt gliomas, and the subgroup with molecular features of glioblastoma, and warns on the importance of integrating molecular features and histology for diagnostic, prognostic, and theranostic purposes.

Published in Neuro Oncol. 2020 Nov 11:noaa258 (Epub ahead of print)

Predictors of response to targeted therapy in *BRAF* V600-mutant gliomas

Background

BRAF, an oncogene encoding for a member of the RAF serine/threonine protein kinase family, has been reported in several human cancers. *BRAF* V600E mutations are especially frequent in melanoma and non-small cell lung cancer and can be effectively targeted by RAF inhibitors (RAFi) (Chapman *et al.*, 2011) (Hyman *et al.*, 2015). MEK inhibitors (MEKi), agents that inhibit the downstream signal associated with BRAF activation, are often used in association to RAFi to impede, or at least delay, the development of resistance and prolong the efficacy of RAFi (Johnson *et al.*, 2015). To date, there are three combinations of RAFi and MEKi approved by the European Medicines Agency for the treatment of patients with advanced *BRAF* V600-mutant melanoma: vemurafenib-cobimetinib, dabrafenib-trametinib, and encorafenib-binimetinib, all of which have shown to provide substantial benefits in terms of overall survival compared to conventional treatments.

The *BRAF* V600E mutation is uncommon in primary brain tumors, being primarily detected in gangliogliomas, pleomorphic astrocytomas, and pilocytic astrocytomas, and only rarely in high-grade diffuse gliomas (Schreck, Grossman and Pratilas, 2019). Despite its rarity, the accurate detection of *BRAF* V600 mutations is of capital importance, as it can provide a viable treatment option for these rare tumors that mostly affect children and young adults and show limited response to cytotoxic treatments. As RAFi/MEKi are not yet approved for this indication, current evidence on their efficacy in glioma patients is limited to individual cases or small cohorts of patients treated within basket trials (Hyman *et al.*, 2015) (Kaley *et al.*, 2018) (Wen, Alexander, *et al.*, 2018) (Wen, De Greve, *et al.*, 2018). As a result, several issues remain unsolved with regard to patient selection, the need to associate MEKi, and the efficacy of rechallenge at recurrence. The aim of this study was to analyze a large cohort of adult patients treated with RAFi/MEKi because of *BRAF* V600-mutant recurrent or disseminated gliomas, in order to assess response rates in a real-life setting and identify predictors of response.

Patients and methods

We performed a retrospective research in the institutional databases of six neuro-oncology departments in France (Foch Hospital, Suresnes; Pitié-Salpetrière Hospital, Paris; Insitut Gustave Roussy, Villejuif; Hopital Neurologique Pierre Wertheimer, Bron) and Italy (Istituto Neurologico Besta, Milano; Ospedale Universitario, Pisa) for adult patients with recurrent or disseminated *BRAF* V600-mutant gliomas treated with RAFi/MEKi (February 2012 - January 2020), including two patients whose cases had been previously published as case reports (Touat *et al.*, 2018) (Pasqualetti *et al.*, 2019).

Histological diagnoses were locally reviewed by expert neuropathologists. The *BRAF* V600 status was obtained by standard PCR amplification followed by Sanger sequencing or by NGS. Clinical data and MRI scans were collected from referring centers and centrally reviewed. As all tumors displayed contrast enhancement at the time of treatment with RAFi/MEKi, tumor response was assessed using the criteria of the Response Assessment in Neuro-Oncology (RANO) working group for high grade gliomas (Wen *et al.*, 2010). Percentage variations in tumor burden in individual patients were calculated comparing the sum of the products of maximal cross-sectional diameters of enhancing lesions at baseline and at best RANO response. Treatment schemes followed in all cases the recommendations of the European Medicines Agency for *BRAF* V600-mutant melanoma (Table 13).

Table 13. Posology and route of administration of vemurafenib, dabrafenib, cobimetinib and trametinib, as approved by the European Medicines Agency for the treatment of metastatic or unresectable *BRAF* V600-mutant melanoma.

Drug	Posology	Route of administration
Vemurafenib (Zelboraf®)	960 mg twice daily	oral
Dabrafenib (Tafinlar®)	150 mg twice daily	oral
Cobimetinib (Cotellic®)	60 mg once daily for 21 consecutive days followed by a 7-day break	oral
Trametinib (Mekinst®)	2 mg once daily	oral

Treatment was continued until progression or unacceptable toxicity. Treatment-related adverse events were recorded using the Common Terminology Criteria for Adverse Events, version 5.0.

Statistical analyses were performed using the "R" software and related packages. Categorical variables were compared using the Fisher's exact test. Quantitative variables were compared using the Mann-Whitney (two groups) or the Kruskal-Wallis (three groups) tests. PFS was defined as the time interval between the start of RAFi/MEKi and tumor progression (or last follow-up in censored patients). OS was defined as the time interval between the start of RAFi/MEKi and death (or last-follow-up in censored patients). PFS and OS were estimated using the Kaplan-Meier method, and survival curves were compared using the log-rank test. The established threshold for statistical significance was p=0.05. The Cox model was used for continuous variables survival analyses. Ethical approval was obtained from the institutional review board of the leading center (Foch Hospital, Suresnes, France).

Results

Twenty-eight adults with supratentorial *BRAF*-mutant gliomas were included in the study [gangliogliomas (9/28, 32%) (1 low-grade, 8 high-grade), pleomorphic xanthoastrocytomas (PXA) (9/28, 28%) (3 low-grade, 6 high-grade), diffuse gliomas (10/28, 36%) (8 *IDH*-wildtype glioblastomas, 1 *IDH*-mutant glioblastoma, 1 *IDH*-

wildtype anaplastic astrocytoma)]. RAFi/MEKi were administered as first-line treatment in two patients with disseminated tumors and in the setting of recurrence in the remaining 26 patients. Nine patients were treated within clinical trials (NCT01524978 and NCT02034110), and 19 were treated off-label as part of expanded access programs. Thirteen patients received RAFi as single agents (13/28, 46%) (vemurafenib, n=11; dabrafenib, n=2) and 15 a combination of RAFi and MEKi (15/28, 54%) (vemurafenib+cobimetinib, n=5; dabrafenib+trametinib, n=10). Eleven patients experienced treatment-related adverse events (11/28, 39%), of grade 1-2 (10/28, 36%) (rash, arthralgia, nausea/diarrhea, increased lymphocyte count, thrombocytopenia) or grade 3 (1/28, 4%) (increased aminotransferases) maximum severity. The incidence of adverse events did not significantly differ among treatment groups (6/13 (46%) patients receiving RAFi alone vs. 5/15 (33%) patients receiving RAFi plus MEKi, p=0.60). Individual changes in tumor burden, depending on histology and timeliness of RAFi/MEKi administration, are reported in Figure 32 (panel A and B).

Figure 32. Individual changes in tumor burden at best RANO response (panel A, B); PFS (panel C) and OS (panel D) based on best RANO response. Panel A: waterfall plot illustrating individual changes in tumor burden based on histology; gangliogliomas (light blue), pleomorphic xanthoastrocytomas (PXA) (yellow), diffuse gliomas (grey). Panel B: waterfall plot illustrating individual changes in tumor burden based on the timing of RAF/MEK administration: first/second line of treatment (dark orange), third/fourth line of treatment (pink). Panel C: PFS in patients achieving CR/PR (red line) vs. patients achieving SD (blue line) vs. patients experiencing PD (green line) (18 vs. 9 vs. 2 months, p<0.0001). Panel D: OS in patients achieving CR/PR (red line) vs. patients achieving SD (blue line) vs. patients experiencing PD (green line) (not reached vs. 24 vs. 5 months, p<0.0001).
CR/PR=complete/partial response; SD=stable disease; PD=progressive disease; PXA=pleomorphic xanthoastrocytomas.

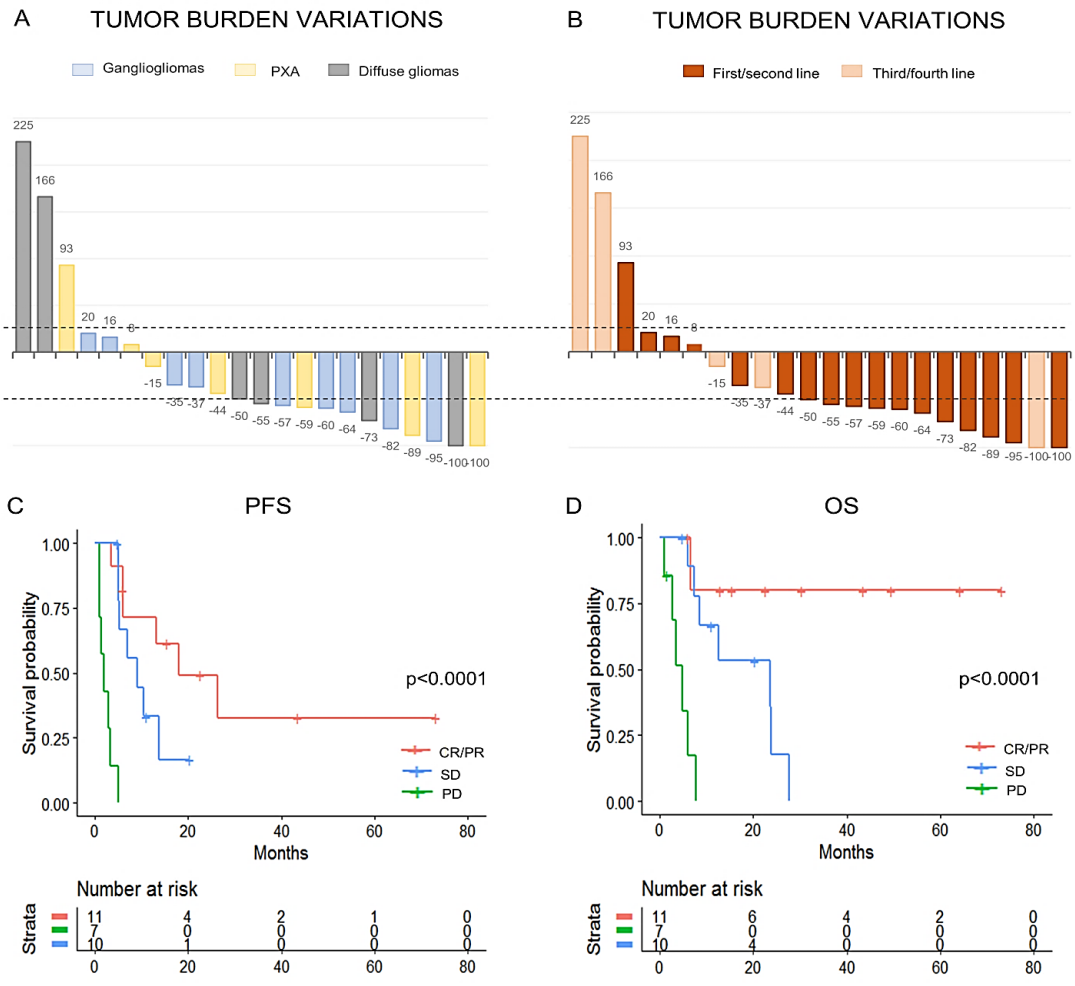

Eleven patients showed a partial (PR) or complete (CR) response (11/28, 39%), ten patients achieved a condition of stable disease (SD) (10/28, 36%), and seven experienced progressive disease (PD) (7/28, 25%) (Table 14).

Table 14. Clinical features in the whole cohort and in the three subgroups identified by best RANO response. CR/PR=complete/partial response, NR=not reached, PD=progressive disease, PXA=pleomorphic xanthoastrocytoma, RAFi/MEKi= RAF/MEK inhibitors, SD=stable disease.

	whole cohort (n=28)	**CR/PR (n=11)**	**SD (n=10)**	**PD (n=7)**	**p**
Age at treatment, median (range)	36 (18-67)	32 (18-56)	40 (21-67)	37 (29-63)	0.16
Male gender	10/28 (36%)	4/11 (36%)	3/10 (30%)	3/7 (43%)	0.89
Multifocal/disseminated:	9/28 (32%)	3/11 (27%)	3/10 (30%)	3/7 (43%)	
• at diagnosis:					
- PXA, grade II	1/28 (4%)	1/11 (9%)	0/10 (0%)	0/7 (0%)	
- Ganglioglioma, grade III	1/28 (4%)	0/11 (0%)	1/10 (10%)	0/7 (0%)	
• at recurrence:					
- Glioblastoma, grade IV	4/28 (14%)	2/11 (18%)	0/10 (0%)	2/7 (29%)	
- Anaplastic astrocytoma, grade III	1/28 (4%)	0/11 (0%)	0/10 (0%)	1/7 (14%)	
- PXA, grade II	2/28 (7%)	0/11 (0%)	2/10 (20%)	0/7 (0%)	
Locally recurrent:	19/28 (68%)	8/11 (73%)	7/10 (70%)	4/7 (57%)	
- Glioblastoma, grade IV	5/28 (18%)	1/11 (9%)	2/10 (20%)	2/7 (29%)	
- PXA, grade III	6/28 (21%)	2/11 (18%)	3/10 (30%)	1/7 (14%)	
- Ganglioglioma, grade III	7/28 (25%)	5/11 (45%)	1/10 (10%)	1/7 (14%)	
- Ganglioglioma, grade I	1/28 (4%)	0/11 (0%)	1/10 (10%)	0/7 (0%)	
Extent of resection:					
- biopsy	4/28 (14%)	0/11 (0%)	2/10 (20%)	2/7 (29%)	0.25
- partial resection	13/28 (46%)	6/11 (55%)	3/10 (30%)	4/7 (57%)	
- complete resection	11/28 (39%)	5/11 (45%)	5/10 (50%)	1/7 (14%)	
Previous radiotherapy	26/28 (93%)	10/11 (91%)	9/10 (90%)	7/7 (100%)	1
Previous chemotherapy	17/28 (61%)	7/11 (64%)	5/10 (50%)	5/7 (71%)	0.70
Timing of administration of RAFi/MEKi:					
- first-line treatment	2/28 (7%)	1/11 (9%)	1/10 (10%)	0/7 (0%)	
- second-line treatment	18/28 (64%)	9/11 (82%)	5/10 (50%)	4/7 (57%)	0.35
- third- or fourth-line treatment	8/28 (29%)	1/11 (9%)	4/10 (40%)	3/7 (43%)	
RAFi/MEKi administered:					
- vemurafenib alone	11/28 (39%)	6/11 (55%)	3/10 (30%)	2/7 (29%)	
- vemurafenib+cobimetinib	5/28 (18%)	1/11 (9%)	2/10 (20%)	2/7 (29%)	0.68
- dabrafenib alone	2/28 (7%)	1/11 (9%)	0/10 (0%)	1/7 (14%)	
- dabrafenib+trametinib	10/28 (54%)	3/11 (27%)	5/10 (50%)	2/7 (29%)	
KPS at RAFi/MEKi initiation, median (range)	80 (60-100)	80 (60-100)	70 (60-80)	80 (60-90)	**0.037**
KPS at best RANO response, median (range)	80 (40-100)	90 (60-100)	80 (60-90)	60 (40-80)	**<0.01**
Percentage variation in tumor burden, median	-53%	-78%	-25%	+55%	**<0.001**
Median PFS, months (95% CI)	7 (5-26)	18 (6-NR)	9 (5-NR)	2 (1-NR)	**<0.0001**
Survival proportion at 24 months	39%	80%	18%	0%	**<0.0001**

Patients with PR/CR experienced a median reduction of -78% in their tumor burden (e.g., Figure 33, panel A-D) and an increase of +10 points in their median KPS. Patients achieving a condition of SD experienced a median decrease of -25% in their tumor burden (e.g., Figure 33, panel E-H) and an increase of +10 points in their median KPS. Patients experiencing PD rapidly deteriorated under treatment (+55% in tumor burden and -20 points in median KPS).

Figure 33. Imaging findings before and after treatment with RAFi/MEKi. Panel A-D: Axial T1-weighted MRI after gadolinium injection (panel A,C) and ^{18}F-DOPA PET images (panel B,D), acquired before (panel A, B) and after (panel C, D) treatment show a remarkable reduction of the nodule of contrast enhancement compared to baseline, accompanied by a parallel reduction of tumor hypermetabolism (SUV max 1.7 vs. 3.8) in a patient with a left temporal anaplastic ganglioglioma displaying a PR to vemurafenib. Panel E-H: T1-weighted images after gadolinium injection of cervical (panel E,F) and lumbar (panel G,H) spine acquired before (panel E,G) and after (panel F,H) treatment with vemurafenib+cobimetinib show a dramatic reduction of the enhancement of meninges and cauda equina nerve roots in a patient with extensive meningeal dissemination from a supratentorial anaplastic ganglioglioma meeting RANO criteria for SD. Panel I-N: Axial T1-weighted MRI after gadolinium injection illustrating the response to the first (panel I,J), second (panel K,L) and third (panel M,N) line of RAFi/MEKi in a patient with right parietal anaplastic ganglioglioma. Panel I-J: MRI before (panel I) and after (panel J) initial treatment vemurafenib, resulting in a prolonged PR (13 months). Panel K,L: MRI before (panel K) and after (panel L) rechallenge with vemurafenib+cobimetinib, resulting in a sustained CR (17 months). Panel M,N: MRI before (panel M) and after (panel N) a novel rechallenge with dabrafenib+trametinib, resulting in a sustained PR (24 months). The images referring to the first two lines of RAFi/MEKi have been previously published (Touat *et al*., 2018).

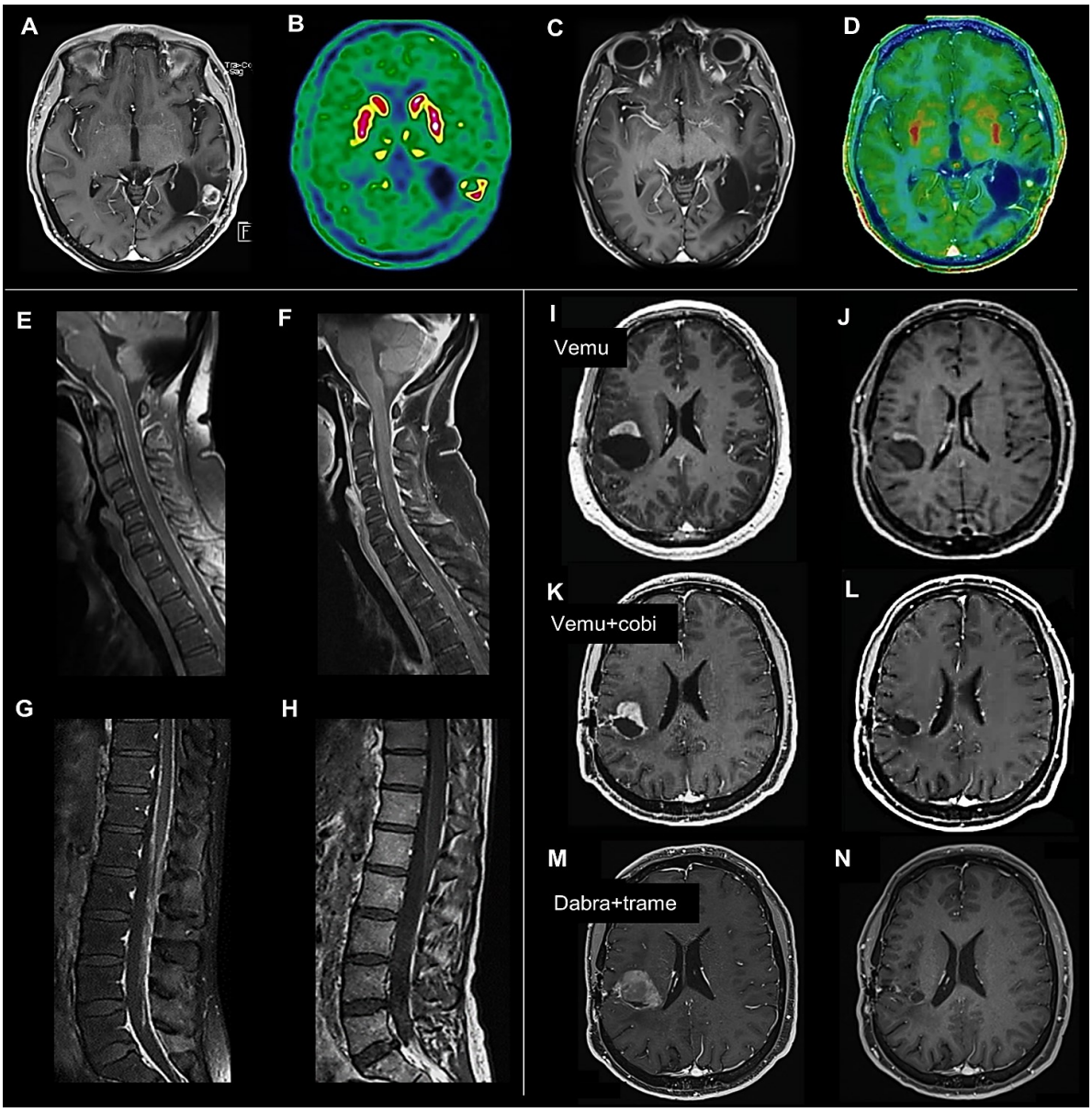

The median PFS in "responders" (PR/CR) was 18 months (vs. 9 months in patients with SD and 2 months in patients with PD, p<0.0001) (Figure 32, panel C). Responders had higher KPS (median: 80 vs. 70 points, p=0.018), tended to be younger (median age: 32 vs. 38 years-old, p=0.061) and to be treated at an earlier disease stage (administration as first or second-line treatment: 10/11 (91%) vs. 10/17 (59%), p=0.099) compared to "non-responders" (SD/PD). Responders experienced a substantially longer median PFS on RAF/MEKi than achieved with previous standard treatments (i.e., radiotherapy ± concomitant chemotherapy) (18 vs. 7 months, p=0.013) (Figure 34, panel A). We observed no statistically significant differences in response rates based on histology (3/10 (30%) for diffuse gliomas vs. 3/9 (33%) for PXA vs. 5/9 (56%) for gangliogliomas, p=0.62) or based on receiving a combination of RAFi and MEKi compared to RAFi alone (4/15 (27%) vs. 7/13 (54%), p=0.25).

Figure 34. PFS on RAFi/MEKi compared to the PFS previously achieved with standard treatment. Panel A: PFS in patients achieving CR/PR: PFS on RAF/MEKi (PFS2, blue line) vs. PFS on the previous line of treatment (PFS1, red line) (18 vs. 7 months, p=0.013). Panel B: PFS in patients achieving SD: PFS on RAF/MEKi (PFS2, blue line) vs. PFS on the previous line of treatment (PFS1, red line) (11 vs. 10 months, p=0.73). Panel C: PFS in patients experiencing PD: PFS on RAF/MEKi (PFS2, blue line) vs. PFS on the previous line of treatment (PFS1, red line) (2 vs. 7 months, p=0.0013).

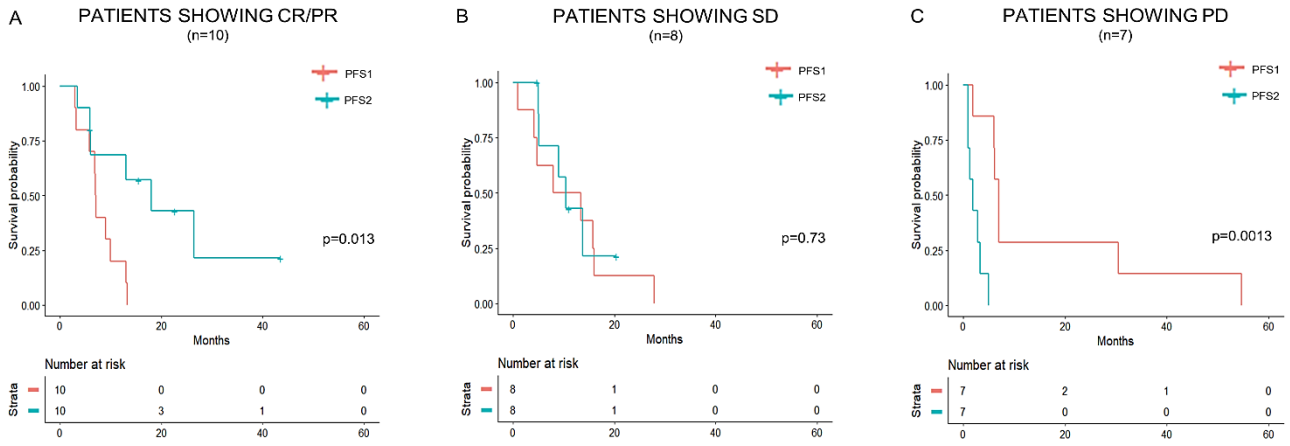

Five patients with tumors recurring after PR (n=4) or SD (n=1) were rechallenged with RAFi/MEKi, with a long-lasting CR/PR in two, a condition of SD in one, and of PD in two. One of the patients who had responded to vemurafenib+cobimetinib at rechallenge (Touat *et al.*, 2018) was further rechallenged with dabrafenib+trametinib at progression, with a novel long-lasting PR (Figure 33, panel I-N).

Responders experienced longer OS compared to patients with SD or PD (survival proportion at 24 months: 80% vs. 18% vs. 0%), the curve reaching a stable plateau at 80% survival rate (Figure 32, panel D). In univariate and multivariate analysis, only response to RAFi/MEKi was an independent predictor of OS (hazard ratio=0.15; 95% confidence interval=0.03-0.67, p=0.013).

Discussion

Here we analyzed a large series of adult patients receiving RAFi/MEKi for the treatment of recurrent or disseminated *BRAF* V600-mutant gliomas. Thirty-nine percent of patients were responders, consistently with other reports on high- and low-grade gliomas in adults (Kaley *et al.*, 2018) (Wen, Alexander, *et al.*, 2018) (Wen, De Greve, *et al.*, 2018). Tumor responses were associated with a substantial reduction in tumor burden, significant functional improvement, and prolonged PFS. Response to RAFi/MEKi emerged as an independent predictor of overall survival, suggesting that targeted treatment might help responders to achieve long-term survival. Predictors of response to RAFi/MEKi included better KPS, younger age, and earlier treatment administration. Responders exhibited longer PFS on RAFi/MEKi than achieved with standard cytotoxic therapies, suggesting that, in selected patients, it might be legit to discuss targeted therapy as upfront treatment. Besides gangliogliomas and PXA, responses were observed in 3 out of 9 (33%) patients with GBM. The overall response rate observed in *BRAF*-mutant GBM in our series was remarkable compared to what reported with other second-line agents or targeted approaches (Liu *et al.*, 2020). Although the estimated prevalence of *BRAF* V600 mutations in GBM is low (around 2%) (www.cbioportal.org), given its therapeutic implications, the systematic screening for *BRAF* mutations should be highly encouraged.

Based on the substantial benefit obtained with the first course of treatment, some patients were rechallenged with RAFi/MEKi at progression. Rechallenge was associated with novel prolonged tumor responses in over one third of cases, suggesting that a substantial proportion of patients retain a long-lasting sensitivity to targeted therapy and could be successfully re-treated.

The prolonged tumor responses observed in responders during initial treatment and at rechallenge, together with the remarkable survival rates observed in this population, suggest that targeted therapy might have a "disease-modifying" effect in these patients, slowing down glioma lethal course.

In conclusion, our study confirms the interest of targeted therapy for the management of *BRAF*-mutant adult gliomas in a real-world setting and highlights the importance of systematically screening for this rare but actionable molecular alteration. Deep histo-molecular studies should be encouraged to improve our ability to identify patients who would possibly benefit from the front-line administration of RAFi/MEKi.

Manuscript submitted

References

3C Study Group (2003) 'Vascular factors and risk of dementia: design of the Three-City Study and baseline characteristics of the study population', *Neuroepidemiology*, 22(6), pp. 316–325. doi: 10.1159/000072920.

Aibaidula, A. *et al.* (2017) 'Adult IDH wild-type lower-grade gliomas should be further stratified', *Neuro-Oncology*, 19(10), pp. 1327–1337. doi: 10.1093/neuonc/nox078.

Aihara, K. *et al.* (2014) 'H3F3A K27M mutations in thalamic gliomas from young adult patients', *Neuro-Oncology*, 16(1), pp. 140–146. doi: 10.1093/neuonc/not144.

Alexandrov, L. B. *et al.* (2013) 'Signatures of mutational processes in human cancer', *Nature*, 500(7463), pp. 415–421. doi: 10.1038/nature12477.

Andronesi, O. C. *et al.* (2012) 'Detection of 2-hydroxyglutarate in IDH-mutated glioma patients by in vivo spectral-editing and 2D correlation magnetic resonance spectroscopy', *Science Translational Medicine*, 4(116), p. 116ra4. doi: 10.1126/scitranslmed.3002693.

Andronesi, O. C. *et al.* (2016) 'Treatment Response Assessment in IDH-Mutant Glioma Patients by Noninvasive 3D Functional Spectroscopic Mapping of 2-Hydroxyglutarate', *Clinical Cancer Research: An Official Journal of the American Association for Cancer Research*, 22(7), pp. 1632–1641. doi: 10.1158/1078-0432.CCR-15-0656.

Andronesi, O. C. *et al.* (2018) 'Pharmacodynamics of mutant-IDH1 inhibitors in glioma patients probed by in vivo 3D MRS imaging of 2-hydroxyglutarate', *Nature Communications*, 9(1), p. 1474. doi: 10.1038/s41467-018-03905-6.

Ango, F. *et al.* (2004) 'Ankyrin-based subcellular gradient of neurofascin, an immunoglobulin family protein, directs GABAergic innervation at purkinje axon initial segment', *Cell*, 119(2), pp. 257–272. doi: 10.1016/j.cell.2004.10.004.

Baumert, B. G. *et al.* (2016) 'Temozolomide chemotherapy versus radiotherapy in high-risk low-grade glioma (EORTC 22033-26033): a randomised, open-label, phase 3 intergroup study', *The Lancet. Oncology*, 17(11), pp. 1521–1532. doi: 10.1016/S1470-2045(16)30313-8.

Bell, E. H. *et al.* (2020) 'Comprehensive Genomic Analysis in NRG Oncology/RTOG 9802: A Phase III Trial of Radiation Versus Radiation Plus Procarbazine, Lomustine (CCNU), and Vincristine in High-Risk Low-Grade Glioma', *Journal of Clinical Oncology: Official Journal of the American Society of Clinical Oncology*, p. JCO1902983. doi: 10.1200/JCO.19.02983.

Bennett, J. T. *et al.* (2016) 'Mosaic Activating Mutations in FGFR1 Cause Encephalocraniocutaneous Lipomatosis', *American Journal of Human Genetics*, 98(3), pp. 579–587. doi: 10.1016/j.ajhg.2016.02.006.

Best, M. G. *et al.* (2015) 'Liquid biopsies in patients with diffuse glioma', *Acta Neuropathologica*, 129(6), pp. 849–865. doi: 10.1007/s00401-015-1399-y.

Bettegowda, C. *et al.* (2014) 'Detection of circulating tumor DNA in early- and late-stage human malignancies', *Science Translational Medicine*, 6(224), p. 224ra24. doi: 10.1126/scitranslmed.3007094.

Blanchard, G. *et al.* (2016) 'Systematic MRI in NF1 children under six years of age for the diagnosis of optic pathway gliomas. Study and outcome of a French cohort', *European journal of paediatric neurology: EJPN: official journal of the European Paediatric Neurology Society*, 20(2), pp. 275–281. doi: 10.1016/j.ejpn.2015.12.002.

Boisselier, B. *et al.* (2012) 'Detection of IDH1 mutation in the plasma of patients with glioma', *Neurology*, 79(16), pp. 1693–1698. doi: 10.1212/WNL.0b013e31826e9b0a.

Bondy, M. L. *et al.* (2008) 'Brain tumor epidemiology: consensus from the Brain Tumor Epidemiology Consortium', *Cancer*, 113(7 Suppl), pp. 1953–1968. doi: 10.1002/cncr.23741.

Branzoli, F. *et al.* (2018) 'Highly specific determination of IDH status using edited in vivo magnetic resonance spectroscopy', *Neuro-Oncology*, 20(7), pp. 907–916. doi: 10.1093/neuonc/nox214.

Brat, D. J. *et al.* (2018) 'cIMPACT-NOW update 3: recommended diagnostic criteria for "Diffuse astrocytic glioma, IDH-wildtype, with molecular features of glioblastoma, WHO grade IV"', *Acta Neuropathologica*, 136(5), pp. 805–810. doi: 10.1007/s00401-018-1913-0.

Brat, D. J. *et al.* (2020) 'cIMPACT-NOW update 5: recommended grading criteria and terminologies for IDH-mutant astrocytomas', *Acta Neuropathologica*, 139(3), pp. 603–608. doi: 10.1007/s00401-020-02127-9.

Brems, H. *et al.* (2009) 'Mechanisms in the pathogenesis of malignant tumours in neurofibromatosis type 1', *The Lancet. Oncology*, 10(5), pp. 508–515. doi: 10.1016/S1470-2045(09)70033-6.

Buckner, J. C. *et al.* (2016) 'Radiation plus Procarbazine, CCNU, and Vincristine in Low-Grade Glioma', *The New England Journal of Medicine*, 374(14), pp. 1344–1355. doi: 10.1056/NEJMoa1500925.

Buczkowicz, P. *et al.* (2014) 'Histopathological spectrum of paediatric diffuse intrinsic pontine glioma: diagnostic and therapeutic implications', *Acta Neuropathologica*, 128(4), pp. 573–581. doi: 10.1007/s00401-014-1319-6.

Cairncross, J. G. *et al.* (1998) 'Specific genetic predictors of chemotherapeutic response and survival in patients with anaplastic oligodendrogliomas', *Journal of the National Cancer Institute*, 90(19), pp. 1473–1479. doi: 10.1093/jnci/90.19.1473.

Cairncross, G. *et al.* (2013) 'Phase III trial of chemoradiotherapy for anaplastic oligodendroglioma: long-term results of RTOG 9402', *Journal of Clinical Oncology: Official Journal of the American Society of Clinical Oncology*, 31(3), pp. 337–343. doi: 10.1200/JCO.2012.43.2674.

Cairncross, J. G. *et al.* (2014) 'Benefit from procarbazine, lomustine, and vincristine in oligodendroglial tumors is associated with mutation of IDH', *Journal of Clinical Oncology: Official Journal of the American Society of Clinical Oncology*, 32(8), pp. 783–790. doi: 10.1200/JCO.2013.49.3726.

Cancer Genome Atlas Research Network *et al.* (2015) 'Comprehensive, Integrative Genomic Analysis of Diffuse Lower-Grade Gliomas', *The New England Journal of Medicine*, 372(26), pp. 2481–2498. doi: 10.1056/NEJMoa1402121.

Castel, D. *et al.* (2015) 'Histone H3F3A and HIST1H3B K27M mutations define two subgroups of diffuse intrinsic pontine gliomas with different prognosis and phenotypes', *Acta Neuropathologica*, 130(6), pp. 815–827. doi: 10.1007/s00401-015-1478-0.

Ceccarelli, M. *et al.* (2016) 'Molecular Profiling Reveals Biologically Discrete Subsets and Pathways of Progression in Diffuse Glioma', *Cell*, 164(3), pp. 550–563. doi: 10.1016/j.cell.2015.12.028.

Chan, A. K.-Y. *et al.* (2015) 'Combination genetic signature stratifies lower-grade gliomas better than histological grade', *Oncotarget*, 6(25), pp. 20885–20901. doi: 10.18632/oncotarget.4928.

Chapman, P. B. *et al.* (2011) 'Improved survival with vemurafenib in melanoma with BRAF V600E mutation', *The New England Journal of Medicine*, 364(26), pp. 2507–2516. doi: 10.1056/NEJMoa1103782.

Chapuy, B. *et al.* (2018) 'Molecular subtypes of diffuse large B cell lymphoma are associated with distinct pathogenic mechanisms and outcomes', *Nature Medicine*, 24(5), pp. 679–690. doi: 10.1038/s41591-018-0016-8.

Chen, W. W. *et al.* (2013) 'BEAMing and Droplet Digital PCR Analysis of Mutant IDH1 mRNA in Glioma Patient Serum and Cerebrospinal Fluid Extracellular Vesicles', *Molecular Therapy. Nucleic Acids*, 2, p. e109. doi: 10.1038/mtna.2013.28.

Choi, C. *et al.* (2013) 'A comparative study of short- and long-TE ^{1}H MRS at 3 T for in vivo detection of 2-hydroxyglutarate in brain tumors', *NMR in biomedicine*, 26(10), pp. 1242–1250. doi: 10.1002/nbm.2943.

Chowdhury, R. *et al.* (2011) 'The oncometabolite 2-hydroxyglutarate inhibits histone lysine demethylases', *EMBO reports*, 12(5), pp. 463–469. doi: 10.1038/embor.2011.43.

Codd, V. *et al.* (2013) 'Identification of seven loci affecting mean telomere length and their association with disease', *Nature Genetics*, 45(4), pp. 422–427, 427e1-2. doi: 10.1038/ng.2528.

Crane, E. *et al.* (2015) 'Condensin-driven remodelling of X chromosome topology during dosage compensation', *Nature*, 523(7559), pp. 240–244. doi: 10.1038/nature14450.

Dang, L. *et al.* (2009) 'Cancer-associated IDH1 mutations produce 2-hydroxyglutarate', *Nature*, 462(7274), pp. 739–744. doi: 10.1038/nature08617.

Dang, L., Yen, K. and Attar, E. C. (2016) 'IDH mutations in cancer and progress toward development of targeted therapeutics', *Annals of Oncology: Official Journal of the European Society for Medical Oncology*, 27(4), pp. 599–608. doi: 10.1093/annonc/mdw013.

De Mattos-Arruda, L. *et al.* (2015) 'Cerebrospinal fluid-derived circulating tumour DNA better represents the genomic alterations of brain tumours than plasma', *Nature Communications*, 6, p. 8839. doi: 10.1038/ncomms9839.

Di Stefano, A. L. *et al.* (2013) 'Association between glioma susceptibility loci and tumour pathology defines specific molecular etiologies', *Neuro-Oncology*, 15(5), pp. 542–547. doi: 10.1093/neuonc/nos284.

Di Stefano, A. L. *et al.* (2015) 'Detection, Characterization, and Inhibition of FGFR-TACC Fusions in IDH Wild-type Glioma', *Clinical Cancer Research: An Official Journal of the American Association for Cancer Research*, 21(14), pp. 3307–3317. doi: 10.1158/1078-0432.CCR-14-2199.

Di Stefano, A. L. *et al.* (2020) 'Clinical, molecular and radiomic profile of gliomas with FGFR3-TACC3 fusions', *Neuro-Oncology*. doi: 10.1093/neuonc/noaa121.

Dixon, J. R. *et al.* (2015) 'Chromatin architecture reorganization during stem cell differentiation', *Nature*, 518(7539), pp. 331–336. doi: 10.1038/nature14222.

Dyson, K. *et al.* (2016) 'FGFR1 N546K and H3F3A K27M mutations in a diffuse leptomeningeal tumour with glial and neuronal markers', *Histopathology*, 69(4), pp. 704–707. doi: 10.1111/his.12983.

Eckel-Passow, J. E. *et al.* (2015) 'Glioma Groups Based on 1p/19q, IDH, and TERT Promoter Mutations in Tumors', *The New England Journal of Medicine*, 372(26), pp. 2499–2508. doi: 10.1056/NEJMoa1407279.

Emir, U. E. *et al.* (2016) 'Noninvasive Quantification of 2-Hydroxyglutarate in Human Gliomas with IDH1 and IDH2 Mutations', *Cancer Research*, 76(1), pp. 43–49. doi: 10.1158/0008-5472.CAN-15-0934.

Enciso-Mora, V. *et al.* (2013) 'Deciphering the 8q24.21 association for glioma', *Human Molecular Genetics*, 22(11), pp. 2293–2302. doi: 10.1093/hmg/ddt063.

Esteller, M. *et al.* (2000) 'Inactivation of the DNA-repair gene MGMT and the clinical response of gliomas to alkylating agents', *The New England Journal of Medicine*, 343(19), pp. 1350–1354. doi: 10.1056/NEJM200011093431901.

Facchinetti, F. *et al.* (2020) 'Facts and New Hopes on Selective FGFR Inhibitors in Solid Tumors', *Clinical Cancer Research: An Official Journal of the American Association for Cancer Research*, 26(4), pp. 764–774. doi: 10.1158/1078-0432.CCR-19-2035.

Feng, J. *et al.* (2015) 'The H3.3 K27M mutation results in a poorer prognosis in brainstem gliomas than thalamic gliomas in adults', *Human Pathology*, 46(11), pp. 1626–1632. doi: 10.1016/j.humpath.2015.07.002.

Figueroa, J. M. *et al.* (2017) 'Detection of wild-type EGFR amplification and EGFRvIII mutation in CSF-derived extracellular vesicles of glioblastoma patients', *Neuro-Oncology*, 19(11), pp. 1494–1502. doi: 10.1093/neuonc/nox085.

Flavahan, W. A. *et al.* (2016) 'Insulator dysfunction and oncogene activation in IDH mutant gliomas', *Nature*, 529(7584), pp. 110–114. doi: 10.1038/nature16490.

Fraser, K. *et al.* (2019) 'Characterization of single microvesicles in plasma from glioblastoma patients', *Neuro-Oncology*, 21(5), pp. 606–615. doi: 10.1093/neuonc/noy187.

Frattini, V. *et al.* (2018) 'A metabolic function of FGFR3-TACC3 gene fusions in cancer', *Nature*, 553(7687), pp. 222–227. doi: 10.1038/nature25171.

Gao, J. *et al.* (2013) 'Integrative analysis of complex cancer genomics and clinical profiles using the cBioPortal', *Science Signaling*, 6(269), p. pl1. doi: 10.1126/scisignal.2004088.

García-Romero, N. *et al.* (2017) 'DNA sequences within glioma-derived extracellular vesicles can cross the intact blood-brain barrier and be detected in peripheral blood of patients', *Oncotarget*, 8(1), pp. 1416–1428. doi: 10.18632/oncotarget.13635.

Gessi, M. *et al.* (2014) 'FGFR1 mutations in Rosette-forming glioneuronal tumors of the fourth ventricle', *Journal of Neuropathology and Experimental Neurology*, 73(6), pp. 580–584. doi: 10.1097/NEN.0000000000000080.

Gladson, C. L., Prayson, R. A. and Liu, W. M. (2010) 'The pathobiology of glioma tumors', *Annual Review of Pathology*, 5, pp. 33–50. doi: 10.1146/annurev-pathol-121808-102109.

Gonda, D. D. *et al.* (2013) 'Neuro-oncologic applications of exosomes, microvesicles, and other nano-sized extracellular particles', *Neurosurgery*, 72(4), pp. 501–510. doi: 10.1227/NEU.0b013e3182846e63.

Gur, G. *et al.* (2004) 'LRIG1 restricts growth factor signaling by enhancing receptor ubiquitylation and degradation', *The EMBO journal*, 23(16), pp. 3270–3281. doi: 10.1038/sj.emboj.7600342.

Gutmann, D. H. *et al.* (2002) 'Gliomas presenting after age 10 in individuals with neurofibromatosis type 1 (NF1)', *Neurology*, 59(5), pp. 759–761. doi: 10.1212/wnl.59.5.759.

Gutmann, D. H. *et al.* (2017) 'Neurofibromatosis type 1', *Nature Reviews. Disease Primers*, 3, p. 17004. doi: 10.1038/nrdp.2017.4.

Hagen, B. and Trinh, V. A. (2014) 'Managing Side Effects of Vemurafenib Therapy for Advanced Melanoma', *Journal of the Advanced Practitioner in Oncology*, 5(6), pp. 400–410.

Harndahl, M. *et al.* (2009) 'Peptide binding to HLA class I molecules: homogenous, high-throughput screening, and affinity assays', *Journal of Biomolecular Screening*, 14(2), pp. 173–180. doi: 10.1177/1087057108329453.

Hasselblatt, M. *et al.* (2018) 'Diffuse Astrocytoma, IDH-Wildtype: A Dissolving Diagnosis', *Journal of Neuropathology and Experimental Neurology*, 77(6), pp. 422–425. doi: 10.1093/jnen/nly012.

Hegi, M. E. *et al.* (2005) 'MGMT gene silencing and benefit from temozolomide in glioblastoma', *The New England Journal of Medicine*, 352(10), pp. 997–1003. doi: 10.1056/NEJMoa043331.

Helfferich, J. *et al.* (2016) 'Neurofibromatosis type 1 associated low grade gliomas: A comparison with sporadic low grade gliomas', *Critical Reviews in Oncology/Hematology*, 104, pp. 30–41. doi: 10.1016/j.critrevonc.2016.05.008.

Henson, J. D. *et al.* (2009) 'DNA C-circles are specific and quantifiable markers of alternative-lengthening-of-telomeres activity', *Nature Biotechnology*, 27(12), pp. 1181–1185. doi: 10.1038/nbt.1587.

Hercberg, S. *et al.* (2004) 'The SU.VI.MAX Study: a randomized, placebo-controlled trial of the health effects of antioxidant vitamins and minerals', *Archives of Internal Medicine*, 164(21), pp. 2335–2342. doi: 10.1001/archinte.164.21.2335.

Houillier, C. *et al.* (2010) 'IDH1 or IDH2 mutations predict longer survival and response to temozolomide in low-grade gliomas', *Neurology*, 75(17), pp. 1560–1566. doi: 10.1212/WNL.0b013e3181f96282.

Huang, T. Y. *et al.* (2017) 'Detection of Histone H3 mutations in cerebrospinal fluid-derived tumor DNA from children with diffuse midline glioma', *Acta Neuropathologica Communications*, 5(1), p. 28. doi: 10.1186/s40478-017-0436-6.

Hyman, D. M. *et al.* (2015) 'Vemurafenib in Multiple Nonmelanoma Cancers with BRAF V600 Mutations', *The New England Journal of Medicine*, 373(8), pp. 726–736. doi: 10.1056/NEJMoa1502309.

Izquierdo, C. *et al.* (2019) 'Radiological Characteristics and Natural History of Adult IDH-Wildtype Astrocytomas with TERT Promoter Mutations', *Neurosurgery*, 85(3), pp. E448–E456. doi: 10.1093/neuros/nyy513.

Jafari-Khouzani, K. *et al.* (2016) 'Volumetric relationship between 2-hydroxyglutarate and FLAIR hyperintensity has potential implications for radiotherapy planning of mutant IDH glioma patients', *Neuro-Oncology*, 18(11), pp. 1569–1578. doi: 10.1093/neuonc/now100.

Jenkins, R. B. *et al.* (2012) 'A low-frequency variant at 8q24.21 is strongly associated with risk of oligodendroglial tumors and astrocytomas with IDH1 or IDH2 mutation', *Nature Genetics*, 44(10), pp. 1122–1125. doi: 10.1038/ng.2388.

Jeschke, J. *et al.* (2017) 'DNA methylation-based immune response signature improves patient diagnosis in multiple cancers', *The Journal of Clinical Investigation*, 127(8), pp. 3090–3102. doi: 10.1172/JCI91095.

Johnson, D. B. *et al.* (2015) 'Acquired BRAF inhibitor resistance: A multicenter meta-analysis of the spectrum and frequencies, clinical behaviour, and phenotypic associations of resistance mechanisms', *European Journal of Cancer (Oxford, England: 1990)*, 51(18), pp. 2792–2799. doi: 10.1016/j.ejca.2015.08.022.

Jones, D. T. W. *et al.* (2013) 'Recurrent somatic alterations of FGFR1 and NTRK2 in pilocytic astrocytoma', *Nature Genetics*, 45(8), pp. 927–932. doi: 10.1038/ng.2682.

Jung, J. *et al.* (2017) 'Nicotinamide metabolism regulates glioblastoma stem cell maintenance', *JCI insight*, 2(10). doi: 10.1172/jci.insight.90019.

Kaley, T. *et al.* (2018) 'BRAF Inhibition in BRAFV600-Mutant Gliomas: Results From the VE-BASKET Study', *Journal of Clinical Oncology*, 36(35), pp. 3477–3484. doi: 10.1200/JCO.2018.78.9990.

Kalinina, J. *et al.* (2012) 'Detection of "oncometabolite" 2-hydroxyglutarate by magnetic resonance analysis as a biomarker of IDH1/2 mutations in glioma', *Journal of Molecular Medicine (Berlin, Germany)*, 90(10), pp. 1161–1171. doi: 10.1007/s00109-012-0888-x.

Kaminska, B. *et al.* (2019) 'Consequences of IDH1/2 Mutations in Gliomas and an Assessment of Inhibitors Targeting Mutated IDH Proteins', *Molecules (Basel, Switzerland)*, 24(5). doi: 10.3390/molecules24050968.

Khuong-Quang, D.-A. *et al.* (2012) 'K27M mutation in histone H3.3 defines clinically and biologically distinct subgroups of pediatric diffuse intrinsic pontine gliomas', *Acta Neuropathologica*, 124(3), pp. 439–447. doi: 10.1007/s00401-012-0998-0.

Killedar, A. *et al.* (2015) 'A Common Cancer Risk-Associated Allele in the hTERT Locus Encodes a Dominant Negative Inhibitor of Telomerase', *PLoS genetics*, 11(6), p. e1005286. doi: 10.1371/journal.pgen.1005286.

Kinnersley, B. *et al.* (2015) 'Genome-wide association study identifies multiple susceptibility loci for glioma', *Nature Communications*, 6, p. 8559. doi: 10.1038/ncomms9559.

Koschmann, C. *et al.* (2016) 'ATRX loss promotes tumor growth and impairs nonhomologous end joining DNA repair in glioma', *Science Translational Medicine*, 8(328), p. 328ra28. doi: 10.1126/scitranslmed.aac8228.

Labussière, M. *et al.* (2010) 'All the 1p19q codeleted gliomas are mutated on IDH1 or IDH2', *Neurology*, 74(23), pp. 1886–1890. doi: 10.1212/WNL.0b013e3181e1cf3a.

Labussière, M. *et al.* (2014a) 'Combined analysis of TERT, EGFR, and IDH status defines distinct prognostic glioblastoma classes', *Neurology*, 83(13), pp. 1200–1206. doi: 10.1212/WNL.0000000000000814.

Labussière, M. *et al.* (2014b) 'TERT promoter mutations in gliomas, genetic associations and clinico-pathological correlations', *British Journal of Cancer*, 111(10), pp. 2024–2032. doi: 10.1038/bjc.2014.538.

Labussière, M. *et al.* (2016) 'Chromosome 17p Homodisomy Is Associated With Better Outcome in 1p19q Non-Codeleted and IDH-Mutated Gliomas', *The Oncologist*, 21(9), pp. 1131–1135. doi: 10.1634/theoncologist.2016-0003.

Larjavaara, S. *et al.* (2007) 'Incidence of gliomas by anatomic location', *Neuro-Oncology*, 9(3), pp. 319–325. doi: 10.1215/15228517-2007-016.

Lasorella, A., Sanson, M. and Iavarone, A. (2017) 'FGFR-TACC gene fusions in human glioma', *Neuro-Oncology*, 19(4), pp. 475–483. doi: 10.1093/neuonc/now240.

Laycock-van Spyk, S. *et al.* (2011) 'Neurofibromatosis type 1-associated tumours: their somatic mutational spectrum and pathogenesis', *Human Genomics*, 5(6), pp. 623–690. doi: 10.1186/1479-7364-5-6-623.

Lee, A. *et al.* (2020) 'Anti-epidermal growth factor receptor therapy for glioblastoma in adults', *The Cochrane Database of Systematic Reviews*, 5, p. CD013238. doi: 10.1002/14651858.CD013238.pub2.

Li, S. *et al.* (2013) 'Overexpression of isocitrate dehydrogenase mutant proteins renders glioma cells more sensitive to radiation', *Neuro-Oncology*, 15(1), pp. 57–68. doi: 10.1093/neuonc/nos261.

Liu, E. K. *et al.* (2020) 'Novel Therapies for Glioblastoma', *Current Neurology and Neuroscience Reports*, 20(7), p. 19. doi: 10.1007/s11910-020-01042-6.

Lombardi, G. *et al.* (2019) 'Regorafenib compared with lomustine in patients with relapsed glioblastoma (REGOMA): a multicentre, open-label, randomised, controlled, phase 2 trial', *The Lancet. Oncology*, 20(1), pp. 110–119. doi: 10.1016/S1470-2045(18)30675-2.

Louis, D. N. *et al.* (2007) 'The 2007 WHO classification of tumours of the central nervous system', *Acta Neuropathologica*, 114(2), pp. 97–109. doi: 10.1007/s00401-007-0243-4.

Louis, D. N. *et al.* (2016) 'The 2016 World Health Organization Classification of Tumors of the Central Nervous System: a summary', *Acta Neuropathologica*, 131(6), pp. 803–820. doi: 10.1007/s00401-016-1545-1.

Madan, A. *et al.* (2015) 'Proton T2 measurement and quantification of lactate in brain tumors by MRS at 3 Tesla in vivo', *Magnetic Resonance in Medicine*, 73(6), pp. 2094–2099. doi: 10.1002/mrm.25352.

Mall, R. *et al.* (2018) 'RGBM: regularized gradient boosting machines for identification of the transcriptional regulators of discrete glioma subtypes', *Nucleic Acids Research*, 46(7), p. e39. doi: 10.1093/nar/gky015.

Manda, S. V. *et al.* (2018) 'Exosomes as a biomarker platform for detecting epidermal growth factor receptor-positive high-grade gliomas', *Journal of Neurosurgery*, 128(4), pp. 1091–1101. doi: 10.3171/2016.11.JNS161187.

Melin, B. S. *et al.* (2017) 'Genome-wide association study of glioma subtypes identifies specific differences in genetic susceptibility to glioblastoma and non-glioblastoma tumors', *Nature Genetics*, 49(5), pp. 789–794. doi: 10.1038/ng.3823.

Messiaen, L. *et al.* (2009) 'Clinical and mutational spectrum of neurofibromatosis type 1-like syndrome', *JAMA*, 302(19), pp. 2111–2118. doi: 10.1001/jama.2009.1663.

Metellus, P. *et al.* (2010) 'Absence of IDH mutation identifies a novel radiologic and molecular subtype of WHO grade II gliomas with dismal prognosis', *Acta Neuropathologica*, 120(6), pp. 719–729. doi: 10.1007/s00401-010-0777-8.

Meyronet, D. *et al.* (2017) 'Characteristics of H3 K27M-mutant gliomas in adults', *Neuro-Oncology*, 19(8), pp. 1127–1134. doi: 10.1093/neuonc/now274.

Nencha, U. *et al.* (2016) 'TERT promoter mutations and rs2853669 polymorphism: prognostic impact and interactions with common alterations in glioblastomas', *Journal of Neuro-Oncology*, 126(3), pp. 441–446. doi: 10.1007/s11060-015-1999-3.

Noerholm, M. *et al.* (2012) 'RNA expression patterns in serum microvesicles from patients with glioblastoma multiforme and controls', *BMC cancer*, 12, p. 22. doi: 10.1186/1471-2407-12-22.

Noushmehr, H. *et al.* (2010) 'Identification of a CpG island methylator phenotype that defines a distinct subgroup of glioma', *Cancer Cell*, 17(5), pp. 510–522. doi: 10.1016/j.ccr.2010.03.017.

Okano, J. *et al.* (2000) 'Akt/protein kinase B isoforms are differentially regulated by epidermal growth factor stimulation', *The Journal of Biological Chemistry*, 275(40), pp. 30934–30942. doi: 10.1074/jbc.M004112200.

Olar, A. *et al.* (2015) 'IDH mutation status and role of WHO grade and mitotic index in overall survival in grade II-III diffuse gliomas', *Acta Neuropathologica*, 129(4), pp. 585–596. doi: 10.1007/s00401-015-1398-z.

Osti, D. *et al.* (2019) 'Clinical Significance of Extracellular Vesicles in Plasma from Glioblastoma Patients', *Clinical Cancer Research: An Official Journal of the American Association for Cancer Research*, 25(1), pp. 266–276. doi: 10.1158/1078-0432.CCR-18-1941.

Ostrom, Q. T. *et al.* (2015) 'CBTRUS Statistical Report: Primary Brain and Central Nervous System Tumors Diagnosed in the United States in 2008-2012', *Neuro-Oncology*, 17 Suppl 4, pp. iv1–iv62. doi: 10.1093/neuonc/nov189.

Parsons, D. W. *et al.* (2008) 'An integrated genomic analysis of human glioblastoma multiforme', *Science (New York, N.Y.)*, 321(5897), pp. 1807–1812. doi: 10.1126/science.1164382.

Pasqualetti, F. *et al.* (2019) 'Dabrafenib treatment in a patient with BRAF V600E ganglioglioma: circulating exosome-derived cancer RNA supports treatment choice and clinical monitoring', *Neuro-Oncology*, 21(12), pp. 1610–1611. doi: 10.1093/neuonc/noz157.

Pentsova, E. I. *et al.* (2016) 'Evaluating Cancer of the Central Nervous System Through Next-Generation Sequencing of Cerebrospinal Fluid', *Journal of Clinical Oncology: Official Journal of the American Society of Clinical Oncology*, 34(20), pp. 2404–2415. doi: 10.1200/JCO.2016.66.6487.

Perry, A. and Wesseling, P. (2016) 'Histologic classification of gliomas', *Handbook of Clinical Neurology*, 134, pp. 71–95. doi: 10.1016/B978-0-12-802997-8.00005-0.

Philpott, C. *et al.* (2017) 'The NF1 somatic mutational landscape in sporadic human cancers', *Human Genomics*, 11(1), p. 13. doi: 10.1186/s40246-017-0109-3.

Picca, A. *et al.* (2018) 'FGFR1 actionable mutations, molecular specificities, and outcome of adult midline gliomas', *Neurology*, 90(23), pp. e2086–e2094. doi: 10.1212/WNL.0000000000005658.

Power, C. and Elliott, J. (2006) 'Cohort profile: 1958 British birth cohort (National Child Development Study)', *International Journal of Epidemiology*, 35(1), pp. 34–41. doi: 10.1093/ije/dyi183.

Provencher, S. W. (2001) 'Automatic quantitation of localized in vivo 1H spectra with LCModel', *NMR in Biomedicine*, 14(4), pp. 260–264. doi: 10.1002/nbm.698.

Rao, S. S. P. *et al.* (2014) 'A 3D map of the human genome at kilobase resolution reveals principles of chromatin looping', *Cell*, 159(7), pp. 1665–1680. doi: 10.1016/j.cell.2014.11.021.

Reardon, D. A. *et al.* (2015) 'Phase I/randomized phase II study of afatinib, an irreversible ErbB family blocker, with or without protracted temozolomide in adults with recurrent glioblastoma', *Neuro-Oncology*, 17(3), pp. 430–439. doi: 10.1093/neuonc/nou160.

Reifenberger, J. *et al.* (1994) 'Molecular genetic analysis of oligodendroglial tumors shows preferential allelic deletions on 19q and 1p', *The American Journal of Pathology*, 145(5), pp. 1175–1190.

Ren, C. *et al.* (2006) 'Identification and characterization of RTVP1/GLIPR1-like genes, a novel p53 target gene cluster', *Genomics*, 88(2), pp. 163–172. doi: 10.1016/j.ygeno.2006.03.021.

Reuss, D. E. *et al.* (2015) 'ATRX and IDH1-R132H immunohistochemistry with subsequent copy number analysis and IDH sequencing as a basis for an "integrated" diagnostic approach for adult astrocytoma, oligodendroglioma and glioblastoma', *Acta Neuropathologica*, 129(1), pp. 133–146. doi: 10.1007/s00401-014-1370-3.

Reyes-Botero, G. *et al.* (2012) 'Adult brainstem gliomas', *The Oncologist*, 17(3), pp. 388–397. doi: 10.1634/theoncologist.2011-0335.

Reyes-Botero, G. *et al.* (2014) 'Molecular analysis of diffuse intrinsic brainstem gliomas in adults', *Journal of Neuro-Oncology*, 116(2), pp. 405–411. doi: 10.1007/s11060-013-1312-2.

Risso, D. *et al.* (2011) 'GC-content normalization for RNA-Seq data', *BMC bioinformatics*, 12, p. 480. doi: 10.1186/1471-2105-12-480.

Rivera, B. *et al.* (2016) 'Germline and somatic FGFR1 abnormalities in dysembryoplastic neuroepithelial tumors', *Acta Neuropathologica*, 131(6), pp. 847–863. doi: 10.1007/s00401-016-1549-x.

Rodriguez, F. J. *et al.* (2008) 'Gliomas in neurofibromatosis type 1: a clinicopathologic study of 100 patients', *Journal of Neuropathology and Experimental Neurology*, 67(3), pp. 240–249. doi: 10.1097/NEN.0b013e318165eb75.

Ryall, S. *et al.* (2016) 'Targeted detection of genetic alterations reveal the prognostic impact of H3K27M and MAPK pathway aberrations in paediatric thalamic glioma', *Acta Neuropathologica Communications*, 4(1), p. 93. doi: 10.1186/s40478-016-0353-0.

Salkeni, M. A. *et al.* (2013) 'Detection of EGFRvIII mutant DNA in the peripheral blood of brain tumor patients', *Journal of Neuro-Oncology*, 115(1), pp. 27–35. doi: 10.1007/s11060-013-1209-0.

Sanson, M. *et al.* (2009) 'Isocitrate dehydrogenase 1 codon 132 mutation is an important prognostic biomarker in gliomas', *Journal of Clinical Oncology: Official Journal of the American Society of Clinical Oncology*, 27(25), pp. 4150–4154. doi: 10.1200/JCO.2009.21.9832.

Sanson, M. *et al.* (2011) 'Chromosome 7p11.2 (EGFR) variation influences glioma risk', *Human Molecular Genetics*, 20(14), pp. 2897–2904. doi: 10.1093/hmg/ddr192.

Schepers, G. E. *et al.* (2000) 'Cloning and characterisation of the Sry-related transcription factor gene Sox8', *Nucleic Acids Research*, 28(6), pp. 1473–1480. doi: 10.1093/nar/28.6.1473.

Schmitt, A. D. *et al.* (2016) 'A Compendium of Chromatin Contact Maps Reveals Spatially Active Regions in the Human Genome', *Cell Reports*, 17(8), pp. 2042–2059. doi: 10.1016/j.celrep.2016.10.061.

Schreck, K. C., Grossman, S. A. and Pratilas, C. A. (2019) 'BRAF Mutations and the Utility of RAF and MEK Inhibitors in Primary Brain Tumors', *Cancers*, 11(9). doi: 10.3390/cancers11091262.

Schumacher, T. N. and Schreiber, R. D. (2015) 'Neoantigens in cancer immunotherapy', *Science (New York, N.Y.)*, 348(6230), pp. 69–74. doi: 10.1126/science.aaa4971.

Schwartzentruber, J. *et al.* (2012) 'Driver mutations in histone H3.3 and chromatin remodelling genes in paediatric glioblastoma', *Nature*, 482(7384), pp. 226–231. doi: 10.1038/nature10833.

Sellmer, L. *et al.* (2017) 'Non-optic glioma in adults and children with neurofibromatosis 1', *Orphanet Journal of Rare Diseases*, 12(1), p. 34. doi: 10.1186/s13023-017-0588-2.

Seminog, O. O. and Goldacre, M. J. (2013) 'Risk of benign tumours of nervous system, and of malignant neoplasms, in people with neurofibromatosis: population-based record-linkage study', *British Journal of Cancer*, 108(1), pp. 193–198. doi: 10.1038/bjc.2012.535.

Sepúlveda-Sánchez, J. M. *et al.* (2017) 'Phase II trial of dacomitinib, a pan-human EGFR tyrosine kinase inhibitor, in recurrent glioblastoma patients with EGFR amplification', *Neuro-Oncology*, 19(11), pp. 1522–1531. doi: 10.1093/neuonc/nox105.

Shete, S. *et al.* (2009) 'Genome-wide association study identifies five susceptibility loci for glioma', *Nature Genetics*, 41(8), pp. 899–904. doi: 10.1038/ng.407.

Shuai, K. *et al.* (1993) 'Polypeptide signalling to the nucleus through tyrosine phosphorylation of Jak and Stat proteins', *Nature*, 366(6455), pp. 580–583. doi: 10.1038/366580a0.

Skog, J. *et al.* (2008) 'Glioblastoma microvesicles transport RNA and proteins that promote tumour growth and provide diagnostic biomarkers', *Nature Cell Biology*, 10(12), pp. 1470–1476. doi: 10.1038/ncb1800.

Solga, A. C. *et al.* (2015) 'RNA Sequencing of Tumor-Associated Microglia Reveals Ccl5 as a Stromal Chemokine Critical for Neurofibromatosis-1 Glioma Growth', *Neoplasia (New York, N.Y.)*, 17(10), pp. 776–788. doi: 10.1016/j.neo.2015.10.002.

Solomon, D. A. *et al.* (2016) 'Diffuse Midline Gliomas with Histone H3-K27M Mutation: A Series of 47 Cases Assessing the Spectrum of Morphologic Variation and Associated Genetic Alterations', *Brain Pathology (Zurich, Switzerland)*, 26(5), pp. 569–580. doi: 10.1111/bpa.12336.

de Souza, C. F. *et al.* (2018) 'A Distinct DNA Methylation Shift in a Subset of Glioma CpG Island Methylator Phenotypes during Tumor Recurrence', *Cell Reports*, 23(2), pp. 637–651. doi: 10.1016/j.celrep.2018.03.107.

Sproviero, D. *et al.* (2018) 'Pathological Proteins Are Transported by Extracellular Vesicles of Sporadic Amyotrophic Lateral Sclerosis Patients', *Frontiers in Neuroscience*, 12, p. 487. doi: 10.3389/fnins.2018.00487.

Stacey, S. N. *et al.* (2011) 'A germline variant in the TP53 polyadenylation signal confers cancer susceptibility', *Nature Genetics*, 43(11), pp. 1098–1103. doi: 10.1038/ng.926.

Stichel, D. *et al.* (2018) 'Distribution of EGFR amplification, combined chromosome 7 gain and chromosome 10 loss, and TERT promoter mutation in brain tumors and their potential for the reclassification of IDHwt astrocytoma to glioblastoma', *Acta Neuropathologica*, 136(5), pp. 793–803. doi: 10.1007/s00401-018-1905-0.

Stupp, R. *et al.* (2005) 'Radiotherapy plus concomitant and adjuvant temozolomide for glioblastoma', *The New England Journal of Medicine*, 352(10), pp. 987–996. doi: 10.1056/NEJMoa043330.

Sturm, D. *et al.* (2012) 'Hotspot mutations in H3F3A and IDH1 define distinct epigenetic and biological subgroups of glioblastoma', *Cancer Cell*, 22(4), pp. 425–437. doi: 10.1016/j.ccr.2012.08.024.

Sud, A., Kinnersley, B. and Houlston, R. S. (2017) 'Genome-wide association studies of cancer: current insights and future perspectives', *Nature Reviews. Cancer*, 17(11), pp. 692–704. doi: 10.1038/nrc.2017.82.

Suzuki, H. *et al.* (2015) 'Mutational landscape and clonal architecture in grade II and III gliomas', *Nature Genetics*, 47(5), pp. 458–468. doi: 10.1038/ng.3273.

Tabouret, E. *et al.* (2016) 'Prognostic impact of the 2016 WHO classification of diffuse gliomas in the French POLA cohort', *Acta Neuropathologica*, 132(4), pp. 625–634. doi: 10.1007/s00401-016-1611-8.

Tesileanu, C. M. S. *et al.* (2020) 'Survival of diffuse astrocytic glioma, IDH1/2 wildtype, with molecular features of glioblastoma, WHO grade IV: a confirmation of the cIMPACT-NOW criteria', *Neuro-Oncology*, 22(4), pp. 515–523. doi: 10.1093/neuonc/noz200.

Theeler, B. J. *et al.* (2015) 'Adult brainstem gliomas: Correlation of clinical and molecular features', *Journal of the Neurological Sciences*, 353(1–2), pp. 92–97. doi: 10.1016/j.jns.2015.04.014.

Tkác, I. *et al.* (1999) 'In vivo 1H NMR spectroscopy of rat brain at 1 ms echo time', *Magnetic Resonance in Medicine*, 41(4), pp. 649–656.

Touat, M. *et al.* (2015) 'Targeting FGFR Signaling in Cancer', *Clinical Cancer Research: An Official Journal of the American Association for Cancer Research*, 21(12), pp. 2684–2694. doi: 10.1158/1078-0432.CCR-14-2329.

Touat, M. *et al.* (2018) 'Vemurafenib and cobimetinib overcome resistance to vemurafenib in BRAF-mutant ganglioglioma', *Neurology*, 91(11), pp. 523–525. doi: 10.1212/WNL.0000000000006171.

Turcan, S. *et al.* (2012) 'IDH1 mutation is sufficient to establish the glioma hypermethylator phenotype', *Nature*, 483(7390), pp. 479–483. doi: 10.1038/nature10866.

Turner, K. M. *et al.* (2015) 'Genomically amplified Akt3 activates DNA repair pathway and promotes glioma progression', *Proceedings of the National Academy of Sciences of the United States of America*, 112(11), pp. 3421–3426. doi: 10.1073/pnas.1414573112.

Uusitalo, E. *et al.* (2015) 'Incidence and mortality of neurofibromatosis: a total population study in Finland', *The Journal of Investigative Dermatology*, 135(3), pp. 904–906. doi: 10.1038/jid.2014.465.

Uusitalo, E. *et al.* (2016) 'Distinctive Cancer Associations in Patients With Neurofibromatosis Type 1', *Journal of Clinical Oncology: Official Journal of the American Society of Clinical Oncology*, 34(17), pp. 1978–1986. doi: 10.1200/JCO.2015.65.3576.

van den Bent, M. J. *et al.* (2003) 'Chromosomal anomalies in oligodendroglial tumors are correlated with clinical features', *Cancer*, 97(5), pp. 1276–1284. doi: 10.1002/cncr.11187.

van den Bent, M. J. *et al.* (2011) 'Response assessment in neuro-oncology (a report of the RANO group): assessment of outcome in trials of diffuse low-grade gliomas', *The Lancet. Oncology*, 12(6), pp. 583–593. doi: 10.1016/S1470-2045(11)70057-2.

van den Bent, M. J. *et al.* (2013) 'Adjuvant procarbazine, lomustine, and vincristine chemotherapy in newly diagnosed anaplastic oligodendroglioma: long-term follow-up of EORTC brain tumor group study 26951', *Journal of Clinical Oncology: Official Journal of the American Society of Clinical Oncology*, 31(3), pp. 344–350. doi: 10.1200/JCO.2012.43.2229.

van den Bent, M. *et al.* (2017) 'Efficacy of depatuxizumab mafodotin (ABT-414) monotherapy in patients with EGFR-amplified, recurrent glioblastoma: results from a multi-center, international study', *Cancer Chemotherapy and Pharmacology*, 80(6), pp. 1209–1217. doi: 10.1007/s00280-017-3451-1.

van den Bent, M. *et al.* (2020) 'INTELLANCE 2/EORTC 1410 randomized phase II study of Depatux-M alone and with temozolomide vs temozolomide or lomustine in recurrent EGFR amplified glioblastoma', *Neuro-Oncology*, 22(5), pp. 684–693. doi: 10.1093/neuonc/noz222.

Walsh, K. M., Codd, V., *et al.* (2015) 'Longer genotypically-estimated leukocyte telomere length is associated with increased adult glioma risk', *Oncotarget*, 6(40), pp. 42468–42477. doi: 10.18632/oncotarget.6468.

Walsh, K. M., Wiencke, J. K., *et al.* (2015) 'Telomere maintenance and the etiology of adult glioma', *Neuro-Oncology*, 17(11), pp. 1445–1452. doi: 10.1093/neuonc/nov082.

Wang, H. *et al.* (2014) 'Trans-ethnic genome-wide association study of colorectal cancer identifies a new susceptibility locus in VTI1A', *Nature Communications*, 5, p. 4613. doi: 10.1038/ncomms5613.

Wang, K. *et al.* (2007) 'PennCNV: an integrated hidden Markov model designed for high-resolution copy number variation detection in whole-genome SNP genotyping data', *Genome Research*, 17(11), pp. 1665–1674. doi: 10.1101/gr.6861907.

Wang, S. *et al.* (2018) 'Programmed death ligand 1 expression and tumor infiltrating lymphocytes in neurofibromatosis type 1 and 2 associated tumors', *Journal of Neuro-Oncology*, 138(1), pp. 183–190. doi: 10.1007/s11060-018-2788-6.

Ward, P. S. *et al.* (2013) 'The potential for isocitrate dehydrogenase mutations to produce 2-hydroxyglutarate depends on allele specificity and subcellular compartmentalization', *The Journal of Biological Chemistry*, 288(6), pp. 3804–3815. doi: 10.1074/jbc.M112.435495.

Wei, J. *et al.* (2015) 'miR-20a mediates temozolomide-resistance in glioblastoma cells via negatively regulating LRIG1 expression', *Biomedicine & Pharmacotherapy = Biomedecine & Pharmacotherapie*, 71, pp. 112–118. doi: 10.1016/j.biopha.2015.01.026.

Weller, M. *et al.* (2017) 'European Association for Neuro-Oncology (EANO) guideline on the diagnosis and treatment of adult astrocytic and oligodendroglial gliomas', *The Lancet. Oncology*, 18(6), pp. e315–e329. doi: 10.1016/S1470-2045(17)30194-8.

Wen, P., Alexander, S., *et al.* (2018) 'RARE-09. EFFICACY AND SAFETY OF DABRAFENIB + TRAMETINIB IN PATIENTS WITH RECURRENT/REFRACTORY BRAF V600E–MUTATED HIGH-GRADE GLIOMA (HGG)', *Neuro-Oncology*, 20(Suppl 6), p. vi238. doi: 10.1093/neuonc/noy148.986.

Wen, P., De Greve, J., *et al.* (2018) 'RARE-11. EFFICACY AND SAFETY OF DABRAFENIB + TRAMETINIB IN PATIENTS WITH RECURRENT/REFRACTORY BRAF V600E–MUTATED LOW-GRADE GLIOMA (LGG)', *Neuro-Oncology*, 20(Suppl 6), pp. vi238–vi239. doi: 10.1093/neuonc/noy148.988.

Wen, P. Y. *et al.* (2010) 'Updated response assessment criteria for high-grade gliomas: response assessment in neuro-oncology working group', *Journal of Clinical Oncology: Official Journal of the American Society of Clinical Oncology*, 28(11), pp. 1963–1972. doi: 10.1200/JCO.2009.26.3541.

Wick, W. *et al.* (2012) 'Temozolomide chemotherapy alone versus radiotherapy alone for malignant astrocytoma in the elderly: the NOA-08 randomised, phase 3 trial', *The Lancet. Oncology*, 13(7), pp. 707–715. doi: 10.1016/S1470-2045(12)70164-X.

Wick, W. *et al.* (2016) 'Long-term analysis of the NOA-04 randomized phase III trial of sequential radiochemotherapy of anaplastic glioma with PCV or temozolomide', *Neuro-Oncology*, 18(11), pp. 1529–1537. doi: 10.1093/neuonc/now133.

Wijnenga, M. M. J. *et al.* (2017) 'Molecular and clinical heterogeneity of adult diffuse low-grade IDH wild-type gliomas: assessment of TERT promoter mutation and chromosome 7 and 10 copy number status allows superior prognostic stratification', *Acta Neuropathologica*, 134(6), pp. 957–959. doi: 10.1007/s00401-017-1781-z.

Wrensch, M. *et al.* (2009) 'Variants in the CDKN2B and RTEL1 regions are associated with high-grade glioma susceptibility', *Nature Genetics*, 41(8), pp. 905–908. doi: 10.1038/ng.408.

Wu, G. *et al.* (2012) 'Somatic histone H3 alterations in pediatric diffuse intrinsic pontine gliomas and non-brainstem glioblastomas', *Nature Genetics*, 44(3), pp. 251–253. doi: 10.1038/ng.1102.

Xu, R. *et al.* (2018) 'Extracellular vesicles in cancer - implications for future improvements in cancer care', *Nature Reviews. Clinical Oncology*, 15(10), pp. 617–638. doi: 10.1038/s41571-018-0036-9.

Xu, W. *et al.* (2011) 'Oncometabolite 2-hydroxyglutarate is a competitive inhibitor of α-ketoglutarate-dependent dioxygenases', *Cancer Cell*, 19(1), pp. 17–30. doi: 10.1016/j.ccr.2010.12.014.

Yan, H. *et al.* (2009) 'IDH1 and IDH2 mutations in gliomas', *The New England Journal of Medicine*, 360(8), pp. 765–773. doi: 10.1056/NEJMoa0808710.

Yang, J.-A. *et al.* (2015) 'LRIG1 enhances the radiosensitivity of radioresistant human glioblastoma U251 cells via attenuation of the EGFR/Akt signaling pathway', *International Journal of Clinical and Experimental Pathology*, 8(4), pp. 3580–3590.

Yoshihara, K. *et al.* (2013) 'Inferring tumour purity and stromal and immune cell admixture from expression data', *Nature Communications*, 4, p. 2612. doi: 10.1038/ncomms3612.

Zhang, C. *et al.* (2015) 'Genetic determinants of telomere length and risk of common cancers: a Mendelian randomization study', *Human Molecular Genetics*, 24(18), pp. 5356–5366. doi: 10.1093/hmg/ddv252.

Zhang, L. *et al.* (2014) 'Exome sequencing identifies somatic gain-of-function PPM1D mutations in brainstem gliomas', *Nature Genetics*, 46(7), pp. 726–730. doi: 10.1038/ng.2995.

Zhang, Y. *et al.* (2015) 'Overexpression of SCLIP promotes growth and motility in glioblastoma cells', *Cancer Biology & Therapy*, 16(1), pp. 97–105. doi: 10.4161/15384047.2014.987037.

Zhao, C. *et al.* (2016) 'Dual regulatory switch through interactions of Tcf7l2/Tcf4 with stage-specific partners propels oligodendroglial maturation', *Nature Communications*, 7, p. 10883. doi: 10.1038/ncomms10883.

Zhou, Q. L. *et al.* (2010) 'A novel pleckstrin homology domain-containing protein enhances insulin-stimulated Akt phosphorylation and GLUT4 translocation in adipocytes', *The Journal of Biological Chemistry*, 285(36), pp. 27581–27589. doi: 10.1074/jbc.M110.146886.

Appendix

ORIGINAL ARTICLE

Stroke-like events after brain radiotherapy: a large series with long-term follow-up

A. L. Di Stefano[a,b,c,*], G. Berzero[d,e,*], F. Ducray[f,g,h], M. Eoli[i], A. Pichiecchio[j,k], L. M. Farina[j], V. Cuccarini[l], M. C. Brunelli[m], L. Diamanti[d,e], S. Condette Auliac[n], A. Salmaggi[i,o], A. Silvani[i], B. Giometto[p], A. Pace[q], A. Vidiri[r], F. Bourdain[a], S. Bastianello[j,k], M. Ceroni[d,k] and E. Marchioni[d]

[a]*Department of Neurology, Hôpital Foch, Suresnes;* [b]*Service de Neurologie 2-Mazarin, AP-HP Pitié-Salpêtrière, Paris;* [c]*Inserm U 1127, CNRS UMR 7225, Institut du Cerveau et de la Moelle Épinière (ICM), Paris, France;* [d]*Neuroncology Unit, IRCCS Mondino Foundation, Pavia;* [e]*PhD Program in Biomedical Sciences, University of Pavia, Pavia, Italy;* [f]*Department of Neuroncology, Hospices Civils de Lyon, Lyon;* [g]*Department of Cancer Cell Plasticity, Cancer Research Centre of Lyon, INSERM U1052, CNRS UMR5286, Lyon;* [h]*Université Claude Bernard Lyon 1, Lyon, France;* [i]*Neuroncology Unit, Fondazione IRCCS Istituto Neurologico Carlo Besta, Milan;* [j]*Neuroradiology Unit, IRCCS Mondino Foundation, Pavia;* [k]*Department of Brain and Behavioral Sciences, University of Pavia, Pavia;* [l]*Neuroradiology Unit, Fondazione IRCCS Istituto Neurologico Carlo Besta, Milan;* [m]*Department of Neurology, Ospedale Ca' Foncello, Treviso, Italy;* [n]*Department of Neuroradiology, Hôpital Foch, Suresnes, France;* [o]*SC Neurologia, Ospedale A. Manzoni, Lecco;* [p]*Neurology Unit, Ospedale S. Antonio, Azienda ULSS6 Euganea, Padova;* [q]*Neuroncology Unit, Regina Elena National Cancer Institute, Rome; and* [r]*Radiology Unit, Regina Elena National Cancer Institute, Rome, Italy*

Keywords:
ALERT syndrome, brain tumor, focal deficit, neurotoxicity, peri-ictal pseudoprogression, radiotherapy, SMART syndrome, stroke

Received 20 June 2018
Accepted 7 November 2018

European Journal of Neurology 2019, **0:** 1–12

doi:10.1111/ene.13870

Background and purpose: Patients with a history of brain radiotherapy can experience acute stroke-like syndromes related to the delayed effects of brain radiation, including stroke-like migraine attacks after radiation therapy syndrome, peri-ictal pseudoprogression and acute late-onset encephalopathy after radiation therapy syndrome. The aim of this study was to collect evidence on the long-term outcome and treatment of these conditions, whose knowledge is undermined by their rarity and fragmented description.

Methods: Cases were collected, both prospectively and retrospectively, amongst six neuro-oncology departments. Inclusion criteria were as follows: (i) history of brain radiotherapy (completed at least 6 months before the acute episode); (ii) new onset of acute/subacute neurological symptoms; (iii) exclusion of all etiologies unrelated to brain irradiation. A review of current literature on stroke-like syndromes was performed to corroborate our findings.

Results: Thirty-two patients with acute neurological conditions attributed to the delayed effects of radiation were identified, including 26 patients with stroke-like syndromes. Patients with stroke-like syndromes commonly presented with a mosaic of symptoms, including focal deficits (77%), encephalopathy (50%), seizures (35%) and headache (35%). Seventy-three percent of them had acute consistent magnetic resonance imaging alterations. Treatment included high-dose steroids in 65% of cases. Twenty-two patients recovered completely (85%). Sixteen patients (62%) experienced relapses (median follow-up 3.5 years). A literature review identified 87 additional stroke-like cases with similar characteristics.

Conclusions: Stroke-like events related to brain irradiation may be associated with permanent sequelae. Steroids are often administered on empirical grounds, as they are thought to accelerate recovery. Relapses are common, highlighting the need to elaborate adequate prevention strategies.

Correspondence: G. Berzero, Neuroncology Unit, IRCCS Mondino Foundation, Via Mondino 2, Pavia, Italy (tel.: + 39 382 380225; fax: + 39 382 380226; e-mail: giulia.berzero@mondino.it).
*These authors contributed equally to the paper.

Introduction

Long-term survivors after brain radiotherapy can experience acute stroke-like events related to the

delayed effects of brain irradiation. The description of these disorders is currently divided into three distinct entities: stroke-like migraine attacks after radiation therapy (SMART) syndrome [1,2], peri-ictal pseudoprogression (PIPG) [3] and acute late-onset encephalopathy after radiation therapy (ALERT) syndrome [4]. Despite being described separately, these syndromes actually share a number of common features, including the long interval from brain irradiation, the acute onset, the association with transient enhancing magnetic resonance imaging (MRI) abnormalities, reversibility and recurrence. All these elements suggest that SMART, PIPG and ALERT may be different entities within the same spectrum of disorders. Although stroke-like syndromes have been described for over a decade, the rarity of these conditions, together with their delayed occurrence, hampers the realization of prospective studies, and current evidence is limited to isolated case reports or small case series. As a result, knowledge on these syndromes remains fragmented and dispersed. To complicate this scenario, patients with a history of brain radiotherapy may also experience actual strokes [5,6], and the potential relationship between stroke and stroke-like events related to brain irradiation is still unclear.

In the present study, a large series of patients with stroke-like events and an extensive review of the literature on this subject are reported, with the aim of collecting evidence on the long-term outcome and treatment of these conditions.

Patients and methods

Present series

A multicentric study group on this topic, including six institutions in Italy and France, was created in 2012. Patients were observed prospectively after the creation of the study group (2012–2017) or identified by retrospective review of institutional databases (1995–2011), using combinations of the following keywords: 'brain tumor', 'radiotherapy', 'encephalopathy', 'coma', 'seizures', 'headache', 'focal deficit', 'transient ischemic attack' and 'stroke'. Inclusion criteria were as follows: (i) a history of brain radiotherapy completed at least 6 months before the acute episode; (ii) new onset of acute/subacute neurological symptoms; (iii) exclusion of all etiologies unrelated to the effects of radiation. Minimal diagnostic work-up included routine blood tests, brain MRI with contrast injection and electroencephalography (EEG). In patients with encephalopathy, cerebrospinal fluid analysis with culture and search for herpesviruses was also required. Additional biological and instrumental assessments were taken into account case by case. After collective revision, only well-documented cases for which all alternative etiologies could be safely excluded were retained in the study. Two neuroradiologists (A.P., L.F.), independent from those who initially evaluated patient cases, reviewed MRI scans and identified recurrent imaging patterns. The study was approved by institutional ethics committees.

Literature review

In order to substantiate our findings, a review of the literature on stroke-like syndromes was performed. A keyword search of MEDLINE was performed and complemented by cross-checking citations. The keyword search of MEDLINE was restricted to papers in English and French published between January 1995 and February 2018, and was performed using combinations of the following keywords: 'radiotherapy', 'neurotoxicity', 'headache', 'stroke-like', 'SMART syndrome', 'status epilepticus', 'peri-ictal pseudoprogression', 'coma' and 'ALERT syndrome'. Figure S1 reports the algorithm for paper selection.

Results

Present series

Thirty-two patients were identified (15 prospective and 17 retrospective cases), including seven cases that had been previously published (patients 1–5 in [4] and patients 10 and 11 in [3]). All 32 patients had acute neurological conditions attributed to the delayed effects of radiation: six patients had small vessel infarcts and 26 patients had stroke-like events.

Stroke-like events

Table 1 reports previous tumor history, clinical–paraclinical features at the time of the acute episode, treatment and outcome in the 26 patients with stroke-like events (patients 1–26).

Previous tumor history. All patients had received brain irradiation. The indications to brain radiotherapy included primary brain tumors (62%), systemic malignancies (27%), intracranial extradural tumors (8%) and vascular malformations (4%). The median age at the time of radiotherapy was 37 years (range 4–69). Twelve patients had received focal radiotherapy (46%) and 13 patients whole-brain or craniospinal radiotherapy (50%); the remaining patient (patient 8) had received both radiotherapy types. Fifteen patients had received systemic chemotherapy (58%). Three patients had a history of intrathecal chemotherapy (12%).

Table 1 Previous tumor history, clinical and paraclinical features at the time of the acute episode, treatment and outcome in the 26 patients with stroke-like events (patients 1–26)

			Tumor history			Clinical and paraclinical features at the time of the acute episode						Treatment and outcome					
								MRI characteristics									
Patient	Sex	Age at RT	Type, location, side	Treatment	Delay since RT (years)	Clinical presentation	EEG	T2/FLAIR	DWI B1000/ ADC	T1 gad	Final diagnosis	Treatment	Recovery (residual deficit)	Time to recovery (days)	Relapse (side)	Final outcome	FU since 1st episode (years)
1	M	30	Gr. III astro, F, L	Su; WBRT (60 Gy); Ch	6	Stupor (GCS 4), aphasia, right hemiplegia, left arm decorticated posturing	Left depression	No cortical HS No cortical-subcortical abnormalities	n.a.	Multiple bilateral (mainly left) cortico-subcortical areas of patchy Enh	ALERT	IV MP 1 g daily (5 days), oral steroids tapering, AED	Partial (hemiparesis)	14	Yes (ipsil. and contral.)	Death from pneumonia	2.5
2	M	37	Gr. II oligo, F, L	WBRT (60 Gy); Ch	17	Confusion, coma (GCS 3), visual hallucinations, dysphagia	Diffuse slowing with left prevalence	No cortical HS No cortical-subcortical abnormalities	No diffusion restriction	No Enh	ALERT	IV MP 1 g daily (5 days), oral steroids tapering, AED	Complete	20	No	Tumor stable disease	6
3	M	17	Gr. III meningioma, P, L	Su; WBRT (60 Gy)	10	Headache, stupor (GCS 4), alternating-side partial motor seizures	Diffuse slowing (right prevalence); isolated epileptic discharges	No cortical HS No cortical-subcortical abnormalities	n.a.	No Enh	ALERT	IM DXM 16 mg daily, oral steroids tapering, AED	Partial (paraparesis, cognitive decline)	24	Yes (ipsil.)	Death from pneumonia	2
4	M	21	CNS involvement of NHL	WBRT (30 Gy)	0.75	Stupor (GCS 10), headache, aphasia, right hemiparesis	Right T-O spike-slow waves complexes	Left rolandic subcortical focal hyperintensities	Left rolandic subcortical focal restriction	Bilateral (mainly left) rolandic subcortical patchy Enh	ALERT	IV MP 1 g daily (5 days), oral steroids tapering, AED	Complete	12	Yes (contral.)	Tumor complete remission	6
5	F	58	Single metastasis, Cerebell	Su; WBRT (30 Gy)	6	Stupor (GCS 8), headache, aphasia, right hemiplegia, right facio-brachial dystonic seizures	Bifrontal slow abnormalities	No cortical HS No cortical-subcortical abnormalities	No diffusion restriction	No Enh	ALERT	IV MP 1 g daily (5 days), oral steroids tapering, AED	Complete	4	No	Tumor stable disease	1.4
6	M	25	Choriocarcinoma, pineal	Su; WBRT; Ch	4	Psychomotor decline, global motor impairment	No epileptic abnormalities	Multiple bilateral focal subcortical and periven. areas of HS	n.a.	Multiple bilateral subcortical and periven. areas of patchy Enh	ALERT	AED	Partial (worsening neuropsy. background)	45	No	Tumor remission	6
7	M	20	Brain metastasis, P, L	Su; WBRT; radiosurgery	2	Right partial motor seizures	No epileptic abnormalities	Multiple focal areas of HS in corpus callosum and left periven. WM	n.a.	Ring Enh of the left anterior periven. lesion	ALERT	Steroids, AED	Complete	3	Yes (ipsil.)	Systemic tumor progression 9 years after 1st episode	9
8	M	4		Su; CS RT	43								Complete	15	No		0.5

(continued)

Table 1 *(Continued)*

			Tumor history			Clinical and paraclinical features at the time of the acute episode						Treatment and outcome					
								MRI characteristics									
Patient	Sex	Age at RT	Type, location, side	Treatment	Delay since RT (years)	Clinical presentation	EEG	T2/FLAIR	DWI B1000/ ADC	T1 gad	Final diagnosis	Treatment	Recovery (residual deficit)	Time to recovery (days)	Relapse (side)	Final outcome	FU since 1st episode (years)
		45	Medullo, Cerebell, L Gr. III meningioma, P-O, R	Su; RT	2	Psychomotor decline, global motor impairment	Bilateral diffuse slow abnormalities	Left P-O cortical HS and swelling	Left P-O foci of cortical HS on B1000 (ADC n.a.)	Left P-O cortical gyriform Enh	SMART/ PIPG	IV DXM 8 mg daily (15 days) followed by tapering, antivirals, antibiotics				Tumor stable disease	
9	M	53	Single metastasis, T, R	Su; WBRT (30 Gy), Ch	7	Psychomotor slowing, left motor seizures	Right T-P-O epileptic discharges	Right T-P-I cortical-juxtacortical HS and swelling	Right T-P focal diffusion restriction	Right T-P gyriform Enh	SMART/ PIPG	AED, steroids	Complete	53	Yes (ipsil.)	Tumor remission	5
10	M	44	GBM, P-O, R	Su; RT; Ch	5	Drowsiness, dysarthria, left arm progressive sensory disturbance, left partial sensory seizures	Right T-P epileptic discharges	Right T-P HS involving both cortex and subcortical deep WM	n.a.	Right T-P cortico-subcortical Enh	SMART/ PIPG	Oral prednisone 40 mg daily (7 days) followed by tapering, AED	Complete	7	Yes (ipsil.)	Tumor complete response	11
11	M	42	Gr. III oligo, F-T, R	Su; RT; Ch	3	Drowsiness, left hemiparesis, left partial motor seizures	Right F epileptic discharges	n.a.	n.a.	Right F-I-T lepto. and cortical-subcortical Enh	SMART/ PIPG	Oral prednisone 40 mg daily (7 days) followed by tapering, AED	Complete	21	Yes (ipsil.)	Tumor stable disease	5
12	M	16	Meningosarcoma, F-T, R	Su; RT (60 Gy)	32	Psychomotor slowing, aphasia, left hemiparesis, left LHH	Right slow and epileptic abnormalities	Right T cortical-subcortical HS and swelling	Right T cortical diffusion restriction	Right T cortical Enh	SMART/ PIPG	IV MP 1 g daily (5 days), oral steroids tapering, AED	Complete	90	No	Tumor remission	1.1
13	M	35	Grade II astro, Cerebell, R	Su; RT	17	Confusion, headache, left LHH	Right F-T slow abnormalities	Right T-P-O cortical-subcortical HS and swelling	Right T-P-O diffusion restriction	Right T-P-O cortical-subcortical Enh	SMART/ PIPG	IV MP 1 g daily (5 days), oral steroids tapering	Complete	8	No	Tumor stable disease	1.5
14	M	69	Gr. II oligo, T-P, R	Su; RT; Ch	12	Confusion, headache, left arm motor deficit, left LHH	Right F-T slow abnormalities	Right T-P mild cortical HS	Right T-P diffusion restriction	Right T-P cortical-subcortical Enh	SMART/ PIPG	IV MP 125 mg daily (5 days), oral steroids tapering, AED	Complete	14	Yes (ipsil.)	Tumor stable disease	3
15	F	42	CNS involvement of NHL	WBRT (40 Gy)	17	Headache, aphasia, right hemiplegia,	Left hemispheric slow abnormalities	Left hemispheric cortical HS	Left hemispheric subcortical	Left hemispheric cortical gyriform Enh	SMART/ PIPG	IV DXM 40 mg daily followed by tapering,	Partial (hemiparesis, aphasia)	90	Yes (ipsil.)	Death from pneumonia	0.75

(continued)

Table 1 *(Continued)*

			Tumor history			Clinical and paraclinical features at the time of the acute episode						Treatment and outcome					
								MRI characteristics									
Patient	Sex	Age at RT	Type, location, side	Treatment	Delay since RT (years)	Clinical presentation	EEG	T2/FLAIR	DWI B1000/ ADC	T1 gad	Final diagnosis	Treatment	Recovery (residual deficit)	Time to recovery (days)	Relapse (side)	Final outcome	FU since 1st episode (years)
						right partial motor seizures			diffusion restriction			antivirals, antibiotics, AED					
16	M	53	Gr. III astro, T-P, L	Su; RT (60 Gy); Ch	10	Headache, aphasia	Left T focal slow abnormalities	Left T-P cortical-subcortical HS and swelling	n.a.	Left T-P punctate cortical Enh	SMART/ PIPG	DXM 4 mg daily (3 months), antivirals	Complete	20	Yes (ipsil.)	Tumor stable disease	3
17	F	37	Gr. III astro, P, L	Su; RT (60 Gy); Ch	20	Headache, aphasia, right hemiparesis	Infraclinical left F epileptic discharges	Left F-P cortical-subcortical HS	Left F cortical focal diffusion restriction	Left rolandic patchy cortical Enh	SMART/ PIPG	NSAID, AED	Complete	6	No	Tumor stable disease	3
18	M	28	Plasmocytoma, left nasal fossa	RT	20	Headache, right LHH	Left T slow and epileptic abnormalities	Left O cortical-subcortical HS and mild swelling	Left O partial focal restriction	Left O cortical Enh	SMART/ PIPG	AED, antiplatelets	Complete	18	No	Tumor remission	1
19	M	61	Chondrosarcoma, P, L	Su; RT; Ch	5	Aphasia, right LHH, right focal seizures	Left T slow post-ictal abnormalities	Left P-O cortical hyperdensity and swelling with cortical gyriform Enh (head CT with contrast)			SMART/ PIPG	AED	Complete	12	Yes (ipsil.)	Tumor remission	11
20	M	14	Medullo, Cerebell	Su; CS RT; intrathecal Mtx; Ch	28	Left partial sensory seizures, left LHH	Left hemispheric slow abnormalities	Right T-P-O cortical HS and swelling	Right T-P-O cortical HS on B1000, partial ADC restriction	Right T-P-O cortical Enh	SMART/ PIPG	IV MP 1 g daily (5 days), oral steroids tapering, AED, antiplatelets	Complete	15	Yes (ipsil. and contral.)	Tumor stable disease	6
21	M	32	Cavernous angioma, pons	RT	33	Right LHH	Left T focal slow abnormalities	Left O cortical HS	No diffusion restriction	Left O gyriform Enh	SMART/ PIPG	IM DXM 8 mg daily (8 days) followed by tapering	Complete	12	No	Tumor stable disease	9
22	M	48	Gr. II oligo-astro, O, R	Su; RT; Ch	8	Left arm paresis	Right T focal slow and epileptic abnormalities	n.a.	Right T-P cortical HS on B1000, partial ADC restriction	Right T-P peritumoral gyriform Enh	SMART/ PIPG	AED	Complete	21	No	Tumor stable disease	3
23	F	39	Gr. II oligo, F, L	Su; Ch; RT (60 Gy)	11	Dysarthria, right-sided sensory disturbance, right hemiparesis	Left focal slow waves	No cortical HS No cortical-subcortical abnormalities	No diffusion restriction	No Enh	Short-lasting focal deficits	Antiplatelets, AED	Complete	<12 h	Yes (ipsil.)	Tumor stable disease	4
24	F	26	Medullo, Cerebell, R	Su; CS RT; intrathecal Mtx+Ara-C; Ch	17	Aphasia	No abnormalities	No cortical HS No cortical-subcortical abnormalities	No diffusion restriction	No Enh	Short-lasting focal deficits	Antiplatelets, AED	Complete	1 h	Yes (ipsil.)	Tumor remission	1.75
25	M	55	Small cell lung cancer	Prophylactic WBRT (36 Gy); Ch	6	Aphasia, left sensory deficit	Right T-P-O slow abnormalities	No cortical HS No cortical-subcortical abnormalities	No diffusion restriction	No Enh	Short-lasting focal deficits	None	Complete	1.5 h	Yes (ipsil.)	Tumor remission	5

(continued)

Table 1 *(Continued)*

			Tumor history			Clinical and paraclinical features at the time of the acute episode						Treatment and outcome				
								MRI characteristics								
Patient	Sex	Age at RT	Type, location, side	Treatment	Delay since RT (years)	Clinical presentation	EEG	T2/FLAIR	DWI B1000/ ADC	T1 gad	Final diagnosis	Treatment	Recovery (residual deficit)	Time to recovery (days)	Relapse (side)	Final outcome	FU since 1st episode (years)
26	M	23	CNS involvement of NHL	WBRT; intrathecal Mtx	12	Dysarthria	No abnormalities	No cortical HS No cortical-subcortical abnormalities	No diffusion restriction	No Enh	Short-lasting focal deficits	Antiplatelets	Complete	<4 h	Yes (ipsil. and contral.)	Tumor remission	20

AED, antiepileptic drugs; ALERT, acute late-onset encephalopathy after radiation therapy; Ara-C, cytarabine; astro, astrocytoma; Cerebell, cerebellum; Ch, chemotherapy; CNS, central nervous system; contral., contralateral; CS, craniospinal; CT, computed tomography; DWI/ADC, Diffusion-Weighted Imaging/Apparent Diffusion Coefficient; DXM, dexamethasone; EEG, electroencephalography; Enh, enhancement; F, frontal; FLAIR, fluid-attenuated inversion recovery; FU, follow-up; GBM, glioblastoma; GCS, Glasgow Coma Scale; Gr, grade; HS, hypersignal; I, insular; IM, intramuscular; ipsil., ipsilateral; IV, intravenous; L, left; lepto, leptomeningeal; LHH, lateral homonymous hemianopia; Medullo, medulloblastoma; MP, methylprednisolone; MRI, magnetic resonance imaging; Mtx, methotrexate; n.a., not available; neuropsy., neuropsychiatric; NHL, non-Hodgkin lymphoma; NSAID, non-steroidal anti-inflammatory drugs; O, occipital; oligo, oligodendroglioma; P, parietal; PCNSL, primary central nervous system lymphoma; periven., periventricular; PIPG, peri-ictal pseudoprogression; R, right; RT, radiotherapy; SMART, stroke-like migraine attacks after radiation therapy; Su, surgery; T, temporal; T1 gad, T1-weighted gadolinium enhanced; WBRT, whole-brain radiotherapy; WM, white matter.

Clinical and paraclinical features at the time of the acute episode. The acute episode occurred after a median delay of 10 years from brain radiotherapy (range 0.75–43). Acute neurological symptoms were preceded (or accompanied) by fever in seven cases (27%) and by elevated blood pressure in one (4%). Clinical presentation was generally characterized by a mosaic of symptoms, including focal deficits (77%), encephalopathy (50%), headache (35%) and seizures (35%). Brain MRI ruled out tumor recurrence and showed mild to severe chronic post-actinic changes in all patients (including progressive leukoencephalopathy, microbleeds and cortical atrophy). Over this chronic ground, 19 out of the 26 patients (73%) had the appearance of acute enhancing MRI alterations. Acute MRI abnormalities were in all cases consistent with acute neurological symptoms and located within brain areas that received irradiation. Based on clinical and MRI features at the time of the acute episode, three clinical–radiological groups were identified.

- ALERT syndrome (patients 1–7): Patients in this group had encephalopathy and/or seizures, associated with stroke-like deficits and/or headache. Encephalopathy ranged from mild psychomotor slowing to severe vigilance impairment and was the dominant clinical feature in most patients. In four of the seven patients (57%), MRI showed acute multifocal abnormalities in the subcortical and/or periventricular white matter characterized by punctuate or ring contrast enhancement (Fig. 1). The remaining three patients had normal MRI findings. All seven patients had received whole-brain radiotherapy, explaining the diffuse/multifocal involvement observed on clinical and radiological grounds.
- SMART syndrome and PIPG (patients 8–22): Patients in this group had focal stroke-like deficits and/or mild encephalopathy, associated with headache and/or seizures. In all 15 patients, MRI showed a unilateral cortical-subcortical area of hyperintensity and swelling on T2/fluid-attenuated inversion recovery (FLAIR) images, with prominent cortical enhancement on T1-weighted images after gadolinium injection (T1 gad) (Fig. 2). The pattern of contrast enhancement was either multilobar and gyriform, as reported in classical SMART cases [2,3], or nodular and peritumoral, as reported in PIPG [4]. The clinical and radiological features of patients in this group corresponded to a strictly unilateral hemispheric dysfunction and, consistently, 12 out of the 15 patients (80%) had received focal radiotherapy over the affected hemisphere.
- Short-lasting focal deficits (patients 23–26): Patients in this group had recurrent episodes characterized by short-lasting (1–12 h) focal deficits without

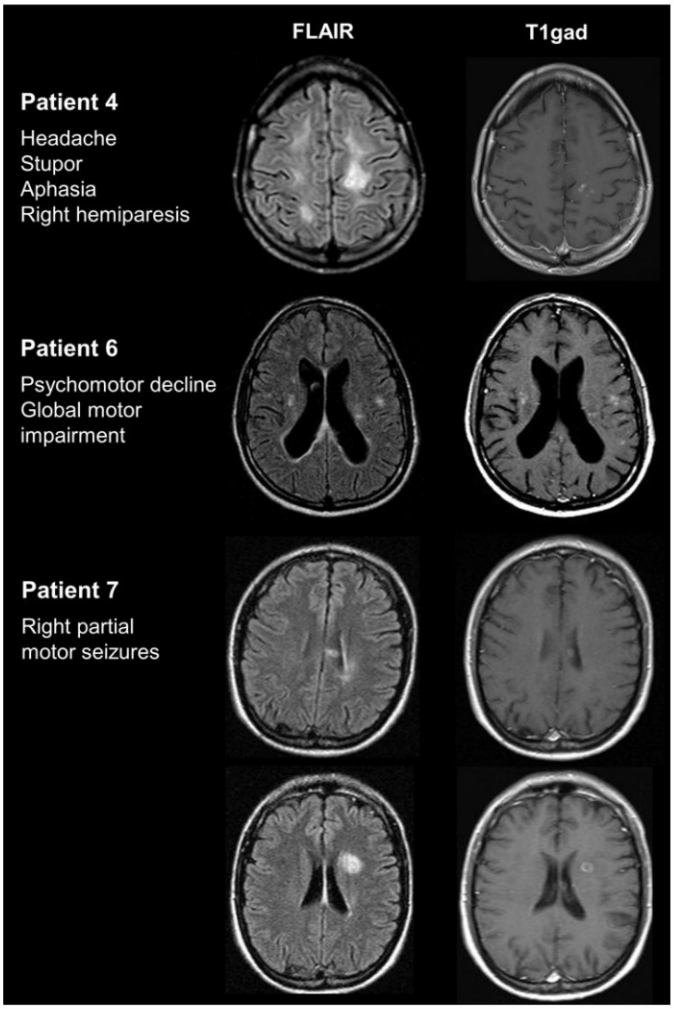

Figure 1 MRI findings in patients with ALERT syndrome. Patient 4: Two focal hyperintensities in the left rolandic subcortical region in the context of multiple confluent white matter lesions on FLAIR images, with patchy enhancement on T1 gad. Patient 6: Multiple bilateral focal subcortical and periventricular hyperintensities on FLAIR images, with patchy enhancement on T1 gad. Patient 7: Multiple focal areas of hyperintensity in left periventricular white matter and corpus callosum on FLAIR images, some of which show mild contrast enhancement on T1 gad; focal hyperintensity with mild mass effect in the left anterior periventricular region with ring contrast enhancement.

headache or other accompanying symptoms. None of them had acute abnormalities on MRI. All four patients underwent a thorough cerebrovascular assessment (carotid ultrasound, intracranial angio-computed tomography (CT) or MR angiogram, thrombophilic panel, electrocardiogram and transthoracic echocardiogram) but no arguments for an atherothromboembolic etiology were found. Clinical characteristics and repeated EEG testing ruled out an epileptic mechanism. Three patients out of the four had received whole-brain or craniospinal radiotherapy (75%); two of the latter had also received intrathecal chemotherapy (50%).

Treatment and outcome. Seventeen of the 26 patients with stroke-like events received high-dose steroids on empirical grounds (65%). Twenty-two patients recovered completely (85%), with a median time to recovery of 14 days (range 1–90). Four patients were left with permanent sequelae (15%). Three patients amongst the latter ultimately developed a steroid-dependent course (i.e. worsening of neurological symptoms at steroid tapering) and died because of steroid-related complications. Acute enhancing MRI alterations (whenever present) resolved in 3–8 months. Sixteen patients experienced subsequent episodes of stroke-like events during follow-up (62%), involving

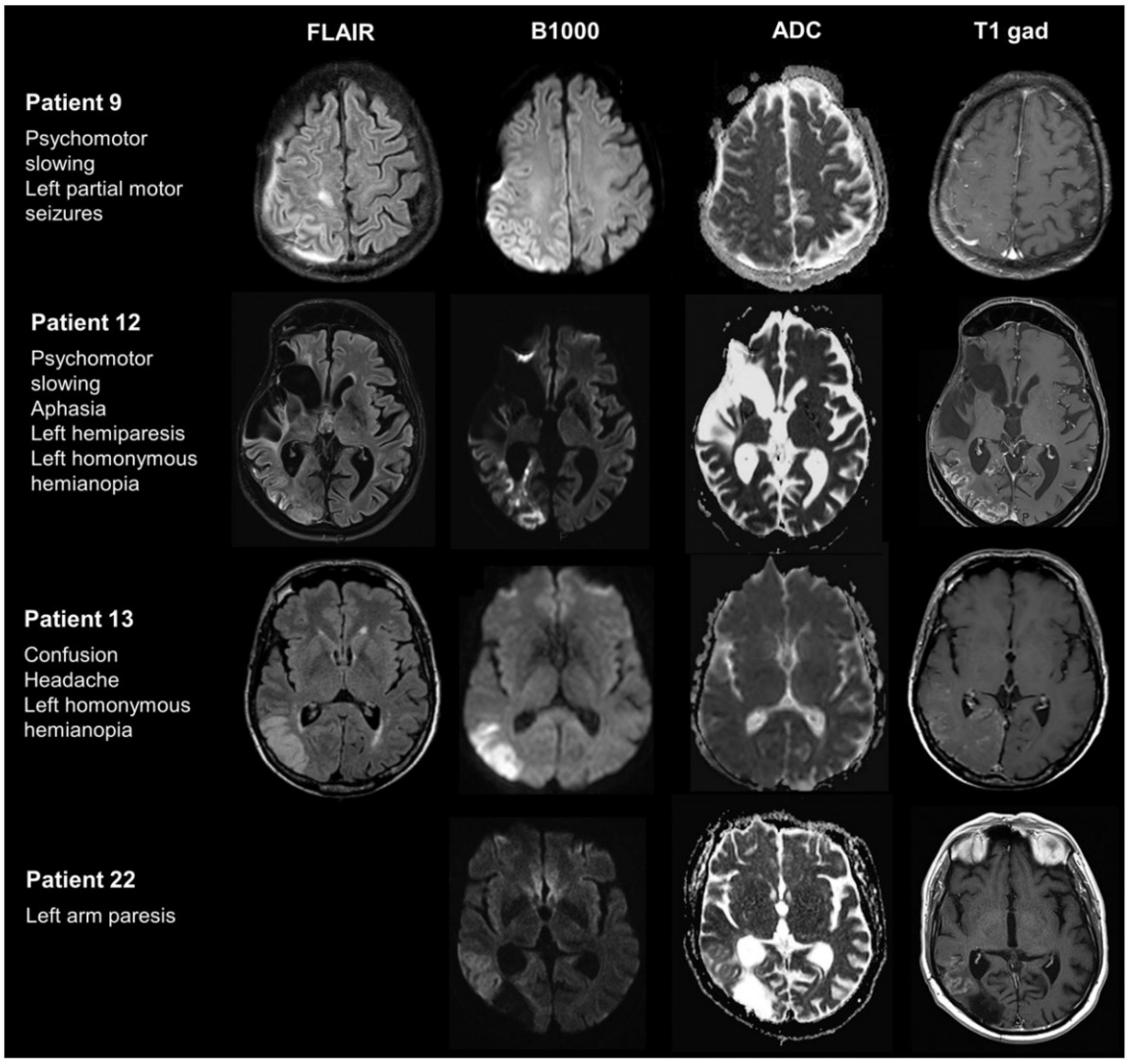

Figure 2 MRI findings in patients with SMART syndrome and PIPG. Patient 9: Right cortical parietal hyperintensity on FLAIR images with focal diffusion restriction on Diffusion-Weighted Imaging/Apparent Diffusion Coefficient (DWI/ADC) and gyriform enhancement on T1 gad. Patient 12: Right temporo-parieto-occipital cortico-subcortical hyperintensity and swelling on FLAIR images, with partial diffusion restriction on DWI/ADC and marked cortical enhancement on T1 gad. Patient 13: Right temporo-occipital cortical-subcortical hypersignal and swelling on FLAIR images, with diffusion restriction on DWI/ADC and cortical-subcortical enhancement on T1 gad. Patient 22: Right cortical peritumoral gyriform hyperintensity on DWI B1000, associated with partial ADC hyposignal and neat cortical enhancement on T1 gad.

the same and/or the contralateral hemisphere (if the latter had received irradiation). Median follow-up duration in the cohort of stroke-like patients was 3.5 years (range 0.5–20).

Small vessel infarcts

Table 2 reports previous tumor history, clinical–paraclinical features, treatment and outcome in the six patients experiencing small vessel infarcts (patients 27–32). Five patients had received focal radiotherapy and one patient whole-brain radiotherapy. The median age at the time of radiotherapy was 34.5 years (range 17–70). Stroke occurred after a median delay of 12 years after brain irradiation (range 1–32). The ischaemic area was located in the periventricular white matter in four cases and in the thalamocapsular region in two (Fig. 3). In all cases, the ischaemic lesion was congruous with acute neurological

Table 2 Previous tumor history, clinical and paraclinical features, treatment and outcome in the six patients with small vessel infarcts (patients 27–32)

			Tumor history			Clinical and paraclinical features at the time of the acute episode						Treatment and outcome					
								MRI characteristics									
Patient	Sex	Age at RT	Type, location, side	Treatment	Delay since RT (years)	Clinical presentation	EEG	T2/FLAIR	DWI B1000/ ADC	T1 gad	Final diagnosis	Treatment	Recovery (residual deficit)	Time to recovery (days)	Relapse (side)	Final outcome	FU since 1st episode (years)
27	M	31	PCNSL, Cerebell	Su; RT; Ch	12	Right sensory deficit	No abnormalities	Left deep insular periven. focal HS	Left insular nodular hyperintensity on B1000 without ADC hyposignal	Left insular nodular Enh	Lacunar stroke	AED	Complete	7	No	Tumor remission	4
28	M	70	GBM, T-I, L	Su+carmustine wafer implant; RT; Ch; cyberknife	1	Aphasia, right hemiparesis	Left F-T focal slow abnormalities	Left capsulo-putaminal nodular hyperintensity	Left capsulo-putaminal nodular HS on B1000, no ADC hyposignal	No Enh	Lacunar stroke	Antiplatelets, AED	Partial (dysphasia)	90	No	Death from tumor progression	0.6
29	M	29	Gr. II oligo, T, R	Su; RT (54 Gy)	21	Left hemiparesis, left sensory deficit	Right T focal slow and epileptic abnormalities	n.a.	Multiple foci of diffusion restriction in right posterior deep WM	n.a.	Lacunar stroke	Antiplatelets, AED	Complete	14	Yes (ipsil.)	Tumor progression 1 year after 1st episode	7
30	F	38	Low grade glioma, T-I, L	RT; Ch	12	Dysarthria, right hemiparesis, right sensory deficit	Left F-T slow abnormalities	Left nodular periven. HS	n.a.	Left periven. nodular Enh	Lacunar stroke	Antiplatelets, AED	Complete	15	Yes (ipsil.)	Tumor progression 2 years after 1st episode	4
31	M	17	Probable germinoma, midline	WBRT	32	Right hemiparesis, right sensory deficit	No abnormalities	Focal area of HS in left periven. WM	Focal area of HS in left periven. WM on B1000 (ADC n.a.)	No Enh	Lacunar stroke	Antiplatelets	Complete	10	Yes (contral.)	Tumor remission	1.5
32	F	58	Pituitary adenoma	Su; RT	6	Left hemiparesis, left sensory deficit	No abnormalities	Focal area of HS in right thalamus	Focal area of diffusion restriction in right thalamus	n.a.	Lacunar stroke	Antiplatelets, AED	Complete	14	Yes (ipsil. and contral.)	Tumor stable disease	1.2

AED, antiepileptic drugs; Cerebell, cerebellum; Ch, chemotherapy; contral., contralateral; DWI/ADC, Diffusion-Weighted Imaging/Apparent Diffusion Coefficient; EEG, electroencephalography; Enh, enhancement; FLAIR, fluid-attenuated inversion recovery; FU, follow-up; GBM, glioblastoma; Gr, grade; HS, hypersignal; I, insular; ipsil., ipsilateral; L, left; MRI, magnetic resonance imaging; n.a., not available; oligo, oligodendroglioma; PCNSL, primary central nervous system lymphoma; periven., periventricular; R, right; RT, radiotherapy; Su, surgery; T, temporal; T1 gad, T1-weighted gadolinium enhanced; WBRT, whole-brain radiotherapy; WM, white matter.

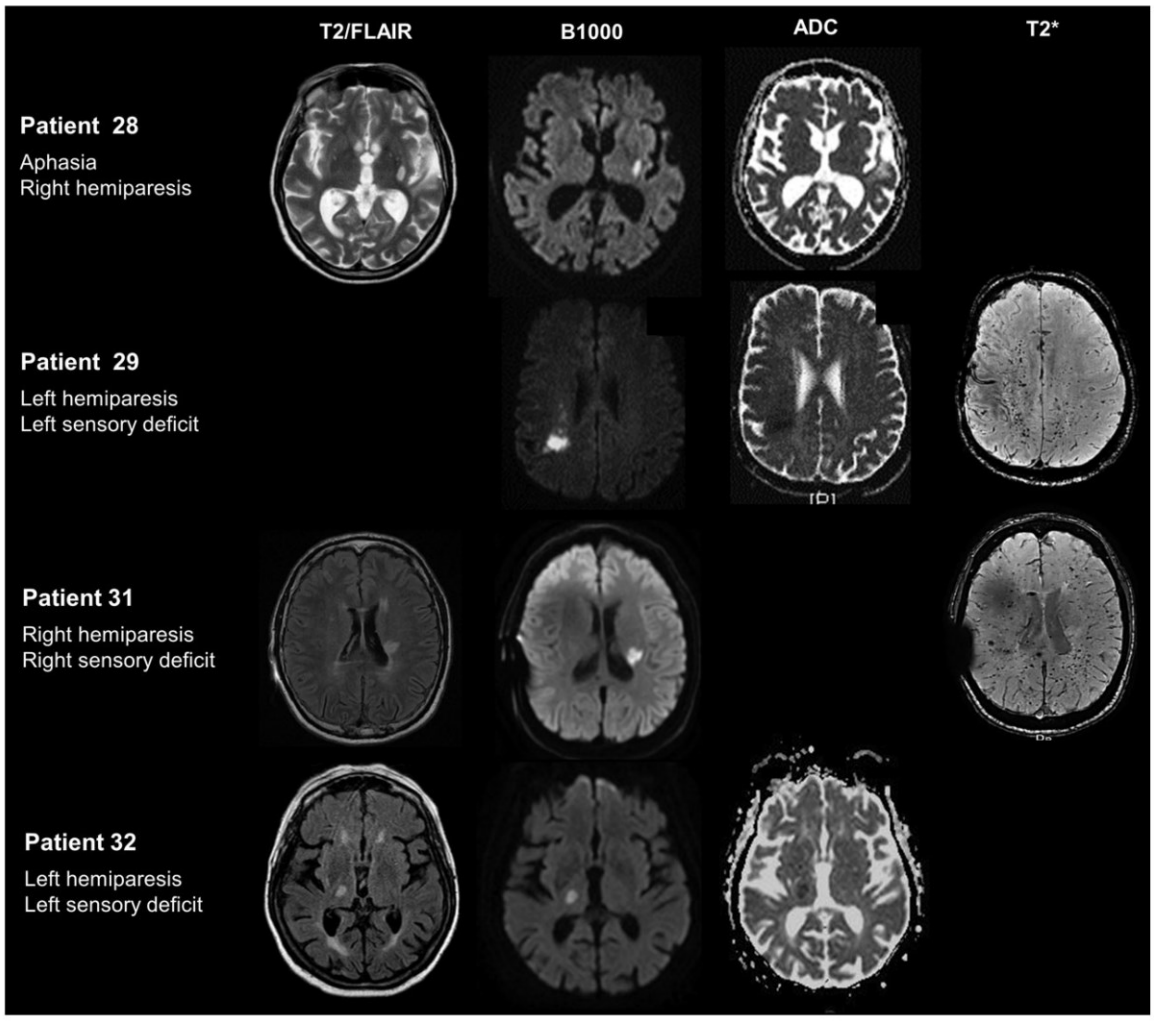

Figure 3 MRI findings in patients with small vessel infarcts. Patient 28: Left capsulo-putaminal nodular hyperintensity on FLAIR and DWI B1000, without diffusion restriction on ADC (MRI performed 13 days after acute onset). Patient 29: Multiple foci of restricted diffusion on DWI/ADC in posterior deep white matter; note the multiple bilateral susceptibility foci on T2*, mainly in the right hemisphere. Patient 31: Focal area of hypersignal in left periventricular white matter on FLAIR and DWI B1000; note the T2* diffuse bilateral focal susceptibility foci in the bihemispheric white matter. Patient 32: Focal area of hypersignal in right thalamus on FLAIR images, with corresponding diffusion restriction in DWI/ADC.

symptoms and located within the radiation port. No source of cardiac or carotid thromboembolism was found. Intracranial vessel evaluation (by MR angiography, CT angiography or ultrasound) disclosed multiple non-critical stenoses in the vessels included in the radiation port in absence of acute vessel occlusions. Five patients out of the six were given antiplatelets. Five patients recovered completely (83%) in 7–15 days. Four patients had subsequent small vessel infarcts (67%) in the same or in other vascular territory involved by radiation.

Literature review

Literature review identified 87 cases of stroke-like syndromes after brain irradiation (Table S1). The indications for brain radiotherapy included primary brain tumors (71%), systemic malignancies (26%) and intracranial extradural tumors (2%). The median age at the time of radiotherapy was 31 years (range 5–71). The acute episode occurred after a median delay of 13 years (range 1–35) from brain radiotherapy. Clinical presentation included stroke-like deficits (87%), headache (72%),

Table 3 Stroke-like events: summary of main clinical–paraclinical features, treatment and outcome in patients in the present series (n = 26) and in the literature (n = 87)

	Present series (n = 26)	Literature review (n = 87)
Previous tumor history		
Tumor type		
Primary brain tumor	16 (62%)	62 (71%)
CNS localizations or prophylaxis in patients with systemic cancer	7 (27%)	23 (26%)
Intracranial extradural tumor	2 (8%)	2 (2%)
Other	1 (4%)	0
RT type		
Focal RT	13 (48%)[b]	36 (53%)[c]
WBRT/CS RT	14 (52%)[b]	32 (47%)[c]
Median age at the time of RT, years (range)	37 (4–69)	31 (5–71)
Intrathecal Ch	3 (12%)	1 (1%)[c]
Systemic Ch	15 (58%)	28 (41%)[c]
Clinical–radiological features during the acute episode		
Median delay after RT, years (range)	10 (0.75–43)	13 (1–35)
Neurological presentation		
Encephalopathy	13 (50%)	36 (41%)
Stroke-like deficits	20 (77%)	76 (87%)
Seizures	9 (35%)	55 (63%)
Headache	9 (35%)	63 (72%)
Acute MRI abnormalities	19 (73%)	75 (86%)
Treatment and outcome		
Steroid administration	17 (65%)	24 (28%)
Steroid dependence[a]	3 (12%)	n.a.
Full recovery	22 (85%)	69 (79%)
Recurrent episodes	16 (62%)	49 (56%)
Median FU, years (range)	3.5 (0.5–20)	1.5 (0.25–14)

Ch, chemotherapy; CNS, central nervous system; CS, craniospinal; FU, follow-up; MRI, magnetic resonance imaging; n.a., not available; RT, radiotherapy; WBRT, whole-brain radiotherapy. [a]Steroid dependence is defined by neurological deterioration at steroid tapering; [b]percentages are calculated over a total of $n + 1$ irradiations (patient 8 was irradiated twice); [c]percentages are calculated over a total of 68 patients, as previous tumor treatments including radiotherapy type are unavailable in 19 cases.

seizures (63%) and encephalopathy (41%). Eighty-six percent of patients had acute consistent MRI alterations. Twenty-eight percent of patients received high-dose steroids. Seventy-nine percent of patients recovered completely. Follow-up information is reported in only 40% of cases. Fifty-six percent of patients experienced relapses of stroke-like events during follow-up (median duration 1.5 years; range 0.25–14).

Discussion

This study reports a large original series of patients with stroke-like events related to the delayed effects of brain irradiation (n = 26) together with a comprehensive review of the literature on this topic (n = 87). The strong point of the study is the magnitude of the resulting cohort (n = 113), which allows solid considerations to be drawn on the clinical–radiological profile and the long-term outcome associated with these conditions. The main limitations of the study concern the lack of details on the total dose and fractionation of radiotherapy, as radiation was administered decades before the acute episode or was performed in other centers, and the fact that steroid administration was not carried out according to standardized protocols, limiting our capacity to conclude on its efficacy.

Table 3 summarizes the clinical–radiological features of stroke-like syndromes in our series and in the literature. Despite the different indications, all patients had received brain radiotherapy. Central nervous system localizations of systemic malignancies represented the indication to brain irradiation in one quarter of cases (27% of patients in our series versus 26% in the literature). Radiotherapy was whole-brain or craniospinal in half the cases (52% of patients in our series versus 47% in the literature), which is remarkable considering the rarity of this treatment modality. The stroke-like episode occurred a decade after brain irradiation (median delay 10 years in our series versus 13 years in the literature), although delays as short as 9 months were also observed. Neurologists should keep in mind that stroke-like events are not exclusive to patients with primary brain tumors or to long-term survivors.

Neurological presentation was characterized by a mosaic of symptoms, of variable severity and duration. Stroke-like deficits were present in the vast majority of patients (77% of patients in our series versus 87% in the literature). Whenever present (35% of patients in our series versus 63% in the literature), seizures had a focal onset and arose from the same hemisphere responsible for stroke-like deficits. Encephalopathy, ranging from mild psychomotor slowing to severe vigilance impairment, was a frequent accompanying feature (50% of patients in our series versus 41% in the literature).

Acute enhancing MRI alterations, located multifocally in the white matter (ALERT, Fig. 1) or unilaterally in the cortical-subcortical region (SMART/PIPG, Fig. 2), were detected in the majority of patients (73% of patients in our series versus 86% in the literature). The remaining patients, including some with severe vigilance impairment (patients 2, 3, 5), had normal findings on MRI, highlighting that neither the presence nor the extent of acute MRI alterations correlates with clinical severity. Despite being reported as separate entities, in the present series SMART syndrome and PIPG were grouped in a common clinical–radiological category, based on the observation that they shared a common

pattern of unilateral cortical dysfunction, in contrast to ALERT patients who displayed a bilateral multifocal impairment.

Steroids are thought to accelerate recovery and thus are often administered in these conditions on empirical grounds. Sixty-five percent of stroke-like patients in our series (versus 28% in the literature) received high-dose steroid treatment. Steroid efficacy was evident in ALERT patients, who experienced rapid vigilance restoration within a few days from steroid introduction, whilst in patients with SMART syndrome or PIPG a neat temporal correlation between steroid introduction and clinical improvement could not be established. Brain irradiation has been associated with vasculitic changes within the wall of small and medium-sized vessels [7], and this might account for the efficacy of steroid treatment observed in ALERT cases. Antiplatelets were administered to three of the four patients with short-lasting focal deficits in our series under the assumption of an atherothrombotic mechanism, but this therapy did not prevent them from experiencing subsequent similar episodes. Their clinical characteristics, together with the lack of alternative causes, suggest that these episodes might correspond to amputated episodes of SMART lacking a radiological correlate.

Complete recovery was observed in 85% of patients in our series (versus 79% in the literature), although in some cases it took weeks to months to fully occur. Permanent neurological deficits concerned a non-negligible proportion of patients (15% in our series versus 21% in the literature), confirming that stroke-like syndromes are not always reversible as initially thought [2,4]. The occurrence of cortical infarcts is one, but not the sole, mechanism that can be responsible for permanent sequelae during SMART episodes (Fig. S2) [2]. Relapses were very common (62% in our series versus 56% in the literature), highlighting the need to elaborate adequate prevention strategies.

Patients with a history of brain irradiation seem prone not only to stroke-like events but also to actual strokes, and whether these two groups of conditions are related is still unclear. In our series, major strokes due to large vessel thrombosis were not observed. This probably reflects a selection bias, as all recruiting centers were neuro-oncology departments and therefore did not admit patients with large vessel strokes. All stroke cases in our series corresponded to small vessel infarcts attributed to previous brain radiation. Patients experiencing small vessel infarcts shared some common features with patients experiencing stroke-like events, including previous treatment modalities, acute clinical presentation and relapse rate. These similarities, together with the observation that some patients with stroke-like syndromes (patients 20, 26) also had antecedents of small vessel strokes, suggest that these two groups of conditions might share a common pathological substrate. This substrate could reside in the permanent endothelial dysfunction induced by radiation [8], leading alternatively to transient blood–brain barrier disruption (SMART syndrome) or to thrombosis and infarct (small vessel strokes). However, further evidence is needed to clarify the etiology of the syndromes and elaborate adequate prevention strategies.

Acknowledgements

Anna Luisa Di Stefano was supported by Premio Riquier. The study had no targeted funding.

Disclosure of conflicts of interest

The authors declare no financial or other conflicts of interest.

Supporting Information

Additional Supporting Information may be found in the online version of this article:

Figure S1. This flow chart illustrates the algorithm followed to select literature cases.
Figure S2. SMART episode with cortical infarct (patient number 20).
Table S1. Previous tumor history, clinical and paraclinical features at the time of the acute episode, treatment and outcome in the 87 patients with stroke-like syndromes identified in literature.

References

1. Black DF, Bartleson JD, Bell ML, Lachance DH. SMART: stroke-like migraine attacks after radiation therapy. *Cephalalgia* 2006; **26:** 1137–1142.
2. Black DF, Morris JM, Lindell EP, *et al.* Stroke-like migraine attacks after radiation therapy (SMART) syndrome is not always completely reversible: a case series. *AJNR Am J Neuroradiol* 2013; **34:** 2298–2303.
3. Rheims S, Ricard D, van den Bent M, *et al.* Peri-ictal pseudoprogression in patients with brain tumor. *Neuro Oncol* 2011; **13:** 775–782.
4. Di Stefano AL, Berzero G, Vitali P, *et al.* Acute late-onset encephalopathy after radiotherapy: an unusual life-threatening complication. *Neurology* 2013; **81:** 1014–1017.
5. Kreisl TN, Toothaker T, Karimi S, DeAngelis LM. Ischemic stroke in patients with primary brain tumors. *Neurology* 2008; **70:** 2314–2320.
6. Plummer C, Henderson RD, O'Sullivan JD, Read SJ. Ischemic stroke and transient ischemic attack after head and neck radiotherapy: a review. *Stroke* 2011; **42:** 2410–2418.
7. Rauch PJ, Park HS, Knisely JP, Chiang VL, Vortmeyer AO. Delayed radiation-induced vasculitic leukoencephalopathy. *Int J Radiat Oncol Biol Phys* 2012; **83:** 369–375.
8. Hopewell JW, van der Kogel AJ. Pathophysiological mechanisms leading to the development of late radiation-induced damage to the central nervous system. *Front Radiat Ther Oncol* 1999; **33:** 265–275.

Acknowledgements

Thanks to the Mondino Foundation for the scholarship that allowed me to carry on my studies and complete my PhD. Thanks to my tutor, Enrico Marchioni, for his guidance in this journey.

Thanks to all my colleagues and friends at Mondino Foundation.

Thanks to Marc Sanson, Anna Luisa Di Stefano, and Dimitri Psimaras, who have taught and supported me tirelessly during my years of research at Pitié-Salpêtrière. Thanks to Jean-Yves Delattre, a great mentor, and an even greater man.

Et ventis adversis.